COMPUTATIONAL AND EXPERIMENTAL MODELLING OF THE HUMAN UPPER AIRWAY ACOUSTICS WITH APPLICATION TO OBSTRUCTIVE SLEEP APNEA DIAGNOSIS DURING WAKEFULNESS

By

Walid Hicham Ashraf

A Thesis submitted to the Faculty of Graduate and Postdoctoral Studies of

The University of Manitoba

in partial fulfillment of the requirements of the degree of

DOCTOR OF PHILOSOPHY

Biomedical Engineering Program

University of Manitoba

Winnipeg, Canada

ABSTRACT

Obstructive Sleep Apnea (OSA) is a highly prevalent sleep-related breathing disorder characterized by repetitive upper airway collapse during sleep. Despite its clinical significance, current diagnostic techniques remain resource-intensive and often inaccessible. This thesis proposes two modelling approaches aimed at characterizing upper airway acoustics and investigates their potential application as non-invasive, quick and reliable OSA diagnosis during wakefulness.

The first approach involves a hybrid aero-acoustic simulation framework that decouples airflow dynamics and sound propagation. Using patient-specific airway geometries reconstructed from high-resolution CT scans, Large Eddy Simulation (LES) was employed to model unsteady inspiratory flow. Aero-acoustic sources were extracted using Lighthill's analogy and mapped onto a finite element mesh to solve the wave equation for acoustic propagation. This enabled detailed analysis of how anatomical features—including velopharyngeal, oropharyngeal, and tracheal constrictions—alter airflow patterns, acoustic pressure distribution, and resonance frequencies at the trachea. The results demonstrated strong correlations between geometrical narrowing and frequency shifts in tracheal breathing sound spectra.

The second approach develops an empirical acoustic transfer function estimation between the mouth and the trachea during controlled wakefulness breathing. Participants were exposed to broadband and chirp input signals at the mouth, and tracheal responses were recorded to estimate the transfer function. A novel piezoelectric contact microphone was developed to record the sounds with minimal background interference. Statistical analysis revealed repeatable and individualized transfer functions, with significant spectral variations corresponding to anatomical differences and potential airway obstruction.

Together, these approaches provide a comprehensive understanding of the relationship between the upper airway anatomy, airflow mechanics, and the spectral content of breathing sounds. The findings support the feasibility of using tracheal acoustic responses during wakefulness for OSA diagnosis. In addition, they provide mechanistic insights into OSA pathophysiology by linking specific acoustic signatures to underlying anatomical abnormalities. This enables not only OSA classification, but also identification of the likely anatomical contributors to obstruction in each case. Such individualized insights advance the understanding of the disorder mechanism and pave the way for more targeted, personalized therapeutic strategies. Furthermore, the methodology establishes the groundwork for developing accessible, non-invasive, and personalized screening tools for sleep-disordered breathing.

ACKNOWLEDGEMENT

First and foremost, I would like to express my deepest gratitude to my supervisor, **Prof. Zahra Moussavi** for her unwavering guidance, support, and encouragement throughout my research journey. Her expertise, critical insights, and assistance have been instrumental in shaping this work and in my development as a researcher.

I am also sincerely grateful to the members of my advisory committee, **Prof. Brian Lithgow**, and **Prof. Adrian West**, for their constructive feedback, valuable discussions, and continued support throughout the various stages of my thesis. My gratitude is extended to **Prof. Jeffrey Fredberg** for his insightful advice and generous academic support.

I wish to acknowledge **Research Manitoba**, **Mathematics of Information Technology and Complex Systems (MITACS), and the Faculty of Graduate Studies of the University of Manitoba** for providing the financial support that made this research possible. I am also thankful to **Sir Gordon P. Osler** for establishing a graduate scholarship at the University of Manitoba, which further supported my academic pursuits.

Special thanks go to my colleagues in the **Acoustic Team** for their collaboration, encouragement, and for fostering a positive stimulating research environment.

Lastly, I also extend my appreciation to **the participants** involved in the experimental and clinical aspects of this research. Without their involvement, this study would not have been possible.

To my wife, daughter, and son
For your endless love, patience and encouragement.

And to my parents and sister
For laying the foundation of my journey with your unwavering support.

CONTRIBUTION OF AUTHORS

This dissertation is presented as a combined (sandwich) thesis and consists of five individual papers; each prepared as part of the author's doctoral research under the supervision of Prof. Zahra Moussavi. Four of these papers (Chapters Four, Five, Six and Seven) have been published in peer-reviewed journals and one manuscript (Chapter Three) has been published in peer-reviewed conference proceedings.

Mr. Walid Ashraf has been the main contributor and first author of all the manuscripts presented in this thesis. His contributions to the work include developing the research questions, designing and conducting experiments, simulations, and validation, performing data analysis, interpreting results, and drafting and revising the manuscripts. He was also responsible for integrating clinical and engineering aspects of the studies and ensuring that all methodological and ethical standards were met. **Prof. Zahra Moussavi**, as the principal supervisor, provided continuous guidance on the conceptual development of the research, interpretation of results, and manuscript revisions. She also contributed to the refinement of research objectives and obtaining ethics approval. **Prof. Jeffrey Fredberg** assisted in data validation and reviewing the manuscripts in Chapter Four and Five.

Prof. Brian Lithgow assisted in reviewing the manuscript in Chapter Seven. **Dr. Ahmed Elwali** and **Mr. Ali Alqudah** contributed to conceptualization of the manuscript in Chapter Seven. **Mr. Matthew Band** and **Ms. Lingyu Zhao** contributed to data collection in the manuscript in Chapter Seven.

TABLE OF CONTENTS

LIST OF TABLES

LIST OF FIGURES

LIST OF ABBREVIATIONS

OSA	Obstructive sleep apnea
EEG	Electroencephalogram
EOG	Electrooculography
ECG	Electrocardiogram
EMG	Electromyography
PSG	Polysomnography
AHI	Apnea-Hypopnea index
BMI	Body mass index
TBS	Tracheal breathing sounds
CT	Computed Tomography
MRI	Magnetic Resonance Imaging
PAP	Positive airway pressure
CFD	Computational Fluid Dynamics
Re	Reynolds Number
RANS	Reynolds-Averaged Navier-Stokes
FSI	Fluid-Structure Interaction
P_{crit}	Critical Closing Pressure
MAS	Mandibular Advancement Splint
MARPE	Miniscrew-Assisted Rapid Palatal Expansion
FEM	Finite Element Modelling
REM	Rapid Eye Movement

LES	Large Eddy Simulation
DNS	Direct Numerical Simulation
FW-H	Ffowcs Williams–Hawkings
FFT	Fast Fourier Transformation
C_p	Coefficient of Pressure
CSA	Cross-Sectional Area
APE	Acoustic Perturbation Equations
UA	Upper Airway

CHAPTER ONE: MOTIVATION AND RESEARCH OBJECTIVES

1.1 Motivation

Obstructive sleep apnea (OSA) remains a major health challenge worldwide, yet current diagnostic methods are slow, costly, and resource-intensive. Polysomnography (PSG), the diagnostic gold standard, provides accurate classification of OSA severity but requires overnight monitoring in specialized facilities, contributing to long delays in diagnosis and treatment initiation. These limitations emphasize the urgent need for faster, more accessible, and non-invasive screening tools with comparable accuracy to PSG, while providing insight into the pathophysiology of OSA.

Tracheal breathing sounds (TBS) recorded during wakefulness is a promising alternative. TBS acquisition is simple, rapid, and inexpensive, making it feasible for large-scale screening. However, while spectral features of TBS have been shown to distinguish OSA from non-OSA with encouraging accuracy, their physiological interpretation remains limited. Specifically, the influence of anatomical variations in the upper airway on the acoustic properties of TBS remains insufficiently characterized, and this lack of mechanistic understanding constrains the diagnostic and clinical utility of sound-based methods.

Computational and experimental models provide an opportunity to bridge this gap by linking airway structure, airflow dynamics, and acoustic signatures. This dissertation proposes two modelling approaches: (1) a hybrid aero-acoustic simulation framework to model and validate the generation and propagation of tracheal breathing sounds, and (2) an empirical methodology for estimating the acoustic transfer function of the upper airway. Together, these approaches aim to improve the interpretability and diagnostic accuracy of TBS, provide mechanistic insights into the

anatomical determinants of OSA, and lay the groundwork for accessible, personalized, reproducible, and non-invasive diagnostic strategies.

1.2 Goals and objectives

Although considerable effort has been made to acoustically model the upper airway, existing approaches have several limitations. Many models are based on simplified geometries that fail to capture the anatomical complexity and inter-patient variability of the human airway. Critical structural features such as asymmetries in the nasal passage, and variable pharyngeal constrictions are often excluded, despite their critical roles in airflow behaviour and sound generation. Moreover, most existing studies either lack experimental validation or validate their models using idealized or oversimplified airway geometries, limiting their clinical relevance. Importantly, the relationship between upper airway anatomy and the characteristics of TBS remains underexplored. In addition, while TBS has been proposed as a non-invasive tool for screening OSA, most classification approaches rely on spectral features, without linking them to specific anatomical or physiological characteristics, limiting interpretability and diagnostic precision.

Furthermore, although the typical frequency content of TBS lies within the [100–3000] Hz range [1], a model that enables extraction of information of the upper airway across a broader frequency spectrum could provide deeper insight into upper airway function and pathology. Therefore, the primary goal of this dissertation is to develop an anatomically accurate aero-acoustic model of the upper airway capable of simulating tracheal breathing sounds and to investigate the influence of the anatomical features such as pharyngeal constriction size and location, and tracheal length on the simulated sounds. Furthermore, this dissertation has a secondary goal to formulate an empirical acoustic transfer function of the upper airway that is robust and consistent across an extended frequency range (up to 5000 Hz), enabling the extraction

of clinically relevant information and supporting potential OSA classification. To achieve these goals, the specific objectives are as follows:

Primary goal: Developing an anatomically accurate aero-acoustic model of the upper airway.

Objective 1.1: **Develop and experimentally validate an aero-acoustic model of a simplified tube with a constriction.**

As an initial step toward validating the aero-acoustic simulation framework, this objective involves simulating sound generation due to airflow through a simplified tube with a geometric constriction. The primary aim is to iteratively refine the numerical methodology by benchmarking it against controlled experimental results. An experimental setup will be constructed to systematically investigate the influence of various constriction sizes on the resulting acoustic spectra. This approach will provide fundamental insights into the effects of flow disturbances caused by geometric features and serve as a foundational step before extending the model to anatomically realistic upper airways.

Objective 1.2: **Develop an aero-acoustic model of a realistic upper airway of a healthy participant and validate TBS clinically (in-vivo).**

This objective extends the validated modelling framework to anatomically realistic upper airway geometries obtained from CT scan of a healthy participant. Simulations will be conducted under physiologically relevant boundary conditions, and their acoustic output will be compared with in-vivo TBS recordings obtained from the participant. The purpose is to establish a reliable modelling platform that replicates real-life breathing acoustics.

Objective 1.3: **Investigate the influence of anatomical features on the simulated breathing sounds.**

To better understand the relationship between upper airway morphology and acoustic output, a series of sensitivity analyses will be carried out by systematically altering key anatomical features within the aero-acoustic model. Parameters such as the size and location of pharyngeal constrictions and tracheal length will be modified, based on clinically observed characteristics from individuals with OSA, to assess their effect on the simulated TBS spectrum. Quantifying these effects will help identify which anatomical variations most significantly influence acoustic characteristics, ultimately contributing to the interpretability and diagnostic relevance of TBS simulations.

Objective 1.4: **Extend the aero-acoustic model to a realistic upper airway of an OSA participant and assess the effectiveness of the anatomical features detected.**

An anatomically accurate model of the upper airway from a participant diagnosed with OSA is reconstructed and integrated into the aero-acoustic simulation framework. The anatomical features, identified in Objective 1.3 as influential, will be specifically examined in the context of this OSA participant's airway geometry. Their individual and combined effects on the simulated tracheal breathing sounds will be evaluated to determine whether the acoustic signatures predicted by the sensitivity analyses are manifested in the OSA case. This analysis will help validate the role of these features in real clinical cases and assess their potential as acoustic biomarkers for OSA.

Secondary goal: Formulate an empirical acoustic transfer function of the upper airway.

Objective 2.1: **Design and test a contact-based piezoelectric microphone for robust TBS recording and empirical transfer function setup.**

A contact-based piezoelectric microphone is developed and tested to accurately capture body-conducted sounds with minimal interference from environmental and background noise. This microphone serves two critical purposes. First, it plays a central role in the experimental setup

for estimating the acoustic transfer function of the upper airway. In this setup, a known sound is introduced through a speaker positioned in the participant's mouth, and the resulting output is recorded at the suprasternal notch. To ensure that the captured signal represents sound transmitted through the airway, and not contaminated by airborne sound from the speaker, effective isolation from external noise is essential. Second, the microphone is used to record TBS while suppressing airborne sound generated at the mouth or nose.

Objective 2.2: **Develop an empirical acoustic transfer function of the upper airway of healthy individuals and assess its intra-day and inter-day consistency.**

The upper airway can be treated as an acoustic filter that shapes the frequency content of sounds propagating from the mouth/nose to the trachea. Using controlled input signals (e.g. white noise) introduced orally and recordings obtained from the contact piezo-electric microphone placed at the suprasternal notch, an empirical transfer function can be estimated for each participant. The repeatability of this test is assessed intra-day and inter-day to select the most consistent protocol.

Objective 2.3: **Examine correlations between transfer function parameters and participant demographics, to evaluate the potential of the model in personalized diagnosis or classification of OSA.**

The transfer function parameters reflect the individual's airway morphology. A statistical analysis is conducted to explore how the empirical transfer function relates to participants' demographics (e.g. BMI, height and neck circumference). The objective is to assess whether the acoustic transfer function can serve as a personalized diagnostic signature for airway health and OSA classification.

1.3 Thesis Structure

This dissertation is organized into eight chapters and two appendices.

Chapter One provides the motivation of this work, and outlines the goals, specific research objectives, and the scope of the study.

Chapter Two provides the foundation for this work. It begins with an introduction to tracheal breathing sounds and their clinical significance, particularly in the context of OSA. A comprehensive literature review follows, summarizing existing approaches in both experimental and computational modelling applied to the upper airway. The key research gaps and challenges in simulating and interpreting TBS are identified.

The following five chapters consist of 5 individual manuscripts; four published in peer-reviewed journals and one published in peer-reviewed conference proceedings.

Chapter Three **partially** addresses **objective 1.1** and presents an experimental study that investigates the relationship between airflow and sound generation in a simplified airway model with a constriction. A 3D-printed tube with varying circular constrictions was used to mimic changes in airway constriction in a simplified manner, with tracheal breathing sounds recorded at multiple locations under different flow rates. This foundational study highlights the influence of localized airway narrowing on sound characteristics and sets the stage for further modelling of flow-acoustic interactions in anatomically realistic upper airway geometries.

Chapter Four addresses **objective 1.1**, **objective 1.2** and **partially objective 1.3** by outlining the simulation methodology used to model sound generation and propagation in simplified tube with a constriction. The computational framework, including the governing equations, turbulence models, mesh generation, and acoustic analogy is described. The chapter also covers the boundary conditions applied in both flow and acoustic simulations and explains

the procedures used to validate simulation results against experimental data. Building upon this validated framework, the methodology is extended to an anatomically realistic upper airway model reconstructed from high-resolution CT scan data. The anatomical model is meshed and simulated under conditions mimicking physiological inspiration. The resulting flow and acoustic fields are analyzed, and simulated TBS are compared with actual tracheal recordings obtained from the healthy individual. Key aerodynamic features (e.g., turbulence zones, pressure drops, coefficient of pressure) and their associated acoustic emissions are explored. This chapter demonstrates the capability of the proposed model to replicate clinically relevant sound characteristics, representing a significant validation step in the development of the aero-acoustic simulation framework.

Chapter Five addresses **objective 1.3 and objective 1.4** by investigating the influence of specific anatomical features on the simulated TBS. Using systematic modifications in the upper airway geometry, sensitivity analyses are performed to assess how these morphological parameters, such as regional narrowing and airway length, alter both the aerodynamic behavior and the resulting acoustic spectrum. The chapter explores how changes in airway shape and constriction severity impact turbulence intensity, airway resistance, and spectral content of the generated sounds. The findings contribute to a deeper understanding of the role of anatomical features in shaping the TBS spectrum and support the identification of potential acoustic biomarkers for detecting and characterizing upper airway abnormalities.

Chapter Six addresses **objective 2.1** and presents the design and testing of a custom contact piezoelectric microphone optimized for tracheal sound recording. The design emphasizes minimal susceptibility to ambient and background noise by capturing vibrations transmitted through the skin rather than airborne sound. The microphone is tested under controlled conditions to assess its sensitivity, frequency response, and robustness. The results demonstrate the

microphone's reliability and accuracy in capturing TBS, establishing its essential role in the subsequent transfer function experiments and clinical studies.

Chapter Seven addresses **objective 2.2 and objective 2.3** and focuses on the empirical characterization of the acoustic transfer function of the upper airway in healthy individuals. Using the custom-built contact microphone, controlled input signals are introduced through the mouth, and the resulting tracheal outputs are recorded. The estimated transfer function is analyzed to understand how sound propagates through the airway and is shaped by anatomical structures.

The chapter evaluates the reproducibility of the transfer function by assessing its consistency within a single day (intra-day) and across multiple days (inter-day). These findings offer important insights into the stability and diagnostic potential of the upper airway transfer function, laying the groundwork for potential applications in OSA screening and classification.

Chapter Eight concludes the work and summarizes the main findings and contributions of the research. The chapter also reflects on the limitations of the current study and suggests directions for future work.

Appendix A presents the governing equations and numerical modelling approaches used in the computational fluid dynamics (CFD) simulations. It includes detailed formulations for both Reynolds-Averaged Navier–Stokes (RANS) and Large Eddy Simulation (LES) models, as well as the theoretical foundation of Lighthill's acoustic analogy for aero-acoustic source prediction.

Appendix B provides supplementary visualizations from the aero-acoustic simulations of the simplified tube model. It includes additional contour plots of flow and acoustic fields that support the results discussed in Chapter Three, offering further insight into the spatial distribution of key aerodynamic and acoustic variables.

CHAPTER TWO: INTRODUCTION AND BACKGROUND

2.1 Background

Sleep apnea is a prevalent, underdiagnosed sleeping disorder associated with several clinical conditions such as cardiovascular disease, depression, diabetes and daytime hypersomnolence [2], [3]. It is characterized by a complete (apnea) or partial (hypopnea) cessation of breath during sleep that lasts > 10 sec and is associated with >3% drop in blood oxygen saturation [4]. There are three types of sleep apnea: Central sleep apnea, obstructive sleep apnea (OSA), and mixed sleep apnea [5]. Central sleep apnea is characterized by a temporary cessation of respiratory effort due to diminished neural output from the brainstem [2], while OSA – accounting for approximately 84% of sleep apnea cases [6] – occurs due to the partial or complete collapse of the upper airway during sleep. Mixed sleep apnea features characteristics of both central sleep apnea and OSA. This dissertation focuses on OSA, given its higher prevalence and clinical significance.

2.1.1 Clinical Presentation of OSA

OSA is typically characterized by a range of nocturnal and daytime symptoms resulting from repeated episodes of the upper airway obstruction during sleep. Common nocturnal symptoms include habitual loud snoring, gasping or choking during sleep, and frequent nocturnal awakenings. These episodes lead to fragmented sleep and reduced oxygen saturation. As a result, patients often experience excessive daytime sleepiness, morning headaches, impaired concentration, irritability, and fatigue [7]. In severe cases, untreated OSA can significantly affect quality of life, and it is associated with cognitive dysfunction, mood disturbances, and increased risk of motor vehicle accidents [8]. Furthermore, several demographic and anthropometric

factors—such as age, body mass index (BMI), male sex, and neck circumference—have been shown to correlate significantly with the presence and severity of OSA [9]. The severity of OSA is quantified using the Apnea-Hypopnea Index (AHI), defined as the number of apneas and hypopneas per hour of sleep. Based on AHI values, OSA patients are categorized as mild (5–15 events per hour), moderate (15–30 events per hour), or severe (>30 events per hour). AHI is typically measured during an overnight sleep study known as polysomnography (PSG).

2.1.2 Screening and Diagnosis

PSG is considered the gold standard for sleep apnea diagnosis. It involves comprehensive overnight monitoring, including electroencephalography (EEG), electrooculography (EOG), electrocardiography (ECG), electromyography (EMG), respiratory airflow, oxygen saturation, and thoracoabdominal movements. While PSG provides a high level of diagnostic accuracy, it is associated with several limitations: It is expensive, time-consuming, and requires specialized equipment and trained personnel. For that reason, patients often face long wait times; exceeding 12 months in some locations in Canada [10], while in Manitoba the waitlist can reach up to 5,000 patients [11]. Therefore, OSA imposes a high economic burden on the healthcare system, accounting for billions of dollars annually in both direct and indirect costs [3], [12].

Notably, while numerous portable monitoring devices have been developed for the diagnosis of OSA, they still require overnight recordings and subsequent verification by a trained sleep specialist or respirologist [13]. Thus, fast screening questionnaires (e.g., Epworth sleepiness score, STOP-Bang, Berlin, etc.) are commonly used based on the aforementioned correlated parameters such as age, gender, weight, and smoking history. While these questionnaires demonstrate high sensitivity, their specificity remains very low, approximately 36% [14]. This

challenge is particularly critical in preoperative settings, where undiagnosed OSA significantly increases perioperative risk [15]. Since there is usually insufficient time to conduct PSG, anesthesiologists often depend on questionnaires, which can lead to inefficient allocation of perioperative resources. Therefore, there is a need for a screening tool that addresses the limitations of both polysomnography (PSG), namely its high cost, lengthy wait times, and requirement for specialized expertise, and questionnaire-based methods, which are limited by very low specificity.

Recently, several studies have explored the potential of tracheal breathing sounds (TBS) [16], [17], [18] and voice analysis [19], [20] as diagnostic tools for OSA diagnosis during wakefulness. The underlying hypothesis of these studies is based on the existence of anatomical and morphological differences between OSA and non-OSA individuals reported in [21], [22]. Increased pharyngeal length, higher dilator muscle activity, and longer/thicker soft palate were observed in OSA individuals [22]. These characteristics imply a narrower (higher collapsible) airway cavity and higher tissue stiffness for OSA individuals, which can be detected by breathing sounds generated due to airflow turbulence in the upper airway during wakefulness.

As air moves through the airway, it interacts with the surrounding anatomical structures, producing turbulence and pressure fluctuations that generate acoustic signals. In OSA patients, the altered airway geometry modifies the acoustic properties of these sounds. These differences can be captured and analyzed through signal processing techniques to identify distinctive spectral features associated with OSA. For instance, the study in [17] demonstrated that TBS analysis during wakefulness could classify between OSA and non-OSA with an accuracy of 81.1%, with a sensitivity of 84.4% and a specificity of 77%. Similarly, an accuracy of 83.92% was reported in [16] using TBS spectral features alone, which increased to 84.53% when combined with anthropometric features such as BMI, age, and gender. Two sound features identified in their study

were: (1) the ratio of the mean summed power spectra of the inspiration and expiration phases in the 130–250 Hz band to the 1200–1300 Hz band while breathing through the mouth, (2) the slope of the power spectrum of the inspiration phase in 210–350 Hz band, also during mouth breathing. In another study [23], an accuracy of 86.4% was achieved, with a sensitivity of 84.6% and a specificity of 88.9%. Their algorithm utilized the fourth formant frequency of breathing sounds and breath-to-breath variability of its amplitude as spectral features, along with BMI as an anthropometric parameter. Despite these promising results, the physiological interpretation of the extracted spectral features and their direct association with airway collapse remains insufficiently explored. Moreover, the specific effects of morphological changes in the upper airway on TBS have not yet been thoroughly investigated, highlighting the need for further research in this area.

2.1.3 Clinical Challenges in OSA Treatment

The detailed mechanism of the upper airway collapse in OSA remains unclear. In particular, the exact location of airway occlusion and its association with the physiological and anatomical factors influencing are in question. Different methods, such as fluoroscopy, nasopharyngoscopy, pressure measurements, computed tomography (CT) scanning, and magnetic resonance imaging (MRI), have been used to extract the precise location of the collapse. However, these methods are time-consuming, expensive, and not readily available in clinical settings.

Consequently, due to lack of a complete knowledge of the pathophysiology of the sleep apnea, no current treatment method has been shown to be capable of completely eliminating OSA. Although continuous positive airway pressure (CPAP) therapy is considered the gold standard treatment, with a success rate of approximately 50% [24], its long-term adherence and effectiveness are limited. Nevertheless, the CPAP is an OSA management regardless of knowing

the main cause of the OSA. That said, alternative treatments do exist, including surgical interventions such as maxillomandibular advancement, uvulopalatopharyngoplasty, nasal surgery, tongue base reduction, or genioglossal advancement [25], [26]. However, these approaches often exhibit variable and generally low success rates, which can result in challenging clinical decision-making. The variable success rate in OSA treatment is largely influenced by the limited accessibility of simple, scalable, non-invasive tools for patient-specific endotyping [27], [28]. While airway collapse is recognized as the hallmark of OSA, the precise mechanisms underlying this collapse, such as the location of obstruction, the role of tissue compliance, and the contribution of regional airway narrowing, remain poorly defined. Furthermore, OSA is a heterogeneous disorder [29]; patients may present with varying sites of collapse (velopharyngeal, oropharyngeal, or multi-level), different airway shapes, and distinct patterns of airflow obstruction. Without a reliable tool to characterize these morphological variations, treatment selection often relies on trial-and-error, contributing to variable and often low success rates of interventions such as surgery or oral appliances. For example, procedures like uvulopalatopharyngoplasty may fail if the primary site of obstruction or narrowing is not identified [30]. Therefore, there is a need for diagnostic and research tools capable of quantitatively characterizing upper airway morphology and linking these structural features to airflow dynamics and acoustic signatures. Such tools would not only improve mechanistic understanding of OSA pathophysiology but also support personalized treatment planning and enhance therapeutic outcomes. Given the aforementioned limitations, computational modelling and numerical simulations have emerged as promising tools to enhance our understanding of upper airway mechanics in obstructive sleep apnea (OSA).

2.1.4 Computational Modelling of The Upper Airway

Due to the complexity of the upper airway structure, establishing a quantitative relationship between airway structure and function remains challenging [31]. In recent years, numerical simulations have become a prominent tool for exploring various biomechanical and physiological processes. Researchers have employed a range of computational modelling techniques to elucidate the mechanisms of pharyngeal airway collapse, examine the interaction between airflow dynamics and airway deformation, evaluate the effectiveness of OSA treatment strategies, and simulate the aero-acoustic behaviour of the airway.

2.1.4.1 Application of Computational Fluid Dynamics

One commonly used approach involves computational fluid dynamics (CFD), which is crucial in characterizing airflow patterns within the upper airway. The breathing airflow within the human upper airway is inherently complex and can exhibit laminar, transitional, or turbulent flow regimes depending on the local geometry, flow rate, and physiological conditions [32]. For simplicity, some studies have employed a laminar flow model, assuming a low Reynolds number ($Re < 2000$) throughout the upper airway [33], [34], [35], [36]. However, this simplification may not accurately capture the airflow behaviour in all regions of the upper airway, particularly where anatomical narrowing leads to flow acceleration and transition from laminar to turbulent regimes. Consequently, turbulence models are more suitable for analyzing airflow characteristics in the pharyngeal airway, where intricate flow patterns and instabilities often occur. The study in [37] investigated the aerodynamic characteristics of 58 individuals with mild, moderate and severe OSA using steady-state Reynolds-Averaged Navier Stokes (RANS), κ- ω shear stress transport turbulence model. The mean velocity was higher in patients with severe OSA compared to those

with mild and moderate conditions. Furthermore, they identified a statistically significant correlation between AHI and both the maximum velocity and the airway resistance. Airway resistance is typically calculated using Eq. 2-1:

$$R = \frac{\Delta P}{Q} \qquad 2\text{-}1$$

Where ΔP is the pressure drop between the inlet and the outlet boundaries, and Q is the volumetric flow rate. Furthermore, recent advancements in computational modelling have yielded valuable insights into the impact of therapeutic interventions on upper airway dynamics, demonstrating how numerical simulations can inform clinical practices and support the development of personalized treatment strategies. For instance, the study in [38] employed CFD to investigate the impact of oral appliance therapy on the upper airway in OSA patients. Before treatment, regions of low pressure were identified in the velopharynx, oropharynx and hypopharynx, with the most pronounced drop observed in the velopharynx region – an area particularly susceptible to airway collapse. Although the overall pressure profile remained similar following treatment, the pressure gradients were significantly reduced, indicating improved airway stability. Notably, the study also reported a strong correlation between the change in AHI and the change in the square root of the maximum pharyngeal pressure drop across seven OSA participants, reinforcing the potential of CFD as a predictive tool for treatment efficacy.

However, a key limitation of CFD models is the assumption of rigid walls in the airway, thus preventing a comprehensive explanation for airway occlusion. Therefore, to address the compliance and collapsibility of the airway soft tissue, a more accurate modelling tool, such as fluid-structure interaction (FSI), has been used.

2.1.4.2 Application of Fluid-Structure Interaction

FSI framework enables the simulation of interactions between dynamic airflow and the compliant soft tissues that compose the upper airway, revealing critical insights into airflow characteristics, tissue deformation, and the effectiveness of various treatment options for OSA [39]. One application of FSI involves elucidating the mechanisms of pharyngeal airway collapse. The study in [40] demonstrated that airway collapse can result from a positive feedback loop between the deformation of the anterior airway wall and the pressure gradient across the airway cross-section. The study identified that the pressure differential between the anterior and posterior walls leads to a narrowing of the airway, with the anterior wall playing a dominant role in collapse dynamics. It is known that the pressure difference between mouth/nasal passage and the alveoli affects the airway resistance. Notably, the curvature of the anterior wall was found to correlate with OSA, suggesting that patients with narrower airway or larger airway wall curvature are more vulnerable to obstruction. The work in [41] adopted a 3D FSI model to investigate the mechanism of pharyngeal collapse and snoring. The results showed that airway occlusion could occur at the region of the velopharynx in the absence of neurological control and gravity due to the high negative static pressure at this location during inspiration. The study also observed a minor deformation of the velopharyngeal wall during expiration, attributed to a reduction in outward pressure forces. In [42], the pharyngeal collapse of the passive movement of the soft palate during calm respiration was simulated using a 3D FSI model . Their study revealed that airway narrowing can also occur during expiration due to posterior displacement of the soft palate, causing a narrowing in the airway between the soft palate and the posterior pharyngeal wall. The same finding was previously reported by [43] who simulated soft palate deformation before and after nasal surgery. Similarly, the study in [44] reported that soft palate deformation is more pronounced

during expiration than inspiration. Their results suggested that complete airway obstruction is more likely in narrower airways, where the posterior wall displaces significantly toward the soft palate. In addition, partial obstruction was observed under the same conditions in models with wider airways.

Anatomical variation also influences airway collapse sites. Previous work [45] investigated the effect of skeletal deformity on the prevalence of OSA using an FSI model. By simulating the upper airway of a patient with mandibular retrusion, they found that the airway occlusion tended to occur between the epiglottis and the oropharynx. This was attributed to a localized region of minimum pressure. Their findings were consistent with those reported in [46], which showed that although the velopharynx showed minimal displacement, a substantial pressure drop in that region led to airway collapse at the oropharyngeal segment. Similarly, substantial deformation along the airway between the nasal cavity and the trachea was reported in [47] . Interestingly, the location of maximum deformation did not correspond to the region of minimum pressure, which was instead found near the laryngeal-tracheal junction. This suggests that the site of minimum pressure alone may not reliably predict the actual location of airway collapse.

Additionally, sleeping position may play an important role in airway deformation and the onset of obstruction. In biomechanical modelling, sleeping posture is typically represented by the application of gravitational forces [39]. The study in [48] demonstrated that the pharyngeal deformation was significantly influenced by the Young's modulus of the tongue and soft palate when gravitational effects were included in the simulation. This deformation was not observed in the absence of gravity, highlighting the importance of posture in OSA pathophysiology. Furthermore, their results showed that in the supine position, airway obstruction may not solely

result from negative pressure during inspiration; the gravitational weight of the tongue can also contribute to airway collapse by displacing soft tissues posteriorly.

Snoring has also been regarded as a preliminary indicator of OSA. Using a 3D FSI model, the study in [41] predicted soft palate flutter with a dominant frequency of 17.8 Hz. Interestingly, their simulation identified snoring as occurring during the expiratory phase through the nasal cavity, in contrast to the more commonly reported inspiratory snoring in clinical observations. The authors attributed this discrepancy to the application of a closed oral cavity boundary condition in their model. However, the physiological implications of this boundary condition—and how it might influence the timing and mechanism of snoring—were not thoroughly addressed in their study.

Furthermore, a sensitivity study was conducted in [49] to explore the effects of the mechanical properties of the airway's tissue, tongue, and soft palate on airway collapsibility. Their findings indicated that the collapse pressure was most sensitive to the Young's modulus of the tongue. Similarly, the study in [42] compared two linear models with different soft palate stiffness and observed greater compliance and deformation in the model with a lower Young's modulus. They concluded that soft tissue stiffness could serve as an indicator of airway compliance. It is important to note that most computational studies have employed simplified assumptions, typically modelling upper airway tissues as linear elastic materials using previously reported values for Young's modulus and Poisson's ratio. However, other studies have implemented more realistic material behaviour. For instance, the soft tissue of the upper airway was considered as viscoelastic, or, quasi-incompressible material, reflecting their high water content and associated high Poisson's ratio [40], [50], [51]. In [52], the viscoelastic properties of the soft tissue were derived ex-vivo by accounting for their non-linear properties, while the work in [53] used magnetic resonance

elastography to measure the viscoelastic properties of the tongue and soft palate in vivo. However, tissue mechanical properties are patient-specific, resulting in inaccurate simulation outcomes when incorporating universal properties. Consequently, some research groups have included the hyper-elasticity behaviour of the soft tissues of the airway in their models. For instance, Yeoh and Ogden hyper-elastic models were employed in [54] to characterize the soft palate and tongue mechanics more accurately.

Furthermore, several studies considered the effect of the nasal cavity on the airflow field. The study in [41] concluded that the nasal valve plays a significant role in airflow resistance and reported that pressure drops across the nostrils accounted for approximately half of the total pressure drop across the upper airway. This finding was supported in [55], where 50% pressure reduction was observed when the nasal cavity was omitted from their model. Similarly, the study in [56] incorporated the nasal cavity into both numerical and experimental models to assess the impact of nasal resistance on airway collapsibility, showing that reduced nasal resistance increased the peak flow rate in a collapsible airway—highlighting its significant influence on the pressure field. Conversely, the nasal cavity was excluded from the simulation in [45] assuming that the pressure change within the nostrils was negligible, contributing less than 10% of the total pressure drop within the pharyngeal region. This simplification was supported in [57] where a CFD study was conducted using anatomically accurate airway models and noted that, although the nasal cavity can introduce turbulence upstream of the pharynx and its exclusion may lead to unrealistic upstream pressure profiles, its inclusion had minimal effect on downstream airflow results. The study in [57] suggested a simplification of the nasal cavity to a convergent channel capable of reproducing the correct flow conditions upstream of the pharynx. This finding was later adopted in [58] to reduce the computational cost. Overall, the inclusion or simplification of the nasal cavity

in airway modelling remains dependent on the specific objectives of the study, with previous works demonstrating both physiological benefits and computational trade-offs.

One of the most clinically relevant metrics used to quantify the mechanical stability of the pharyngeal airway is the critical closing pressure, or P_{crit}. The critical pressure (P_{crit}) is defined as the pharyngeal pressure drop at which airway collapse occurs with a cessation of airflow [59]. In general, non-OSA subjects tend to exhibit a sub-atmospheric P_{crit}, whereas OSA subjects tend to have a higher P_{crit} (closer to atmospheric pressure) than a non-OSA subject, indicating a lower pressure drop is required to induce airway collapse. P_{crit} values above the ambient atmospheric pressure indicate an increasingly greater propensity for an airway to collapse. In [44], a P_{crit} of -2.1 cmH_2O was reported using 2D FSI incorporating a laminar flow model constructed from a magnetic resonance image of a healthy subject. To simulate a narrower airway, the posterior airway wall of the original MRI was displaced by half the distance between the tip of the soft palate and the airway wall. This modification resulted in an increased P_{crit} to -1.25 cmH_2O. The study concluded that an increase of Young's modulus of the soft palate from 25 kPa to 100 kPa led to a 3.5-fold decrease in P_{crit}, indicating the critical influence of tissue stiffness on airway collapsibility. Expanding upon this work, the study in [59] proposed dividing P_{crit} into two components: passive and active. Passive P_{crit} was defined as the closing pressure reflecting the contribution of mechanical loads on the collapsibility of the pharyngeal airway. Active P_{crit}, on the other hand, was defined as the closing pressure reflecting the contribution of mechanical loads and neural reflex responses. The work in [59] compared measured (active and passive) and simulated P_{crit} on children with OSA. Significant agreement was observed between the measured passive P_{crit} and the simulated P_{crit}; thus, concluding that the simulated P_{crit} better reflected passive rather than active P_{crit}. Additionally, the study reported a Pearson correlation of 0.56 ($p = 0.002$), 0.62 ($p \leq$

0.0001) and 0.83 ($p \leq 0.0001$) between AHI and the measured passive, measured active, and simulated P_{crit}, respectively. Further insights were provided in [60], who developed 3D finite element models of six OSA patients with varying upper airway anatomies. P_{crit} ranged from -0.1 to -4.1 cmH_2O. Their analysis revealed that the mean width of the soft palate had the highest correlation with P_{crit}, and there was no correlation between the minimum airway space and P_{crit}. However, they did not consider the effect of FSI in their study. Since two-way coupling FSI includes the feedback of the tissue deformation on the airflow characteristics, its exclusion from a model would affect P_{crit}. The study in [31] showed that the soft palate of an OSA patient was hypertrophic with a rapid change in velocity and pressure gradients, resulting in a narrower airway compared to healthy individuals. These dynamic changes suggest that increased local pressure and velocity gradients can cause substantial soft palate displacement, promoting pharyngeal collapse. Similarly, FSI analysis of the upper airway before and after mandibular advancement splint (MAS) treatment was implemented in [46]. The pressure at the posterior region of the oropharynx was lower than that at the anterior region as the flow was attached to the posterior oropharynx wall, which initiated the collapse of the airway wall. These findings demonstrate that anatomical and mechanical variations in the upper airway structure have a significant influence on airway collapsibility and the pathophysiology of OSA.

FSI modelling additionally provides insights into the efficacy of therapeutic strategies for OSA. The use of computational modelling in the analysis of OSA treatment is considered a non-invasive method capable of assessing the effectiveness of different treatment responses. Simulation may help predict treatment success in patient specific models. The study in [61] reported a decrease in the flow resistance inside the oropharynx after MAS by virtually modifying the original upper airway model of an OSA patient to mimic the surgical adjustment. The study in

[62] adopted the approach of virtual surgery (adenoidectomy, palatoplasty, and genioglossus advancement) by reducing the thickness of the adenoid, palate, and tongue tissues by 10 mm, 6 mm, and 2 mm, respectively, from the MRI scan acquired for an OSA patient. Following the virtual surgery, velopharyngeal resistance and velum displacement were reduced by 66% and 63%, respectively [62]. However, it should be noted that their virtual surgery was not validated experimentally pre- and post-operation; thus, its efficacy remains theoretical. A different virtual approach was examined in [63], where a suture-patch device applying a pulling force to the tongue was modelled to keep the airway open. The study was able to identify the optimum position of the patch, and the minimum force required to prevent airway collapse, while taking into consideration the patient's comfort. Nevertheless, muscle forces were not included in that study. The effect of MAS therapy was further assessed in [46] using magnetic resonance images of the patient before and after treatment. The results showed that deformation was reduced in the oropharynx region although the volume increase occurred at the velopharyngeal region after MAS. This finding indicated that geometric modification was not the only contributor to the treatment response; thus, multiple factors should be considered in the selection of a treatment method. This finding was discussed in [64] where 3D FSI simulations were performed for three OSA patients before and after nasal surgery. Although the nasal resistance decreased in all patients, the soft palate displacement for the most severe OSA patient was higher than before the surgery. Therefore, it was recommended to combine other treatment methods for that patient. In [65], the effect of miniscrew-assisted rapid palatal expansion (MARPE) on the airway geometry and flow characteristics was investigated in an OSA patient. An increase in the cross-sectional area of the airway and a decrease in the airway resistance were observed. Thus, the study suggested MARPE as an alternative treatment for patients who refuse a positive airway pressure device or cannot

undergo MAS. In summary, numerical simulations have an essential role in OSA treatment through virtual surgery. Although a numerical simulation may need patient-specific geometries, accurate input parameters and flow models, and high computational time, it may well provide quantitative evidence for critical clinical decisions.

2.1.4.3 Application of Aero-Acoustic Modelling

While CFD and FSI approaches are effective in analyzing the mechanical and aerodynamic behaviour of the upper airway, aero-acoustic modelling provides essential insights into the mechanisms of sound generation and propagation during respiration. This capability is particularly relevant for the non-invasive diagnosis and continuous monitoring of sleep-related breathing disorders such as OSA. Respiratory sounds—especially those altered due to structural or functional airway changes—offer a valuable physiological signal that can be leveraged for clinical assessment, provided that their sources and propagation are well understood.

Previous studies have applied aero-acoustic simulations to investigate various physiological and pathological conditions of the upper airway, including phonation, stridor, and breathing sounds. For instance, the study in [66] simulated stridorous sound inside the upper airway using a one-way coupled fluid-structure-acoustic model, demonstrating a relationship between the characteristics of the stridor noise and the location and size of the airway obstruction. Their results indicated significantly higher sound pressure levels at the tracheal outlet in the stridorous model compared to the healthy model, although no frequency shift was observed between the two conditions. In contrast, a slight shift in the resonating frequencies with the increase of flowrate was reported in [67]. The study also observed an increase in the sound amplitudes as the flowrate increased from 0.32 L/s to 1 L/s, suggesting that flow-induced changes can influence both the spectral content and intensity of breathing sounds. Similarly, the effect of

dynamic glottal aperture on the breathing sound generation was investigated in [68] using an upper airway model under four different breathing scenarios (combination of constant and sinusoidal flow rate with rigid and dynamic glottis). Their findings showed that flow speed through the glottis was a key determinant of sound intensity, and that glottal aperture dilation from 64 to 140 mm^2 contributed to a 20-35 dB decrease in the sound power. Further anatomical specificity was addressed in [69], where the aerodynamic sound contributions from distinct anatomical regions of the upper airway—including the uvula, pharynx, and glottis— were examined and their relative impact was quantified. The study noted that uvular obstruction increased the sound pressure level and decreased the fundamental frequency at an inhalation rate of 0.5 L/s. Moreover, it was observed that the nasopharynx predominantly contributed to the low-frequency acoustic energy, while the airway narrowing, due to the uvular blockage, was responsible for energy shifts toward higher frequencies in the range of 15-20 kHz. These findings suggest that spectral features of breathing sounds could serve as diagnostic indicators for localized anatomical obstructions. Nevertheless, the comprehensive relationship between upper airway anatomical variations and OSA-specific acoustic features remains insufficiently characterized through computational aero-acoustics. Most existing models either simplify anatomical geometry or lack validation against realistic physiological conditions, thus underscoring the need for patient-specific, validated aero-acoustic simulations that integrate both flow dynamics and sound propagation in a realistic clinical context.

Although recent advances in computational fluid dynamics (CFD) and aero-acoustic modelling have enabled more accurate simulation of breathing sounds, current studies often rely on simplified anatomical geometries or lack validation against real patient data. Moreover, existing research predominantly focuses on general respiratory airflow or speech sounds, while tracheal

breathing sounds—especially in the context of obstructive sleep apnea (OSA)—remain underexplored. The complex relationship between upper airway geometry and the resulting frequency response of breathing sounds has not been thoroughly quantified. Furthermore, there is a scarcity of models that can link patient-specific anatomical features to acoustic characteristics in a clinically meaningful way.

This study addresses these gaps by combining CFD simulations with acoustic finite element modelling (FEM) using patient-specific airway geometries. It aims to establish a clearer connection between anatomical constrictions and the frequency content of tracheal sounds, thereby providing a foundation for non-invasive diagnostic tools for conditions such as OSA.

2.2 Anatomy and Physiology of The Human Upper Airway

The human upper airway plays a central role in several vital functions, including respiration, phonation and deglutition. It serves as the primary conduit for air passage into the lower respiratory tract and is structurally and functionally adapted to facilitate the simultaneous processes of breathing, speaking, and eating. As illustrated in Fig. 2-1 [70], the upper airway begins at the nasal and oral cavities, separated by the hard palate, a bony structure forming the anterior roof of the mouth. Posterior to the hard palate lies the soft palate, a flexible and muscular structure that dynamically modulates airflow direction during respiration and prevents food from entering the nasal cavity during deglutition. The airway continues posteriorly into the pharynx, a muscular tube divided into three anatomical regions: the nasopharynx (extending from the nasal cavity to the soft palate), oropharynx (from the soft palate to the epiglottis), and laryngopharynx (from the epiglottis to the larynx). The pharynx serves as a shared pathway for both air and food, necessitating precise neuromuscular coordination to prevent aspiration. Inferior to the pharynx lies the larynx, commonly known as the voice box, which houses the vocal folds and is essential for

sound production and airway protection during swallowing. Finally, the trachea extends from the larynx into the thoracic cavity, serving as a rigid guideway for air to enter the lower respiratory tract, ultimately enabling gas exchange in the lungs.

Structurally, the upper airway comprises tissues with varying biomechanical properties, arranged in a stiffness gradient from hard to soft; ranging from bone (e.g., hard palate), to cartilage (e.g., laryngeal framework), to muscle, ligament, and soft tissue [71]. This heterogeneity plays a significant role in the dynamic behaviour of the airway during the respiratory cycle. Additionally, the autonomic nervous system, in coordination with the central nervous system, regulates the tone of the pharyngeal dilator muscles, which help maintain airway patency, particularly during sleep [72]. The neuromuscular control of these muscles is critical, as their dysfunction or weakening can lead to airway collapse, a key feature in respiratory disorders such as obstructive sleep apnea (OSA).

Consequently, both the morphological characteristics of the upper airway and its neuromuscular control significantly influence the development and manifestation of various upper airway pathologies. In particular, anatomical narrowing or collapsibility—especially in the pharyngeal region—can result in airflow limitations and abnormal sound generation, which are hallmarks of conditions such as OSA, snoring, and stridor. Previous studies have shown that patients with OSA tend to have a smaller pharyngeal airway compared to healthy individuals [73]. This observation was initially reported in [74] where CT scans were used to assess 30 awake participants, including 20 OSA patients. Their findings indicated that OSA patients exhibited reduced airway area in the regions of nasopharynx, oropharynx and hypopharynx, with the site and severity of narrowing varying among individuals. Similarly, the study in [75] utilized volumetric MRI to evaluate the anatomical risk factors for OSA and found that patients with OSA

had significantly increased upper airway soft tissue volumes. Notably, the tongue and lateral pharyngeal wall volumes were identified as independent risk factors. These findings underscore the importance of a detailed understanding of upper airway anatomy and function for the accurate diagnosis, modelling, and treatment of respiratory and sleep-related disorders, particularly obstructive sleep apnea (OSA).

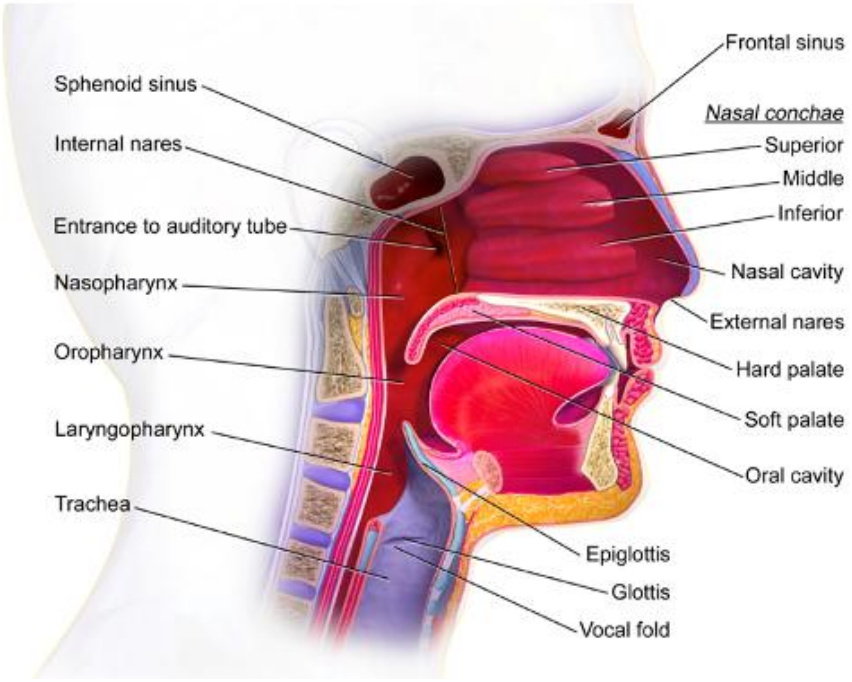

Fig. 2-1: Anatomical illustration of the upper airway [70]. Image licensed under CC BY 4.0

2.3 Pathophysiology of OSA

OSA is a complex disorder characterized by recurrent episodes of upper airway obstruction during sleep, leading to intermittent hypoxia and sleep fragmentation. The pathophysiology of OSA is multifactorial, involving anatomical, neuromuscular, and physiological mechanisms that contribute to airway collapse and its systemic consequences. To maintain upper airway patency during breathing, a balance must be achieved between the compliance of the airway – which is significantly influenced by anatomical features such as shape, size, and soft tissue composition –

and the level of pharyngeal dilator muscle activation [76]. Airway compliance, defined as the change in volume per unit change in transmural pressure, plays a critical role in determining the airway's susceptibility to collapse under negative inspiratory pressures. A highly compliant airway deforms more easily under sub-atmospheric pressures, particularly during inspiration when intraluminal pressure becomes negative relative to surrounding tissue pressures. During wakefulness, the tonic activity in the upper airway muscles, such as the genioglossus and pharyngeal constrictors, maintains airway patency despite potential narrowing [77], [78]. This neuromuscular compensation counteracts the collapsing forces acting on the pharyngeal walls during breathing. However, during sleep, especially in rapid eye movement (REM) phases, the muscle activity is significantly reduced, leading to reduced neuromuscular support and increased susceptibility to airway collapse [73]. This cyclical collapse and reopening of the upper airway trigger a cascade of pathophysiological responses. The obstruction leads to apnea (complete cessation of airflow) or hypopnea (partial airflow limitation), which in turn causes hypoxemia and hypercapnia. These changes in blood gas composition activate chemoreceptors and elicit cortical arousals, which restore upper airway muscle tone and reestablish airflow [2], [79], [80], [81]. However, the arousals themselves fragment sleep architecture and prevent the attainment of deep, restorative sleep stages. The repetitive nature of these events results in chronic sympathetic nervous system activation, contributing to systemic hypertension and cardiovascular disease [82], [83]. An additional contributor to OSA pathophysiology is ventilatory control instability, typically assessed via loop gain. In Engineering, loop gain is used to determine the stability of a feedback loop system [84]. In the context of sleep apnea physiology, loop gain refers to the sensitivity of the respiratory control system to deviations in ventilation and reflects how strongly the body responds to changes in CO_2 or O_2 [85], [86]. A high loop gain system is more prone to overshooting

in response to an apnea-induced hypoxic event, leading to alternating periods of hyperventilation and hypoventilation. This instability fosters periodic breathing and promotes recurrent apneas, particularly in individuals whose anatomical or neuromuscular vulnerabilities already compromise airway patency. Studies show that severe OSA patients tend to exhibit higher loop gain, resulting in a less stable ventilatory control system [87], [88].

Furthermore, an important concept in understanding upper airway collapsibility is the critical closing pressure (P_{crit}). As previously mentioned, P_{crit} represents the pressure at which the upper airway collapses and airflow ceases. In physiological terms, a more positive P_{crit} indicates a more collapsible airway, whereas a negative P_{crit} reflects a more stable airway structure. To conceptualize this phenomenon, the upper airway has been modelled as a collapsible tube situated between two rigid segments; nasal segment upstream and tracheal segment downstream as illustrated in Fig.2-2 [89], [90], [91]. This model, derived from the Starling resistor concept, provides a mechanical framework to describe pharyngeal airflow regulation through pressure dynamics. In this model, the pressure within the upstream (nasal) rigid segment is denoted as P_U (often approximated as nasal pressure), the downstream pressure at the tracheal end is P_D (tracheal pressure), and the pressure surrounding the collapsible pharyngeal segment, reflecting tissue pressure, is P_{crit}. The mechanical behavior of the airway under this model depends on the relationship between these three pressures. For instance, if $P_U > P_D > P_{crit}$, the pharyngeal segment will remain patent with unrestricted airflow, governed by the pressure gradient between the upstream and downstream pressures. However, when $P_U > P_{crit} > P_D$, the airway becomes partially collapsed. In this flow-limited state, although airflow persists, it is restricted due to dynamic narrowing, and increases in upstream pressure do not lead to proportional increases in airflow. This condition is commonly observed during snoring or hypopnea events in OSA patients. In the

case when $P_{crit} > P_U > P_D$, the pharyngeal segment collapses completely, resulting in total airflow obstruction and an apneic event, as often seen in individuals with severe OSA. In healthy individuals without OSA, Pcrit is typically sub-atmospheric, meaning that the airway remains patent even at low intraluminal pressures. In contrast, patients with OSA often exhibit a supra-atmospheric or near-zero Pcrit, indicating a highly collapsible airway that requires continuous positive pressure to remain open during sleep [92], [93]. Pcrit is influenced by both anatomical and neuromuscular factors. Anatomical narrowing or increased soft tissue volume (e.g., enlarged tongue or lateral pharyngeal walls) increases Pcrit, while activation of dilator muscles lowers it by stabilizing the pharyngeal wall. Thus, Pcrit not only reflects the mechanical properties of the upper airway but also captures the dynamic interaction between anatomical vulnerability and neuromuscular compensation. It has become a key parameter in research and clinical studies for assessing the severity of upper airway collapsibility and the effectiveness of therapeutic interventions such as continuous positive airway pressure (CPAP), mandibular advancement devices, or hypoglossal nerve stimulation.

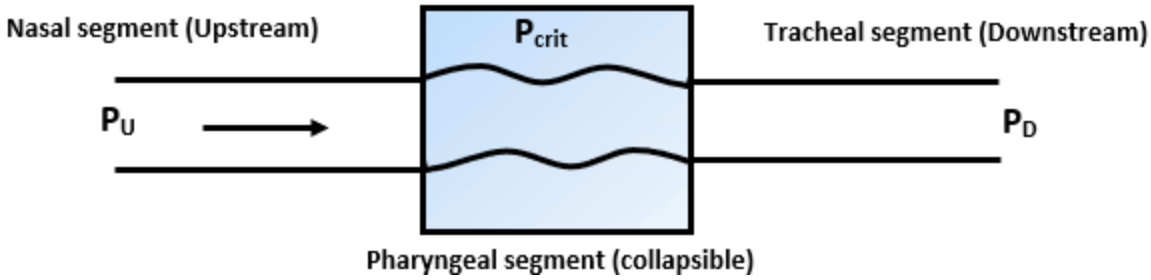

Fig. 2-2: Starling resistor model of the upper airway represented as a collapsible segment characterized by critical closing pressure (P_{crit}) connected by a rigid upstream nasal segment with upstream pressure (P_U) and a downstream tracheal segment with downstream pressure (P_D). Adapted from [89]

Contemporary models of OSA pathophysiology advocate a "multifactorial threshold model," emphasizing that the disorder arises when multiple physiological traits converge to breach

the threshold for airway collapse. These include anatomical compromise, inadequate muscle compensation, high loop gain and low arousal threshold, among others. Importantly, each of these traits is modifiable, offering the potential for tailored treatment approaches. For instance, patients with primary anatomical compromise may benefit most from continuous positive airway pressure (CPAP), mandibular advancement devices, or surgical intervention, while those with ventilatory control abnormalities may respond better to pharmacologic agents aimed at reducing loop gain (e.g., acetazolamide) [85], [94], [95] or increasing neuromuscular tone (e.g., noradrenergic or serotonergic agents) [96].

2.4 Respiratory mechanics

The primary function of the respiratory system is to facilitate the exchange of gases, delivering oxygen from the external environment to the body's tissues while simultaneously eliminating carbon dioxide, a metabolic waste product. This essential process, known as pulmonary ventilation, relies on the intricate mechanics of breathing, which are governed by the physical principles of pressure and volume dynamics. Air movement into and out of the lungs occurs as a result of pressure gradients established between the atmosphere and the small air sacs within the lungs, known as alveoli. These pressure gradients are created by changes in the volume of the thoracic cavity during the processes of inhalation and exhalation.

A fundamental principle governing respiratory mechanics is Boyle's law, which states that at a constant temperature, the pressure of a gas is inversely proportional to its volume. In the context of the respiratory system, this means that when the volume of the thoracic cavity increases, the pressure inside the lungs (intrapulmonary or alveolar pressure) decreases, causing air to flow in from the atmosphere. Conversely, when the thoracic volume decreases, alveolar pressure rises above atmospheric pressure, resulting in the expulsion of air from the lungs. Thus, ventilation is

fundamentally a process of creating favorable pressure differentials by altering lung volume through the coordinated activity of respiratory muscles.

During inspiration, the diaphragm contracts and flattens, and the external intercostal muscles elevate the rib cage, expanding the thoracic cavity. This expansion reduces intrapleural pressure (the pressure within the pleural space) and, in turn, lowers alveolar pressure below atmospheric levels. As a result, air flows passively into the lungs until alveolar and atmospheric pressures equalize. Importantly, the airways themselves must remain patent throughout this process, and the pressures within the lumen of the upper and lower airways, collectively referred to as intraluminal pressures, play a critical role in ensuring that airflow is unimpeded.

The dynamics of intraluminal pressure are particularly significant in collapsible airway regions, such as the pharynx. Here, the maintenance of airway patency depends not only on anatomical features but also on the balance between internal luminal pressures and the surrounding extraluminal (tissue) pressures. A drop in intraluminal pressure during inspiration, especially in the presence of negative pleural pressures, can promote airway narrowing or collapse if not counteracted by sufficient muscular tone or structural support. This is a key consideration in conditions like obstructive sleep apnea, where mechanical instability of the upper airway during inspiration leads to airflow limitation or complete obstruction.

Alveolar pressure, the pressure within the alveoli, is the primary driver of airflow during breathing. At rest, when no air is moving, alveolar pressure equals atmospheric pressure (usually defined as 0 cmH_2O). During quiet inspiration, alveolar pressure drops to approximately -1 cmH_2O drawing air into the lungs. With expiration, especially during passive breathing, the relaxation of the inspiratory muscles causes the thoracic volume to decrease, raising alveolar pressure to around

+1 cmH_2O and expelling air. During forced expiration, such as coughing or vigorous breathing, alveolar pressures can rise significantly, further promoting airflow out of the lungs.

Another important concept is transpulmonary pressure, the difference between alveolar pressure and intrapleural pressure. This pressure gradient keeps the lungs inflated against their natural elastic recoil. If intrapleural pressure becomes equal to or greater than alveolar pressure, such as in cases of pneumothorax, the lung may collapse. Maintaining a positive transpulmonary pressure throughout the respiratory cycle is essential for effective ventilation and alveolar stability (See Fig. 2-3 for a schematic of pressure relationships within the thoracic cavity).

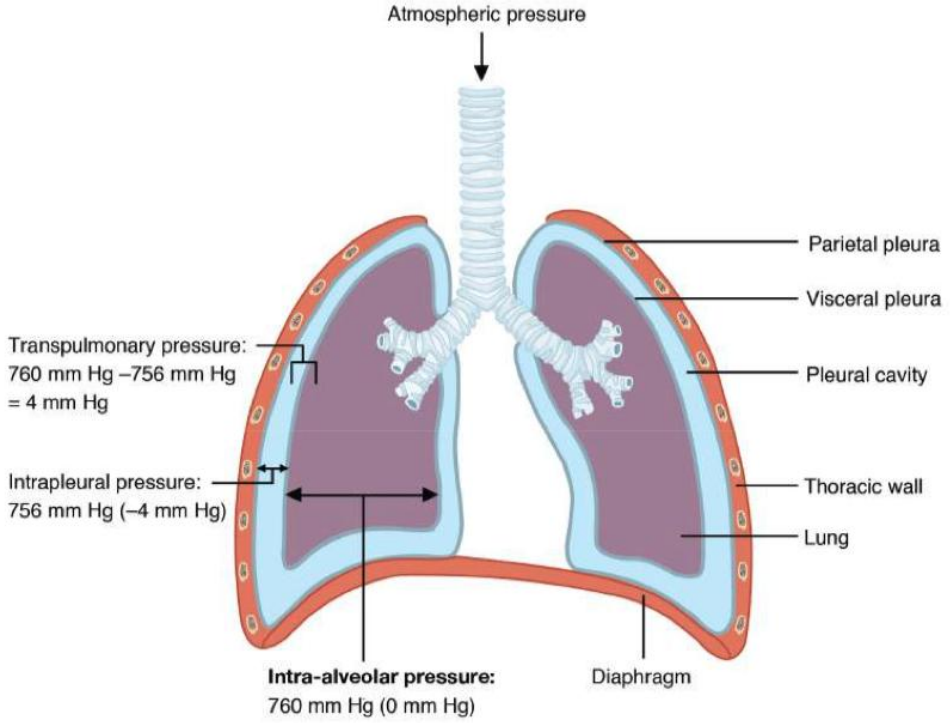

Fig. 2-3: Pressure relationships in the thoracic cavity. This diagram illustrates the pressure gradients critical to pulmonary ventilation. Intra-alveolar pressure (760 mm Hg or 0 mm Hg gauge) is equal to atmospheric pressure at rest, while intrapleural pressure (756 mm Hg, or -4mm Hg gauge) remains slightly negative to prevent lung collapse. The transpulmonary pressure (difference between intra-alveolar and intrapleural pressure) maintains lung expansion. The diagram also shows the anatomical relationship between the visceral pleura, parietal pleura, pleural cavity, lungs, and thoracic wall. [97] copyright © 2019 by Lindsay M. Biga, Staci Bronson, Sierra Dawson,

Airway resistance and lung compliance also modulate the mechanics of breathing. Resistance is influenced by the diameter of the airways and the viscosity of the inhaled air, as described by Poiseuille's law. In diseases like asthma or chronic obstructive pulmonary disease (COPD), increased airway resistance can significantly hinder airflow, necessitating greater muscular effort to achieve adequate ventilation. Lung compliance, defined as the change in lung volume per unit change in transpulmonary pressure, reflects the distensibility of the lung tissue. High compliance means the lungs can expand easily, while low compliance, as seen in pulmonary fibrosis, indicates stiffness and difficulty in lung expansion.

Moreover, the interaction between alveolar pressure and atmospheric pressure is not merely a passive consequence of volume changes but is finely regulated by neural and chemical feedback mechanisms. Central and peripheral chemoreceptors continuously monitor arterial levels of CO_2, O_2, and pH, adjusting respiratory rate and tidal volume accordingly to maintain homeostasis [98].

The mechanics of breathing represent a dynamic interplay between anatomical structures, muscular activity, and fundamental physical laws governing gas behavior. Alveolar and intraluminal pressures, modulated by changes in thoracic volume and tissue mechanics, create the necessary pressure gradients for airflow. Boyle's law provides a foundational understanding of how these volume and pressure changes drive ventilation, while factors such as airway resistance, lung compliance, and pleural pressure differentials ensure the system operates efficiently. A comprehensive understanding of these mechanics is essential for diagnosing and treating respiratory disorders, modelling airflow in clinical simulations, and designing effective ventilatory support systems.

References

[1] H. Pasterkamp, S. S. Kraman, and G. R. Wodicka, “Respiratory sounds. Advances beyond the stethoscope.,” *Am. J. Respir. Crit. Care Med.*, vol. 156, no. 3 Pt 1, pp. 974–987, Sep. 1997, doi: 10.1164/ajrccm.156.3.9701115.

[2] J. A. Dempsey, S. C. Veasey, B. J. Morgan, and C. P. O’Donnell, “Pathophysiology of Sleep Apnea,” *Physiol. Rev.*, vol. 90, no. 1, pp. 47–112, Jan. 2010, doi: 10.1152/physrev.00043.2008.

[3] P. R. EASTWOOD *et al.*, “Obstructive Sleep Apnoea: From pathogenesis to treatment: Current controversies and future directions,” *Respirology*, vol. 15, no. 4, pp. 587–595, Jan. 2010, doi: 10.1111/j.1440-1843.2009.01699.x.

[4] R. B. Berry *et al.*, “Rules for scoring respiratory events in sleep: Update of the 2007 AASM manual for the scoring of sleep and associated events,” *J. Clin. Sleep Med.*, vol. 8, no. 5, pp. 597–619, 2012, doi: 10.5664/jcsm.2172.

[5] C. A. Kushida *et al.*, “Guideline Update Practice Parameters for the Indications for Polysomnography and Related Procedures: An Update for 2005,” *J. Clin. Sleep Med.*, vol. 13, no. 3, pp. 479–504, 2017, [Online]. Available: https://j2vjt3dnbra3ps7ll1clb4q2-wpengine.netdna-ssl.com/wp-content/uploads/2017/07/PP_Polysomnography.pdf

[6] T. I. Morgenthaler, V. Kagramanov, V. Hanak, and P. A. Decker, “Complex sleep apnea syndrome: Is it a unique clinical syndrome?,” *Sleep*, vol. 29, no. 9, pp. 1203–1209, 2006, doi: 10.1093/sleep/29.9.1203.

[7] P. S. R. K. R. R. S. R. W. E. W. Epstein LJ; Kristo D; Strollo PJ; Friedman N; Malhotra MD, “Clinical Guideline for the Evaluation , Management and Long-term Care of,” *J. Clin. Sleep Med.*, vol. 5, no. 3, pp. 263–276, 2009.

[8] R. C. Stansbury and P. J. Strollo, “Clinical manifestations of sleep apnea,” *J. Thorac. Dis.*, vol. 7, no. 9, pp. E298–E310, 2015, doi: 10.3978/j.issn.2072-1439.2015.09.13.

[9] T. Young *et al.*, “Predictors of sleep-disordered breathing in community-dwelling adults: the Sleep Heart Health Study,” *Arch. Intern. Med.*, vol. 162, no. 8, pp. 893–900, 2002.

[10] M. Povitz *et al.*, “Clinical pathways and wait times for OSA care in Ontario, Canada: A population cohort study,” *Can. J. Respir. Crit. Care, Sleep Med.*, vol. 3, no. 2, pp. 91–99, 2019, doi: 10.1080/24745332.2018.1512841.

[11] T. Byrne and J. Weston, “Polysomnography & Sleep Medicine A Jurisdictional Scan P R E P A R E D B Y,” no. May, 2019, [Online]. Available: www.insideoutresearch.ca

[12] N. Alghanim, V. R. Comondore, J. Fleetham, C. A. Marra, and N. T. Ayas, “The economic impact of obstructive sleep apnea,” Feb. 2008. doi: 10.1007/s00408-007-9055-5.

[13] A. L. Chesson, R. B. Berry, and A. Pack, “Practice parameters for the use of portable monitoring devices in the investigation of suspected obstructive sleep apnea in adults,” *Sleep*, vol. 26, no. 7, pp. 907–913, 2003, doi: 10.1093/sleep/26.7.907.

[14] M. Nagappa *et al.*, “Validation of the STOP-Bang Questionnaire as a Screening Tool for Obstructive Sleep Apnea among Different Populations: A Systematic Review and Meta-Analysis,” *PLoS One*, vol. 10, no. 12, p. e0143697, Dec. 2015, doi: 10.1371/journal.pone.0143697.

[15] Q. L. Johnson and A. Netzer, “Opiate Analgesics and the Perioperative Management of Patients with Obstructive Sleep Apnea,” *Mo. Med.*, vol. 112, no. 6, pp. 435–438, 2015.

[16] A. Elwali and Z. Moussavi, “Obstructive Sleep Apnea Screening and Airway Structure Characterization During Wakefulness Using Tracheal Breathing Sounds,” *Ann. Biomed.*

Eng., vol. 45, no. 3, pp. 839–850, Mar. 2017, doi: 10.1007/s10439-016-1720-5.

[17] F. Hajipour, M. J. Jozani, A. Elwali, and Z. Moussavi, "Regularized logistic regression for obstructive sleep apnea screening during wakefulness using daytime tracheal breathing sounds and anthropometric information," *Med. Biol. Eng. Comput.*, vol. 57, no. 12, pp. 2641–2655, Dec. 2019, doi: 10.1007/s11517-019-02052-4.

[18] J. Solà-Soler, J. Antonio Fiz Fernandez, A. Torres, and R. Jané, *Identification of Obstructive Sleep Apnea Patients from Tracheal Breath Sound Analysis During Wakefulness in Polysomnographic Studies*. 2014. doi: 10.0/Linux-x86_64.

[19] E. Goldshtein, A. Tarasiuk, and Y. Zigel, "Automatic detection of obstructive sleep apnea using speech signals," *IEEE Trans. Biomed. Eng.*, vol. 58, no. 5, pp. 1373–1382, May 2011, doi: 10.1109/TBME.2010.2100096.

[20] J. Solé-Casals *et al.*, "Detection of severe obstructive sleep apnea through voice analysis," *Appl. Soft Comput. J.*, vol. 23, no. October 2014, pp. 346–354, 2014, doi: 10.1016/j.asoc.2014.06.017.

[21] Y. Finkelstein *et al.*, "Velopharyngeal anatomy in patients with obstructive sleep apnea versus normal subjects," *J. Oral Maxillofac. Surg.*, vol. 72, no. 7, pp. 1350–1372, 2014, doi: 10.1016/j.joms.2013.12.006.

[22] Z. Lan, A. Itoi, M. Takashima, M. Oda, and K. Tomoda, "Difference of pharyngeal morphology and mechanical property between OSAHS patients and normal subjects," *Auris Nasus Larynx*, vol. 33, no. 4, pp. 433–439, Dec. 2006, doi: 10.1016/j.anl.2006.03.009.

[23] J. Sola-Soler, J. A. Fiz, A. Torres, and R. Jane, "Identification of Obstructive Sleep Apnea patients from tracheal breath sound analysis during wakefulness in polysomnographic

studies," *2014 36th Annu. Int. Conf. IEEE Eng. Med. Biol. Soc. EMBC 2014*, pp. 4232–4235, 2014, doi: 10.1109/EMBC.2014.6944558.

[24] L. Grote, J. Hedner, R. Grunstein, and H. Kraiczi, "Therapy with nCPAP: Incomplete elimination of sleep related breathing disorder," *Eur. Respir. J.*, vol. 16, no. 5, pp. 921–927, 2000, doi: 10.1183/09031936.00.16592100.

[25] K. A. Ferguson, K. Heighway, and R. R. F. Ruby, "A randomized trial of laser-assisted uvulopalatoplasty in the treatment of mild obstructive sleep apnea," *Am. J. Respir. Crit. Care Med.*, vol. 167, no. 1, pp. 15–19, 2003, doi: 10.1164/rccm.2108050.

[26] C. H. J. Won, K. K. Li, and C. Guilleminault, "Surgical treatment of obstructive sleep apnea: Upper airway and maxillomandibular surgery," *Proc. Am. Thorac. Soc.*, vol. 5, no. 2, pp. 193–199, 2008, doi: 10.1513/pats.200708-121MG.

[27] E. Finnsson *et al.*, "Sleep apnea endotypes : from the physiological laboratory to scalable polysomnographic measures," 2022.

[28] B. A. Edwards, S. Redline, S. A. Sands, and R. L. Owens, "CONCISE TRANSLATIONAL REVIEW More Than the Sum of the Respiratory Events : Personalized Medicine Approaches for Obstructive Sleep Apnea," vol. 200, pp. 691–703, 2019, doi: 10.1164/rccm.201901-0014TR.

[29] S. Redline, A. Azarbarzin, and Y. Peker, "Obstructive sleep apnoea heterogeneity and cardiovascular disease," *Nat. Rev. Cardiol.*, vol. 20, no. 8, pp. 560–573, 2023, doi: 10.1038/s41569-023-00846-6.

[30] A. E. Sher, K. B. Schechtman, and J. F. Piccirillo, "The Efficacy of Surgical Modifications of the Upper Airway in Adults With Obstructive Sleep Apnea Syndrome," *Sleep*, vol. 19, no. 2, pp. 156–177, 1996, doi: 10.1093/sleep/19.2.156.

[31] X. Sun, C. Yu, Y. Wang, and Y. Liu, "Numerical simulation of soft palate movement and airflow in human upper airway by fluid-structure interaction method," *Acta Mech. Sin. Xuebao*, vol. 23, no. 4, pp. 359–367, Aug. 2007, doi: 10.1007/s10409-007-0083-4.

[32] W. M. Faizal *et al.*, "Computational fluid dynamics modelling of human upper airway: A review," Nov. 01, 2020, *Elsevier Ireland Ltd*. doi: 10.1016/j.cmpb.2020.105627.

[33] Y. Huang, A. Malhotra, and D. P. White, "Computational simulation of human upper airway collapse using a pressure-/state-dependent model of genioglossal muscle contraction under laminar flow conditions," *J. Appl. Physiol.*, vol. 99, no. 3, pp. 1138–1148, Sep. 2005, doi: 10.1152/japplphysiol.00668.2004.

[34] L. Schickhofer, B. Semlitsch, and M. Mihăescu, "Numerical flow simulations of a flexible plate attached to an obstacle in crossflow," *Springer Proc. Phys.*, vol. 185, pp. 195–201, 2016, doi: 10.1007/978-3-319-30602-5_25.

[35] Tetlow, "Analogue Computational Modeling of Upper-Airway Dynamics," *9th Int. Conf. Flow-Induced Vib.*, pp. 1–6, 2008, [Online]. Available: papers2://publication/uuid/9DCCFDD5-0C78-4DC8-B1A1-93EA61688067

[36] X. L. Yang, Y. Liu, R. M. C. So, and J. M. Yang, "The effect of inlet velocity profile on the bifurcation COPD airway flow," *Comput. Biol. Med.*, vol. 36, no. 2, pp. 181–194, 2006, doi: 10.1016/j.compbiomed.2004.11.002.

[37] H. Chen *et al.*, "Comparison of anatomic and aerodynamic characteristics of the upper airway among edentulous mild, moderate, and severe obstructive sleep apnea in older adults," *J. Clin. Sleep Med.*, vol. 18, no. 3, pp. 759–768, 2022, doi: 10.5664/jcsm.9716.

[38] M. Zhao, T. Barber, P. Cistulli, K. Sutherland, and G. Rosengarten, "Computational fluid dynamics for the assessment of upper airway response to oral appliance treatment in

obstructive sleep apnea," *J. Biomech.*, vol. 46, no. 1, pp. 142–150, 2013, doi: 10.1016/j.jbiomech.2012.10.033.

[39] W. Ashraf, N. Jacobson, N. Popplewell, and Z. Moussavi, "Fluid–structure interaction modelling of the upper airway with and without obstructive sleep apnea: a review," *Med. Biol. Eng. Comput.*, May 2022, doi: 10.1007/s11517-022-02592-2.

[40] R. H. Huang, X. P. Li, and Q. G. Rong, "Control mechanism for the upper airway collapse in patients with obstructive sleep apnea syndrome: A finite element study," *Sci. China Life Sci.*, vol. 56, no. 4, pp. 366–372, Apr. 2013, doi: 10.1007/s11427-013-4448-6.

[41] J. Pirnar, L. Dolenc-Grošelj, I. Fajdiga, and I. Žun, "Computational fluid-structure interaction simulation of airflow in the human upper airway," *J. Biomech.*, vol. 48, no. 13, pp. 3685–3691, Oct. 2015, doi: 10.1016/j.jbiomech.2015.08.017.

[42] J. H. Zhu, H. P. Lee, K. M. Lim, S. J. Lee, L. S. L. Teo, and D. Y. Wang, "Passive movement of human soft palate during respiration: A simulation of 3D fluid/structure interaction," *J. Biomech.*, vol. 45, no. 11, pp. 1992–2000, Jul. 2012, doi: 10.1016/j.jbiomech.2012.04.027.

[43] Y. Wang *et al.*, "Fluid-structure interaction modeling of upper airways before and after nasal surgery for obstructive sleep apnea.," *Int. j. numer. method. biomed. eng.*, vol. 28, no. 5, pp. 528–546, May 2012, doi: 10.1002/cnm.1486.

[44] G. Mylavarapu, M. Mihaescu, E. Gutmark, S. Murugappan, and M. Kalra, "Fluid structure interaction analysis in human upper airways to understand sleep apnea," *48th AIAA Aerosp. Sci. Meet. Incl. New Horizons Forum Aerosp. Expo.*, no. January 2010, pp. 1–9, 2010, doi: 10.2514/6.2010-1264.

[45] J. S. Na, H.-D. Jung, H.-J. Cho, * Yoon, J. Choi, and J. S. Lee, "Computational analysis of

airflow dynamics for predicting collapsible sites in the upper airways: a preliminary study," *J Appl Physiol*, vol. 126, pp. 330–340, 2019, doi: 10.1152/japplphysiol.00522.2018.-The.

[46] M. Zhao, T. Barber, P. A. Cistulli, K. Sutherland, and G. Rosengarten, "Simulation of upper airway occlusion without and with mandibular advancement in obstructive sleep apnea using fluid-structure interaction," *J. Biomech.*, vol. 46, no. 15, pp. 2586–2592, Oct. 2013, doi: 10.1016/j.jbiomech.2013.08.010.

[47] S. H. Kim, S. K. Chung, and Y. Na, "Numerical investigation of flow-induced deformation along the human respiratory upper airway," *J. Mech. Sci. Technol.*, vol. 29, no. 12, pp. 5267–5272, 2015, doi: 10.1007/s12206-015-1128-4.

[48] O. Bafkar *et al.*, "Impact of sleeping position, gravitational force = effective tissue stiffness on obstructive sleep apnoea," *J. Biomech.*, vol. 104, May 2020, doi: 10.1016/j.jbiomech.2020.109715.

[49] C. Xu, M. J. Brennick, L. Dougherty, and D. M. Wootton, "Modeling upper airway collapse by a finite element model with regional tissue properties," *Med. Eng. Phys.*, vol. 31, no. 10, pp. 1343–1348, Dec. 2009, doi: 10.1016/j.medengphy.2009.08.006.

[50] H. Luo, A. Scholp, and J. J. Jiang, "The Finite Element Simulation of the Upper Airway of Patients with Moderate and Severe Obstructive Sleep Apnea Hypopnea Syndrome," *Biomed Res. Int.*, vol. 2017, 2017, doi: 10.1155/2017/7058519.

[51] R. Huang and Q. Rong, "Respiration simulation of human upper airway for analysis of obstructive sleep apnea syndrome," *Lect. Notes Comput. Sci. (including Subser. Lect. Notes Artif. Intell. Lect. Notes Bioinformatics)*, vol. 6330 LNBI, no. PART 3, pp. 588–596, 2010, doi: 10.1007/978-3-642-15615-1_69.

[52] J. Z. Wu, R. G. Dong, and A. W. Schopper, “Analysis of effects of friction on the deformation behavior of soft tissues in unconfined compression tests,” *J. Biomech.*, vol. 37, no. 1, pp. 147–155, 2004, doi: 10.1016/S0021-9290(03)00240-9.

[53] S. Cheng, S. C. Gandevia, M. Green, R. Sinkus, and L. E. Bilston, “Viscoelastic properties of the tongue and soft palate using MR elastography,” *J. Biomech.*, vol. 44, no. 3, pp. 450–454, Feb. 2011, doi: 10.1016/j.jbiomech.2010.09.027.

[54] S. M. H. Haddad, S. S. Dhaliwal, B. W. Rotenberg, H. M. Ladak, and A. Samani, “Estimation of the hyperelastic parameters of fresh human oropharyngeal soft tissues using indentation testing,” *J. Mech. Behav. Biomed. Mater.*, vol. 108, Aug. 2020, doi: 10.1016/j.jmbbm.2020.103798.

[55] A. Pugachev *et al.*, “Application of patient-specific simulation workflow for obstructive sleep apnea diagnosis and treatment with a mandibular advancement device,” *Int. j. numer. method. biomed. eng.*, vol. 36, no. 8, pp. 1–14, 2020, doi: 10.1002/cnm.3350.

[56] T. B. Le, M. G. Moghaddam, B. T. Woodson, and G. J. M. Garcia, “Airflow limitation in a collapsible model of the human pharynx: physical mechanisms studied with fluid-structure interaction simulations and experiments,” *Physiol. Rep.*, vol. 7, no. 10, pp. 1–16, 2019, doi: 10.14814/phy2.14099.

[57] J. Cisonni, A. D. Lucey, A. J. C. King, S. M. S. Islam, R. Lewis, and M. S. Goonewardene, “Numerical simulation of pharyngeal airflow applied to obstructive sleep apnea: effect of the nasal cavity in anatomically accurate airway models,” *Med. Biol. Eng. Comput.*, vol. 53, no. 11, pp. 1129–1139, 2015, doi: 10.1007/s11517-015-1399-z.

[58] Y. Liu, J. Mitchell, Y. Chen, W. Yim, W. Chu, and R. C. Wang, “Study of the upper airway of obstructive sleep apnea patient using fluid structure interaction,” *Respir.*

Physiol. Neurobiol., vol. 249, pp. 54–61, 2018, doi: 10.1016/j.resp.2018.01.005.

[59] Mylavarapu G et al, "Predicting critical closing pressure in children with obstructive sleep apnea using fluid structure interaction simulations.," *J Appl Physiol japplphysiol.00694.2020*, 2021.

[60] M. Henrik Strand Moxness, F. Wülker, B. Helge Skallerud, and S. Nordgård, "Simulation of the upper airways in patients with obstructive sleep apnea and nasal obstruction: A novel finite element method," *Laryngoscope Investig. Otolaryngol.*, vol. 3, no. 2, pp. 82–93, 2018, doi: 10.1002/lio2.140.

[61] Q. Rong, S. Ren, and Q. Li, "Effect of upper airway shape on obstructive sleep apnea syndrome: Numerical simulation by fluid-structure interaction method," *J. Mech. Med. Biol.*, vol. 13, no. 6, pp. 1–8, 2013, doi: 10.1142/S0219519413400095.

[62] D. R. Subramaniam, R. Arens, M. E. Wagshul, S. Sin, D. M. Wootton, and E. J. Gutmark, "Biomechanics of the soft-palate in sleep apnea patients with polycystic ovarian syndrome," *J. Biomech.*, vol. 76, pp. 8–15, 2018, doi: 10.1016/j.jbiomech.2018.05.013.

[63] L. Yang, C. Yitung, Y. Woosoon, and W. Robert C, "Study of the Suture-Patch Device through the Tongue for Sleep Apnea using Fluid-Structure Interaction Modeling," *J. Otolaryngol. Rhinol.*, vol. 4, no. 2, pp. 1–9, 2018, doi: 10.23937/2572-4193.1510048.

[64] G. Wang, C. Yu, and Y. Wang, "THE DISTRIBUTIONS of AIRFLOW WITHIN the UPPER AIRWAY and POSTURE CHANGES of SOFT PALATE in PATIENTS with OSAHS after NASAL STRUCTURAL CORRECTION," *Biomed. Eng. - Appl. Basis Commun.*, vol. 30, no. 2, 2018, doi: 10.4015/S1016237218500175.

[65] J. S. Hur, H. H. Kim, J. Y. Choi, S. H. Suh, and S. H. Baek, "Investigation of the effects of miniscrew-assisted rapid palatal expansion on airflow in the upper airway of an adult

patient with obstructive sleep apnea syndrome using computational fluidstructure interaction analysis," *Korean J. Orthod.*, vol. 47, no. 6, pp. 353–364, 2017, doi: 10.4041/kjod.2017.47.6.353.

[66] W. C. P. van der Velden, A. H. van Zuijlen, A. T. de Jong, C. T. Lynch, L. J. Hoeve, and H. Bijl, "Acoustic simulation of a patient's obstructed airway," *Comput. Methods Biomech. Biomed. Engin.*, vol. 19, no. 2, pp. 144–158, Jan. 2016, doi: 10.1080/10255842.2014.996877.

[67] P. T. Gamage, "Modeling of flow generated sound in a constricted duct at low Mach number flow," *eprint arXiv:1801.09674*, 2018, [Online]. Available: http://arxiv.org/abs/1801.09674%0Ahttp://dx.doi.org/10.13140/RG.2.2.17805.03048%0A http://arxiv.org/abs/1801.09674%0Ahttp://dx.doi.org/10.13140/RG.2.2.17805.03048

[68] J. Xi, Z. Wang, K. Talaat, C. Glide-Hurst, and H. Dong, "Numerical study of dynamic glottis and tidal breathing on respiratory sounds in a human upper airway model," *Sleep Breath.*, vol. 22, no. 2, pp. 463–479, May 2018, doi: 10.1007/s11325-017-1588-0.

[69] J. Xi, X. Si, J. Kim, G. Su, and H. Dong, "Modeling the pharyngeal anatomical effects on breathing resistance and aerodynamically generated sound," *Med. Biol. Eng. Comput.*, vol. 52, no. 7, pp. 567–577, 2014, doi: 10.1007/s11517-014-1160-z.

[70] 2014)another Blausen.com staff (29 August, "Medical gallery of Blausen Medical 2014," *WikiJournal Med.*, vol. 1, no. 2, 2014, doi: 10.15347/wjm/2014.010.

[71] F. Vogt, "Towards an interactive framework for upper airway modeling : integration of acoustic, biomechanic, and parametric modeling methods," no. April, 2009, [Online]. Available: https://open.library.ubc.ca/collections/24/items/1.0067236

[72] M. P. McKinley, V. D. O'Loughlin, and E. Pennefather-O'Brien, *Human anatomy*, Sixth

edit. New York, NY: McGraw-Hill Education, 2021.

[73] D. P. White, “The pathogenesis of obstructive sleep apnea: Advances in the past 100 years,” *Am. J. Respir. Cell Mol. Biol.*, vol. 34, no. 1, pp. 1–6, 2006, doi: 10.1165/rcmb.2005-0317OE.

[74] E. F. Haponik, P. L. Smith, M. E. Bohlman, R. P. Allen, S. M. Goldman, and E. R. Bleecker, “Computerized tomography in obstructive sleep apnea. Correlation of airway size with physiology during sleep and wakefulness,” *Am. Rev. Respir. Dis.*, vol. 127, no. 2, pp. 221–226, 1983, doi: 10.1164/arrd.1983.127.2.221.

[75] R. J. Schwab, W. B. Gefter, E. A. Hoffman, K. B. Gupta, and A. I. Pack, “Dynamic upper airway imaging during awake respiration in normal subjects and patients with sleep disordered breathing,” *Am. Rev. Respir. Dis.*, vol. 148, no. 5, pp. 1385–1400, 1993, doi: 10.1164/ajrccm/148.5.1385.

[76] R. L. Horner, “Motor control of the pharyngeal musculature and implications for the pathogenesis of obstructive sleep apnea,” *Sleep*, vol. 19, no. 10, pp. 827–853, 1996, doi: 10.1093/sleep/19.10.827.

[77] W. S. Mezzanotte, D. J. Tangel, and D. P. White, “Waking genioglossal electromyogram in sleep apnea patients versus normal controls (a neuromuscular compensatory mechanism),” *J. Clin. Invest.*, vol. 89, no. 5, pp. 1571–1579, 1992, doi: 10.1172/jci115751.

[78] A. S. Jordan, D. G. McSharry, and A. Malhotra, “Adult obstructive sleep apnoea.,” *Lancet (London, England)*, vol. 383, no. 9918, pp. 736–747, Feb. 2014, doi: 10.1016/S0140-6736(13)60734-5.

[79] P. G. Guyenet, “Regulation of breathing and autonomic outflows by chemoreceptors,”

Compr. Physiol., vol. 4, no. 4, pp. 1511–1562, 2014, doi: 10.1002/cphy.c140004.

[80] P. Sagaut, S. Deck, and M. Terracol, *Multiscale and Multiresolution Approaches in Turbulence*. Imperial College Press, 2006. [Online]. Available: https://books.google.ca/books?id=1oHxzXPFOwoC

[81] K. Gleeson, C. W. Zwillich, and D. P. White, "The influence of increasing ventilatory effort on arousal from sleep," *Am. Rev. Respir. Dis.*, vol. 142, no. 2, pp. 295–300, 1990, doi: 10.1164/ajrccm/142.2.295.

[82] K. Narkiewicz, N. Montano, C. Cogliati, P. J. H. Van De Borne, M. E. Dyken, and V. K. Somers, "Altered cardiovascular variability in obstructive sleep apnea," *Circulation*, vol. 98, no. 11, pp. 1071–1077, 1998, doi: 10.1161/01.CIR.98.11.1071.

[83] V. K. Somers, M. E. Dyken, M. P. Clary, and F. M. Abboud, "Sympathetic neural mechanisms in obstructive sleep apnea," *J. Clin. Invest.*, vol. 96, no. 4, pp. 1897–1904, 1995, doi: 10.1172/JCI118235.

[84] S. A. Joosten *et al.*, "HHS Public Access," vol. 22, no. 8, pp. 1662–1669, 2018, doi: 10.1111/resp.13108.Dynamic.

[85] B. A. Edwards *et al.*, "Acetazolamide improves loop gain but not the other physiological traits causing obstructive sleep apnoea," *J. Physiol.*, vol. 590, no. 5, pp. 1199–1211, 2012, doi: 10.1113/jphysiol.2011.223925.

[86] A. Wellman *et al.*, "A method for measuring and modeling the physiological traits causing obstructive sleep apnea.," *J. Appl. Physiol.*, vol. 110, no. 6, pp. 1627–1637, Jun. 2011, doi: 10.1152/japplphysiol.00972.2010.

[87] M. Younes, M. Ostrowski, W. Thompson, C. Leslie, and W. Shewchuk, "Chemical control stability in patients with obstructive sleep apnea," *Am. J. Respir. Crit. Care Med.*,

vol. 163, no. 5, pp. 1181–1190, 2001, doi: 10.1164/ajrccm.163.5.2007013.

[88] D. J. Eckert, D. P. White, A. S. Jordan, A. Malhotra, and A. Wellman, "Defining phenotypic causes of obstructive sleep apnea: Identification of novel therapeutic targets," *Am. J. Respir. Crit. Care Med.*, vol. 188, no. 8, pp. 996–1004, 2013, doi: 10.1164/rccm.201303-0448OC.

[89] A. R. Schwartz, P. L. Smith, R. A. Wise, I. Bankman, and S. Permutt, "Effect of positive nasal pressure on upper airway pressure-flow relationships," *J. Appl. Physiol.*, vol. 66, no. 4, pp. 1626–1634, Apr. 1989, doi: 10.1152/jappl.1989.66.4.1626.

[90] I. C. Gleadhill, A. R. Schwartz, N. Schubert, R. A. Wise, S. Permutt, and P. L. Smith, "Upper airway collapsibility in snorers and in patients with obstructive hypopnea and apnea," *Am. Rev. Respir. Dis.*, vol. 143, no. 6, pp. 1300–1303, 1991, doi: 10.1164/ajrccm/143.6.1300.

[91] D. R. Hillman, P. R. Platt, and P. R. Eastwood, "The upper airway during anaesthesia," *Br. J. Anaesth.*, vol. 91, no. 1, pp. 31–39, 2003, doi: 10.1093/bja/aeg126.

[92] S. Isono, J. E. Remmers, A. Tanaka, Y. Sho, J. Sato, and T. Nishino, "Anatomy of pharynx in patients with obstructive sleep apnea and in normal subjects," *J. Appl. Physiol.*, vol. 82, no. 4, pp. 1319–1326, 1997, doi: 10.1152/jappl.1997.82.4.1319.

[93] A. R. Schwartz, D. W. Eisele, and P. L. Smith, "PHARYNGEAL AIRWAY OBSTRUCTION IN OBSTRUCTIVE SLEEP APNEA," *Otolaryngol. Clin. North Am.*, vol. 31, no. 6, pp. 911–918, Dec. 1998, doi: 10.1016/S0030-6665(05)70098-0.

[94] H. Tojima, F. Kunitomo, H. Kimura, K. Tatsumi, T. Kuriyama, and Y. Honda, "Effects of acetazolamide in patients with the sleep apnoea syndrome.," *Thorax*, vol. 43, no. 2, pp. 113–119, Feb. 1988, doi: 10.1136/thx.43.2.113.

[95] J. T. Sharp, W. S. Druz, V. D'Souza, and E. Diamond, "Effect of metabolic acidosis upon sleep apnea.," *Chest*, vol. 87, no. 5, pp. 619–624, May 1985, doi: 10.1378/chest.87.5.619.

[96] A. Witkowska, J. Jaromirska, A. Gabryelska, and M. Sochal, "Obstructive Sleep Apnea and Serotoninergic Signalling Pathway: Pathomechanism and Therapeutic Potential," *Int. J. Mol. Sci.*, vol. 25, no. 17, 2024, doi: 10.3390/ijms25179427.

[97] L. M. Biga *et al.*, *Anatomy & physiology*. OpenStax/Oregon State University, 2020.

[98] J. E. Brinkman, F. Toro, and S. Sharma, "Physiology, respiratory drive," 2018.

CHAPTER THREE: AN EXPERIMENTAL INVESTIGATION ON THE EFFECT OF AIRFLOW ON THE SOUND GENERATED IN A SIMPLIFIED TUBE WITH A CONSTRICTION REPRESENTING TRACHEA FOR OBSTRUCTIVE SLEEP APNEA DIAGNOSIS DURING WAKEFULNESS

Walid Ashraf[1], and Zahra Moussavi[1]

1. Biomedical Engineering Program, University of Manitoba, Winnipeg, Canada

CMBES Proceedings 46 (2024) (https://proceedings.cmbes.ca/index.php/proceedings/article/view/1081)

Abstract

Obstructive sleep apnea (OSA) diagnosis using tracheal breathing sound analysis during wakefulness has already shown great potential with an accuracy of 84.5% compared to the gold-standard polysomnography (PSG). The inclusion of geometrical parameters in the acoustic diagnosis of OSA during wakefulness may not only increase the accuracy but also provide insight into OSA pathology. In this study, we aimed to develop an upper airway model for a flow-sound relationship in the presence of a constriction (e.g. increased airway stiffness and/or collapsibility). The geometrical change selected for this study is a circular constriction representing tracheal narrowing. An experimental measurement was conducted on a 3D-printed model of a tube with a constriction while recording the airflow-generated sound at three locations. Several constriction sizes were tested at different airflow rates. The results show a higher frequency shift for the resonating frequencies for the smaller constrictions. In addition, larger slopes of the logarithmic relationship between airflow and the generated sound power were observed for the larger constrictions. These findings are encouraging for future studies to evaluate the mathematical

relationship between the tracheal breathing sounds in the presence of different constriction sizes for a realistic upper airway geometry.

3.1 Introduction

Obstructive sleep apnea (OSA) is a prevalent sleeping disorder associated with several clinical conditions such as cardiovascular disease, depression, diabetes and daytime hypersomnolence [1]. It is characterized by either a complete (apnea) or partial (hypopnea) collapse of the upper airway during sleep that lasts >10 sec and is also associated with a >3% drop in blood oxygen saturation. Polysomnography (PSG) is considered the gold standard for OSA diagnosis. Given that PSG is an expensive and time-consuming test requiring highly skilled labor and has a long wait, OSA is still massively underdiagnosed [2]. PSG's economic burden on the healthcare system accounts for billions of dollars annually [3]. In addition, PSG is not a suitable option to diagnose OSA prior to a surgery for patients requiring full anesthesia due to lack of time for a sleep study. Thus, fast screening questionnaires (Ex: STOP-Bang, Berlin) are usually employed using parameters such as age, gender, weight, smoking history, etc. Although these questionnaires have high sensitivity, their specificity is very low (~36%) [4]. In the last decade, several studies have been conducted on OSA diagnosis using tracheal breathing sounds (TBS) [5], [6] and voice analysis [7], [8]during wakefulness. The underlying rationale of these studies is based on imaging studies that provided evidence for the existence of anatomical and morphological differences between OSA and non-OSA individuals during wakefulness [9], [10], where an increased pharyngeal length, higher dilator muscle activity and longer/thicker, soft palate were observed in OSA individuals [10]. These characteristics can potentially be detected by breathing sounds generated due to airflow turbulence in an upper airway with these deformities. The study in [6] reported an accuracy of 83.92% using sound features only and 84.53% using sound features

and anthropometric features such as BMI, age, and gender. The study employed spectral and bi-spectral features of the tracheal sound signal generated due to breathing; however, anatomical and morphological features were not included.

The combination of the anatomical features of the upper airway structure and the spectral features may then benefit OSA classification by understanding the effect of the upper airway geometry on TBS. Extensive research has been previously conducted regarding TBS modelling and the sound generation mechanism. The study in [11] developed a dynamic acoustic model of the respiratory tract including the sound sources generated due to turbulent flow with a focus on the glottal aperture variation. The respiratory tract consisted of short sections with each section represented by a lumped acoustic circuit element. The sound pressure and velocity were considered analogous to voltage and electrical current respectively. The model predicted an increase in the sound power with the increase of respiration flow rate (0.5 to 2 L/s) with the greatest increase observed between 0.5 and 1 L/s. In addition, the sound power was greater during the expiration phase than during the inspiration phase, based on measurements performed on 4 participants, due to the smaller glottal opening size during expiration [11]. However, no specific parameter has been reported to evaluate the effect of the opening size on the rate of increase in the sound power. The study in [12] employed the power law relationship between the respiratory flow and the sound power as in Eq. 3-1:

$$P = K \times Q^{\alpha} \qquad 3\text{-}1$$

where P is the sound power and Q is the respiratory flow rate. K and α are model constants that vary based on several factors in the sound generation mechanism in the upper airway. Furthermore, the study in [13] employed Eq. 3-1 to study the variation in the respiratory flow-sound relationship between OSA and non-OSA during wakefulness and sleep, while assessing the

effect of different levels of airway obstruction. The study was performed on experimental patients' recordings of TBS rather than upper airway modelling. It was found that the power factor (α) varied significantly from wakefulness to sleep for OSA patients only, which depicts the dependency of the power factor on the airway collapsibility while the tracheal length was found to be a significant factor affecting the parameter K [13].

The above results show a great interest in a study that evaluates the effect of the upper airway narrowing size and location on the flow-sound relationship parameters quantitatively. The findings could be helpful for the classification of OSA and non-OSA individuals. Therefore, the purpose of this study is to experimentally study the effect of a constriction size in a simplified tube, representing trachea, on the sound generated due to airflow. In addition, the effect of the airflow rate is investigated.

3.2 Methodology

Fig. 3-1 shows a schematic of the experimental test setup. A compressor was used as the flow source which was attached to a rotameter serving as the flow control meter. The outlet of the rotameter was connected to the simplified tube model. The trachea was simplified as a circular tube with a constant diameter of 20 mm and a total length of 280 mm. An inlet tube with a diameter of 4 mm was added to facilitate the attachment to the flow control meter. The tube was constricted at a distance of 100 mm from the inlet. The CAD model of the simplified tube is shown in Fig. 3-2. The simplified tube model was 3D printed using PLA material. The complete setup, excluding the flow source and flowmeter, was placed in a small anechoic chamber to reduce the acoustic reflections. The sound was recorded for 5 seconds of continuous flow using Sony ECM-77B microphones with a sensitivity of -52 ± 2 dB at three microphone locations. Microphones 1 and 2 were placed on the tube surface with direct contact with the flow and located 175 mm and 225 mm

from the inlet, respectively. Microphone 3 was placed at the tube centerline located 50 mm from the outlet. The voltage signals were amplified, filtered with a 3 kHz low pass filter, 0.05 kHz high pass filter and sampled at 10 kHz using Biopac DA 100C. The raw voltage-time domain signals were then converted to pressure signals which were then segmented with a Hamming window of size 250 ms and 50% overlap. The frequency components were calculated utilizing fast Fourier transformation. The sound pressure level (SPL) was calculated for each microphone using Eq. 3-2.

$$SPL = 20log\frac{P}{P_{ref}} \qquad 3\text{-}2$$

where; P is the measured acoustic pressure in Pascal and P_{ref} is the reference acoustic pressure (threshold of hearing) and is equal to 2 x 10^{-5} Pascal. The test was conducted for three constriction diameters (5 mm opening/ 75% constriction, 10 mm opening/ 50% constriction and 15 mm/ 75% constriction) and at 7 flow rates (8 L/min to 20 L/min with a step of 2 L/min). Finally, the logarithmic relationship between the airflow rate and the acoustic power is investigated.

It was expected to observe a strong effect from the jet noise generated at the inlet vicinity due to the large area change at this location. To reduce this non-physiological effect, the test was repeated using a longer tube (340 mm) containing cell foam at the inlet to dampen out the noise generated at the inlet. The new microphones' locations were 235 mm and 285 mm from the inlet and 50 mm from the outlet for microphones 1, 2 and 3, respectively.

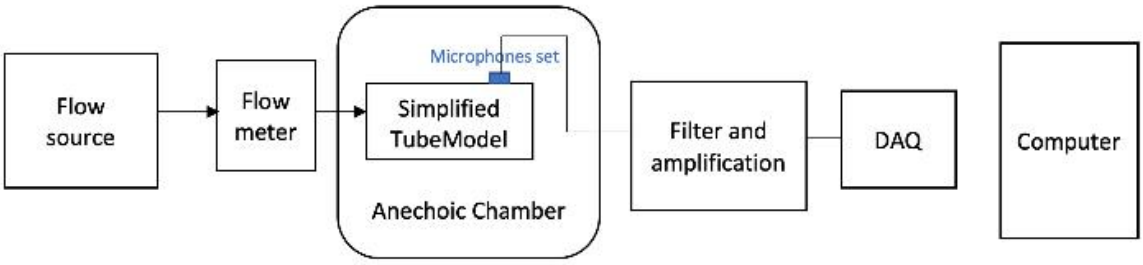

Fig. 3-1: Schematic of the testing setup

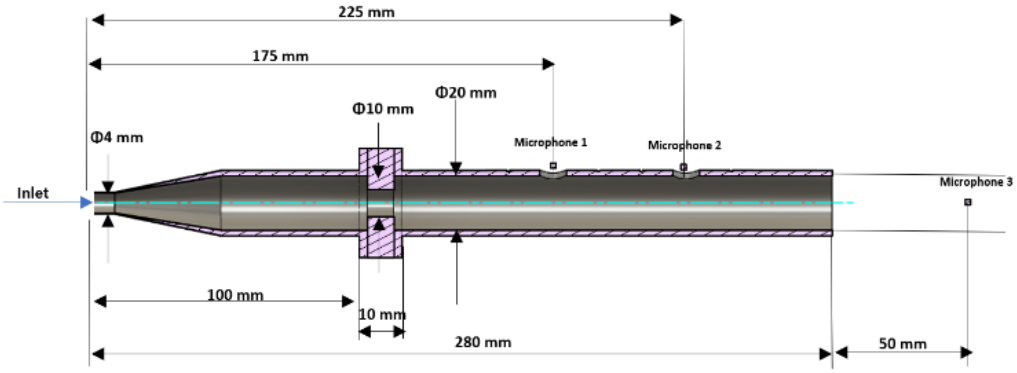

Fig.3-2: Simplified Tube CAD model with the location of the three microphones

3.3 Results

Fig. 3-3 shows the sound pressure level measured at three different constriction sizes (25%, 50% and 75%) using the 280 mm long tube model without the cell foam. There was no change in the 1st resonating frequency between the three constrictions since the tube length did not change. However, there was a frequency shift at the 2nd and 3rd resonating frequencies implying a relationship between the constriction size and these frequencies. Moreover, higher amplitudes were observed at the larger constriction openings, especially at higher frequencies. This can be explained by the greater effect of the jet noise occurring at the inlet vicinity as previously mentioned. Larger areas allow for larger pressure amplitudes to be captured by the microphones downstream of the flow. Therefore, to magnify the physiological significance of the constriction in the tube model, the longer tube of 340 mm in length with added cell foam at the inlet was tested.

Fig. 3-4 shows the results of this new setup. For this experiment, two additional constriction sizes (7 mm opening diameter/65% constriction and 8 mm opening diameter/60% constriction) were added to the test to amplify the inference. Several observations are depicted in this plot. First, the sound pressure measured at the two microphones placed on the tube surface was able to classify between the five constrictions, especially in the low-frequency region (below 500 Hz). Larger amplitudes are expected at the higher constrictions due to the larger area change generating higher flow turbulence, as shown in Fig. 3-4.

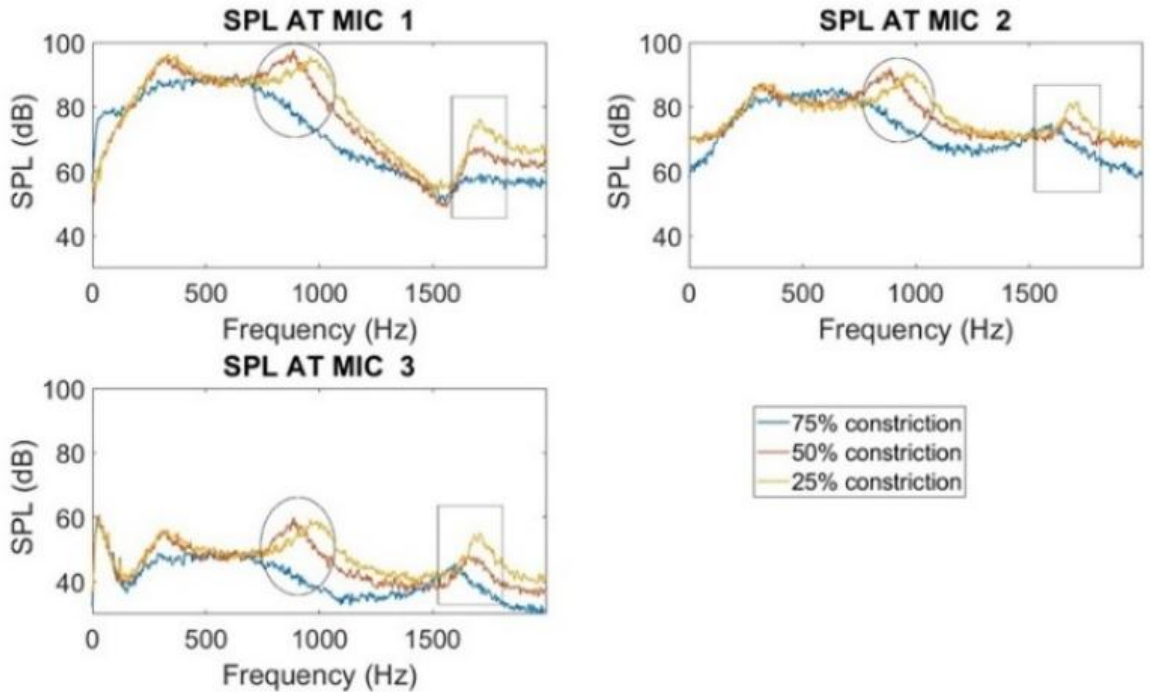

Fig.3-3: Experimental sound pressure level (SPL) of three constriction sizes measured at the three microphones (tube length = 280 mm without cell foam)

Furthermore, the logarithmic root mean square (RMS) pressure is plotted against the inlet flow rate. As shown in Fig. 3-5, steeper slopes were observed at higher constrictions, depicting an increase in the growth rate of the sound power for smaller opening sizes when the flow rate was elevated.

3.4 Discussion

OSA classification during wakefulness using the spectral features of tracheal breathing sounds along with anthropometric features has already been proven. However, the inclusion of geometrical features and breathing airflow has not been analyzed. This study aimed to experimentally measure the sound pressure level generated due to airflow inside a tube with a constriction to study the effect of the constriction size and the flow rate on the generated sound. Two tests were performed for this objective. The first test involved direct measurement of the sound generated in the tube without eliminating the effect of jet noise while the second test included the use of cell foam before the constriction opening to study the effect of the constriction solely. The results of this study have shown a resonance frequency shift towards higher frequencies when reducing the constriction (larger opening diameter). Moreover, higher sound power was observed at increased flow rates with an increased logarithmic slope for larger constrictions. This finding came in line with those in [13] that reported an increase in the logarithmic slope of the flow-sound power relationship from wakefulness to sleep with a significant change for OSA individuals. In addition, the study in [14] investigated the sensitivity of TBS to degrees of respiratory airflow obstruction by measuring the airflow of acromegaly and healthy participants with the aid of orifice plates of different sizes. Higher sound power was found for smaller orifice diameters for both groups. In addition, acromegaly patients showed increased sound power compared to the healthy participants [14]. These findings show a great potential for quantifying the relationship between the breathing flow rate and the constriction size; thus, providing more rationale for the classification of OSA during wakefulness and assessing the constriction size of an OSA patient using tracheal breathing sounds only.

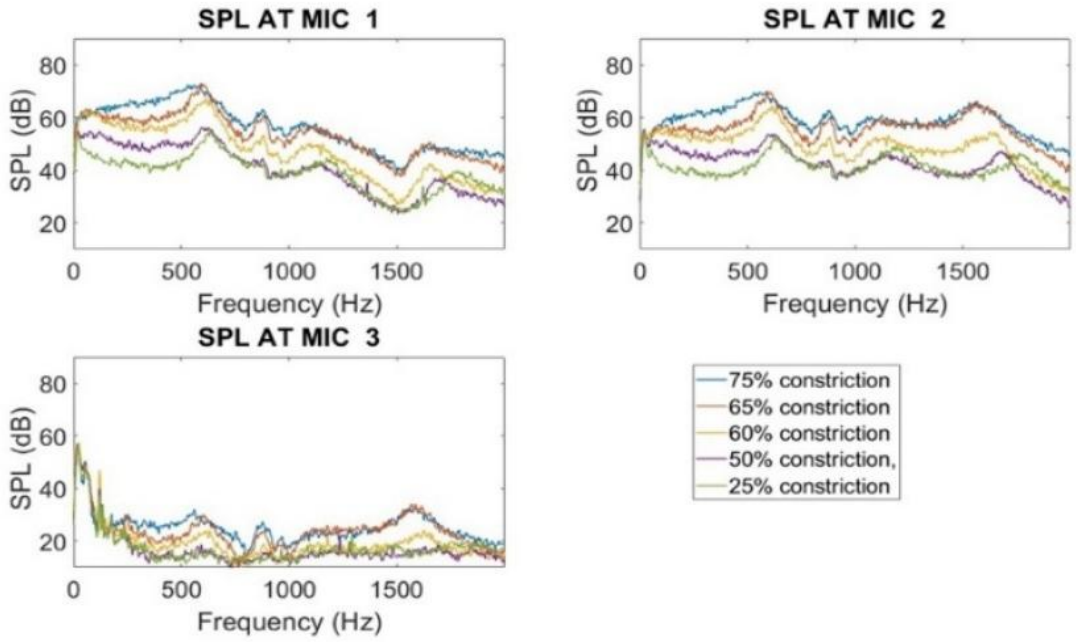

Fig.3-4: Experimental sound pressure level (SPL) at 5 constriction sizes measured at the three microphones (tube length =340 mm with cell foam)

This study encounters two primary limitations. Firstly, there is a geometric oversimplification of the trachea, as the experiment employs a tube with a sharp constriction, disregarding the various shapes of tracheal narrowing seen in OSA patients, such as tube, hourglass, and bottle shapes as demonstrated in [9]. A future study should explore the impact of these diverse shapes on TBS. Secondly, the rigid material used in the 3D printed model fails to accurately represent the high damping for sound amplitudes caused by human skin. This constraint could be mitigated in a future study by incorporating a more pliable 3D printing material with acoustic properties resembling human skin and by creating a realistic 3D model of the upper airway through CT scans.

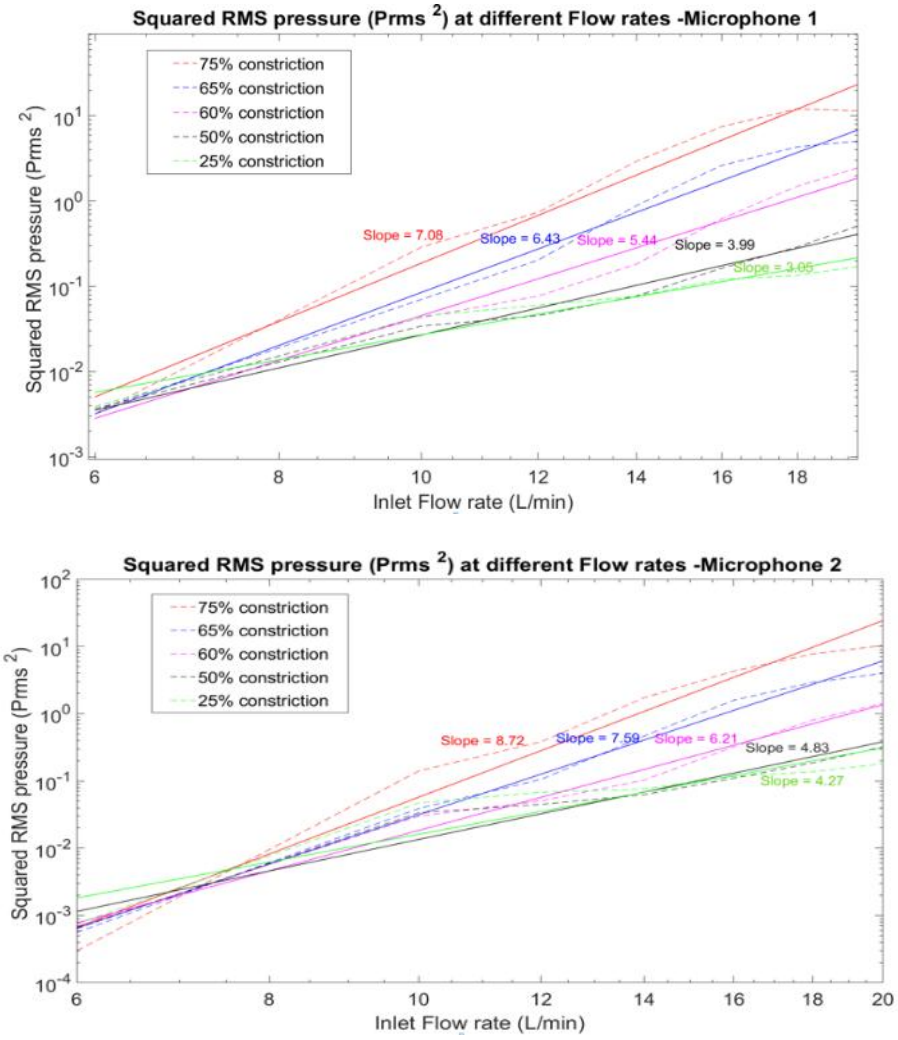

Fig. 3-5: Experimental logarithmic RMS pressure squared vs the inlet flow rate measured at the three microphones for the five constriction sizes for microphone 1 (upper figure) and microphone 2 (lower figure), (Measured ----Dash line, Fitted line—Solid line)

3.5 Summary

This study reports the results of an experimental upper airway modeling implemented on a simplified tube with a constriction representing trachea. Despite the oversimplification of the model, many important findings have been drawn and validated. There is a strong relationship between the frequency shift and the constriction size, representing tracheal narrowing. In addition, the evaluation of the slope of the logarithmic relationship between the airflow rate and the sound power could serve as a factor in OSA classification during wakefulness. These results indicate

great potential for further studies assessing the geometrical features of the upper airway and their effect on TBS to help in the diagnosis of OSA during wakefulness.

References

[1] J. A. Dempsey, S. C. Veasey, B. J. Morgan, and C. P. O'Donnell, "Pathophysiology of Sleep Apnea," *Physiol Rev*, vol. 90, no. 1, pp. 47–112, Jan. 2010, doi: 10.1152/physrev.00043.2008.

[2] M. Kato, T. Adachi, Y. Koshino, and V. K. Somers, "Obstructive sleep apnea and cardiovascular disease," *Circulation Journal*, vol. 73, no. 8, pp. 1363–1370, 2009, doi: 10.1253/circj.CJ-09-0364.

[3] N. Alghanim, V. R. Comondore, J. Fleetham, C. A. Marra, and N. T. Ayas, "The economic impact of obstructive sleep apnea," *Lung*, vol. 186, no. 1. pp. 7–12, Feb. 2008. doi: 10.1007/s00408-007-9055-5.

[4] M. Nagappa *et al.*, "Validation of the STOP-Bang Questionnaire as a Screening Tool for Obstructive Sleep Apnea among Different Populations: A Systematic Review and Meta-Analysis," *PLoS One*, vol. 10, no. 12, p. e0143697, Dec. 2015, doi: 10.1371/journal.pone.0143697.

[5] A. Elwali and Z. Moussavi, "Obstructive Sleep Apnea Screening and Airway Structure Characterization During Wakefulness Using Tracheal Breathing Sounds," *Ann Biomed Eng*, vol. 45, no. 3, pp. 839–850, Mar. 2017, doi: 10.1007/s10439-016-1720-5.

[6] A. Elwali and Z. Moussavi, "A Novel Decision-Making Procedure during Wakefulness for Screening Obstructive Sleep Apnea using Anthropometric Information and Tracheal Breathing Sounds," *Sci Rep*, vol. 9, no. 1, Dec. 2019, doi: 10.1038/s41598-019-47998-5.

[7] J. Solé-Casals *et al.*, "Detection of severe obstructive sleep apnea through voice analysis," *Applied Soft Computing Journal*, vol. 23, no. October 2014, pp. 346–354, 2014, doi: 10.1016/j.asoc.2014.06.017.

[8] F. Espinoza-Cuadros, R. Fernández-Pozo, D. T. Toledano, J. D. Alcázar-Ramírez, E. López-Gonzalo, and L. A. Hernández-Gómez, "Speech Signal and Facial Image Processing for Obstructive Sleep Apnea Assessment," *Comput Math Methods Med*, vol. 2015, 2015, doi: 10.1155/2015/489761.

[9] Y. Finkelstein *et al.*, "Velopharyngeal anatomy in patients with obstructive sleep apnea versus normal subjects," *Journal of Oral and Maxillofacial Surgery*, vol. 72, no. 7, pp. 1350–1372, 2014, doi: 10.1016/j.joms.2013.12.006.

[10] Z. Lan, A. Itoi, M. Takashima, M. Oda, and K. Tomoda, "Difference of pharyngeal morphology and mechanical property between OSAHS patients and normal subjects," *Auris Nasus Larynx*, vol. 33, no. 4, pp. 433–439, Dec. 2006, doi: 10.1016/j.anl.2006.03.009.

[11] V. P. Harper, H. Pasterkamp, H. Kiyokawa, and G. R. Wodicka, "Modeling and measurement of flow effects on tracheal sounds," *IEEE Trans Biomed Eng*, vol. 50, no. 1, pp. 1–10, 2003, doi: 10.1109/TBME.2002.807327.

[12] N. Gavriely and D. W. Cugell, "Airflow effects on amplitude and spectral content of normal breath sounds," *J Appl Physiol*, vol. 80, no. 1, pp. 5–13, 1996, doi: 10.1152/jappl.1996.80.1.5.

[13] A. Yadollahi, A. Montazeri, A. Azarbarzin, and Z. Moussavi, "Respiratory flow-sound relationship during both wakefulness and sleep and its variation in relation to sleep apnea," *Ann Biomed Eng*, vol. 41, no. 3, pp. 537–546, 2013, doi: 10.1007/s10439-012-0692-3.

[14] N. A. Lima Junior, N. V. Oliveira, A. B. W. Tavares, A. J. Lopes, and P. L. Melo, "Determining airflow obstruction from tracheal sound analysis: simulated tests and evaluations in patients with acromegaly," *Med Biol Eng Comput*, vol. 60, no. 7, pp. 2001–2014, 2022, doi: 10.1007/s11517-022-02584-2.

CHAPTER FOUR: AEROACOUSTICS OF BREATH SOUNDS IN TRACHEA AND UPPER AIRWAY

Walid Ashraf[1], Jeffrey J. Fredberg[2], and Zahra Moussavi[1,3]

1. Biomedical Engineering Program, University of Manitoba, Winnipeg, Canada
2. Department of Environmental Health, Harvard T. H. Chan School of Public Health, Boston, MA 02115, USA.
3. Department of Electrical and computer engineering, University of Manitoba, Winnipeg, Canada

Applied Acoustics (2026) 241, 111021 (https://doi.org/10.1016/j.apacoust.2025.111021)

Abstract

Tracheal breathing sounds (TBS) are widely used in assessing respiratory disorders such as obstructive sleep apnea but a mechanistic relationship between airway morphology and aero-acoustics remains undefined. Here we use a realistic upper airway model reconstructed from a human CT scan to investigate aerodynamic and acoustic effects of velopharyngeal constriction on TBS. A hybrid aero-acoustic modeling approach was employed, combining computational fluid dynamics (CFD) with acoustic finite element simulation. The model was validated against recorded TBS and showed strong agreement in both amplitude and resonant frequencies. Simulation of four graded degrees of velopharyngeal constriction demonstrated a significant influence of geometric narrowing on airflow dynamics. Specifically, the pressure drop across the velopharyngeal segment ($\Delta P_{velopharynx}$) followed a power law relationship with the percent area change ($\Delta A_{velopharynx}$) with an exponent of 4.93 ($R^2 = 0.998$). Similarly, the dimensionless pressure coefficient (C_p) exhibited a strong correlation with ($\Delta A_{velopharynx}$), with a power law exponent of 1.47 ($R^2 = 0.999$). Wall shear stress (WSS) at the velopharyngeal area increased dramatically with constriction severity, increasing 15-fold from 0.8 Pa to 12 Pa in the most severe case. These aerodynamic changes were closely linked to acoustic responses, leading to upward shifts in resonant frequencies within the [1000-1700] Hz range as the velopharyngeal area increased. These

findings indicate a strong relationship between airway geometry and acoustic response, thus suggesting that TBS could be a valuable tool for quantitative non-invasive assessment of the upper airway in healthy and obstructive sleep apnea populations.

4.1 Introduction

Breathing sounds have been an area of longstanding interest in both clinical and engineering research. Breathing sounds and respiratory acoustics provide qualitative diagnostic insights into the health of an individual's respiratory system [1], [2], [3], [4], [5], [6]. Various conditions, such as Obstructive Sleep Apnea (OSA), chronic obstructive pulmonary disease (COPD), tracheal stenosis, and asthma, exhibit characteristic acoustic signatures that have been attributed to changes in airflow through the central and upper airways. These changes arise mainly from the disease-related differences in upper airway anatomy. For instance, anatomical differences between OSA and non-OSA individuals may include increased in pharyngeal length, increased thickness of the velum and the pharyngeal wall, and narrowed pharyngeal lumen [7]. These anatomical variations are thought to influence airflow and, thereby, sound generation in the upper airway. Up to now, however, the link between anatomy and TBS has been empirical and correlative rather than quantitative and mechanistic.

Consequently, many research groups have explored the use of tracheal breathing sounds (TBS) in diagnosing respiratory disorders such as OSA either during sleep [2], [8], [9] or even wakefulness [5], [10], [11]. Spectral features of TBS have been employed to differentiate OSA from non-OSA patients during wakefulness with classification accuracy of 81.1% [11] and 83.92% [5]. Incorporating anthropometric features like body mass index (BMI), age, and gender alongside spectral features further improved accuracy to 84.53% [5]. In contrast, studies analyzing TBS during sleep focused on detecting disordered breathing events. Using power spectrum

features, One study achieved a sensitivity of 93% with a specificity of 67% at an Apnea-Hypopnea Index (AHI) cut-off of 5 and a sensitivity of 79% with a specificity of 95% at an AHI cut-off of 15 [8]. Similarly, TBS combined with blood oxygen saturation has yielded a sensitivity of 91.6% and a specificity of 97.8% at an AHI threshold of 20 [2]. These findings support the viability of utilizing TBS as an effective diagnostic tool for respiratory disorders with a particular focus on OSA. However, a deeper understanding of the multi-physical mechanisms of sound generation in the upper airway and how anatomical differences affect the acoustic behavior of TBS is essential for enhancing the diagnostic effectiveness of TBS.

The generation of tracheal breathing sounds results from the complex multi-physical interaction between airflow and upper airway geometry. The turbulence generated inside the upper airway during breathing creates hydrodynamic and acoustic pressure fluctuations which propagate to the inner surface of the upper airway. These pressure perturbations cause tissue vibrations that correspond to sound detected at the microphone placed over the suprasternal notch of the trachea.

This interaction falls within the domain of computational aeroacoustics (CAA), a field that combines fluid dynamics and acoustics to model sound generation from turbulent flow. Hybrid methods such as Lighthill's acoustic analogy [12], Curle's dipole extensions [13], and the Ffowcs Williams–Hawkings (FW-H) formulation [14] have been widely applied to simulate low Mach number flows in both free-field and confined flows [15]. While CAA has been widely adopted in several engineering domains, its applications in physiological systems have been gaining attention. For instance, substantial progress has been made in applying CAA to model voice sound production, particularly human phonation [16]. A numerical aero-acoustic larynx model was developed to replicate functional laryngeal disorders such as glottal insufficiency and asymmetrical vocal fold oscillations [17]. The study combined Large Eddy Simulation (LES) with

the acoustic perturbed convective wave equation (PCWE) in a simplified larynx geometry coupled to a vocal tract model. Similarly, Acoustic perturbation equations (APE) were employed to investigate the effect of different glottal configurations on the acoustics of human phonation [18]. A comparative study evaluated Lighthill's analogy and APE in modelling phonation finding that both methods showed good agreement, with an overprediction of Lighthill's analogy in the sound pressure level of the fundamental frequency [19]. That study also incorporated 2D coupled fluid-structure interaction to simulate the airflow generated due to vibration of vocal folds during phonation and compared the results with a 3D computational fluid dynamics (CFD) model driven by prescribed vocal folds motion. A pressure boundary condition was found necessary in the CFD model to capture the physical effects. Additionally, realistic vocal tract geometries reconstructed from magnetic resonance Imaging (MRI) have been employed to identify the flow-induced sound and acoustic sources in voiced speech using FW-H analogy [20]. Beyond phonation, few studies focused on applying CAA to the pharyngeal airway in the context of breathing-related disorders. For instance, the effects of pharyngeal anatomical effects on the breathing resistance and acoustic generation showed that uvular constriction significantly elevated both pressure drop and sound power levels [21]. A one-way coupled fluid-structure-acoustic interaction model was developed to study the sound generated from turbulent airflow and vibrating tissue in a partially obstructed pharyngeal airway [22], and another study identified that the highest sound pressure occurred downstream of the glottis [23]. Furthermore, the validation of CAA methodologies in confined flows has received significant attention. A study compared Lighthill's analogy and Ribner's dilatation equation [24] on a computational domain consisting of a rectangular duct with a diaphragm [25]. Ribner's approach decomposes the fluctuating pressure field into two components: a pseudo-sound (associated with near-field hydrodynamic fluctuations) and a true

acoustic pressure that propagates through the medium. While both formulations showed good agreement with experimental measurements, Lighthill's analogy demonstrated slightly higher predictive accuracy [25]. Similarly, in a comparison between Lighthill's analogy and Curle's analogy in a diaphragm-confined rectangular duct, the flow field was modelled using delayed detached eddy simulation (DDES), a hybrid Reynold average Navier-Stokes (RANS)-LES approach [26]. The results indicated good agreement for both methods within the frequency range of 200-3500 Hz with Lighthill's analogy offering advantages due to its volumetric 3D description of the aero-acoustic source terms, which is especially beneficial for confined geometries. Additionally, The acoustic source terms of Lighthill's analogy, PCWE and Ribner's formulation were investigated numerically on a circular duct with a halfmoon shaped orifice [27].

Taken together, this past work establishes that numerical simulations provide new opportunities for studying breathing sounds in unprecedented mechanistic detail. Numerical CFD simulations, such as Large Eddy Simulations (LES) and Direct Numerical Simulations (DNS), allow us to model complex turbulent airflow through anatomically realistic geometries of the airway. These geometries are typically derived from medical imaging techniques such as computed tomography (CT) or magnetic resonance imaging (MRI). These imaging techniques ensure the inclusion of patient-specific anatomical features that shape airflow dynamics and sound production. Coupled with acoustical theories, such as Lighthill's theory of turbulent sound generation [12], these simulations enable the detailed mechanistic analysis of sound propagation, frequency distribution, and amplitude characteristics of breathing sounds.

Here we employed CAA to simulate breathing sounds within the upper airway. A high-resolution CT scan was used to reconstruct realistic airway geometry, preserving critical anatomical features. The numerical analysis explored the influence of various structures on the

acoustic signature of breathing. We focused upon how airway constrictions, such as those seen in OSA, modify aero-acoustic behavior of the generated sounds. We validated the numerical results with experimental data recorded from the trachea of a healthy participant. The experimental setup involved placing a microphone over the suprasternal notch of trachea to capture the actual sound profile during breathing. To the best of the authors' knowledge, this study is the first to validate an aero-acoustic numerical model using actual recordings of breathing sounds for the whole TBS frequency bandwidth.

4.2 Materials and Methods

4.2.1 Simplified Airway Model geometry

The numerical simulation was initially conducted on a simplified tube model with a constriction, as illustrated in Fig. 4-1 [28], before being applied on a realistic upper airway geometry. The tube model had a diameter of 20 mm, narrowing to 10 mm in the constriction region. The inlet diameter was set to 4 mm to match the experimental setup described in [28]. The tube length measured 280 mm. The purpose of this initial simulation was twofold: first, to experimentally validate the complete numerical simulation methodology using a 3D-printed model of the simplified tube, thereby facilitating the tuning of CFD and FEM model parameters and boundary conditions. Second, to gain preliminary insights into the effect of constriction size on the acoustic response of airflow within a tube, as discussed in [28]. For the experimental validation, a steady airflow of 18 L/min was introduced at the tube inlet. The setup was housed within an anechoic chamber to suppress external acoustic interference. A SONY ECM-77B condenser microphone (sensitivity: -52 ± 2 dB) was positioned 50 mm downstream from the tube outlet along the centerline to capture the radiated sound. The signal was amplified using a BIOPAC DA100C

amplifier module and sampled at 10 kHz. Further details concerning the experimental setup and signal processing were provided in [28].

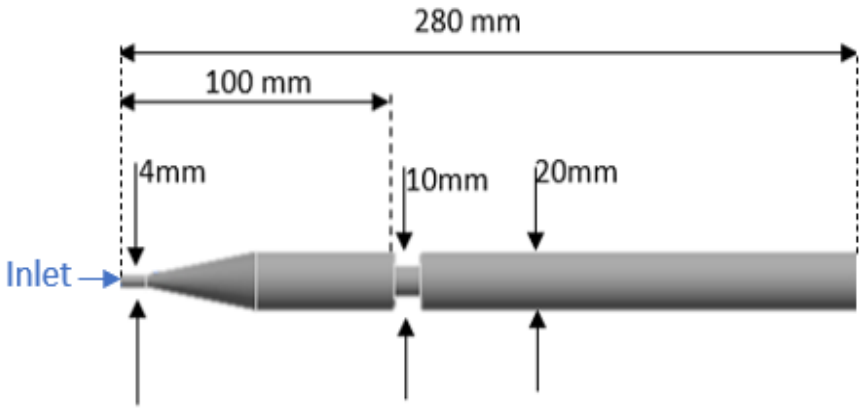

Fig.4-1: Cross section of the CAD model of the simplified tube with constriction [28]

4.2.2 Data collection and generation of the upper airway CAD model

4.2.2.1 Airway model segmentation

Following the validation of the simplified tube model, the second stage of validation involved comparing the simulated sounds with actual tracheal breathing sounds (TBS) recorded from a healthy subject (Female - 76 years old). The numerical simulation was applied to a realistic upper airway model reconstructed from a CT scan of the same subject with the aid of semi-automatic segmentation software ITK-SNAP [29]. The segmented 3D CAD geometry undergoes a two-stage refinement process to ensure accuracy and smoothness. In the first stage, Autodesk Fusion 360 software is used to eliminate voids and correct any geometric irregularities that arise from the segmentation process. This correction was essential for preserving the anatomical fidelity of the model while maintaining a mesh suitable for numerical simulations. In the second stage, Blender software was employed to smooth the airway walls and prepare the inlets and outlets for boundary condition application in the numerical simulations. This step ensured the creation of a

continuous, high-quality surface, minimizing potential numerical artifacts that could arise during the simulation. The upper airway 3D geometry is shown in Fig. 4-2.

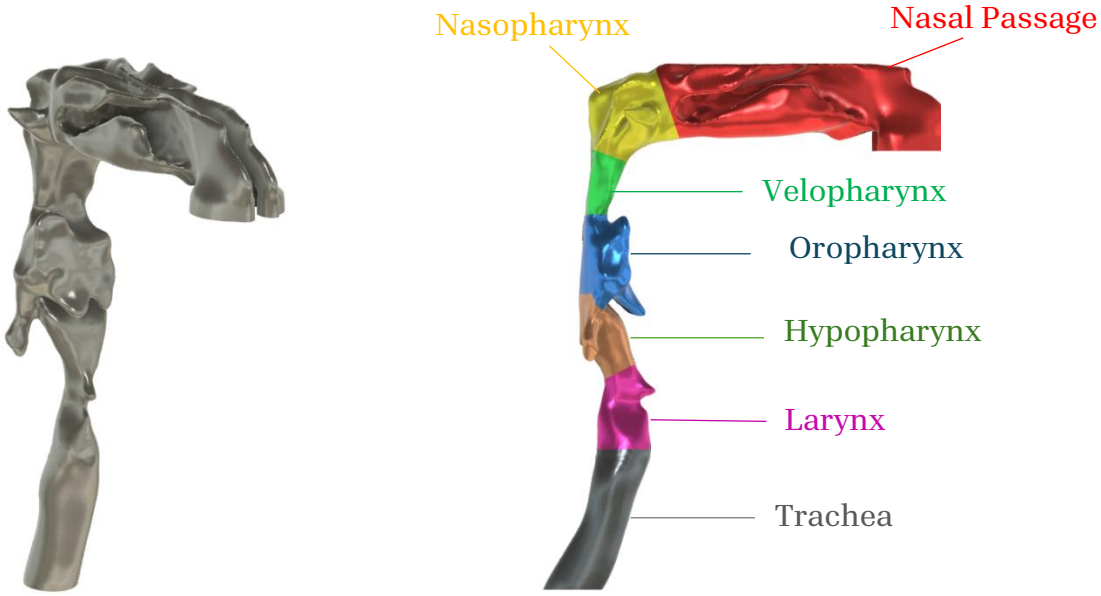

Fig.4-2: 3D CAD model of the upper airway segmented from CT scan of a healthy subject.

4.2.2.2 TBS recording protocol and signal processing

Tracheal breathing sounds (TBS) were recorded from the healthy subject for validation using a SONY ECM-77B microphone positioned over the suprasternal notch, while the subject was in supine position, aligning with the subject's posture during the CT scan for consistency. The recording protocol involved the subject performing a deep inhalation, holding their breath for three seconds followed by a deep exhalation, repeated for five full breathing cycles through the nose, with closed mouth [5], [30]. The recorded sound signals were sampled at 11,025 Hz and processed using a fourth-order Butterworth filter, with a band-pass range of [75-3000] Hz. For analysis, a segment corresponding to 50% of the duration centered around the peak of the inspiratory phase was selected, resulting in an approximately 300 ms window. This segment is identified as a stationary signal [31] and suitable for comparison with a simulation setup designed to replicate

steady inspiratory conditions using a constant-pressure drop. A detailed description of the pre-processing and signal analysis procedures can be found in [5]. This study was approved by the Biomedical Research Ethics Board of the University of Manitoba and the subject signed an informed consent prior to the experiment.

4.2.3 Computational Aero-acoustic (CAA) Simulation Process

Computational Aero-acoustic (CAA) simulations can be performed using either a direct or a hybrid approach. The direct method involves solving the compressible Navier-Stokes equations, where the pressure calculation accounts for both hydrodynamic and acoustic fluctuating components. While this approach provides a complete representation of the flow and sound generation, it is computationally expensive due to the need for high spatial and temporal resolutions to capture the entire range of acoustic frequencies. Consequently, its use is limited in practical engineering applications. In contrast, the hybrid approach employs a decoupled methodology, separating the generation of aero-acoustic sources from the acoustic propagation. Hybrid approaches based on acoustic analogies are specially well suited for low Mach number flows and acoustically compact sources [32]. This makes them ideal for modeling physiological systems such as breathing sounds, where the flow is generally subsonic (Ma <0.2). In this study, it is assumed that the acoustic waves generated by breathing do not influence the airflow dynamics, justifying the use of a hybrid approach. This assumption is often referred as the weak acoustic coupling. The hybrid approach combines Computational Fluid Dynamics (CFD) for airflow

analysis with Finite Element Modelling (FEM) for acoustic propagation, enabling a comprehensive assessment of both aerodynamic behavior and acoustic characteristics.

4.2.3.1 CFD simulation

The airflow dynamics within the upper airway are governed by the incompressible Navier-Stokes equations, which ensure the conservation of mass and momentum. These are given by the continuity equation (4-1) and the momentum equation (4-2).

$$\frac{\partial u_i}{\partial x_i} = 0 \qquad 4\text{-}1$$

$$\frac{\partial u_i}{\partial t} + u_j \frac{\partial u_i}{\partial x_j} = -\frac{1}{\rho}\frac{\partial P}{\partial x_i} + \nu \frac{\partial^2 u_i}{\partial x_j \partial x_j} \qquad 4\text{-}2$$

Where $\boldsymbol{i}$ and $\boldsymbol{j}$ are the cartesian tensor notation, $\boldsymbol{u}$ the velocity vector, $\boldsymbol{P}$ the pressure, $\boldsymbol{\rho}$ the fluid density, and $\boldsymbol{\nu}$ the kinematic viscosity respectively.

Turbulence is inherently a chaotic and unsteady phenomenon characterized by swirling vortices that induce velocity and pressure fluctuations in the flow [33]. These vortices, or eddies, span a wide range of length scales, from large energy-containing structures to small dissipative scales where kinetic energy is converted into heat. In computational aero-acoustics, accurately capturing these eddies is critical, as they serve as the primary sources of sound. Therefore, resolving these eddies is essential to ensure the precision of aero-acoustic source calculations.

In this study, the transient Large Eddy Simulation (LES) is employed to model turbulent airflow within the upper airway due to its ability to explicitly resolve the large-scale turbulent structures that are most influential in sound generation [34]. LES achieves this by filtering the Navier-Stokes equations, separating the velocity field into resolved and subgrid scale components.

The resolved eddies are directly computed, while the effects of the smaller, subgrid scales are modeled using a subgrid-scale (SGS) model [35]. This approach ensures a balance between computational efficiency and accuracy, as it avoids the excessive computational cost of resolving all scales, as required in Direct Numerical Simulation (DNS), while providing a more accurate representation of turbulence than Reynolds-Averaged Navier-Stokes (RANS) models. In LES, an arbitrary filtered flow variable $\tilde{\boldsymbol{\phi}}(\boldsymbol{x})$ can be defined by the convolution of the instantaneous variable and the filter function $\boldsymbol{G}$. It is expressed as:

$$\tilde{\phi}(x) = \int \phi(x')G(x - x', \Delta)dx' \qquad 4\text{-}3$$

where ϕ is the instantaneous unfiltered flow variable, D is the fluid domain, and Δ is the filter width, typically set based on the mesh size. The filtered Navier Stokes equations then become:

$$\frac{\partial \tilde{u}_i}{\partial x_i} = 0 \qquad 4\text{-}4$$

$$\frac{\partial \tilde{u}_i}{\partial t} + \tilde{u}_j \frac{\partial \tilde{u}_i}{\partial x_j} = -\frac{1}{\rho}\frac{\partial \tilde{p}}{\partial x_i} + \nu \frac{\partial^2 \tilde{u}_i}{\partial x_j \partial x_j} - \frac{\partial \tilde{\tau}_{ij}{}^{SGS}}{\partial x_j} \qquad 4\text{-}5$$

Where $\tilde{\tau}_{ij}{}^{SGS}$ denotes the subgrid scale stress tensor. In this study, the subgrid scale stress is modeled using Smagorinsky-Lilly model [36], [37], [38] for its high performance in wall bounded flow as shown in [39], where the Smagorinsky constant (C_s) is set to 0.1. The simulation was initialized using a steady-state RANS solution with the k-ω SST turbulence model, providing an initial condition for LES. This hybrid approach allowed the LES to start from a physically realistic flow field, reducing the computational cost of developing turbulence from rest. The RANS solution also offered insights into turbulence characteristics, informing decisions on mesh

refinement and boundary conditions. Moreover, it had been shown in [40] that the frequency band of the normal tracheal breathing sounds is >100 Hz and <3000 Hz, therefore, in accordance with [5] , the upper frequency limit in this study was set at 2500 Hz. The transient LES equations were conducted with a constant time step of $1e^{-4}$ second over 8000-time steps. The first 1000-time steps were dedicated solely to achieving a fully developed flow and ensuring numerical stability, while the subsequent 7000-time steps were retained for acoustic simulations, yielding a physical simulation time of 0.7 seconds. The discretized governing equations were solved in ANSYS Fluent using the SIMPLE (Semi-Implicit Method for Pressure Linked Equations) algorithm for the pressure-velocity coupling [41]; while bounded central-differencing scheme was employed for the momentum discretization and bounded second order implicit was adopted for the transient formulation.

4.2.3.2 Acoustic Finite element model

The instantaneous velocity fields obtained from the CFD simulation were mapped onto a new finite element model in the frequency domain to compute the aero-acoustic sound sources. Several aero-acoustic analogies can be employed for this purpose, each providing a framework to relate the unsteady flow field to the resulting sound generation. For instance, the studies in [21], [22] utilized the Ffowcs Williams-Hawking's (FW-H) analogy. The study in [23] adopted the acoustic perturbation equations (APE), while [42] employed the Lighthill's analogy. Since FW-H is more suitable for external flow scenarios and far-field acoustic prediction, thus Lighthill's analogy was implemented in this study. Lighthill's acoustic analogy is based on the reformulation of the Navier-Stokes equations to isolate acoustic sources within the turbulent flow [12]. The analogy treats sound generation as a consequence of fluctuating stress and density fields. The

governing equation for Lighthill's analogy is derived from the conservation of mass and momentum and can be expressed as:

$$\frac{1}{c^2}\frac{\partial^2 p'}{\partial t^2} - \frac{\partial^2 p'}{\partial {x_i}^2} = \frac{\partial^2 T_{ij}}{\partial x_i \partial x_j} \qquad 4\text{-}6$$

where,

$$p' = c^2(\rho - \rho_0) \qquad 4\text{-}7$$

and c is the speed of sound, ρ is the fluid density, ρ_0 is the ambient density, and p' is related to the total pressure p through $p' = p - p_0$, where p_0 is the ambient pressure. T_{ij} is the Lighthill stress tensor and can be approximated for low Mach number flow as:

$$T_{ij} \approx \rho u_j u_j \qquad 4\text{-}8$$

The computation of aero-acoustic sound sources was conducted using ACTRAN-Acoustics software. The instantaneous velocity fields from the LES simulations served as input to ACTRAN, where the propagation of acoustic waves was simulated using the finite element method (FEM). The FEM solution of the acoustic wave equation provided the sound pressure level (SPL) at specified microphone location within the acoustic domain, allowing for direct comparison with experimental measurements and validation of the numerical model.

4.2.4 Meshing and Boundary conditions

4.2.4.1 Simulation 1: Simplified airway model

For the CFD simulation, a mass flow inlet boundary condition of 0.0003675 kg/s was applied at the tube inlet, corresponding to a volume flow rate of 18 L/min and an air density of 1.225 kg/m^3. A large buffer volume was added to the tube outlet to minimize potential backflow and ensure numerical stability by allowing the flow to fully develop before exiting the domain. At

the outlet, atmospheric pressure (zero-gauge pressure) was imposed. The walls of the tube were modeled with a no-slip boundary condition. The fluid domain was discretized using tetrahedral cells. According to Pope [43], the computational grid for LES should resolve at least 80% of the turbulent kinetic energy, which was achieved by maintaining a minimum of 5 to 20 cells across the integral length scale [41]. This requirement led to an average mesh size of 0.3 mm. To accurately capture the near-wall effects, an inflation layer mesh consisting of 15 prism layers was added along the tube wall. The total thickness of the inflation layers was 0.8 mm, with a growth rate of 1.2. This setup ensured that the wall-adjacent cells maintain a non-dimensional wall distance $y^+ < 1$, critical for resolving the turbulent boundary layer. The final mesh comprised approximately 4 million elements, balancing computational efficiency and the resolution needed to capture the flow dynamics accurately.

For the acoustic simulation, a propagation domain was added at the outlet to account for sound propagation, while infinite surface elements were applied at the boundaries of this domain to prevent reflections of acoustic waves. The propagation domain was discretized using a finite element mesh consisting of quadratic tetrahedral elements, ensuring that each wavelength is resolved with at least six elements. Given that the maximum frequency of interest (f_{max}) is 2500 Hz and the speed of sound (c) in air is 343 m/s, the smallest wavelength (λ_{min}) can be calculated as:

$$\lambda_{min} = \frac{c}{f_{max}} \qquad 4\text{-}9$$

The average element size of the acoustic domain mesh was 3 mm; corresponding to 45 elements per the smallest wavelength. The following configuration resulted in approximately 39,000 3D elements and 2,600 infinite surface elements. MUMPS (multifrontal massively parallel

sparse direct solver) was employed to solve the system of equations formulated by the finite element method. The frequency response curve was then plotted at a microphone placed along the centerline, at a distance of 50 mm from the outlet.

4.2.4.2 Simulation 2: Upper airway model

As for the CFD simulation of the second model, a zero-gauge pressure boundary condition was applied at the inlet (nostrils), while a pressure drop of -280 Pa (-2.8 cmH_2O) was imposed at the outlet (trachea). This pressure-driven setup was selected to simulate the peak inspiratory flow, corresponding to the 300 ms stationary segment identified in the tracheal breathing sound recordings [31]. By approximating the flow during this quasi-steady peak phase of inspiration, the simulation enabled a meaningful comparison with the experimentally recorded signals. The walls of the airway were treated with a no-slip boundary condition. The mesh was refined in regions of high curvature and constrictions to capture key flow features, ensuring proper resolution of turbulent structures in the LES stage. 12 Inflation layers with a total thickness of 1.2 mm were added near the walls. A grid independence study was conducted using four mesh resolutions comprising approximately 1.3 million, 2.0 million, 2.9 million, and 6.7 million elements. The analysis was performed at t = 0.4 s, focusing on two key aerodynamic indicators: (1) the pressure drop across the velopharyngeal segment, and (2) the mean velocity measured at two probe points located at the entrance and exit of the velopharyngeal region. The results from each mesh were compared against the finest mesh (6.7 million elements) as the reference. For the pressure drop, the deviation from the reference solution was 5.9%, 2.2%, and 1.8% for the 1.3M, 2.0M, and 2.9M meshes, respectively. Similarly, the velocity probes showed deviations of 2.4%, 0.3%, and 0.17% across the same mesh sizes. These results indicate that mesh refinement beyond 2.9 million elements yields minimal changes in the key flow metrics (<2%), confirming that the 2.9 million

element mesh provides a sufficient balance between computational cost and solution accuracy. Additionally, the mesh resolution was verified to ensure that over 80% of the turbulent kinetic energy was resolved.

For the acoustic simulation, large propagation domains were added at both the inlet and outlet to capture wave behavior effectively. Since the flow is modeled during inspiration phase, the infinite surface element was set at the inlet to prevent acoustic wave reflections. The finite element mesh consisted of quadratic tetrahedral elements, maintaining an average element size of 3 mm resulting in approximately 40,000 3D elements and 2000 infinite surface elements. The frequency response curve was plotted at a microphone located within the propagation domain added to the outlet (trachea), capturing the tracheal breathing sounds.

4.2.5 Geometrical modifications of the upper airway model

To study the effect of velopharyngeal narrowing on the acoustic response of the airway, the upper airway geometry was modified using Blender software. Four distinct modifications were applied to the original geometry to investigate how changes in the airway shape influence the frequency response and acoustic characteristics of the flow. These modifications focused on the velopharyngeal region, where constrictions or narrowing can significantly impact airflow dynamics and sound generation. The modifications included two levels of narrowing, with reductions of 27.4% and 68.9% in the minimum cross-sectional area (CSA), and two levels of enlargement, with increases of 79.0% and 177.8%, all relative to the baseline geometry. These values were chosen to span a physiologically relevant range as supported by previous clinical imaging studies [44], [45]. In particular, healthy participants were reported to have a velopharyngeal CSA of 98.3±32.5 mm^2 (mean ± std), while individuals with OSA showed a

significantly reduced CSA of 52.3±23.6 mm^2 during wakefulness, corresponding to a reduction of approximately 47% compared to healthy controls [44]. In another study, the maximum and minimum CSA values for OSA participants were reported as 91±40 mm^2 and 64±30 mm^2, respectively, while those for BMI-, age- and gender- matched healthy controls were reported substantially larger at 153±84 mm^2 (maximum) and 106±29 mm^2 (minimum) [45]. These anatomical benchmarks support the clinical relevance of our geometric modifications, which span from severely narrowed configurations consistent with OSA pathology to expanded airway conditions that mimic therapeutic outcomes or inter-subject variability in healthy population. Fig. 4-3 shows the CSA of the velopharynx for the different modifications, along with the original airway geometry. The modified models were then used to perform simulations and analyze the corresponding changes in the tracheal breathing sounds. These geometrical alterations will allow for a detailed understanding of how specific anatomical variations influence the aero-acoustic behavior in the context of obstructive sleep apnea (OSA) and healthy airway conditions

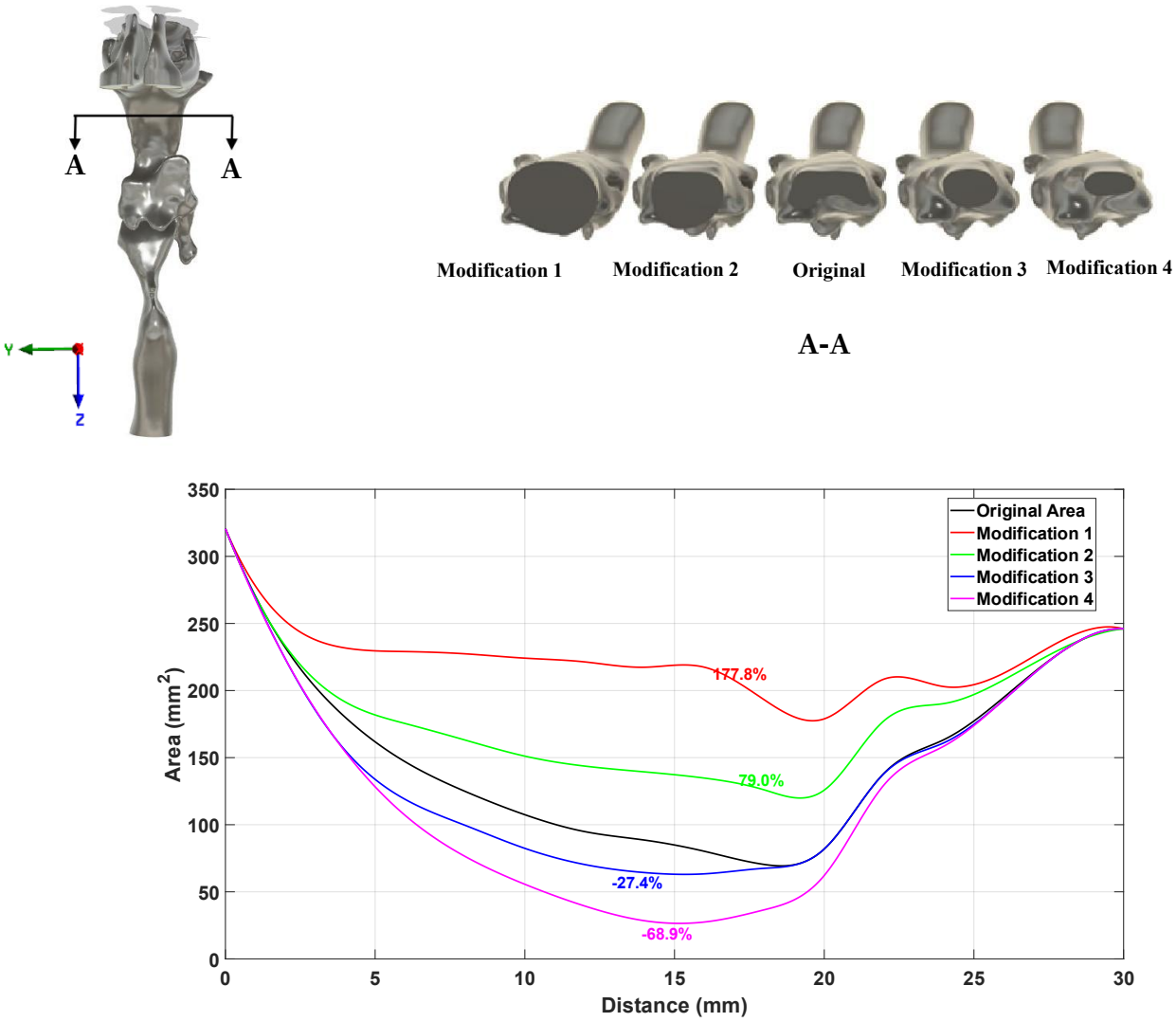

Fig.4-3: Top- Cross-sectional view of the velopharyngeal region showing geometric modifications of the upper airway (Middle: Original geometry; Left: Modifications 1 & 2 with larger cross-sectional area; Right: Modifications 3 & 4 with smaller cross-sectional area). Bottom – Cross sectional area vs z- distance in the velopharyngeal area indicating maximum percentage changes from the original cross-sectional area.

4.3 Results and Discussion

4.3.1 Acoustic Validation

The frequency response curve at the microphone placed outside the flow region for Simulation 1 (the simplified airway model) was compared against the experimental data in [28].

Fig. 4-4 shows the experimental and simulated response curves. A strong agreement between the two curves indicates that the model accurately captured the key acoustic features of the sound generated due to flow inside a constricted tube, particularly the primary resonant frequencies. The simulated curve exhibited the same general frequency distribution as the experimental data, with less than 4% deviation in capturing the resonant frequencies and only minor discrepancies in amplitude at higher frequencies. These discrepancies may be attributed to experimental and numerical errors. For instance, the experimental setup involved a direct connection between the flow source and the tube model, which may have introduced sound reflections and resulted in elevated amplitudes. Additionally, numerical simplifications such as idealized boundary conditions, simplifications in wall damping and the exclusion of microphone casing effects could have contributed to amplitude mismatches at higher frequencies. Nevertheless, the overall agreement between the simulation and the experiment was strong, indicating that the simulation methodology is robust and can be reliably applied to the more complex geometry of the upper airway.

Fig. 4-5 shows the comparison between the actual and simulated tracheal breathing sounds (TBS) of the healthy participant (Simulation 2). Likewise, a strong agreement was observed capturing the resonating frequencies of the sound generated due to breathing for that specific subject. This further supports the robustness of the simulation approach in accurately modelling the acoustic response of the upper airway in a healthy participant.

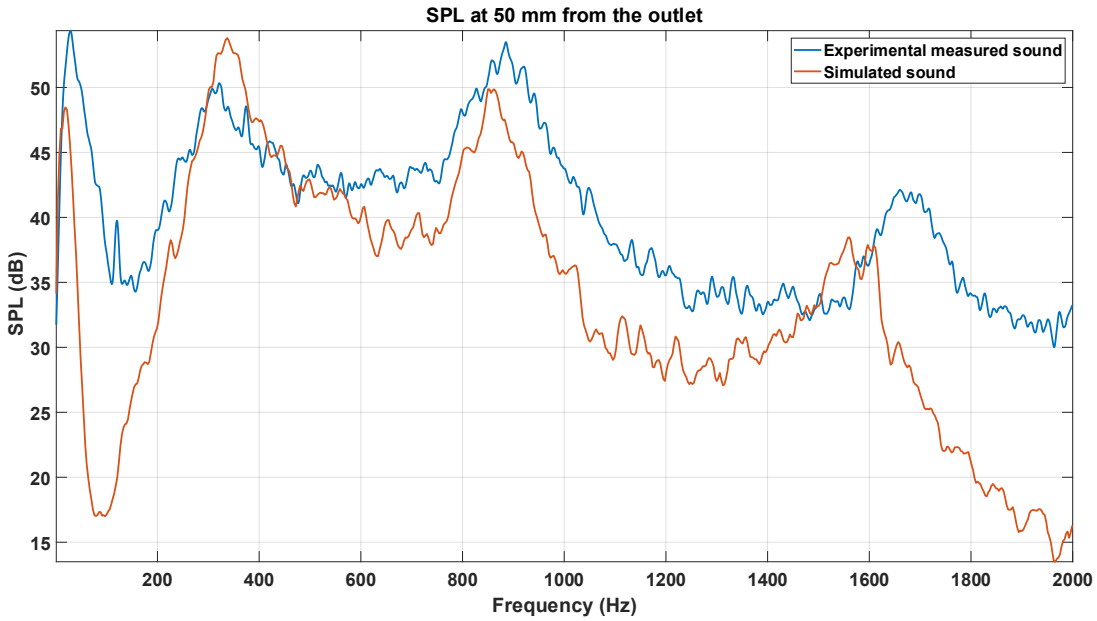

Fig.4-4: Experimental Vs Simulated frequency response curve at a microphone placed 50 mm from the outlet of the simplified tube model.

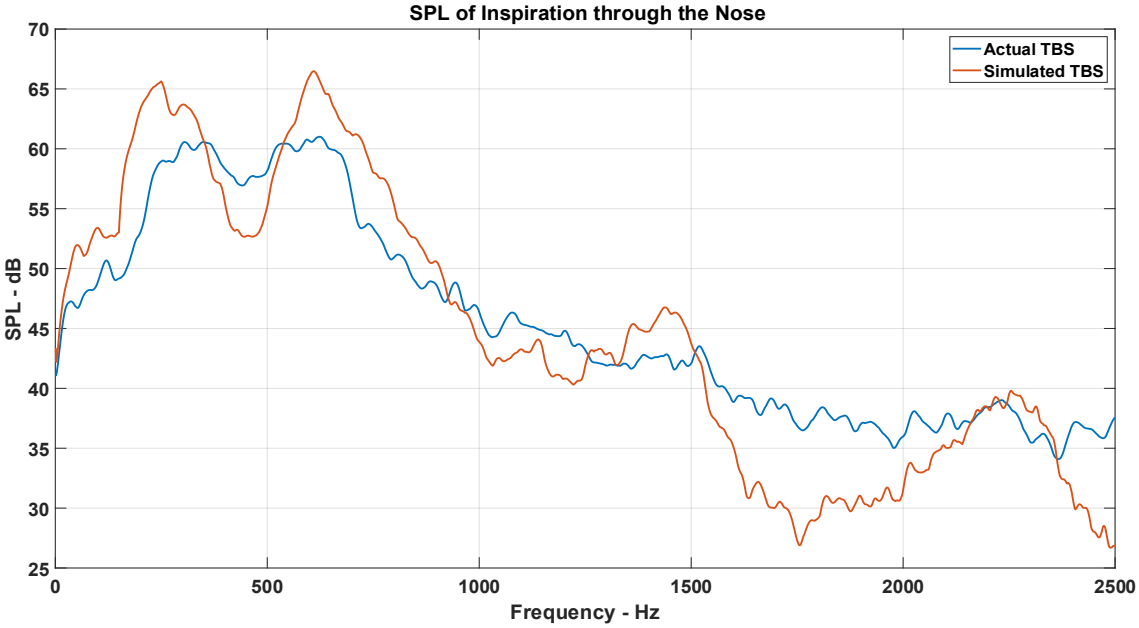

Fig.4-5: Actual Vs Simulated Tracheal Breathing Sounds (TBS) of a healthy subject.

4.3.2 Aero-dynamic characteristics of the upper airway

With the validated simulation methodology, the study examined the impact of anatomical changes in the upper airway, specifically velopharyngeal constriction, on aerodynamic characteristics and acoustic responses. Both the original airway geometry and four modified versions (see Fig. 4-3) were analyzed to identify trends in pressure distribution and airflow patterns. These modifications reflect varying degrees of velopharyngeal constriction and expansion to assess their effects comprehensively. Fig. 4-6 presents the average pressure contours over the mid-sagittal plane for all five simulated cases at t=0.8 sec. It is observed that modification 4 with the largest constriction level exhibited the highest-pressure gradient at the velopharyngeal zone. To further investigate these trends, Fig. 4-7(a) illustrates the mean pressure distribution along the centerline of the pharyngeal region for all cases. The results reveal that Modification 4 had the steepest pressure slope, indicating a sharp pressure drop in the constriction region. Despite Modification 3 was also representing a narrowed geometry, its pressure slope was less pronounced compared to Modification 4. This can be attributed to Modification 4 significantly reducing the effective cross-sectional area at the constriction, which exacerbates flow resistance and leads to a more dramatic pressure drop. An important finding is that the relationship between pressure change and constriction level was not a linear relationship. While moderate narrowing (e.g., in Modification 3) caused a noticeable pressure to drop, the increase in pressure gradient became disproportionately larger in Modification 4, where the constriction was more severe. This nonlinear dependence emerged because, as the cross-sectional area decreases, the flow velocity must increase significantly to maintain mass continuity. This elevated velocity led to a quadratic increase in dynamic pressure, further amplifying the pressure drop due to increased viscous resistance and intensified inertial effects. Additionally, a critical observation is that the dramatic

pressure drop occurs when the cross-sectional area at the constriction approached a specific threshold. Beyond this threshold, the flow transitioned from a relatively laminar flow to one dominated by turbulence and flow separation, amplifying energy losses. In modification 4, the constriction was sufficiently severe to induce such a transition, resulting in exponential resistance growth and an amplified pressure drop. This was also evident in the velocity streamlines in Fig. 4-8, where flow separation and recirculation are observed downstream of the velopharyngeal constriction, particularly in the oropharynx region. The maximum velocity in the velopharyngeal region reached approximately 23.1 m/s in modification 4, markedly higher than in the other configurations: 11 m/s, 6.8 m/s, 6.7 m/s, and 9.8 m/s in modifications 3, 2, and 1 and in the original geometry, respectively. It had been previously shown that the site of the upper airway collapse for OSA patients was influenced by the specific location of the pressure drop [46]. Furthermore, Fig. 4-7(b) shows the mean velocity magnitude distribution along the centerline of the pharyngeal region in the mid-sagittal plane. For Modification 4, the maximum velocity was observed at the constriction zone, whereas for all the other cases, the maximum velocity was observed at the glottic region (larynx zone). This distinction provides further evidence of a critical velopharyngeal constriction limit, beyond which flow characteristics undergo significant changes. This is consistent with findings in [47], where tracheal stenosis in a smoothed airway model showed dramatic pressure drops at 85% and 90% constriction levels.

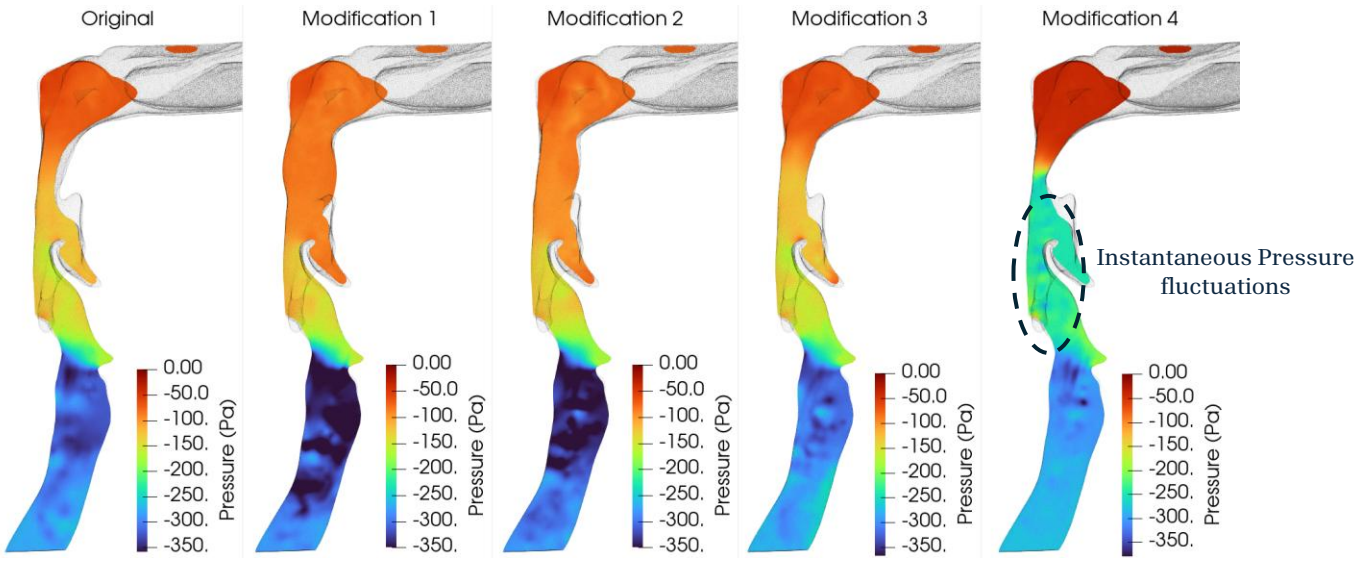

Fig.4-6: Pressure field of the upper airway at t=0.8 sec. (from nasopharynx to the trachea outlet) in mid-sagittal plane for the original airway geometry and the 4 modifications (see Fig.4-3).

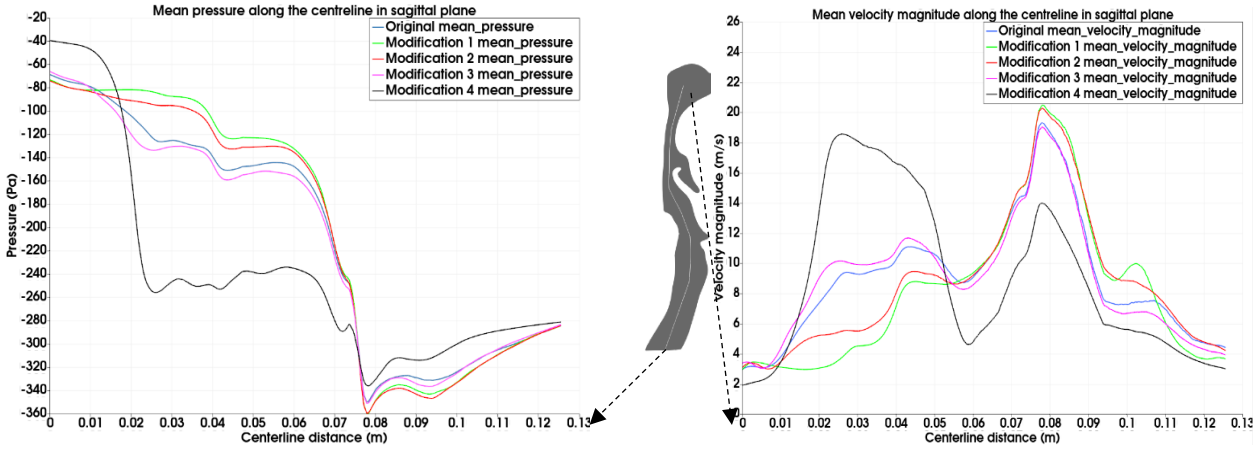

Fig.4-7: (a) Mean pressure distribution along the centreline of the upper airway (from nasopharynx to the trachea outlet). (b) Mean velocity magnitude distribution along the centreline of upper airway (from nasopharynx to the trachea outlet)

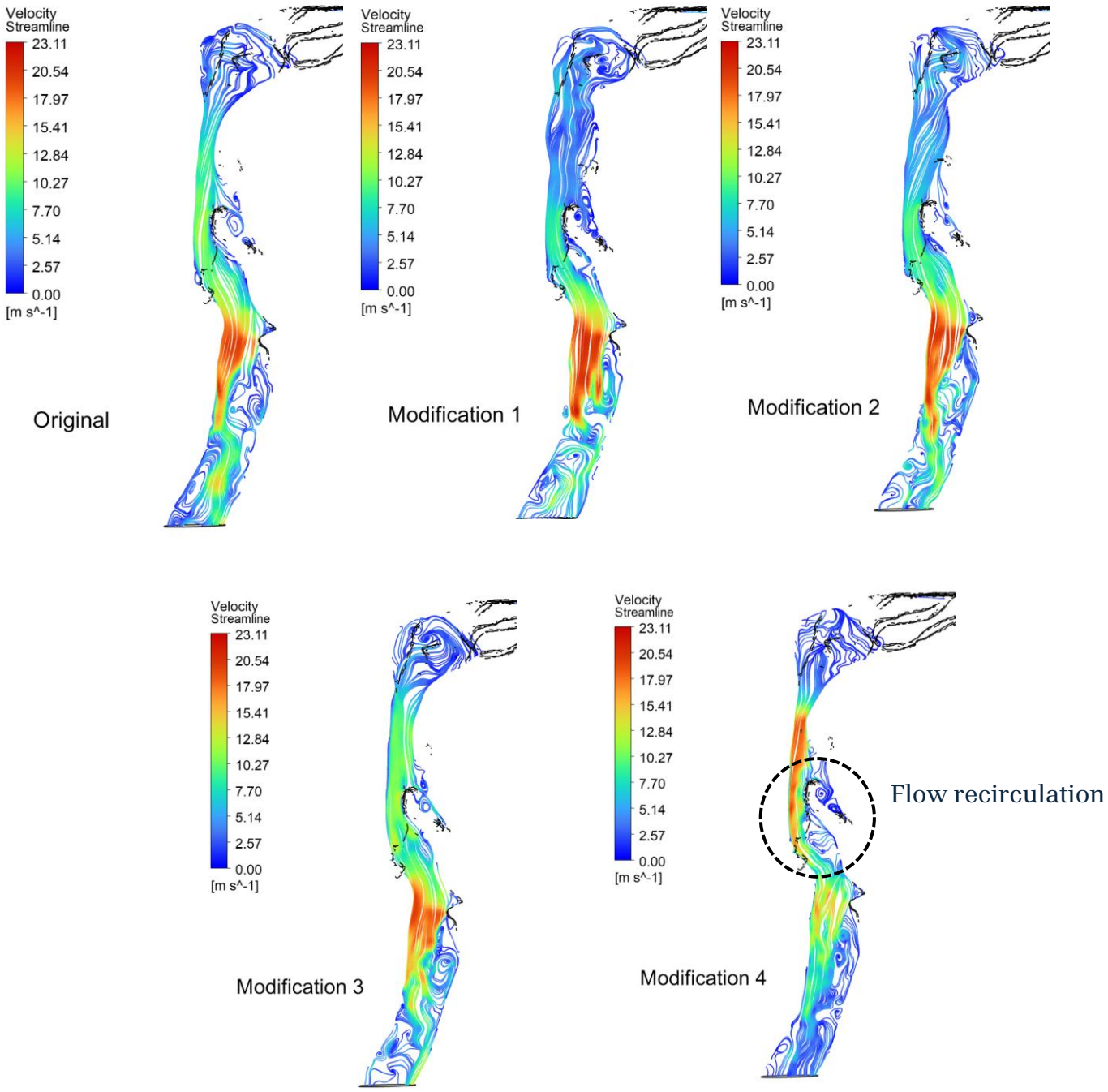

Fig.4-8: Velocity streamlines at t=0.8 sec. of the upper airway (from nasopharynx to the trachea outlet) in mid-sagittal plane for the original airway geometry and the 4 modifications coloured by velocity magnitude. (see Fig.4-3).

Additionally, as shown in Fig. 4-9, the wall shear stress (WSS) peaked at 12 Pa in the velopharyngeal region of modification 4, compared to 0.8 Pa at modification 1, representing a 15-

fold increase in WSS across the full range of configurations. WSS is an important indicator of the frictional forces exerted by the fluid on the airway walls, which is influenced by factors such as the flow rate, geometry, and constriction level. From the figure, it is observed that as the degree of constriction increases, particularly in Modifications 3 and 4, there is a marked increase in WSS at the constricted regions. The elevated WSS in Modification 4 reflects the substantial acceleration of airflow and the onset of turbulence caused by the severe geometric narrowing, which significantly amplifies frictional forces within the airway. Such increased shear stress can contribute to airway remodelling or damage over prolonged periods, which is often a concern in pathophysiological conditions such as OSA [48], [49]. Fig. 4-10 shows the resolved turbulent kinetic energy (TKE) for the 5 simulated cases. TKE quantifies the turbulence intensity within the airflow and is critical for understanding the aerodynamics of breathing. Additionally, the increase of TKE is associated with increased sound sources and sound pressure levels, as shown in studies involving tracheal stenosis [22], [50]. Previous research [51] suggested that TKE could serve as an indicator for assessing the severity of OSA through its relationship with the Apnea-Hypopnea Index (AHI). Across all simulated cases, elevated TKE was observed in the larynx region, where the glottic opening was located. The glottic opening size varies with breathing conditions. In this study, the airway geometry was based on a CT scan of a participant in a supine position with shallow breathing, resulting in a minimal glottic opening and high TKE in this region for all cases. Notably, Modification 4 demonstrated the highest TKE near the constriction, suggesting that in this scenario, the primary sound source would be associated with the velopharyngeal area.

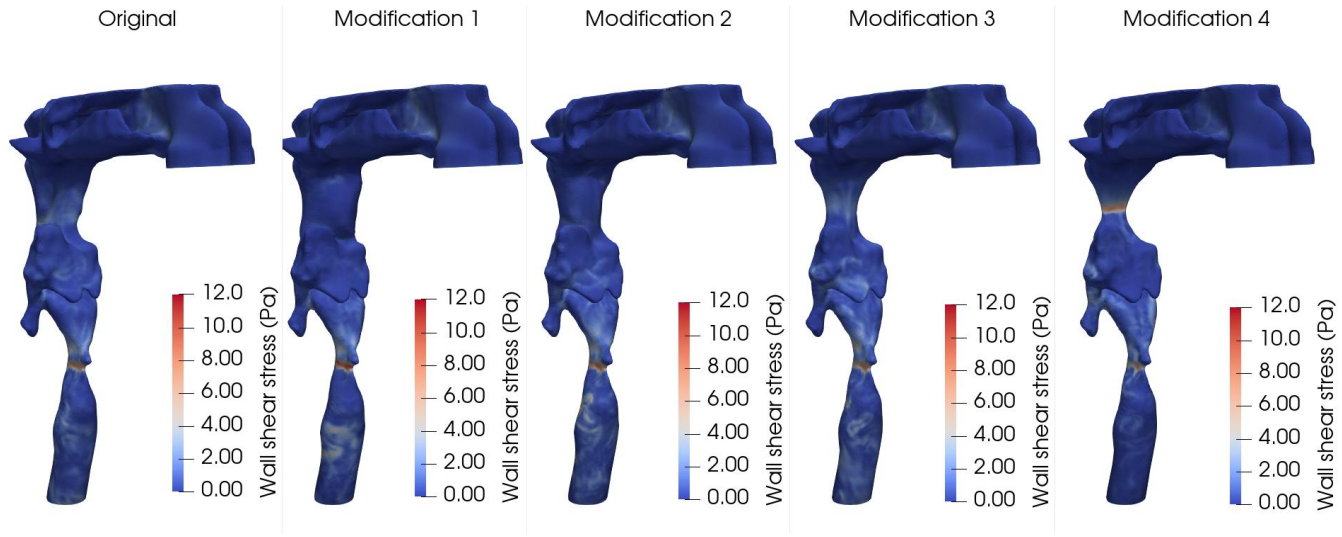

Fig.4-9:Wall Shear Stress of the upper airway at t=0.8 sec. (from nasopharynx to the trachea outlet) in mid-sagittal plane for the original airway geometry and the 4 modifications (see Fig.4-3).

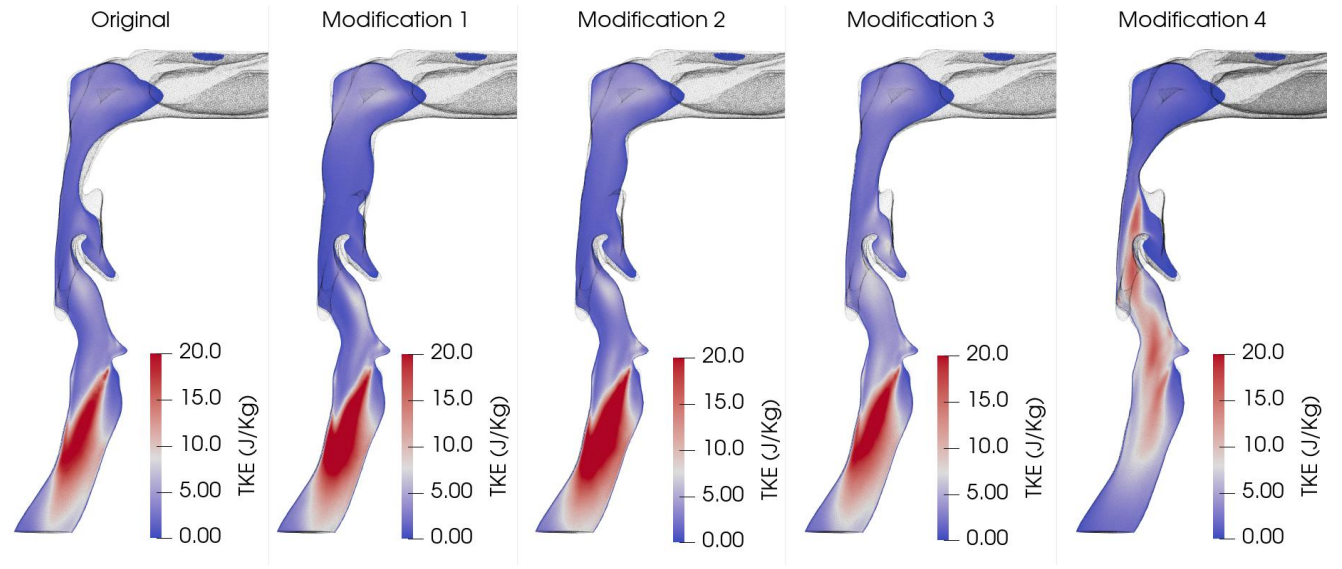

Fig.4-10:Turbulent Kinetic energy (TKE) of the upper airway at t=0.8 sec. (from nasopharynx to the trachea outlet) in mid-sagittal plane for the original airway geometry and the 4 modifications (see Fig.4-3).

Furthermore, we quantified the geometric severity of each modification by calculating the percentage area change ($\Delta A_{velopharynx}$) within the velopharyngeal segment for each modified geometry as shown in Fig.4-11(a). The upstream and downstream cross-sectional areas were extracted from two axial planes separated by 17 mm. This anatomical metric was then correlated

with the local pressure drop ($\Delta P_{velopharynx}$) and the dimensionless pressure coefficient (C_p), defined as the ratio of the pressure drop over the dynamic pressure.

$$C_p = \frac{\Delta P_{velopharynx}}{\frac{1}{2} \times \rho \times \bar{V}^2} \qquad \textit{4-10}$$

Where $\Delta P_{velopharynx}$ is the pressure drop across the velopharyngeal segment calculated as the absolute difference between the average pressure of the upstream and downstream planes of the velopharynx, $\rho = 1.225\ kg/m^3$ is the air density and $\bar{V}$ is the average bulk velocity of the velopharynx region. The results in Fig. 4-11(b) reveal a strong nonlinear relationship between $\Delta A_{velopharynx}$ and $\Delta P_{velopharynx}$well captured by a power-law fit with an exponent of 4.93 (R^2= 0.998). This steep power supports the finding that minor increases in the geometric constriction beyond critical threshold lead to large pressure losses and hence increases the likelihood of airway collapse [52]. Similarly, Fig.4-11(c) shows a strong dependence between C_p and constriction severity, following a nearly linear trend with an exponent of 1.47 (R^2= 0.999). The use of C_p as a normalized metric has been previously shown to correlate with AHI [53], [54] indicating that C_p could potentially serve as an indicator for OSA classification. This implies that anatomical variation of the airway, specifically velopharyngeal constriction, may be leveraged for OSA screening and identifying its severity during wakefulness.

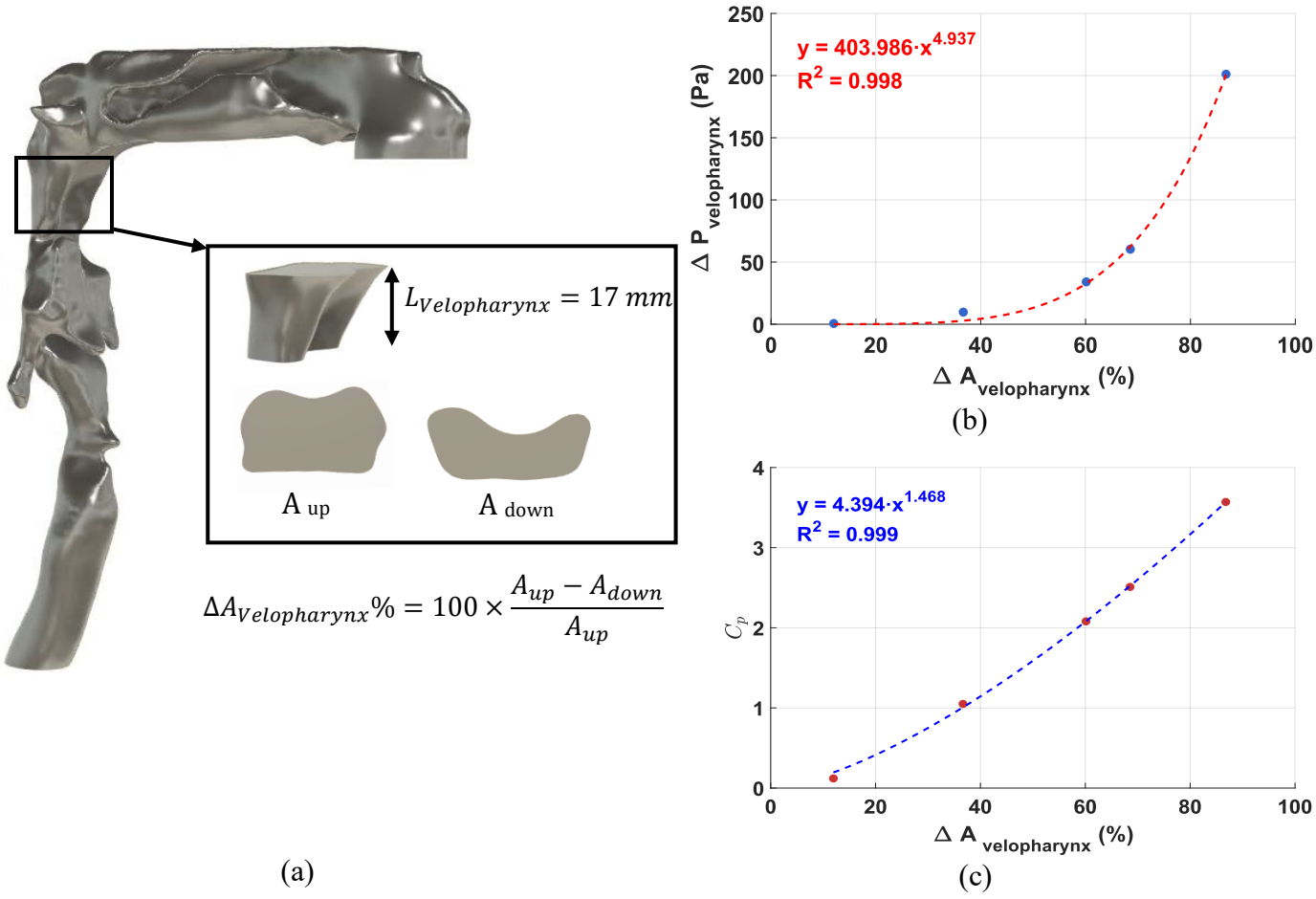

Fig.4-11: (a) Visualization of velopharyngeal cross-sectional area and percent area change calculation. The full patient-specific upper airway (original model) is shown in grey with the velopharyngeal region of interest outlined by a black box. The zoomed-in inset displays the upstream (A_{up}) and the downstream (A_{down}) planes of the velopharynx. The axial distance between the two planes is 17 mm. (b) Pressure drop ($\Delta P_{velopharynx}$) in (Pa) across the velopharyngeal segment plotted against the percent area change ($\Delta A_{velopharynx}$) for each model. Data points represent individual airway model, and the dashed line denotes a power- law best fit with an exponent of 4.93 (R^2=0.998). (c) Variation of the dimensionless pressure coefficient (C_p) with percent area change ($\Delta A_{velopharynx}$) for each model. The dashed line represents a power-law fit, yielding an exponent of 1.47 (R^2=0.999).

4.3.3 Effect of the velopharyngeal constriction on the acoustic response

The acoustic response of the upper airway was analyzed for the original geometry and the four modified versions to investigate the effect of velopharyngeal constriction on the frequency characteristics of tracheal breathing sounds. Fig. 4-12 presents the frequency response curves calculated at a microphone positioned near the tracheal outlet for all five simulated cases. The

analysis identified four main formant frequencies across all simulated cases, with their frequency ranges consistent with findings reported in [55]. Notably, a shift in the resonating frequency within the range of [1000–1700] Hz towards higher frequencies was observed as the velopharyngeal area increased. This shift highlights the sensitivity of the primary resonance frequency to changes in the velopharyngeal geometry, emphasizing its role in airway acoustics. The correlation between the constriction geometry and acoustic resonance behavior aligns with prior experimental findings reported in [28], where similar trends were observed using a simplified tube model (corresponding to simulation 1 in this study). However, the current study advances these findings by providing a more anatomically realistic representation of the upper airway, enabling a deeper understanding of how complex geometrical features influence acoustic behavior.

In contrast, the remaining formant frequencies remained relatively stable across the geometries. This suggests that other structural factors, such as the consistent airway length maintained across all cases, predominantly governed these frequencies. These findings highlight the potential of formant frequency patterns as reliable acoustic markers for evaluating anatomical and functional changes in the upper airway. These insights are vital for advancing non-invasive diagnostic methodologies that leverage acoustic markers to assess airway health and detect conditions such as obstructive sleep apnea, utilizing tracheal breathing sounds (TBS) during wakefulness. Furthermore, this finding demonstrates the significant potential of TBS in identifying the constriction level of the upper airway, offering a promising approach for clinical applications. However, future research involving larger, clinically stratified cohorts is necessary to validate the diagnostic robustness of TBS-based acoustic markers. Quantitative tools such as receiver operating characteristic (ROC) analysis should be employed to assess sensitivity and specificity, establish diagnostic thresholds, and evaluate the discriminative power of TBS features between OSA and

healthy populations. Further, while the current study focused on validating the acoustic response of TBS and correlating it with anatomical changes, future work should incorporate acoustic source decomposition to quantify the relative acoustic power contribution of the dipole and quadrupole sources, thereby providing deeper insight into sound generation mechanisms within the upper airway.

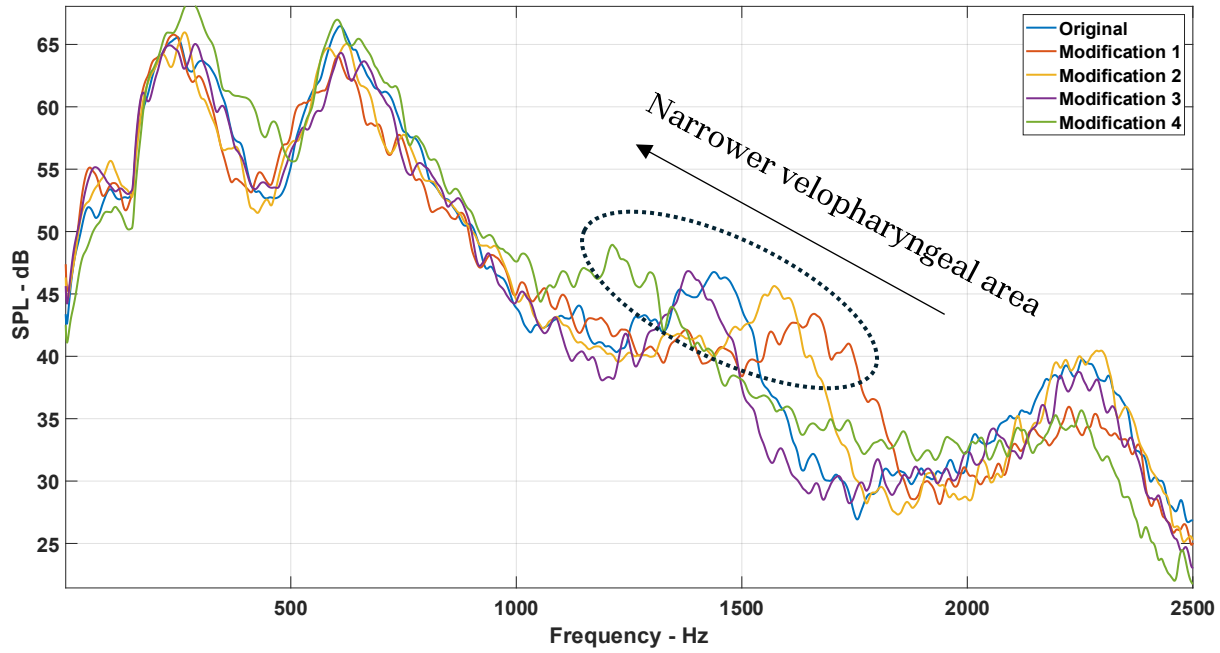

Fig.4-12: Frequency response curve of the sound generated at the trachea for the 5 simulated cases indicating the effect of the velopharyngeal constriction.

4.4 Conclusion

This study validated an aero-acoustic simulation of tracheal breathing sounds (TBS) using a reconstructed CT scan model of the upper airway. The validated model was used to investigate the impact of velopharyngeal constriction on upper airway aerodynamics and acoustic response. Simulations were performed on the original geometry and four modified versions with varying levels of velopharyngeal constriction. Results showed that increasing the constriction beyond a

certain threshold led to significant aerodynamic changes, including higher wall shear stress, increased turbulent kinetic energy, and a sharper pressure drop. These aerodynamic alterations were closely linked to shifts in the acoustic response, with a clear frequency shift towards higher frequencies as the velopharyngeal area decreased. This finding underscores the strong relationship between airway geometry and acoustic resonance characteristics. The study highlights the potential of using TBS as a non-invasive diagnostic tool for assessing airway health. The limitations of this study include the use of constant pressure boundary conditions, which were applied to model a quasi-steady segment of peak inspiration. While appropriate for the selected analysis window, this approach does not capture the transient flow dynamics present during the full respiratory cycle. Additionally, the airway walls were assumed to be rigid, thereby excluding fluid-structure-acoustic interactions that may play a role in sound generation through wall motion, particularly from monopole sources. However, this simplification is justified given that the simulation specifically targets tracheal breathing sounds during wakefulness, a condition marked by relatively stable airway geometry and minimal wall compliance. Future research should focus on further correlating anatomical features with breathing sounds and developing an analytical model based on these findings, with the aim of supporting clinical studies and improving diagnosis and monitoring of conditions such as obstructive sleep apnea.

References

[1] H. Pasterkamp and I. Sanchez, “Tracheal sounds in upper airway obstruction,” *Chest*, vol. 102, no. 3, pp. 963–965, 1992, doi: 10.1378/chest.102.3.963.

[2] A. Yadollahi, E. Giannouli, and Z. Moussavi, “Sleep apnea monitoring and diagnosis based on pulse oximetery and tracheal sound signals,” *Med. Biol. Eng. Comput.*, vol. 48, pp. 1087–1097, 2010.

[3] S. Rietveld and L. H. M. Rijssenbeek-Nouwens, “Diagnostics of spontaneous cough in childhood asthma: Results of continuous tracheal sound recording in the homes of children,” *Chest*, vol. 113, no. 1, pp. 50–54, 1998, doi: 10.1378/chest.113.1.50.

[4] M. Yonemaru *et al.*, “Detection of tracheal stenosis by frequency analysis of tracheal sounds.,” *J. Appl. Physiol.*, vol. 75, no. 2, pp. 605–612, Aug. 1993, doi: 10.1152/jappl.1993.75.2.605.

[5] A. Elwali and Z. Moussavi, “Obstructive Sleep Apnea Screening and Airway Structure Characterization During Wakefulness Using Tracheal Breathing Sounds,” *Ann. Biomed. Eng.*, vol. 45, no. 3, pp. 839–850, Mar. 2017, doi: 10.1007/s10439-016-1720-5.

[6] A. Montazeri, E. Giannouli, and Z. Moussavi, “Assessment of obstructive sleep apnea and its severity during wakefulness,” *Ann. Biomed. Eng.*, vol. 40, no. 4, pp. 916–924, 2012, doi: 10.1007/s10439-011-0456-5.

[7] Y. Finkelstein *et al.*, “Velopharyngeal anatomy in patients with obstructive sleep apnea versus normal subjects,” *J. Oral Maxillofac. Surg.*, vol. 72, no. 7, pp. 1350–1372, 2014, doi: 10.1016/j.joms.2013.12.006.

[8] H. Nakano, M. Hayashi, E. Ohshima, N. Nishikata, and T. Shinohara, “Validation of a new system of tracheal sound analysis for the diagnosis of sleep apnea-hypopnea syndrome,” *Sleep*, vol. 27, no. 5, pp. 951–957, 2004, doi: 10.1093/sleep/27.5.951.

[9] H. Nakano, T. Furukawa, and T. Tanigawa, “Tracheal sound analysis using a deep neural network to detect sleep apnea,” *J. Clin. Sleep Med.*, vol. 15, no. 8, pp. 1125–1133, 2019, doi: 10.5664/jcsm.7804.

[10] J. Solà-Soler, J. Antonio Fiz Fernandez, A. Torres, and R. Jané, *Identification of Obstructive Sleep Apnea Patients from Tracheal Breath Sound Analysis During Wakefulness in*

Polysomnographic Studies. 2014. doi: 10.0/Linux-x86_64.

[11] F. Hajipour, M. J. Jozani, A. Elwali, and Z. Moussavi, "Regularized logistic regression for obstructive sleep apnea screening during wakefulness using daytime tracheal breathing sounds and anthropometric information," *Med. Biol. Eng. Comput.*, vol. 57, no. 12, pp. 2641–2655, Dec. 2019, doi: 10.1007/s11517-019-02052-4.

[12] Michael James Lighthill, "On sound generated aerodynamically I. General theory," *Proc. R. Soc. London. Ser. A. Math. Phys. Sci.*, vol. 211, no. 1107, pp. 564–587, Mar. 1952, doi: 10.1098/rspa.1952.0060.

[13] N. Curle, "The influence of solid boundaries upon aerodynamic sound," *Proc. R. Soc. London. Ser. A. Math. Phys. Sci.*, vol. 231, no. 1187, pp. 505–514, 1955.

[14] J. E. F. Williams and D. L. Hawkings, "Sound generation by turbulence and surfaces in arbitrary motion," *Philos. Trans. R. Soc. London. Ser. A, Math. Phys. Sci.*, pp. 321–342, 1969.

[15] S. Schoder and M. Kaltenbacher, "Hybrid Aeroacoustic Computations: State of Art and New Achievements," *J. Theor. Comput. Acoust.*, vol. 27, no. 4, pp. 1–33, 2019, doi: 10.1142/S2591728519500208.

[16] M. Döllinger, Z. Zhang, S. Schoder, P. Šidlof, B. Tur, and S. Kniesburges, "Overview on state-of-the-art numerical modeling of the phonation process," *Acta Acust.*, vol. 7, 2023, doi: 10.1051/aacus/2023014.

[17] S. Falk *et al.*, "3D-FV-FE Aeroacoustic Larynx Model for Investigation of Functional Based Voice Disorders," *Front. Physiol.*, vol. 12, no. March, pp. 1–17, 2021, doi: 10.3389/fphys.2021.616985.

[18] S. Zörner, P. Šidlof, A. Hüppe, and M. Kaltenbacher, "Flow and acoustic effects in the

larynx for varying geometries," *Acta Acust. united with Acust.*, vol. 102, no. 2, pp. 257–267, 2016, doi: 10.3813/AAA.918942.

[19] M. Kaltenbacher, S. Zörner, A. Hüppe, and P. Sidlof, "3D numerical simulations of human phonation," *11th World Congr. Comput. Mech. WCCM 2014, 5th Eur. Conf. Comput. Mech. ECCM 2014 6th Eur. Conf. Comput. Fluid Dyn. ECFD 2014*, no. Wccm Xi, pp. 5941–5951, 2014.

[20] L. Schickhofer and M. Mihaescu, "Analysis of the aerodynamic sound of speech through static vocal tract models of various glottal shapes," *J. Biomech.*, vol. 99, no. xxxx, p. 109484, 2020, doi: 10.1016/j.jbiomech.2019.109484.

[21] J. Xi, X. Si, J. Kim, G. Su, and H. Dong, "Modeling the pharyngeal anatomical effects on breathing resistance and aerodynamically generated sound," *Med. Biol. Eng. Comput.*, vol. 52, no. 7, pp. 567–577, 2014, doi: 10.1007/s11517-014-1160-z.

[22] W. C. P. van der Velden, A. H. van Zuijlen, A. T. de Jong, C. T. Lynch, L. J. Hoeve, and H. Bijl, "Acoustic simulation of a patient's obstructed airway," *Comput. Methods Biomech. Biomed. Engin.*, vol. 19, no. 2, pp. 144–158, Jan. 2016, doi: 10.1080/10255842.2014.996877.

[23] P. T. Gamage, "Modeling of flow generated sound in a constricted duct at low Mach number flow," *eprint arXiv:1801.09674*, 2018, [Online]. Available: http://arxiv.org/abs/1801.09674%0Ahttp://dx.doi.org/10.13140/RG.2.2.17805.03048%0Ahttp://arxiv.org/abs/1801.09674%0Ahttp://dx.doi.org/10.13140/RG.2.2.17805.03048

[24] H. S. Ribner, "Aerodynamic Sound from Fluid Dilatations," *UTIA Rep.*, no. 86, pp. 1–101, 1962.

[25] S. De Reboul, E. Perrey-debain, and N. Zerbib, "Hybrid methods for duct aeroacoustics

simulations," no. 1, pp. 387–391, 2020.

[26] N. Zerbib, A. H. Lassen Mebarek, and M. Escouflaire, "Use OpenFoam coupled with the Finite Element Method suitable for Computational AeroAcoustics," *proceedings, 4th OpenFoam Users Conf. Col. Ger.*, no. October, 2016.

[27] P. Maurerlehner *et al.*, "Aeroacoustic formulations for confined flows based on incompressible flow data," *Acta Acust.*, vol. 6, 2022, doi: 10.1051/aacus/2022041.

[28] W. Ashraf and Z. Moussavi, "An experimental investigation on the effect of airflow on the sound generated in a simplified tube with a constriction representing trachea for obstructive sleep apnea diagnosis during wakefulness," *C. Proc.*, vol. 46, 2024, [Online]. Available: https://proceedings.cmbes.ca/index.php/proceedings/article/view/1081

[29] P. A. Yushkevich *et al.*, "User-guided 3D active contour segmentation of anatomical structures: Significantly improved efficiency and reliability," *Neuroimage*, vol. 31, no. 3, pp. 1116–1128, 2006, doi: https://doi.org/10.1016/j.neuroimage.2006.01.015.

[30] W. Ashraf and Z. Moussavi, "Design and Analysis of a Contact Piezo Microphone for Recording Tracheal Breathing Sounds," *Sensors*, vol. 24, no. 17, 2024, doi: 10.3390/s24175511.

[31] A. Yadollahi and Z. Moussavi, "Acoustical flow estimation: review and validation," *IEEE Eng Med Biol Mag*, vol. 26, no. 1, pp. 56–61, 2007.

[32] S. Schoder *et al.*, "Hybrid aeroacoustic approach for the efficient numerical simulation of human phonation," *J. Acoust. Soc. Am.*, vol. 147, no. 2, pp. 1179–1194, 2020, doi: 10.1121/10.0000785.

[33] W. K. George, "Lectures in Turbulence for the 21st Century," 2013.

[34] M. Kaltenbacher, M. Escobar, S. Becker, and I. Ali, "Computational Aeroacoustics based

on Lighthill's Acoustic Analogy," in *Computational Acoustics of Noise Propagation in Fluids - Finite and Boundary Element Methods*, Berlin, Heidelberg: Springer Berlin Heidelberg, pp. 115–142. doi: 10.1007/978-3-540-77448-8_5.

[35] S. B. Pope, "Ten questions concerning the large-eddy simulation of turbulent flows," *New J. Phys.*, vol. 6, pp. 0–24, 2004, doi: 10.1088/1367-2630/6/1/035.

[36] J. Smagorinsky, "General circulation experiments with the primitive equations: I. The basic experiment," *Mon. Weather Rev.*, vol. 91, no. 3, pp. 99–164, 1963.

[37] D. K. Lilly, "A proposed modification of the germano sugrid-scale closure method," *Phys Fluids A*, vol. 4, pp. 633–635, 1992.

[38] M. Germano, U. Piomelli, P. Moin, and W. H. Cabot, "A dynamic subgrid-scale eddy viscosity model," *Phys. Fluids A Fluid Dyn.*, vol. 3, no. 7, pp. 1760–1765, 1991.

[39] P. Sagaut, S. Deck, and M. Terracol, *Multiscale and multiresolution approaches in turbulence (second edition)*. 2013.

[40] H. Pasterkamp, S. S. Kraman, and G. R. Wodicka, "Respiratory sounds. Advances beyond the stethoscope.," *Am. J. Respir. Crit. Care Med.*, vol. 156, no. 3 Pt 1, pp. 974–987, Sep. 1997, doi: 10.1164/ajrccm.156.3.9701115.

[41] S. V. Patankar, *Numerical Heat Transfer and Fluid Flow*. CRC Press, 2018. doi: 10.1201/9781482234213.

[42] C. T. Lynch, "The numerical acoustic and fluid flow analysis on a CT-scan derived upper airway model of a stridor patient."

[43] S. B. Pope, *Turbulent Flows*. Cambridge: Cambridge University Press, 2000. doi: DOI: 10.1017/CBO9780511840531.

[44] K. Kairaitis, S. Foster, J. Amatoury, M. Verma, J. R. Wheatley, and T. C. Amis, "Pharyngeal

mucosal wall folds in subjects with obstructive sleep apnea," *J. Appl. Physiol.*, vol. 118, no. 6, pp. 707–715, 2015, doi: 10.1152/japplphysiol.00691.2014.

[45] J. H. Walsh *et al.*, "Evaluation of pharyngeal shape and size using anatomical optical coherence tomography in individuals with and without obstructive sleep apnoea," *J. Sleep Res.*, vol. 17, no. 2, pp. 230–238, 2008, doi: 10.1111/j.1365-2869.2008.00647.x.

[46] M. Zhao, T. Barber, P. A. Cistulli, K. Sutherland, and G. Rosengarten, "Simulation of upper airway occlusion without and with mandibular advancement in obstructive sleep apnea using fluid-structure interaction," *J. Biomech.*, vol. 46, no. 15, pp. 2586–2592, Oct. 2013, doi: 10.1016/j.jbiomech.2013.08.010.

[47] M. Brouns *et al.*, "Tracheal stenosis: A flow dynamics study," *J. Appl. Physiol.*, vol. 102, no. 3, pp. 1178–1184, 2007, doi: 10.1152/japplphysiol.01063.2006.

[48] S. J. Jeong, W. S. Kim, and S. J. Sung, "Numerical investigation on the flow characteristics and aerodynamic force of the upper airway of patient with obstructive sleep apnea using computational fluid dynamics," *Med. Eng. Phys.*, vol. 29, no. 6, pp. 637–651, 2007, doi: 10.1016/j.medengphy.2006.08.017.

[49] A. S. Green, "Modelling of peak-flow wall shear stress in major airways of the lung," *J. Biomech.*, vol. 37, no. 5, pp. 661–667, 2004, doi: 10.1016/j.jbiomech.2003.09.024.

[50] M. Foucart, "Aeroacoustic investigation of a stridor patient's upper respiratory system," pp. 1–242, 2015.

[51] W. M. Faizal *et al.*, "Turbulent Kinetic Energy of Flow during Inhale and Exhale to Characterize the Severity of Obstructive Sleep Apnea Patient," *C. - Comput. Model. Eng. Sci.*, vol. 136, no. 1, pp. 43–61, 2023, doi: 10.32604/cmes.2023.022716.

[52] J. Cisonni *et al.*, "Effect of the velopharynx on intraluminal pressures in reconstructed

pharynges derived from individuals with and without sleep apnea," *J. Biomech.*, vol. 46, no. 14, pp. 2504–2512, 2013, doi: 10.1016/j.jbiomech.2013.07.007.

[53] M. Zhao, T. Barber, P. Cistulli, K. Sutherland, and G. Rosengarten, "Computational fluid dynamics for the assessment of upper airway response to oral appliance treatment in obstructive sleep apnea," *J. Biomech.*, vol. 46, no. 1, pp. 142–150, 2013, doi: 10.1016/j.jbiomech.2012.10.033.

[54] S. Taherian, H. Rahai, S. Lopez, J. Shin, and B. Jafari, "Evaluation of human obstructive sleep apnea using computational fluid dynamics," *Commun. Biol.*, vol. 2, no. 1, pp. 1–8, 2019, doi: 10.1038/s42003-019-0668-z.

[55] A. Yadollahi and Z. Moussavi, "Formant analysis of breath and snore sounds," *Proc. 31st Annu. Int. Conf. IEEE Eng. Med. Biol. Soc. Eng. Futur. Biomed. EMBC 2009*, pp. 2563–2566, 2009, doi: 10.1109/IEMBS.2009.5335292.

CHAPTER FIVE: ANATOMICAL DETERMINANTS OF TRACHEAL BREATHING SOUNDS: A COMPUTATIONAL STUDY OF AIRWAY NARROWING AND OBSTRUCTIVE SLEEP APNEA

Walid Ashraf[1], Jeffrey J. Fredberg[2], and Zahra Moussavi[1,3]

1. Biomedical Engineering Program, University of Manitoba, Winnipeg, Canada.
2. Department of Environmental Health, Harvard T. H. Chan School of Public Health, Boston, MA 02115, USA.
3. Department of Electrical and Computer Engineering, University of Manitoba, Winnipeg, Canada.

Diagnostics 2025, 15(24), 3108 (https://doi.org/10.3390/diagnostics15243108)

Abstract

Background: Tracheal breathing sounds (TBS) have demonstrated strong potential as a non-invasive, wakefulness-based diagnostic tool for obstructive sleep apnea (OSA); yet the relationship between specific upper airway anatomical features and the resulting TBS spectra remains insufficiently understood. This study aims to enhance the diagnostic utility of TBS in OSA by investigating how the upper airway anatomy influences TBS spectral characteristics.

Method: Patient-specific computational models of the upper airway were reconstructed from high-resolution CT scans of a healthy subject and an individual with OSA. Additional variants were generated with targeted constrictions at the velopharynx, oropharynx, and trachea, based on clinically reported anatomical ranges. Airflow dynamics were simulated using Large Eddy Simulation (LES), and the resulting acoustic responses were computed via Lighthill's acoustic analogy within a hybrid aero-acoustic framework.

Results: Oropharyngeal constriction generated the most spatially concentrated vorticity patterns among single-region constricted models. Airway Resistance analysis revealed that severe velopharyngeal and oropharyngeal constrictions contributed most to regional airway resistance.

Spectral analysis showed that velopharyngeal narrowing produced a progressive downward shift in the third resonance peak (1000–1700 Hz), while oropharyngeal narrowing induced an upward shift of the third peak and a downward shift of the fourth peak (1700-2500 Hz). These frequency shifts were attributed to the effective role of acoustic mass and airway compliance.

Conclusions: Anatomical modifications of the upper airway produce region-specific changes in both flow and acoustic responses. These findings support the use of TBS spectral analysis for non-invasive localization of airway obstructions in OSA.

5.1 Introduction

5.1.1 TBS relevance

Breathing sounds remain an important part of a constellation of methods used to diagnose respiratory disorders including asthma, chronic obstructive pulmonary disease (COPD), and obstructive sleep apnea (OSA) [1], [2], [3], [4]. These sounds arise from the interaction between airflow and anatomical structures in the respiratory tract. Among various types of respiratory sounds, tracheal breathing sounds (TBS) have gained particular interest due to their dependence upon central and upper airway (UA) morphology and their potential to detect airflow abnormalities within these anatomical regions.

OSA is characterized by recurrent airway collapse during sleep. Despite its high prevalence and significant health implications, OSA remains significantly underdiagnosed [5], [6]. While overnight polysomnography (PSG) remains the current gold standard for OSA diagnosis, PSG is expensive, not readily available and resource-intensive; it requires specialized equipment, overnight patient monitoring and trained personnel. Consequently, these demands result in long wait times and limited feasibility in acute care settings such as intensive care units (ICUs) or prior

to surgeries requiring general anesthesia [7], [8]. These shortcomings underscore the growing need for non-invasive, accessible, and cost-effective alternatives for screening and diagnosis. In this context, analysis of TBS recorded in few minutes during wakefulness presents a promising diagnostic tool. TBS can be recorded non-invasively at the suprasternal notch, offering the possibility of detecting anatomical and functional abnormalities and thus lowering the need for PSG studies [9], [10]. Unlike lung sounds, which are often attenuated by surrounding tissues, TBS are less filtered and more directly influenced by structural changes in the UA. This fact makes them particularly suitable for identifying airway constrictions and flow disturbances that are central to disorders like OSA.

5.1.2 Anatomical determinants

The diagnostic utility of TBS arises from their sensitivity to biomechanical parameters such as local airflow velocity, wall compliance, and airflow obstruction. When air moves through a narrowed or an irregular structure within the airway, local pressure and velocity fluctuations produce acoustic features, such as amplitude changes and shifts in resonant frequencies. Importantly, these acoustic features vary systematically with anatomical and physiological alterations [11]. This sensitivity to geometry makes TBS a promising tool for identifying the severity and location of obstructions in conditions such as OSA. Structural narrowing, particularly in the velopharyngeal and oropharyngeal regions, has been observed to persist even during wakefulness, thus influencing the acoustic response and offering diagnostic insights [12], [13], [14].

Airway geometry plays a central role in the pathophysiology of OSA. Several imaging studies have shown that variability in airway geometry during wakefulness, such as reduced cross-

sectional area [15], [16], increased airway collapsibility [17], [18], and altered airway shape [13] are strong predictors of airway collapse during sleep. A significant correlation was found between the UA length and the respiratory disturbance index, a metric used to assess OSA severity [19]. Similar trends were observed when the UA length was normalized to body height, further supporting the role of airway elongation in OSA pathogenesis [20]. Additionally, the cross-sectional shape of the velopharynx differs between OSA patients and healthy individuals, tending to be more circular in OSA patients and more elliptical in healthy participants during sleep [17]. Individuals with OSA also exhibit increased pharyngeal length, a thicker posterior pharyngeal wall and reduced pharyngeal width, collectively contributing to a more constricted velopharyngeal segment [13]. Smaller cross-sectional areas in the oropharyngeal and nasopharyngeal regions were reported in individuals with OSA compared to those in healthy controls [18]. Consequently, researchers investigated the relationship between the UA geometry and TBS. For instance, the increase in inspiratory sounds' intensity from upright to supine posture was higher in OSA than in healthy individuals [10]. An inverse relationship was reported between body height, which is associated with tracheal length [21], and the resonance frequencies of TBS [22], [23]. In patients with tracheal stenosis, TBS amplitude near 1 kHz was reported to be elevated compared to that in healthy controls, highlighting the sensitivity of TBS to localized UA constrictions [24].

5.1.3 Rationale for TBS Modelling

Despite these anatomical insights, the use of TBS in clinical diagnosis remains limited due to lack of mechanistic understanding of how specific anatomical features influence the acoustic response. Most diagnostic applications rely on empirical signal processing methods with limited connection between the measured sounds and the underlying physiology. Bridging this gap

requires a mechanistic approach that links anatomy to breathing sound generation. Computational modelling has emerged as a powerful and non-invasive tool in respiratory physiology and biomedical engineering. By combining computational fluid dynamics (CFD) to capture airflow patterns and turbulence, with acoustic finite element modelling (FEM) to capture resulting acoustic radiation, insights might be obtained that are not accessible through clinical and experimental measurements alone. Such modelling enables the quantification of key physical variables such as pressure gradients, turbulent kinetic energy (TKE), wall shear stress (WSS), and local velocity distributions, which are essential for identifying aero-acoustic source mechanisms [11]. These variables can be spatially mapped and correlated with specific airway geometries, providing a framework for linking anatomical features to airflow dynamics and acoustic biomarkers. Moreover, aero-acoustic modelling facilitates parametric studies where individual anatomical features can be systematically varied, isolating their impact on the resulting sound signature, a benefit not feasible in vivo.

In this study, we aimed to address the research gap, namely, the incomplete understanding of how the UA anatomical traits affect the acoustic spectral features of TBS. Here, we investigate the effect of various anatomical features, such as oropharyngeal and tracheal constrictions, airway length and their interactions, on TBS using a one-way coupled aero-acoustic simulation modelling approach applied to anatomically realistic UA models reconstructed from CT scans of both a healthy individual and an individual with OSA. Previous work on TBS-based OSA assessment has primarily relied on empirical signal processing and statistical or machine-learning models [25,26] without explicit mechanistic modelling of how regional airway anatomy shapes the sound spectrum. In parallel, several computational models of the UA have examined the impact of anatomy on airflow dynamics [27] and on breathing or snoring sounds [28,29]. However, these

studies have either focused on specific structures (e.g. the glottis in [28]) or on snoring-related acoustics, and the specific influence of velopharyngeal, oropharyngeal, and tracheal geometry on tracheal breathing sounds has remained largely unexplored. In this context, the present study provides, to the best of our knowledge, the first patient-specific computational framework that systematically quantifies the resulting changes in tracheal breathing sound spectra, thereby establishing a mechanistic link between localized anatomical features and TBS characteristics.

5.2 Materials And Methods

An overview of the methodology employed is illustrated in Fig. 5-1. Part of the workflow, including the aero-acoustic simulation framework, CFD computation, and acoustic Finite Element Modelling (FEM), has been described and validated in our prior work [11]. Section 5.2.1 summarizes these previously validated components. In this study, we build upon that foundation by extending the analysis to examine the influence of specific anatomical features, including oropharyngeal and tracheal narrowing, airway length, and their interactions, on tracheal breathing sounds (TBS). The new contributions, detailed in section 5.2.2, focus on integrating anatomical modifications into the simulation pipeline, validating their effects through subject-specific geometries. Feature extraction was performed to explore the diagnostic relevance of these findings in distinguishing between healthy and OSA airways.

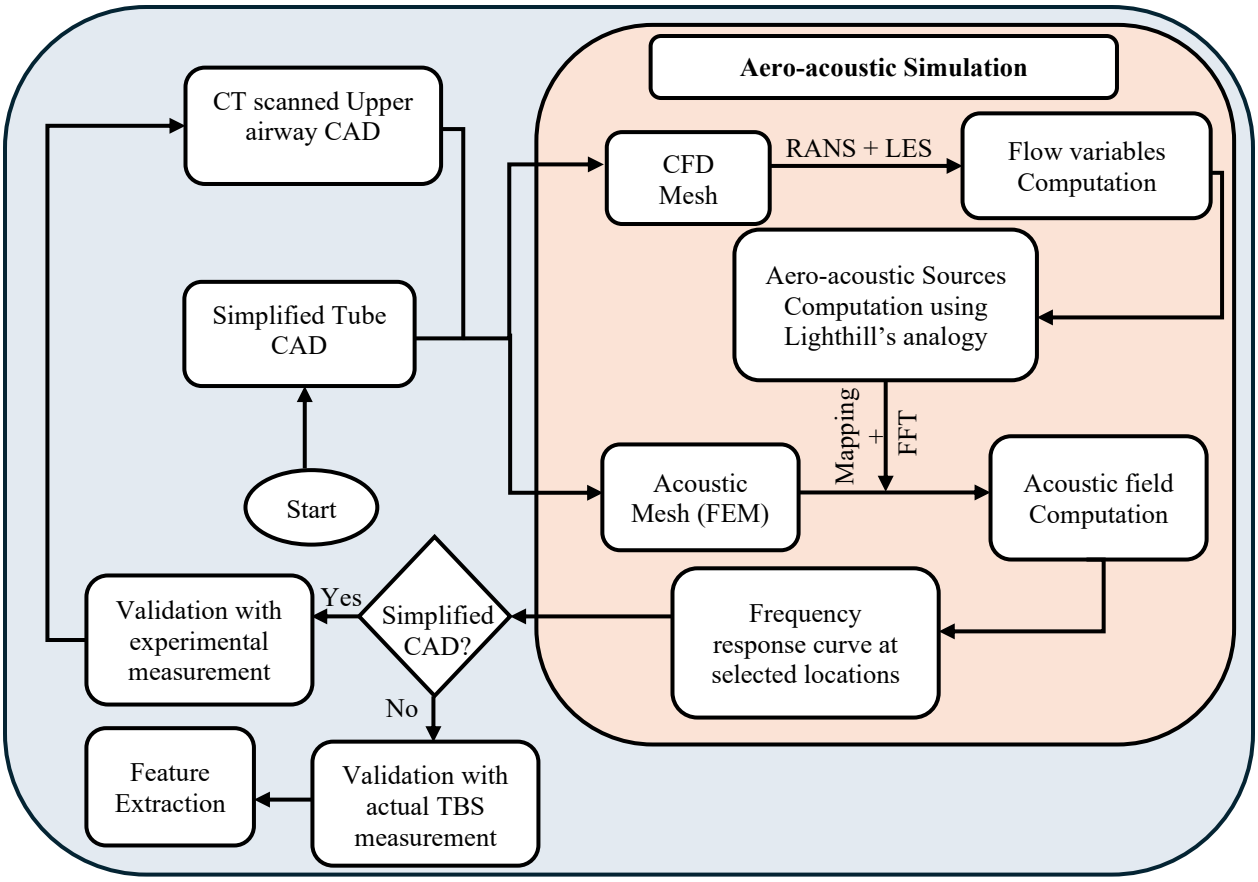

Fig. 5-1: Flow Chart of the methodology procedures, based on the work presented in [11].

This study was approved by the Biomedical Research Ethics Board of the University of Manitoba [B2022:226 (HS25583)]. Subject-specific airway geometries were reconstructed from high-resolution CT scans of two participants: a healthy 76Y female (height: 146 cm, BMI: 27.2 kg/m^2) with no reported respiratory disorder and a 47Y male (height: 165 cm, BMI=28.7 kg/m^2) with clinically diagnosed severe OSA. The individual with OSA exhibited an apnea-hypopnea index (AHI) of 58 events per hour (85.2 events/hour in supine position). The CT volumes had a matrix size of 512 × 512 × 1057 voxels and a voxel size of 0.4375 × 0.4375 × 0.335 mm^3. The age difference between the healthy and OSA participants may introduce potential confounding due to age-related changes in soft tissues and airway dimensions; this is acknowledged and further

discussed in the limitations section. Semi-automatic segmentation using ITK-SNAP [30] was applied to reconstruct the 3D UA geometries from each scan. Post-processing was performed to ensure anatomical accuracy and mesh quality, using Autodesk Fusion 360 for gap filling and Blender for wall smoothing and inlet/outlet preparation. Surface smoothing was performed to remove stair-step and aliasing artifacts while maintaining changes in minimum cross-sectional areas in each anatomical segment below 2% and in total airway volume below 1% relative to the original segmentation. Figure 5-2 shows the CAD geometries for the airway of both participants.

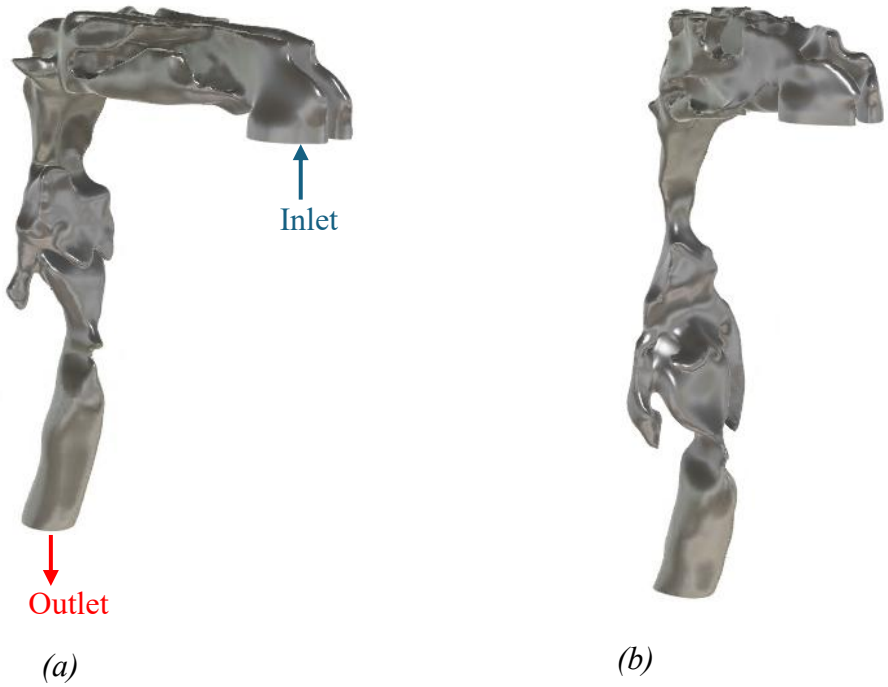

Fig. 5-2: CAD model of the upper airway of (a) healthy participant and (b) OSA participant.

5.2.1 Aero-Acoustic Simulation Framework

Aero-acoustic simulations can be performed using either a direct or hybrid approach. In this study, a hybrid method based on Lighthill's analogy [31] was employed due to its computational efficiency and suitability for low Mach number flows [32] such as those observed in human respiration. The hybrid approach decomposes the simulation into two sequential steps.

The first step involves a steady state Reynolds-Averaged Navier–Stokes (RANS) simulation, which is used to initialize the flow field and provide stable initial conditions, followed by unsteady, incompressible, scale-resolving finite volume CFD using large eddy simulation (LES) to capture the flow field and turbulent structures responsible for sound generation. Smagorinsky–Lilly subgrid-scale model was employed to model the effect of unresolved small-scale turbulence [33,34]. In the second step, the aero-acoustic source terms, derived from the CFD simulation, are mapped onto a coarser finite element model (FEM), where the acoustic wave propagation is computed in the frequency domain by solving the variational form of the wave equation. This modelling approach relies on several assumptions; first, the flow is incompressible and isentropic, which is valid for low Mach number flow ($Ma < 0.2$), and therefore, the convection effects can be neglected ; second the influence of acoustic waves on the flow field is negligible, justifying the one-way coupling; third the acoustic source is compact relative to the wavelength of interest.

A pressure drop of 2.8 cmH_2O between the inlet (nostrils) and outlet (trachea) of the UA was applied to simulate the plateau of peak inspiratory flow. This was implemented by setting the nostrils (inlet) to atmospheric pressure and applying a subglottic pressure of -2.8 cmH_2O at the tracheal outlet [11]. This value is consistent with the reported range of inspiratory pressure [35] and, in the present study, resulted in an inspiratory flow rate of approximately 33 L/min which is inline with flow rates commonly used in the literature [36,37] . This setup was chosen to align with the validation study presented in [11], where the acoustic analysis was based on a stationary 300 ms segment of tracheal breathing sounds (TBS) corresponding to maximum inspiratory effort. The CFD simulation was performed using ANSYS-Fluent (2024-R2) with a fixed time step of 0.0001 s for 8000-time steps. A no-slip boundary condition was imposed on the airway walls. The CFD mesh consisted of approximately 2.9M elements for the healthy model and 3.6 M elements for the

OSA model. Boundary layer refinement ensured that wall-adjacent cells maintained $y^+ < 1$ for accurate near-wall resolution. Mesh quality was assessed using cell skewness and orthogonal quality. The average skewness was 0.28 (95% of the cells <0.50) for the healthy model and 0.27 (95% of the cells <0.52) for the OSA model, while the average orthogonal quality was 0.70 and 0.73, respectively. The unsteady velocity fluctuations obtained from LES CFD were transformed into frequency domain and mapped onto the finite element mesh for acoustic analysis in ACTRAN-Acoustics software (2024.1). The acoustic domain was discretized using second order (quadratic) tetrahedral elements, ensuring a minimum of 45 elements per acoustic wavelength, enabling accurate sound propagation modelling up to 2500 Hz. Infinite elements [38] were assigned to the inlet surface to simulate anechoic conditions and prevent non-physical reflections. At the tracheal outlet, a normalized impedance boundary condition was imposed to approximate realistic boundary loading. To account for tissue damping and sound absorption, a normalized surface impedance of 500 (relative to air) was applied to the airway walls. The microphone probe for recording tracheal breathing sounds in the simulation was placed in the extended tracheal propagation domain downstream of the tracheal outlet, matching the position used in the experimental validation [11]. The full simulation framework, including solver configurations, governing equations, meshing and boundary conditions, has been described in detail in our previous work [11].

5.2.2 Anatomical Feature Extraction

To investigate the anatomical determinants of TBS, a series of anatomical variations were introduced into the UA geometries. These variations targeted specific regions, namely the velopharynx, oropharynx, and trachea, and were guided by reported ranges of airway dimensions

for OSA patients in previous clinical and imaging studies. For instance, velopharyngeal minimum cross-sectional area (CSA) was reported as 35.3±23.5 mm^2 (mean ± std) in 17 OSA patients during wakefulness [17], while oropharyngeal minimum CSA was reported as 203±95.3 mm^2 in 20 OSA adults [14]; and 61.45±45.03 mm^2 in 33 OSA children [39]. Although pharyngeal narrowing is a well-documented characteristic of OSA, recent evidence also highlights the role of tracheal constriction in the disorder manifestation and severity [40,41]. In this study, each anatomical region was altered to simulate two levels of constriction: mild and severe. For instance, velopharyngeal constriction reduced the CSA from 85 mm^2 (healthy) to 62 mm^2 (-27%) for mild narrowing and to 26 mm^2 (-69%) for severe narrowing. Oropharyngeal constrictions resulted in CSA reductions from 190 mm^2 to 85 mm^2 (-55%) and 30 mm^2 (-84%) for mild and severe conditions, respectively. Tracheal constriction decreased CSA from 166 mm^2 to 67 mm^2 (-60%) and 36 mm^2 (-78%) for mild and severe cases. Additionally, tracheal length was extended to reflect inter-individual anatomical variability: mild elongation increased length from 135 mm to 155 mm (+15%), while severe elongation extended it to 175 mm (+30%). These constrictions were imposed manually on the airway surface in Blender by locally narrowing the target segment; after each modification, the minimum CSA was measured on cross-sectional planes, and the geometry was iteratively adjusted until the desired percentage reduction was obtained. The selected “mild” and “severe” percentages were not based on a single fixed percentile but were tuned to produce anatomically plausible CSAs that lie within the ranges reported in OSA imaging studies and to generate clearly distinct moderate versus pronounced narrowing scenarios. The effects of velopharyngeal narrowing were investigated in prior work [11] and are included here for comparative purposes. All modifications were implemented on the CT-based healthy airway model to isolate the acoustic impact of each anatomical feature while preserving overall boundary

conditions and flow dynamics. In addition to the primitive modifications applied to individual regions, several combined configurations were developed to examine the interactive effects of multilevel airway alterations. This framework resulted in a total of 15 UA configurations added to the original geometry. A complete summary of the anatomical modifications, including targeted regions, constriction severity, and geometric variations, is provided in Table 5-1. In addition, the minimum cross-sectional area and segmented volume of each targeted airway region of the primitive models and OSA model are summarized in Table 5-2.

Figure 5-3 illustrates the anatomical variations described above. It displays the healthy CT-based airway model alongside region-specific zoomed-in views for the velopharynx, oropharynx, and trachea. Each panel illustrates the geometric variations corresponding to mild and severe constriction levels, as well as the progressive elongation of the trachea. Furthermore, to evaluate the clinical relevance of the observed acoustic changes, a simulation based on the CT scan of the OSA participant will be conducted [42]. This serves as a verification step to assess whether the parametric variations introduced in the modified models reflect physiologically realistic acoustic behavior in OSA conditions.

Table 5-1: Summary of anatomical modifications applied to the CT-based healthy airway model. Primitive models represent isolated modifications to individual anatomical regions, while combination models incorporate multilevel alterations.

	Model ID	**Target Region**			**Constriction Level**		**Length Extension Level**		**Variation from original model**			
		VP	**OP**	**Tr**	**Mild**	**Severe**	**Mild**	**Severe**	**Min CSA**	**%**	**Length**	**%**
Primitive models	Model 1	†**			†				85 → 62 mm^2	-27%		
	Model 2	†				†			85 → 26 mm^2	-69%		
	Model 3		†		†				190 → 85 mm^2	-55%		
	Model 4		†			†			190 → 30 mm^2	-84%		

	Model 5			†	†				166 → 67 mm^2	-60%		
	Model 6			†		†			166 → 36 mm^2	-78%		
	Model 7			†			†				135 → 155 mm	15%
	Model 8			†				†			135→ 175 mm	30%
Combinations	Model 9	†	†			††			Model 2 + Model 4			
	Model 10	†		†		††			Model 2 + Model 6			
	Model 11	†		†		†		†	Model 2 + Model 8			
	Model 12		†	†		††			Model 4 + Model 6			
	Model 13		†	†		†		†	Model 4 + Model 8			
	Model 14			†		†		†	Model 6 + Model 8			
	Model 15	†	†	†		†††			Model 2 + Model 4 + Model 6			

**†= constriction in a single target region; ††=constriction in two regions, †††= constriction in three regions. VP: Velopharynx; OP: Oropharynx; Tr: Trachea; Min CSA: minimum cross-sectional area.

Table 5-2: Volumetric and cross-sectional area (CSA) measurements for each targeted upper airway region (velopharynx, oropharynx, trachea) across the healthy baseline, individual modification models, and the OSA geometry. For each region, both the segmented volume (in mm^3) and the minimum cross-sectional area (in mm^2) are listed.

Model	**Velopharynx**		**Oropharynx**		**Trachea**	
	Volume (mm^3)	**min CSA (mm^2)**	**Volume (mm^3)**	**Min CSA (mm^2)**	**Volume (mm^3)**	**Min CSA (mm^2)**
Healthy Original	2616	85	6009	190	6517	166
Model 1	2291	62				
Model 2	2031	26				
Model 3			4798	85		
Model 4			3683	30		
Model 5					5859	67
Model 6					5530	36
OSA	1540	28	6003	110	11,373	255

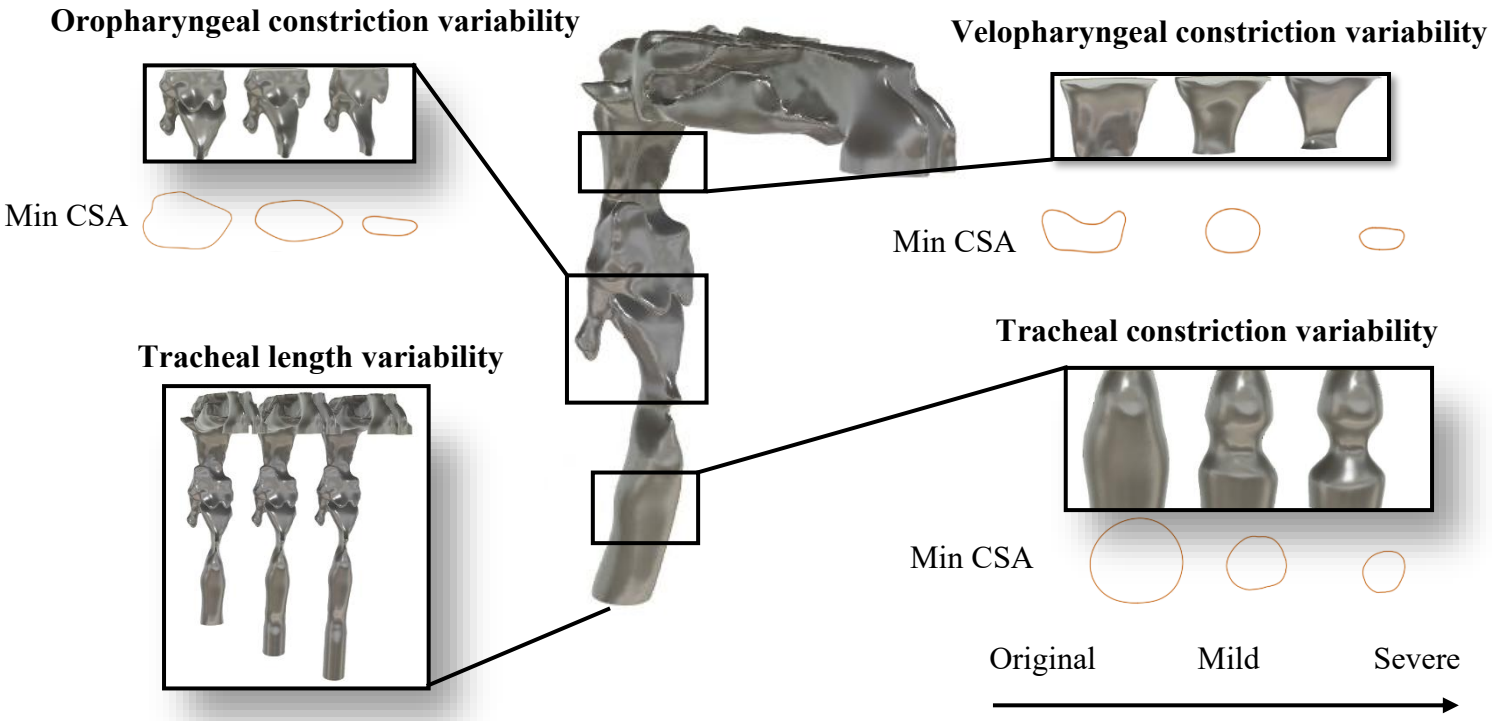

Fig. 5-3 : Anatomical modifications applied to the healthy airway model. Zoomed-in views show constriction and length-extension variants for the velopharynx, oropharynx, and trachea, used to simulate patient-specific anatomical changes based on OSA-related variability.

5.3 Results

5.3.1 Aerodynamics

Figure 5-4 illustrates a comparison of airflow dynamics within the UA, emphasizing differences in vortical structures (Fig. 5-4(a)) and turbulent kinetic energy (TKE) distribution (Fig. 5-4(b)) between the healthy (original) model and the obstructive sleep apnea (OSA) model at t=0.8s. In the OSA model, a pronounced anatomical narrowing is observed in the velopharyngeal region, with ~80% reduction in cross-sectional area (CSA) at the point of minimum constriction. The vortical structures are visualized using iso-surfaces of Q-criterion at 2×10^7 s^{-2}, colored by local velocity magnitude. The Q-criterion isolates regions where the rotational component of the

flow dominates over the strain rate, thereby highlighting areas of vortex formation. The OSA model exhibits intense and dense vortex cores, clearly observed in and downstream of the velopharyngeal constriction, corresponding to strong shear layers and the development of jet-like turbulent flow and downstream recirculation zones. These structures are associated with elevated velocity magnitude, reaching 23.1 m/s, indicating localized flow acceleration and transition to turbulence due to the anatomical obstruction. This further indicates the increase in the quadrupole sound sources at the constriction zone [43]. Although the dipole sources, associated with unsteady wall pressure fluctuations, are typically more dominant in low Mach number flows [44], the presence of intense vortical structures suggests that quadrupole sources may also contribute to sound generation in pathological cases like OSA. In contrast, the healthy model exhibits significantly fewer and weaker vortex structures in the velopharyngeal zone, indicative of a predominantly laminar flow regime. The maximum TKE in the velopharyngeal region increased from approximately 7.9 J/kg in the healthy model to 19.5 J/kg in the OSA model (≈2.5-fold increase), and the volume-average TKE within this region rose from 1.5 J/kg to 4.7 J/kg (≈3-fold increase). The TKE distribution (Fig. 5-4(b)) further supports these observations, with the OSA model exhibiting higher energy levels in the velopharyngeal region. This elevated TKE reflects the conversion of mean flow energy into turbulent fluctuations, which can also modulate the acoustic signature of the UA.

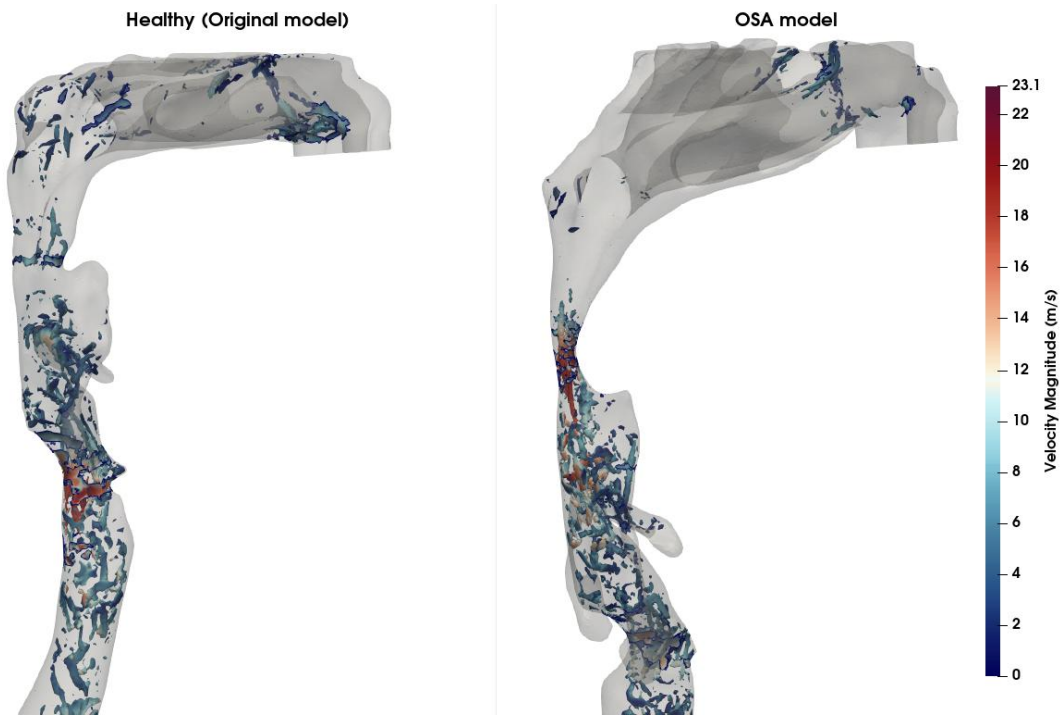

(a)

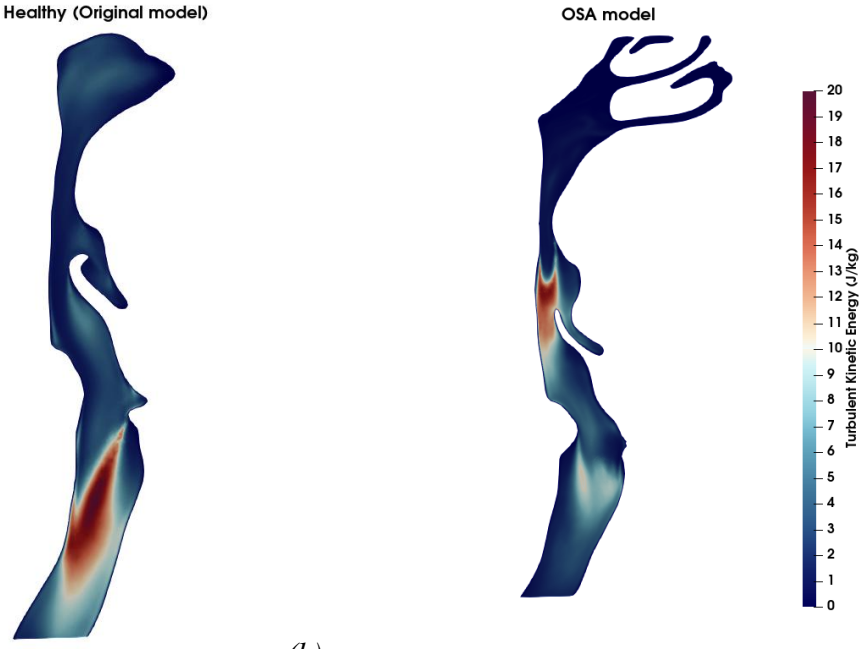

(b)

Fig. 5-4: Comparison of flow features between healthy and OSA upper airway models. (a) Coherent vortex structures visualized using iso-surfaces of the Q-criterion ($Q = 2 \times 10^7\ s^{-2}$), overlaid and colored by velocity magnitude (m/s) at t=0.8s. In the OSA model (right), elevated velocity regions and dense vortical structures are visible near the pharyngeal constriction, indicating increased shear and potential transition to turbulence. In contrast, the healthy model (left) exhibits fewer and weaker vortex structures, signifying more stable and laminar flow. (b) Turbulent kinetic energy (TKE)

contours across the airway mid-sagittal plane. The OSA model displays higher TKE values concentrated downstream of the constriction site, demonstrating enhanced turbulence generation due to velopharyngeal narrowing. The healthy model shows lower and more uniformly distributed TKE levels.

Figure 5-5 visualizes the vorticity magnitude in the mid-sagittal plane across six airway models: the healthy original model (a), model 2 with severe velopharyngeal constriction (b), model 4 with severe oropharyngeal constriction (c), model 9 with severe velopharyngeal and oropharyngeal constrictions (d), model 6 with severe tracheal constriction (e), and model 15 with severe velopharyngeal, oropharyngeal and tracheal constrictions (f). The vorticity magnitude captures the rotational intensity of the flow and is indicative of shear layer development and turbulence onset. In the healthy original model, mild vortex shedding is observed near the glottis region. In contrast, the models with geometric narrowing display intensified vorticity, especially downstream of the constricted zones, indicating the formation of shear-driven instabilities. Notably, model 4 (oropharyngeal constriction) exhibits the most intense and spatially concentrated vortex structures among the single-constriction models. This suggests that oropharyngeal narrowing may introduce more severe aerodynamic disturbances compared to other individual constrictions. Furthermore, in models with multiple constrictions (models 9 and 15), complex vortex interactions and elevated rotational intensity are evident along extended regions of the airway. However, it is notable that the magnitude and spatial concentration of vorticity induced by a single severe constriction exceeded those observed in models featuring multiple combined constrictions. This finding suggests that a singular severe constriction may lead to more pronounced aerodynamic disturbances characterized by stronger shear layers, intensified localized vortex shedding, and increased turbulence compared to scenarios involving several constrictions distributed along the airway. Consequently, the presence of a single, critically narrowed region may result in more severe aerodynamic conditions, potentially elevating the risk of

pathophysiological consequences such as increased airway resistance, turbulent kinetic energy, and susceptibility to airway collapse typically associated with OSA.

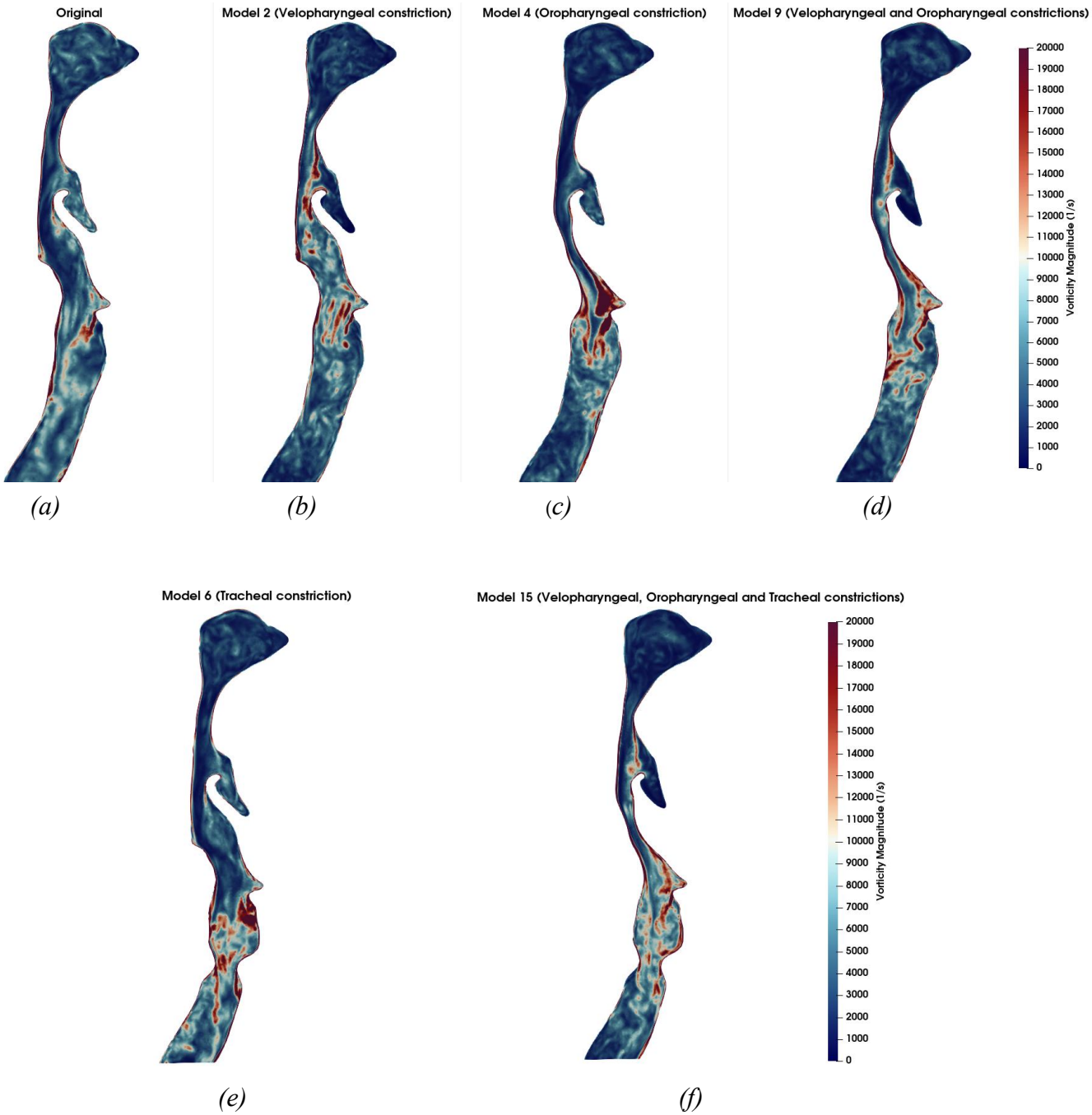

Fig. 5-5: Comparison of vorticity magnitude (in s^{-1}) across different airway geometries under inspiratory flow conditions at t=0.8s. (a) Original (healthy) model; (b) Model 2: Velopharyngeal constriction; (c) Model 4: Oropharyngeal constriction; (d) Model 9: Combined velopharyngeal and oropharyngeal constrictions; (e) Model 6: Tracheal constriction; (f) Model 15: Combined velopharyngeal, oropharyngeal, and tracheal constrictions. Vorticity magnitude fields are shown in sagittal plane slices to highlight the regions of high rotational flow

associated with anatomical narrowing. The color scale is consistent across all subplots, with red indicating stronger vortical structures.

5.3.2 Airway Resistance

The airway resistance was computed in the three targeted regions (velopharynx, oropharynx and trachea) for each model using Equation 5-1:

$$R_{region} = \frac{\Delta P_{region}}{Q}, \qquad 5\text{-}1$$

where R_{region} is the airway resistance in Pa.s/L, ΔP_{region} is the pressure drop across the region of interest in Pa, Q is the volumetric flow rate in L/s. The velopharynx was defined from a plane through the posterior edge of the hard palate to a plane through the tip of the uvula, the oropharynx extended from the uvular plane to a plane through the superior margin of the epiglottis, and the tracheal segment was defined from a plane just below the glottis to the distal tracheal outlet from the glottis. A dimensionless resistance (R^*) was also calculated to quantify the contribution of each targeted region to the overall airway resistance. This ratio was defined as the regional resistance divided by the global airway resistance, where the global airway resistance was computed using the total pressure drop across the airway (from the inlet at the nostrils to the tracheal outlet). Equivalently, this dimensionless ratio also represents the proportion of the total pressure drop occurring across each individual region. Figure 5-6(a) shows the airway resistance computed across the three anatomical regions of interest, for all airway models studied, including the healthy (Original) and OSA configurations. The healthy (original) model had a velopharyngeal resistance of 54 Pa.s/L and an oropharyngeal resistance of 72 Pa.s/L. Model 4, with the severe oropharyngeal constriction, exhibited the highest regional resistance (~458 Pa.s/L) across the primitive models, while model 2, with the severe velopharyngeal constriction, exhibited a nearly similar resistance (~450 Pa.s/L). Model 6, with the severe tracheal constriction showed elevated resistance (~230

Pa.s/L) compared to the mild and original cases; however, its severity was less prominent than the oropharyngeal and velopharyngeal constrictions. Furthermore, models with multiple constrictions generally exhibited reduced regional resistance values compared to models with a single, severe constriction in a corresponding region. However, a notable exception was observed in the velopharyngeal constriction when combined with tracheal length extension (model 11), where resistance slightly increased (~460 Pa.s/L) compared to the individual velopharyngeal constriction (model 2). In fact, the resistances values computed in model 11 resemble closely those of the OSA participant, who presented a similar combination of anatomical features, specifically a severely constricted velopharynx and a comparable tracheal length. To quantify the sensitivity of regional resistance to geometric perturbations, each modified configuration was compared with the healthy geometry. Mild velopharyngeal narrowing (Model 1) increased velopharyngeal resistance by approximately 80% relative to the healthy model, whereas severe velopharyngeal narrowing (Model 2) increased it by about 730%. Mild and severe oropharyngeal constrictions (Models 3 and 4) increased oropharyngeal resistance by approximately 94% and 530%, respectively. Severe tracheal constriction (Model 6) increased local tracheal resistance by more than 2700%, but its impact on global upper-airway resistance remained lower than that of the large pharyngeal constrictions. The progression of the resistance ratio (R^*) with increasing constriction severity for the primitive models is presented in Fig. 5-6(b). Resistance ratios in both the velopharyngeal and oropharyngeal regions exhibited a pronounced increase from mild to severe constriction, with the oropharyngeal region showing marginally higher resistance ratios. Conversely, the tracheal constriction had a comparatively lower influence on resistance, especially evident in the mild constriction case, which closely resembled the resistance ratio of the original model. Additionally, the OSA model displayed a remarkably high resistance ratio in the velopharyngeal region, further

emphasizing the critical contribution of velopharyngeal constriction to overall airway resistance in OSA pathology. Conversely, the OSA model exhibited minimal contribution to resistance from the tracheal and oropharyngeal regions, underscoring the predominance of velopharyngeal narrowing in this participant.

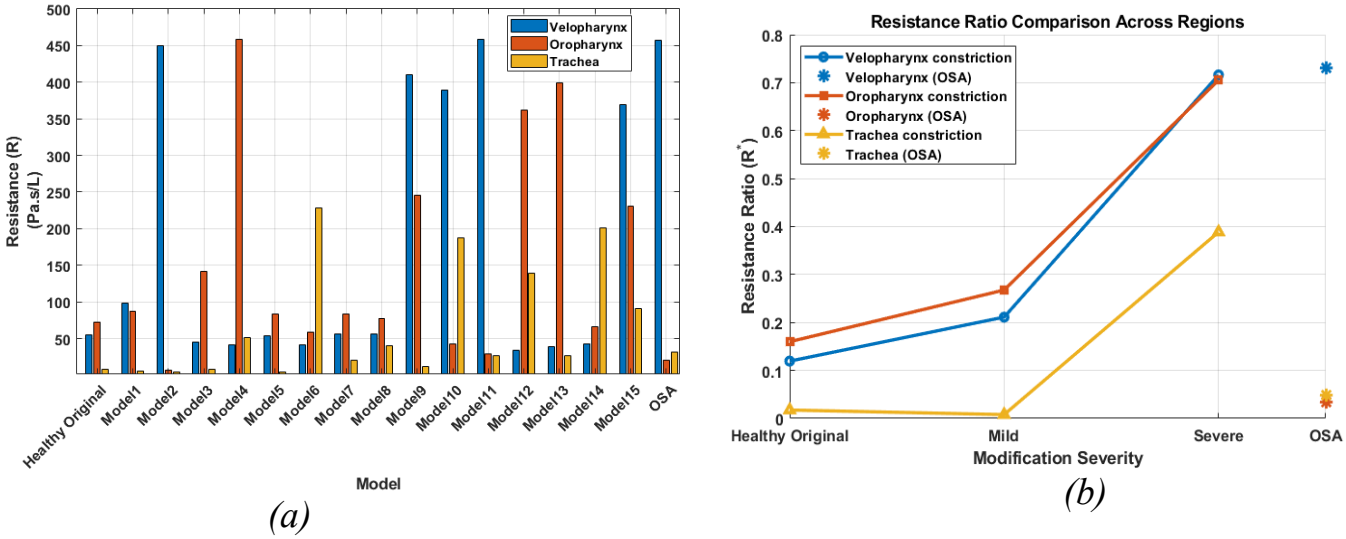

Fig. 5-6: Resistance characteristics across models. (a) Airway resistance (Pa·s/L) for the velopharynx, oropharynx, and trachea across all models, including the original and OSA geometries. (b) Resistance ratio (R^*) progression with increasing constriction severity (Original → Mild → Severe) for each anatomical region, with OSA resistance ratios shown for comparison.

5.3.3 Acoustics

The effect of anatomical modifications on the simulated sound pressure level (SPL) is presented in Fig. 5-7, where the frequency response curves are smoothed using a moving average filter to better visualize key spectral trends. Figure 5-7 compares the original (healthy) model with primitive models exhibiting mild and severe alterations in the three targeted anatomical regions. Several interesting findings emerge. The frequency response of the original model demonstrated four resonance peaks across the spectrum, serving as a baseline for comparison. These peaks were located at approximately 290 Hz, 627 Hz, 1458 Hz, and 2247 Hz. Anatomical modifications induced region-specific shifts in these resonances. For instance, as described in [11],

velopharyngeal narrowing led to a progressive downward shift of the third resonance peak (1000–1700 Hz range), with increasing constriction severity (Fig.5-7(a)). In contrast, oropharyngeal narrowing caused a dual effect: the third peak (1000–1700 Hz) shifted toward higher frequencies, while the fourth peak (1700–2500 Hz) shifted toward lower frequencies, indicating a complex redistribution of spectral energy (Fig.5-7(b)). Furthermore, tracheal narrowing exhibited the least impact on the frequency response, causing only a minor shift in the fourth resonance peak (Fig.5-7(c)). This implies that compared to UA constrictions, airway modifications distal to the glottis may contribute less prominently to acoustic spectral alterations, particularly in the range critical for resonance characterization. Finally, tracheal length extension caused a downward shift in all peak frequencies (Fig.5-7(d)), consistent with the expected acoustic effects of increasing the effective resonating length of the airway [45,46] .

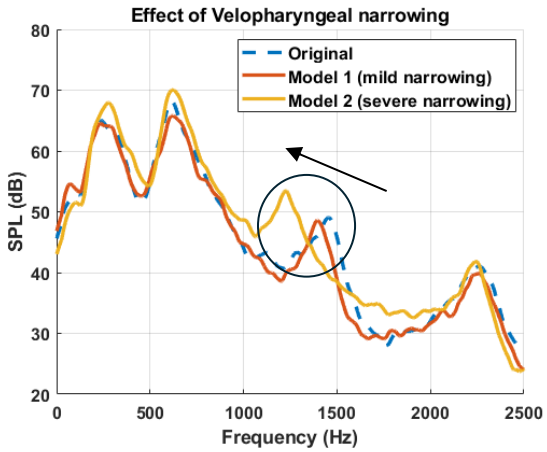

(a)

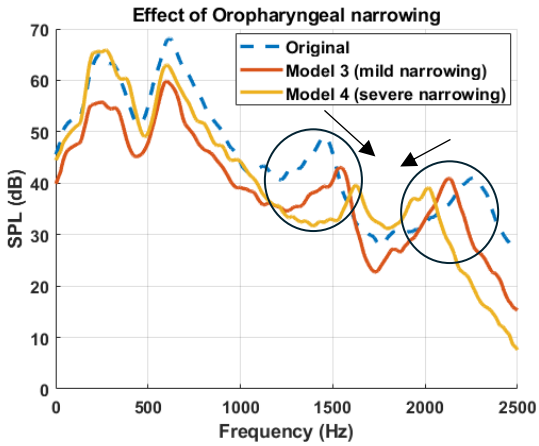

(b)

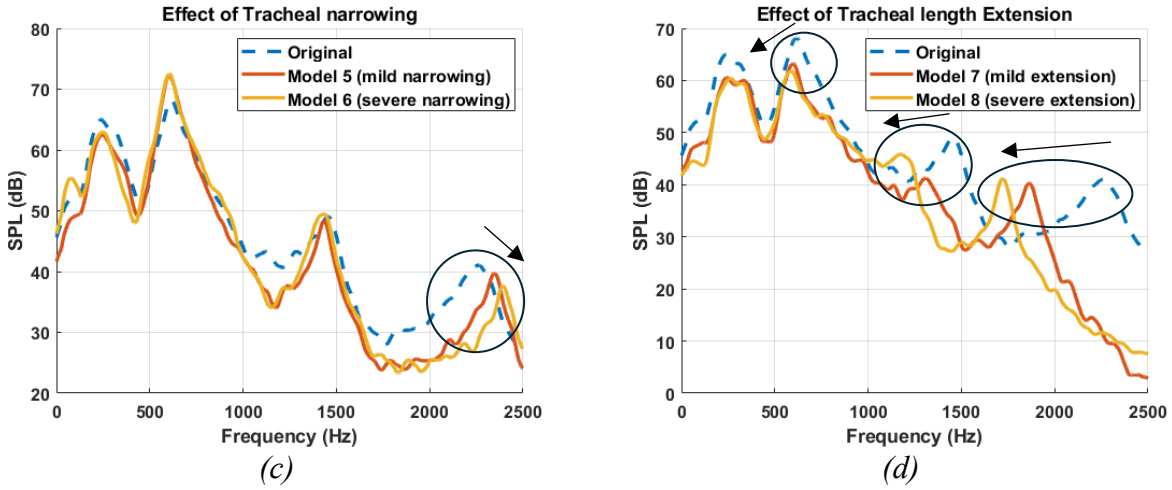

Fig. 5-7: Simulated Frequency response curves at the propagation domain, downstream of the trachea, illustrating the acoustic impact of anatomical modifications to the upper airway. Each subplot compares the original airway model (dashed blue line) with two modified configurations simulating mild and severe alterations at a specific anatomical region: (a) velopharyngeal narrowing (Model 1: mild, Model 2: severe)[11] , (b) oropharyngeal narrowing (Model 3: mild, Model 4: severe), (c) tracheal narrowing (Model 5: mild, Model 6: severe), and (d) tracheal length extension (Model 7: mild, Model 8: severe). Arrows have been added to indicate the direction of spectral shifts in the resonant frequencies as anatomical severity increases.

Furthermore, the simulated sound pressure level (SPL) spectra resulting from combined anatomical modifications to the UA is presented in Fig. 5-8, demonstrating how multilevel constrictions interact acoustically. A key observation across all combined models is the emergence of superimposed spectral patterns, where the resulting acoustic response appears to reflect the cumulative influence of the constituent primitive models. For instance, in Model 9 (velopharyngeal and oropharyngeal narrowing), the frequency response displays both the downward shift of the third resonance peak seen in Model 2 (velopharyngeal narrowing) and the upward shift associated with Model 4 (oropharyngeal narrowing), with the effect of velopharyngeal narrowing being more pronounced, while the downward shift of the fourth resonant frequency matched the one in Model 4. This trend of spectral superposition is consistently observed across the other combination models. Model 10 (velopharyngeal and tracheal narrowing) demonstrated a downward shift in the third resonance frequency, attributed to velopharyngeal narrowing, and an upward shift in the

fourth resonant frequency, consistent with the effect of tracheal narrowing. Similarly, Model 15, incorporating severe constrictions in all three regions, exhibited combined spectral effects from each anatomical modification, with the influence of the velopharyngeal constriction being most dominant, followed by oropharyngeal and then tracheal contribution. These findings suggest that, although flow–acoustic interactions within the UA are fundamentally nonlinear, particularly due to turbulence, unsteady flow separation, and geometric complexity, the system nonetheless exhibits behavior that approximates linear superposition in the frequency domain. This observation supports the notion that, under certain conditions, the spectral responses of individual anatomical modifications can be combined linearly, thereby enabling simplified modelling approaches for acoustic analysis and resonance prediction. It is important to emphasize, however, that the resonance phenomena themselves remain inherently nonlinear, governed by complex interactions between airflow, wall compliance, and geometry-dependent acoustic impedance [47].

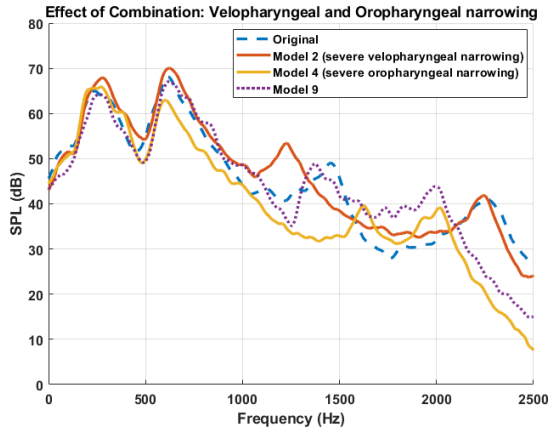

(a)

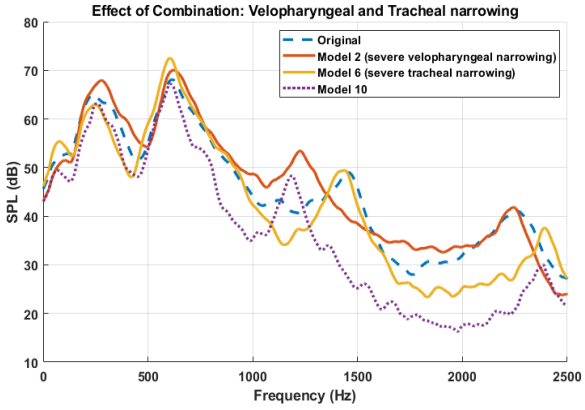

(b)

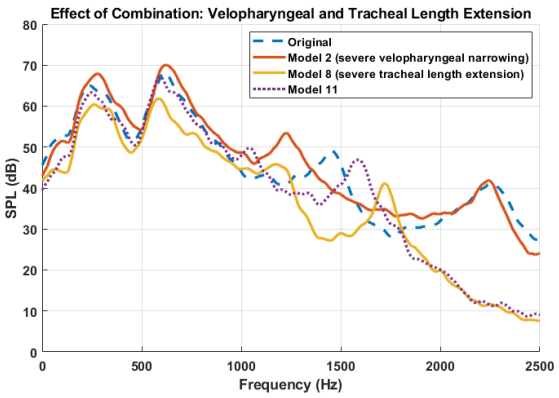

(c)

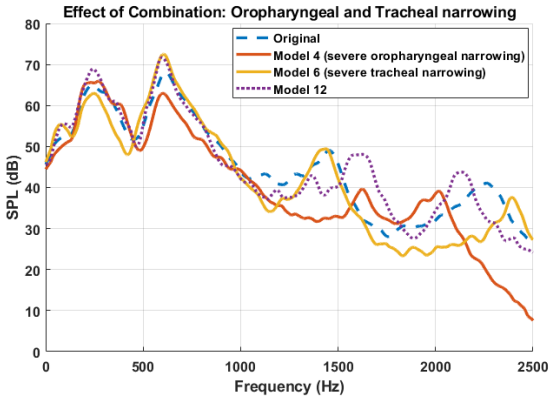

(d)

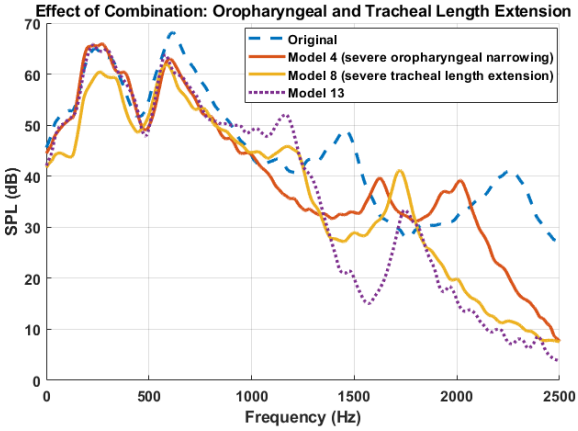

(e)

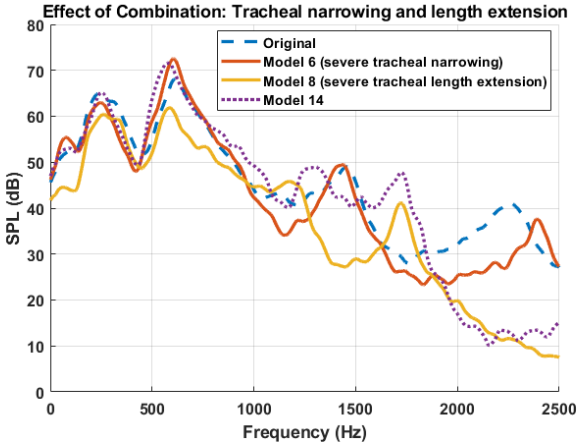

(f)

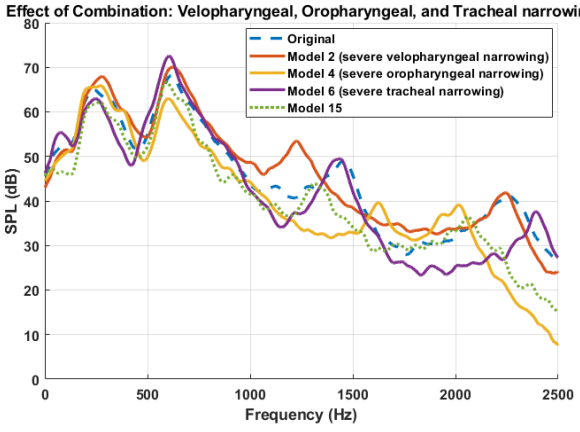

(g)

Fig. 5-8: Comparison of sound pressure level (SPL) spectra for different multilevel anatomical alterations to the upper airway. Each subplot presents the frequency response for combinations of primitive anatomical modifications.(a) Velopharyngeal and oropharyngeal narrowing (Model 2 + Model 4 → Model 9). (b)Velopharyngeal and tracheal narrowing (Model 2 + Model 6 → Model 10). (c) Velopharyngeal narrowing and tracheal length extension (Model 2 + Model 8 → Model 11). (d) Oropharyngeal and tracheal narrowing (Model 4 + Model 6 → Model 12). (e) Oropharyngeal narrowing and tracheal length extension (Model 4 + Model 8 → Model 13). (f) Tracheal narrowing and tracheal length extension (Model 6 + Model 8 → Model 14). (g) Combined velopharyngeal, oropharyngeal, and tracheal narrowing (Model 2 + Model 4 + Model 6 → Model 15). Dotted lines

represent combination models; dashed lines represent the original model. Each curve is smoothed using a moving average filter.

To verify the above findings, the simulated frequency responses of both the healthy (original model) and the OSA participant are plotted in Fig.5-9. The OSA participant's airway had a longer trachea and a significantly narrower velopharyngeal segment compared to that of the healthy participant. Consistent with prior observations from the primitive and combined models, the OSA spectrum demonstrated a downward shift in multiple resonance peaks, particularly the second and third peaks. This pattern aligns with the expected acoustic behavior of tracheal length extension, which lowers resonance frequencies due to an increase in the effective acoustic length of the airway, and the dominant effect of velopharyngeal constriction, which was shown to shift the third resonance peak downward. These findings further validate the hypothesis that specific anatomical changes leave distinct acoustic signatures in the frequency domain.

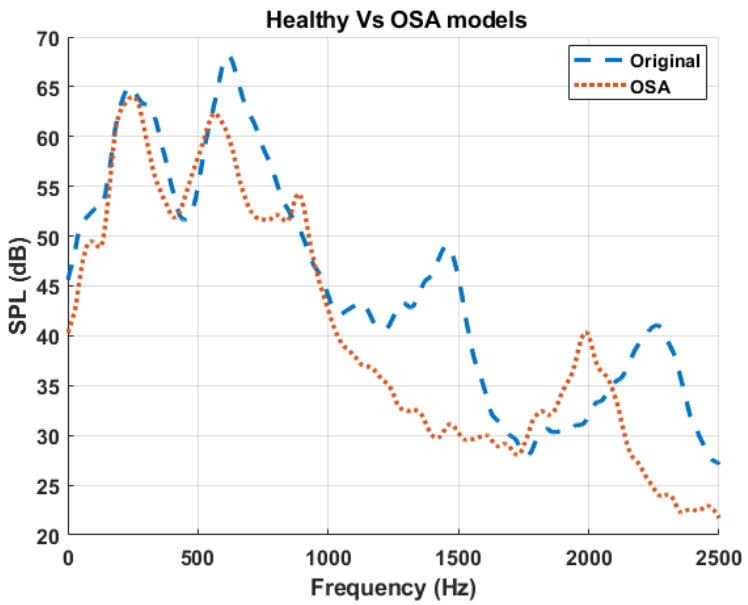

Fig. 5-9: Comparison of sound pressure level (SPL) spectra between the baseline (healthy) model and the OSA participant. The dashed blue curve represents the healthy airway (Original), while the dotted red curve represents the airway geometry from the OSA participant [42].

5.4 Discussion

This study investigated how localized and multilevel anatomical constrictions of the UA influence both aerodynamic resistance and the acoustic response of breathing sounds, with a particular focus on their relevance to the pathophysiology of obstructive sleep apnea (OSA). The findings hold potential clinical implications for the characterization and potential classification of OSA. Through systematic geometric modifications in the velopharynx, oropharynx, and trachea, we quantified the impact of these alterations on vortex formation, pressure drop, resistance distribution, and the resulting acoustic frequency response. These analyses were conducted using a non-invasive, hybrid aero-acoustic simulation framework grounded in Lighthill's analogy and applied to realistic CT-derived UA models from both healthy and severe OSA individuals.

The findings demonstrate distinct differences in airflow behaviors between healthy versus OSA airway geometries. In the OSA model, the presence of severe velopharyngeal narrowing

resulted in intensified vortex formation, characterized by dense and high-energy vortical structures downstream of the constriction. This is consistent with prior findings in vivo MRI and CFD studies that identified the velopharynx as a critical site of dynamic collapse, often associated with shear layer instabilities and high-velocity jet-like inspiratory flow. Specifically, the study in [48] reported that velopharyngeal constriction can generate a focused high-speed jet, commonly referred to as the "pharyngeal jet", that impinges on the posterior pharyngeal wall, thereby increasing local shear forces and promoting turbulence generation. Additionally, analysis of mid-sagittal vorticity revealed that oropharyngeal narrowing (Model 4) produced the most intense and spatially concentrated vortical structures among all individual constriction models. This is noteworthy given that previous clinical studies have also identified the oropharynx as a frequent site of obstruction in OSA patients [12,49] and that oropharyngeal structure represents a significant risk factor for OSA [50]. Our results suggest that, under specific geometric configurations, severe oropharyngeal constriction may induce more pronounced flow disturbances than velopharyngeal narrowing. Interestingly, multilevel constrictions did not always result in the most severe vorticity patterns. Instead, models with a single severe constriction (e.g., Model 4) often exhibited higher localized rotational energy compared to those with distributed moderate constrictions (e.g., Model 9). This suggests that singular anatomical bottlenecks may dominate flow disruption, emphasizing the importance of site-specific anatomical evaluation in clinical settings.

Regional airway resistance was computed for each anatomical segment to evaluate the localized impact of each structural modification. Previous studies have established the role of airway resistance as a biomarker for OSA severity classification. For instance, OSA patients were reported to have airway resistance values approximately three times higher than those of healthy controls, with mean resistances of 1173 Pa·s/L and 374 Pa·s/L, respectively [51]. Strong

correlations between pharyngeal airway resistance and the apnea-hypopnea index (AHI) have also been reported [52,53]. Furthermore, interventions such as oral appliances have been shown to reduce airway resistance by up to 36% in OSA patients [54]. In this study, we investigated the specific impact of anatomical constriction at each segment on the resistance of each anatomical site and its relative on the overall airway resistance. Dimensionless resistance ratios (R*) further illustrated the differential contribution of each anatomical segment to total airway resistance. In both primitive and combined models, velopharyngeal and oropharyngeal segments were the primary contributors to global resistance. In contrast, tracheal constriction, even when severe, exerted a comparatively smaller influence. Notably, Model 11, which combined velopharyngeal constriction with tracheal length extension, resulted in a higher velopharyngeal resistance than the model incorporating velopharyngeal narrowing only. The resistance profile closely resembles that of the OSA participant's geometry. This supports previous findings [55], who demonstrated that UA lengthening, is a structural characteristic of OSA and correlates strongly with AHI. While their study focused on morphological changes and their relationship with AHI, our results extend this understanding by showing that airway elongation can also act with UA narrowing to exacerbate aerodynamic resistance, thereby contributing to the airflow limitation observed in OSA.

Furthermore, the impact of the anatomical modifications on the simulated TBS were studied. The frequency response analysis of the UA models revealed region-specific spectral shifts corresponding to anatomical modifications. In particular, velopharyngeal narrowing produced a progressive downward shift in the third resonance peak (1000–1700 Hz range) with increasing severity [11], while oropharyngeal narrowing resulted in a dual pattern: an upward shift of the third peak and a downward shift of the fourth. These patterns reflect underlying changes in the acoustic properties of the airway segments and can be interpreted using the principles of acoustic

inertance (or acoustic mass) and compliance. In a simplified lumped acoustic system, the resonant frequency of a given segment is determined by the balance between its acoustic compliance (C) and acoustic mass (M) [47], described by:

$$f_r = \frac{1}{2\pi}\sqrt{\frac{1}{MC}} \qquad 5\text{-}2$$

where acoustic mass (M) is given by:

$$M = \frac{\rho L}{A} \qquad 5\text{-}3$$

and acoustic compliance (C) is defined as:

$$C = \frac{V}{\rho c^2} \qquad 5\text{-}4$$

Here, V is the volume, L is the effective length of the segment, A is the cross-sectional area perpendicular to the air column acceleration, ρ is air density, and c is the speed of sound.

In the velopharyngeal constriction models, the narrowing reduces the cross-sectional area A, increasing acoustic mass (M), which in turn lowers the resonant frequency (f_r) explaining the observed downward shift of the third peak. Although the segment volume also decreased, reducing acoustic compliance, the effect of reduced area on acoustic mass was more pronounced. This suggests that the constricted velopharynx behaves as a region dominated by acoustic mass, acting like a bottleneck that delays pressure wave propagation and reduces the system's natural frequency in the [1000-1700] Hz range. Conversely, in oropharyngeal constriction, the third peak shifted upward while the fourth shifted downward. The upward shift is likely due to a reduction in compliance, i.e., reduced oropharyngeal volume V, leading to increased stiffness and a higher f_r. The downward shift of the fourth peak may reflect increased acoustic inertance effects, which

become more influential at higher frequencies. Since acoustic compliance and inertance are both frequency-dependent [47], their relative influence shifts across the spectrum. In this case, the increased influence of acoustic inertance of the airway at higher frequencies likely contributed to the selective lowering of the fourth resonance peak. This complexity suggests that oropharyngeal geometry influences both local and distributed acoustic behaviors, modulating the airway's filtering characteristics in a frequency-dependent manner. This highlights the potential of resonance-based analysis as a tool for inferring site-specific airway alterations from non-invasive tracheal sound measurements, with direct implications for OSA diagnosis.

This study has potential clinical implications. The findings suggest that patient-specific airway models could serve as valuable tools for non-invasive functional assessment of airway mechanics, particularly when combined with tracheal breathing sound (TBS) analysis. The observed spectral shifts in TBS, which correspond to distinct anatomical modifications, support the feasibility of using acoustic signatures as indirect markers of localized airway narrowing or elongation. This could open the door to sound-based screening tools that leverage computational modelling to interpret patient-recorded TBS data in terms of site-specific anatomical abnormalities. Such methods may reduce reliance on full polysomnography and provide accessible and cost-effective screening pathways, particularly in primary care or home-based monitoring settings. Moreover, the demonstrated ability of the model to capture how multilevel constrictions influence spectral patterns may facilitate personalized treatment planning, such as selecting optimal sites for surgical intervention or designing patient-specific oral appliances. Ultimately, this integrative modelling and acoustic approach could complement existing diagnostic methods by providing mechanistic insight into the airflow acoustic interactions underlying OSA pathophysiology. In practical terms, future TBS-based diagnostic algorithms could incorporate

simulation-informed spectral features together with anthropometric and clinical variables in multivariate or machine-learning models to estimate OSA probability and localize the obstruction site. Future work should develop a mathematical formulation of the relationship between airway anatomy and the breathing sounds spectrum using parameterized models and develop algorithms suitable for clinical and home devices, improving the robustness, interpretability, and clinical utility of TBS-based screening tools.

5.5 Limitations

The limitations of this study include the assumption of rigid airway walls, which did not incorporate fluid—structure interactions during inspiration. The absence of wall compliance neglects potential tissue deformation and collapsibility, particularly in regions prone to obstruction such as the velopharynx and oropharynx. CFD boundary conditions included a fixed pressure drop to simulate inspiratory flow. While this approach facilitates comparison across anatomical models, it does not fully capture the transient pressure fluctuations characteristic of natural breathing. In particular, prescribing a single steady pressure drop neglects the acceleration and deceleration phases of inspiration and inter-subject differences in driving pressure associated with lung volume or breathing effort level. Nevertheless, this is justified by the fact that the aero-acoustic model was validated [11] using tracheal breathing sounds recorded during the plateau phase of inspiration, where flow is relatively stable. Accordingly, the absolute resistance and TBS amplitudes reported here should be interpreted as corresponding to a representative inspiratory effort, rather than to the full dynamic range of breathing conditions.

Another important limitation is the restricted participant representation. This study focused on a single healthy subject and one OSA patient, both serving as representative anatomical cases. However, the healthy participant was 76 years old, while the OSA participant was 47 years old,

introducing an age-related anatomical variability that may confound the interpretation of disease-specific findings. Aging affects the UA anatomy through changes in muscle tone, tissue compliance, and airway geometry [56,57]. Although the primary aim of this study was to explore anatomical contributions to acoustic response independent of demographics, the age disparity may still affect the UA shape and resonance characteristics. Therefore, future studies should account for age-matched controls or include larger cohorts with balanced age, sex, and BMI distributions to isolate pathology-specific effects.

Furthermore, while the anatomical modifications applied to the healthy model were guided by clinical imaging data, the study did not explore the full spectrum of OSA anatomical variability, severity levels, or sex-based differences in the UA structure. Future work should include a larger cohort of OSA patients with diverse anatomical phenotypes to improve the generalizability of the findings and strengthen their clinical relevance.

5.6 Conclusion

This study investigated how specific anatomical features of the upper airway influence airflow dynamics and tracheal breathing sounds spectra using one-way coupled aero-acoustic modelling framework. By systematically introducing controlled velopharyngeal, oropharyngeal and tracheal constrictions, as well as the airway elongation, the contribution of each anatomical modification to the airway resistance and acoustic response was examined. The acoustic analysis showed that each anatomical region imprints a distinct and interpretable signature on the TBS frequency response. Velopharyngeal narrowing caused a downward shift of the third resonance peak, oropharyngeal narrowing produced opposite shifts of the third and fourth peaks, tracheal narrowing had a comparatively mild effect, and tracheal elongation lowered all resonances by increasing the effective acoustic length. Multilevel constrictions yielded spectra that closely

resembled a superposition of the corresponding primitive responses. These findings establish a mechanistic link between localized anatomical changes and TBS acoustic response, supporting the use of anatomically informed spectral features as potential non-invasive markers of site-specific airway pathology in OSA.

References

[1] A. Yadollahi, E. Giannouli, and Z. Moussavi, "Sleep apnea monitoring and diagnosis based on pulse oximetery and tracheal sound signals," *Med. Biol. Eng. Comput.*, vol. 48, pp. 1087–1097, 2010.

[2] C. Jácome and A. Marques, "Computerized respiratory sounds in patients with COPD: A systematic review," *COPD J. Chronic Obstr. Pulm. Dis.*, vol. 12, no. 1, pp. 104–112, 2015, doi: 10.3109/15412555.2014.908832.

[3] N. Gavriely, Y. Palti, G. Alroy, and J. B. Grotberg, "Measurement and theory of wheezing breath sounds," *J. Appl. Physiol.*, vol. 57, no. 2, pp. 481–492, 1984.

[4] T. Penzel and A. Sabil, "The use of tracheal sounds for the diagnosis of sleep apnoea.," *Breathe (Sheffield, England)*, vol. 13, no. 2, pp. e37–e45, Jun. 2017, doi: 10.1183/20734735.008817.

[5] T. Young, P. E. Peppard, and D. J. Gottlieb, "Epidemiology of obstructive sleep apnea: A population health perspective," *Am. J. Respir. Crit. Care Med.*, vol. 165, no. 9, pp. 1217–1239, 2002, doi: 10.1164/rccm.2109080.

[6] K. P. Strohl and S. Redline, "Recognition of obstructive sleep apnea.," *Am. J. Respir. Crit. Care Med.*, vol. 154, no. 2, pp. 279–289, Aug. 1996, doi: 10.1164/ajrccm.154.2.8756795.

[7] J. M. Beecroft, M. Ward, M. Younes, S. Crombach, O. Smith, and P. J. Hanly, "Sleep monitoring in the intensive care unit: Comparison of nurse assessment, actigraphy and

polysomnography," *Intensive Care Med.*, vol. 34, no. 11, pp. 2076–2083, 2008, doi: 10.1007/s00134-008-1180-y.

[8] "Practice Guidelines for the Perioperative Management of Patients with Obstructive Sleep Apnea," *Anesthesiology*, vol. 120, no. 2, pp. 268–286, Feb. 2014, doi: 10.1097/ALN.0000000000000053.

[9] A. Elwali and Z. Moussavi, "A Novel Decision Making Procedure during Wakefulness for Screening Obstructive Sleep Apnea using Anthropometric Information and Tracheal Breathing Sounds," *Sci. Rep.*, vol. 9, no. 1, Dec. 2019, doi: 10.1038/s41598-019-47998-5.

[10] H. Pasterkamp, J. Schäfer, and G. R. Wodicka, "Posture-dependent change of tracheal sounds at standardized flows in patients with obstructive sleep apnea," *Chest*, vol. 110, no. 6, pp. 1493–1498, 1996, doi: 10.1378/chest.110.6.1493.

[11] W. Ashraf, J. J. Fredberg, and Z. Moussavi, "Aeroacoustics of breath sounds in trachea and upper airway," *Appl. Acoust.*, vol. 241, p. 111021, Jan. 2026, doi: 10.1016/j.apacoust.2025.111021.

[12] Y. Finkelstein *et al.*, "Velopharyngeal anatomy in patients with obstructive sleep apnea versus normal subjects," *J. Oral Maxillofac. Surg.*, vol. 72, no. 7, pp. 1350–1372, 2014, doi: 10.1016/j.joms.2013.12.006.

[13] J. H. Walsh *et al.*, "Evaluation of pharyngeal shape and size using anatomical optical coherence tomography in individuals with and without obstructive sleep apnoea," *J. Sleep Res.*, vol. 17, no. 2, pp. 230–238, 2008, doi: 10.1111/j.1365-2869.2008.00647.x.

[14] A. N. Rama, S. H. Tekwani, and C. A. Kushida, "Sites of obstruction in obstructive sleep apnea," *Chest*, vol. 122, no. 4, pp. 1139–1147, 2002, doi: 10.1378/chest.122.4.1139.

[15] H. Chen, G. Aarab, M. H. T. de Ruiter, J. de Lange, F. Lobbezoo, and P. F. van der Stelt,

"Three-dimensional imaging of the upper airway anatomy in obstructive sleep apnea: A systematic review," *Sleep Med.*, vol. 21, pp. 19–27, 2016, doi: 10.1016/j.sleep.2016.01.022.

[16] R. L. Horner, S. A. Shea, J. Mcivor, and A. Guz, "Pharyngeal Size and Shape During Wakefulness and Sleep in Patients with Obstructive Sleep Apnoea," 1989.

[17] M. A. Ciscar *et al.*, "Magnetic resonance imaging of the pharynx in OSA patients and healthy subjects," *Eur. Respir. J.*, vol. 17, no. 1, pp. 79–86, 2001, doi: 10.1183/09031936.01.17100790.

[18] R. Calvin, "Radiology Apnea : with Ultrafast," pp. 775–778, 1989.

[19] Y. Segal, A. Malhotra, and G. Pillar, "Upper airway length may be associated with the severity of obstructive sleep apnea syndrome," *Sleep Breath.*, vol. 12, no. 4, pp. 311–316, 2008, doi: 10.1007/s11325-008-0191-9.

[20] Z. Abramson, S. Susarla, M. August, M. Troulis, and L. Kaban, "Three-Dimensional Computed Tomographic Analysis of Airway Anatomy in Patients With Obstructive Sleep Apnea," *J. Oral Maxillofac. Surg.*, vol. 68, no. 2, pp. 354–362, 2010, doi: 10.1016/j.joms.2009.09.087.

[21] N. T. Griscom and M. E. Wohl, "Dimensions of the growing trachea related to body height. Length, anteroposterior and transverse diameters, cross-sectional area, and volume in subjects younger than 20 years of age.," *Am. Rev. Respir. Dis.*, vol. 131, no. 6, pp. 840–844, Jun. 1985, doi: 10.1164/arrd.1985.131.6.840.

[22] I. Sanchez and H. Pasterkamp, "Tracheal sound spectra depend on body height," *Am. Rev. Respir. Dis.*, vol. 148, no. 4, pp. 1083–1087, 1993, doi: 10.1164/ajrccm/148.4_Pt_1.1083.

[23] S. S. Kraman, H. Pasterkamp, M. Kompis, M. Takase, and G. R. Wodicka, "Effects of breathing pathways on tracheal sound spectral features," *Respir. Physiol.*, vol. 111, no. 3,

pp. 295–300, 1998, doi: 10.1016/S0034-5687(97)00113-8.

[24] M. Yonemaru *et al.*, “Detection of tracheal stenosis by frequency analysis of tracheal sounds.,” *J. Appl. Physiol.*, vol. 75, no. 2, pp. 605–612, Aug. 1993, doi: 10.1152/jappl.1993.75.2.605.

[25] N. M. Ghahjaverestan, C. Aguiar, R. Hummel, X. Cao, J. Yu, and T. D. Bradley, “Sleep Apnea Detection by Tracheal Motion and Sound, and Oximetry via Application of Deep Neural Networks,” *Nat. Sci. Sleep*, vol. 15, pp. 423–432, 2023, doi: 10.2147/NSS.S397196.

[26] M. Muñoz Rojo, R. X. A. Pramono, N. Devani, M. Thomas, S. Mandal, and E. Rodriguez-Villegas, “Validation of Tracheal Sound-Based Respiratory Effort Monitoring for Obstructive Sleep Apnoea Diagnosis,” *J. Clin. Med.*, vol. 13, no. 12, 2024, doi: 10.3390/jcm13123628.

[27] S. H. Yeom, J. S. Na, H. D. Jung, H. J. Cho, Y. J. Choi, and J. S. Lee, “Computational analysis of airflow dynamics for predicting collapsible sites in the upper airways: Machine learning approach,” *J. Appl. Physiol.*, vol. 127, no. 4, pp. 959–973, 2019, doi: 10.1152/japplphysiol.01033.2018.

[28] J. Xi, Z. Wang, K. Talaat, C. Glide-Hurst, and H. Dong, “Numerical study of dynamic glottis and tidal breathing on respiratory sounds in a human upper airway model,” *Sleep Breath.*, vol. 22, no. 2, pp. 463–479, May 2018, doi: 10.1007/s11325-017-1588-0.

[29] S. Saha, T. D. Bradley, M. Taheri, Z. Moussavi, and A. Yadollahi, “A Subject-Specific Acoustic Model of the Upper Airway for Snoring Sounds Generation,” *Sci. Rep.*, vol. 6, pp. 1–10, 2016, doi: 10.1038/srep25730.

[30] P. A. Yushkevich *et al.*, “User-guided 3D active contour segmentation of anatomical structures: Significantly improved efficiency and reliability,” *Neuroimage*, vol. 31, no. 3,

pp. 1116–1128, 2006, doi: https://doi.org/10.1016/j.neuroimage.2006.01.015.

[31] Michael James Lighthill, “On sound generated aerodynamically I. General theory,” *Proc. R. Soc. London. Ser. A. Math. Phys. Sci.*, vol. 211, no. 1107, pp. 564–587, Mar. 1952, doi: 10.1098/rspa.1952.0060.

[32] S. Schoder *et al.*, “Hybrid aeroacoustic approach for the efficient numerical simulation of human phonation,” *J. Acoust. Soc. Am.*, vol. 147, no. 2, pp. 1179–1194, 2020, doi: 10.1121/10.0000785.

[33] J. Smagorinsky, “General circulation experiments with the primitive equations: I. The basic experiment,” *Mon. Weather Rev.*, vol. 91, no. 3, pp. 99–164, 1963.

[34] D. K. Lilly, “A proposed modification of the germano sugrid-scale closure method,” *Phys Fluids A*, vol. 4, pp. 633–635, 1992.

[35] M. Zielinska-Krawczyk, R. Krenke, E. M. Grabczak, and R. W. Light, “Pleural manometry–historical background, rationale for use and methods of measurement,” *Respir. Med.*, vol. 136, no. September 2017, pp. 21–28, 2018, doi: 10.1016/j.rmed.2018.01.013.

[36] B. Vara Almirall, H. Calmet, H. Q. Ang, and K. Inthavong, “Flow behavior in idealized & realistic upper airway geometries,” *Comput. Biol. Med.*, vol. 194, no. January, p. 110449, 2025, doi: 10.1016/j.compbiomed.2025.110449.

[37] A. Lancmanová and T. Bodnár, *Numerical simulations of human respiratory flows: a review*, vol. 7, no. 4. Springer International Publishing, 2025. doi: 10.1007/s42452-025-06617-x.

[38] S. Caro, P. Ploumhans, and X. Gallez, “Implementation of Lighthill’s acoustic analogy in a Finite/Infinite Elements framework,” *Collect. Tech. Pap. - 10th AIAA/CEAS Aeroacoustics Conf.*, vol. 2, no. May 2004, pp. 1048–1065, 2004, doi: 10.2514/6.2004-2891.

[39] T. Iwasaki, T. Sugiyama, A. Yanagisawa-Minami, Y. Oku, A. Yokura, and Y. Yamasaki, "Effect of adenoids and tonsil tissue on pediatric obstructive sleep apnea severity determined by computational fluid dynamics," *J. Clin. Sleep Med.*, vol. 16, no. 12, pp. 2021–2028, 2020, doi: 10.5664/jcsm.8736.

[40] I. Rubinstein, T. D. Bradley, N. Zamel, and V. Hoffstein, "Glottic and cervical tracheal narrowing in patients with obstructive sleep apnea," *J. Appl. Physiol.*, vol. 67, no. 6, pp. 2427–2431, 1989, doi: 10.1152/jappl.1989.67.6.2427.

[41] C. Van Holsbeke *et al.*, "Functional respiratory imaging as a tool to assess upper airway patency in children with obstructive sleep apnea," *Sleep Med.*, vol. 14, no. 5, pp. 433–439, 2013, doi: 10.1016/j.sleep.2012.12.005.

[42] W. Ashraf, J. J. Fredberg, and Z. Moussavi, "Aero-acoustic Simulation of Patient-specific Breathing Sounds in Obstructive Sleep Apnea Versus Healthy Airways," *Am. J. Respir. Crit. Care Med.*, vol. 211, no. Abstracts, pp. A3645–A3645, May 2025, doi: 10.1164/ajrccm.2025.211.Abstracts.A3645.

[43] M. Foucart, "Aeroacoustic investigation of a stridor patient's upper respiratory system," pp. 1–242, 2015.

[44] N. Curle, "The influence of solid boundaries upon aerodynamic sound," *Proc. R. Soc. London. Ser. A. Math. Phys. Sci.*, vol. 231, no. 1187, pp. 505–514, 1955.

[45] D. T. Blackstock, *Fundamentals of physical acoustics*. John Wiley & Sons, 2000.

[46] W. Ashraf, A. Alqudah, M. Band, L. Zhao, B. Lithgow, and A. Elwali, "Developing an Empirical Acoustic Transfer Function Model for the Upper Airway," *Ann. Biomed. Eng.*, no. 0123456789, 2025, doi: 10.1007/s10439-025-03883-z.

[47] I. R. Titze, "Acoustic interpretation of resonant voice," *J. Voice*, vol. 15, no. 4, pp. 519–

528, 2001, doi: 10.1016/S0892-1997(01)00052-2.

[48] S. J. Jeong, W. S. Kim, and S. J. Sung, “Numerical investigation on the flow characteristics and aerodynamic force of the upper airway of patient with obstructive sleep apnea using computational fluid dynamics,” *Med. Eng. Phys.*, vol. 29, no. 6, pp. 637–651, 2007, doi: 10.1016/j.medengphy.2006.08.017.

[49] R. J. Schwab, W. B. Gefter, E. A. Hoffman, K. B. Gupta, and A. I. Pack, “Dynamic upper airway imaging during awake respiration in normal subjects and patients with sleep disordered breathing,” *Am. Rev. Respir. Dis.*, vol. 148, no. 5, pp. 1385–1400, 1993, doi: 10.1164/ajrccm/148.5.1385.

[50] J. B. Schellenberg, G. Maislin, and R. J. Schwab, “Physical findings and the risk for obstructive sleep apnea: The importance of oropharyngeal structures,” *Am. J. Respir. Crit. Care Med.*, vol. 162, no. 2 I, pp. 740–748, 2000, doi: 10.1164/ajrccm.162.2.9908123.

[51] A. Yanagisawa-Minami, T. Sugiyama, T. Iwasaki, and Y. Yamasaki, “Primary site identification in children with obstructive sleep apnea by computational fluid dynamics analysis of the upper airway,” *J. Clin. Sleep Med.*, vol. 16, no. 3, pp. 431–439, 2020, doi: 10.5664/JCSM.8224.

[52] J. L. Stauffer *et al.*, “Pharyngeal size and resistance in obstructive sleep apnea,” *Am. Rev. Respir. Dis.*, vol. 136, no. 3, pp. 623–627, 1987, doi: 10.1164/ajrccm/136.3.623.

[53] J. L. Stauffer, D. P. White, and C. W. Zwillich, “Pulmonary function in obstructive sleep apnea. Relationships to pharyngeal resistance and cross-sectional area,” *Chest*, vol. 97, no. 2, pp. 302–307, 1990, doi: 10.1378/chest.97.2.302.

[54] B. Song *et al.*, “Computational fluid dynamics simulation of changes in the morphology and airflow dynamics of the upper airways in OSAHS patients after treatment with oral

appliances," *PLoS One*, vol. 14, no. 11, pp. 1–14, 2019, doi: 10.1371/journal.pone.0219642.

[55] H. Lin *et al.*, "Upper airway lengthening caused by weight increase in obstructive sleep apnea patients," *Respir. Res.*, vol. 21, no. 1, pp. 1–10, 2020, doi: 10.1186/s12931-020-01532-8.

[56] Y. Inamoto *et al.*, "Anatomy of the larynx and pharynx: effects of age, gender and height revealed by multidetector computed tomography," *J. Oral Rehabil.*, vol. 42, no. 9, pp. 670–677, 2015.

[57] A. Malhotra *et al.*, "Aging influences on pharyngeal anatomy and physiology: the predisposition to pharyngeal collapse," *Am. J. Med.*, vol. 119, no. 1, pp. 72.e9-72.e14, 2006, doi: 10.1016/j.amjmed.2005.01.077.

CHAPTER SIX: DESIGN AND ANALYSIS OF A CONTACT PIEZO MICROPHONE FOR RECORDING TRACHEAL BREATHING SOUNDS

Walid Ashraf[1], and Zahra Moussavi[1]

1. Biomedical Engineering Program, University of Manitoba, Winnipeg, Canada

Sensors 2024, 24(17), 5511 (https://doi.org/10.3390/s24175511)

Abstract

Analysis of tracheal breathing sounds (TBS) is a significant area of study in medical diagnostics and monitoring for respiratory diseases and obstructive sleep apnea (OSA). Recorded at the suprasternal notch, TBS can provide detailed insights into the respiratory system's functioning and health. This method has been particularly useful for non-invasive assessments and is used in various clinical settings such as OSA, asthma, respiratory infectious diseases, lung function and detection during either wakefulness or sleep. One of the challenges and limitations of TBS recording is the background noise including speech sound, movement and even non-tracheal breathing sounds propagating in the air. The breathing sounds captured from the nose or mouth can interfere with the tracheal breathing sounds, making it difficult to isolate the sounds necessary for accurate diagnostics. In this study, two surface microphones are proposed to accurately record TBS acquired solely from the trachea. The frequency response of each microphone is compared with a reference microphone. Additionally, the study evaluates the tracheal and lung breathing sounds of six participants recorded using the proposed microphones versus a commercial omnidirectional microphone, both in environments with and without background white noise. The proposed microphones demonstrated reduced susceptibility to background noise particularly in the frequency ranges [1800-2199] Hz and [2200-2599] Hz with

maximum deviation of 2 dB and 2.1 dB, respectively, compared to 9 dB observed in the commercial microphone. The findings of this study have potential implications for improving the accuracy and reliability of respiratory diagnostics in clinical practice.

6.1 Introduction

Tracheal breathing sounds (TBS) have always been beneficial in respiratory assessment, offering non-invasive insights into the functioning of the respiratory system[1–4]. Recorded at the suprasternal notch, TBS are beneficial in diagnosing and screening a range of respiratory conditions, including obstructive sleep apnea (OSA), asthma, and respiratory infections. The quality of TBS signals plays a vital role in the accurate analysis and interpretation of the diagnosis. However, the accuracy of TBS recordings is often compromised by the presence of background noise—encompassing ambient sounds, patient movement, and the interference of other signals such as speech and mouth/nose breathing which can contaminate crucial acoustic details necessary for precise diagnostics. In this paper, we introduce a novel microphone design specifically engineered to capture TBS with exceptional clarity, while effectively minimizing background noise interference.

Previous studies have mostly relied on omni-directional condenser microphones [2,3,5,6]. While effective in capturing sounds from all directions, these devices do not discriminate between TBS and inessential ambient noise. This results in recordings covered with unwanted acoustic signals, requiring sophisticated and computationally expensive post-processing techniques to extract usable diagnostic data. For instance, when recording lung sounds, the use of an air-coupled omnidirectional microphones can result in the desired signal being masked by the ambient breathing sounds captured from the nose or mouth.

The challenge posed by background noise in the recording of TBS has been recognized in clinical practice and research for decades [7]. Efforts to address this issue have included the use of noise-reducing algorithms and advanced signal-processing techniques. However, these methods are time-consuming and can be limited by their complexity and the potential to inadvertently remove clinically relevant sounds along with the noise. Consequently, there remains a substantial need for a more targeted approach to capturing TBS that inherently minimizes capturing unwanted noises at the source.

This study proposes the design of a surface contact microphone designed specifically for the recording of TBS and lung sounds, which incorporates acoustic engineering principles to effectively eliminate the impact of background noise. The new design leverages the use of the piezoelectricity effect to convert the skin displacement due to breathing flow into an electrical signal that could be interpreted as sound.

In summary, the introduction of a noise-eliminating microphone for TBS recording marks a significant advancement in respiratory diagnostics. By addressing the longstanding challenge of background noise in TBS recordings, this technology sets a new standard for the accuracy and reliability of respiratory assessments, potentially transforming both clinical practices and patient outcomes in the field of respiratory care.

6.2 Materials and Methods

6.2.1 Microphone design and performance analysis

Two surface contact microphones were designed for this study with the goal of enhancing the recording quality of tracheal and lung sounds for respiratory screening and diagnosis. The primary focus was to develop microphones capable of detecting tissue displacement caused by

airflow turbulence; thereby, minimizing the capture of environmental noise. The first microphone, designed as cost effective solution, comprises a 20 mm in diameter piezo-electric disc paired with JFET circuit due to its low noise characteristics. The size of the piezo disc was selected to achieve an optimal balance between the sensitivity and practical application. Smaller discs have lower sensitivity due to their limited surface area, while larger discs are usually less comfortable, and dot not fit well at the suprasternal notch, which is the preferred location for TBS recording. A 20 mm disc was determined to be the optimal size. The second design consists of a variable gain amplifier connected to a commercial contact microphone CM-01B. Two tests were performed to evaluate the performance of the microphones against reference microphones.

6.2.1.1 Test 1: Frequency response analysis

The objective of the first test is to compare the microphones' recordings of white noise with those captured by Brüel & Kjær (B&K) surface microphone type 4948-B as a reference microphone. The reference microphone was selected due to its superior performance compared to other surface microphones available in the market. Although its frequency response is well-documented in existing data sheets, conducting the test under identical conditions is crucial to ensure a valid comparison. By controlling all variables—such as the speaker type, anechoic chamber, and microphone positioning—the test isolates the microphones' performance, allowing for a precise evaluation of the new design. The three microphones were placed inside an anechoic chamber at 2 mm distance from a speaker (SP-3114Y Soberton) as shown in Fig. 6-1.

Fig. 6-1: Test 1 setup in the anechoic chamber.

White noise signal in the frequency range of [20-10,000] Hz was generated for a period of 10 sec. The sampling frequency set at 44,100 Hz for all three microphones. The two proposed microphones were connected through TRS jack to a laptop, while B&K microphone was connected to Edirol R-44 audio recorder. The recordings were conducted sequentially to prevent any interference.

6.2.1.2 Test 2: Tracheal and lung sounds recording analysis

A second test was conducted with the purpose of comparing the efficacy of the proposed surface microphones in recording tracheal and lung sounds against Sony ECM-77B omnidirectional microphone. This microphone was being used since it has been employed in previous studies focused on analyzing tracheal breathing sounds [2,5,8,9]. This comparison allows assessing the performance of the proposed surface microphones for their intended application, providing a direct benchmark against a microphone commonly used in similar research. The

specifications of the two proposed microphones and the reference microphones are presented in Table 6-1.

Table 6-1: The specifications of the microphones used for both tests

	Sensitivity (measured at 1 kHz-94 dB SPL)	**Frequency range (Linear)**	**Sensor type (Test involved)**
Piezo-electric microphone	-50 dB (3.2mv/Pa)	[20 - 5000] Hz.	Piezo-electric disc (Tests 1 and 2)
CM-01B	-60 dB (0.9 mv/Pa)	[8 - 2500] Hz.	Piezo-electric (Tests 1 and 2)
Brüel & Kjær type 4948-B	-57 dB (1.4 mv/Pa)	[5-20,000] Hz.	Surface microphone (Test 1)
Sony ECM-77B	-52 dB (2 mv/Pa)	[40-20,000] Hz.	Condenser microphone (Test 2)

Data of six healthy individuals (4 males and 2 females) were included in this test with an average age of 33.6 years and an average BMI of 25.7 kg/m^2. The participants were instructed to take a deep breath from the nose while keeping the mouth closed and hold it for 5 seconds, then exhale. This was then followed by five deep breaths and five tidal breaths which were used for analysis. The microphone in test was placed on the suprasternal notch of each participant for tracheal breathing sounds and on the right side of the chest midclavicular 3rd intercostal space [10] for lung sounds. All participants were sitting in upright position. This test was conducted twice, first in a quiet environment and second with white noise covering a bandwidth of [20-10,000] Hz generated in the background. The frequency range of interest is [100-3000] Hz for TBS and [100-1000] Hz for lung sounds [11]. The sampling frequency for this test was set at 11025 Hz. The subjects' position and microphone placement are illustrated in Fig.6-2.

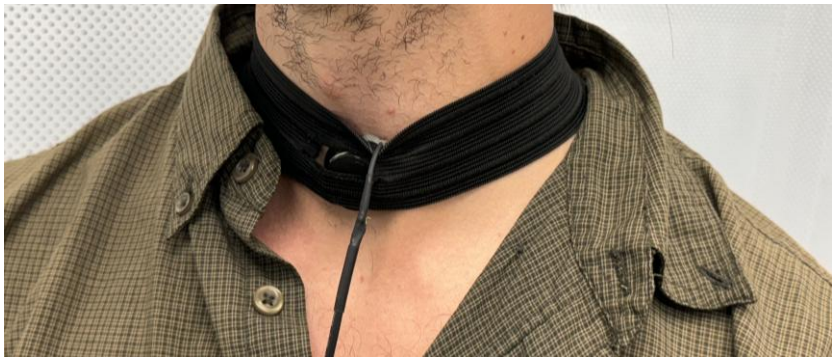

Fig. 6-2: Subject position and microphone placement for Tracheal breathing sounds recording (Test 2).

6.2.2 Pre-Processing and signal analysis

All sound signals were band pass filtered [75-3000] Hz using Butterworth filter of order 4 to reduce the effects of heart beats and 60 Hz harmonics. The sound signals were normalized by its variance and standard deviation and the power spectrum is calculated using Welch method with 10 ms Hanning window size with 50% overlapping between consecutive windows. As for the second test, the central 50% of the time duration around the peak of each respiratory phase was analyzed separately. This duration was selected as the peak of TBS in each phase corresponds roughly to when the breathing airflow plateaus, and the signal can be considered stationary [12]. Each breathing phase was normalized by its variance envelope followed by its standard deviation [13], then segmented using a Hanning window of size 23 ms with 50% overlapping between consecutive segments to calculate the power spectral density (PSD). The average of each breathing phase PSD was then averaged over the number of phases (10 for each respiratory phase). Further details on signal analysis is found in [2]. Moreover, the spectrograms of tracheal and Lung breathing sounds were plotted to visualize the details of the respiratory phases. These visualizations help identify the frequency components impacted by the background noise for each microphone, providing a comparison of their performance in noisy environments. This analysis

aids in understanding how effectively each microphone captures the essential sound signals while minimizing noise interference.

6.2.3 Statistical analysis

A statistical comparison between the two scenarios (without and with background noise) was conducted, denoted by W_1 and W_2, respectively. The PSD was calculated for each respiratory phase as outlined in section 2.2. The frequency range of 200-3000 Hz was divided into seven bands each 400 Hz with no overlap. The average PSD of each respiration phase of each breath in the dB scale was computed for each frequency band. For example, W_1-S_2I_4-F_3 corresponds to the average PSD of the 4th inspiration phase (I_4) of the 2nd participant (S_2) in the 3rd frequency band [800-1200] (F_3) Hz. for the scenario without background noise (W_1). In total, each scenario had 30 data points at each frequency band for each respiratory phase. Since the normality test indicated that the data in most frequency bands did not follow a normal distribution, thus a Wilcoxon test was performed to compare the PSD values between the two scenarios W_1 and W_2 at each frequency band (F_k).

6.3 Results

The average normalized PSD of the microphones' response to white noise signal recordings of the first test is shown in Fig. 6-3. The Brüel & Kjær microphone exhibited a perfect linear response within the tested range of [300-3000] Hz with the smallest RMSE (4.4 dB). This range was chosen because the speaker used in the test has had a linear range starting above 300 Hz, and the upper limit represents the maximum frequency of interest for tracheal breathing sounds. Both the piezo and CM-01B microphones demonstrated an approximately acceptable linear response; however, the piezo microphone showed a lower RMSE (5.8 dB).

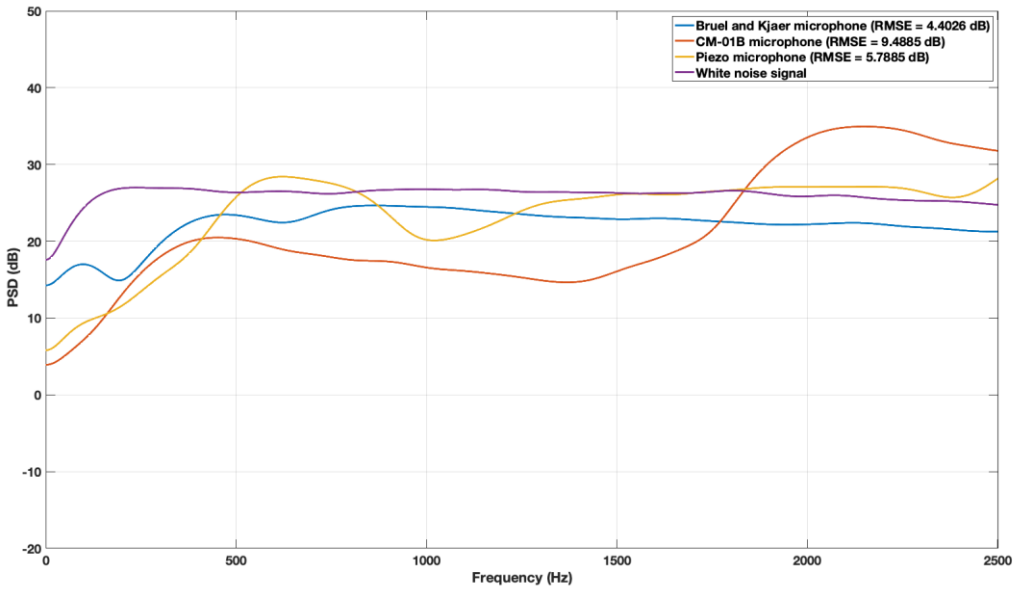

Fig. 6-3: Normalized PSD of the three microphones' (Brüel & Kjær, CM-01B and piezo) recordings of white noise signal (Test 1).

Next, the average normalized PSD of the 6 participants is plotted for each microphone to compare between the frequency response with and without the background white noise. Each respiratory phase is plotted separately. Figure 6-4 shows the effect of the background noise on the Sony microphone for both inspiration and expiration phases. There is a perfect agreement between both scenarios for the low frequency range below 1500 Hz. However, the effect of the background noise is clearly noticeable in the high frequency range (> 1500 Hz.); specially for the inspiration phase with a maximum deviation of 9 dB between W_1 and W_2. Higher amplitudes were observed for scenario W_2; in addition to multiple resonating frequencies were captured by the microphone. This observation is clearly depicted in the spectrogram of a participant' s TBS where the high frequency zone is masked out by the background noise (Fig. 6-5). Furthermore, a good agreement between W_1 and W_2 scenarios can be observed for both CM-01B and piezo microphones with the piezo microphone showing better performance (Figs. 6-7 and 6-9).

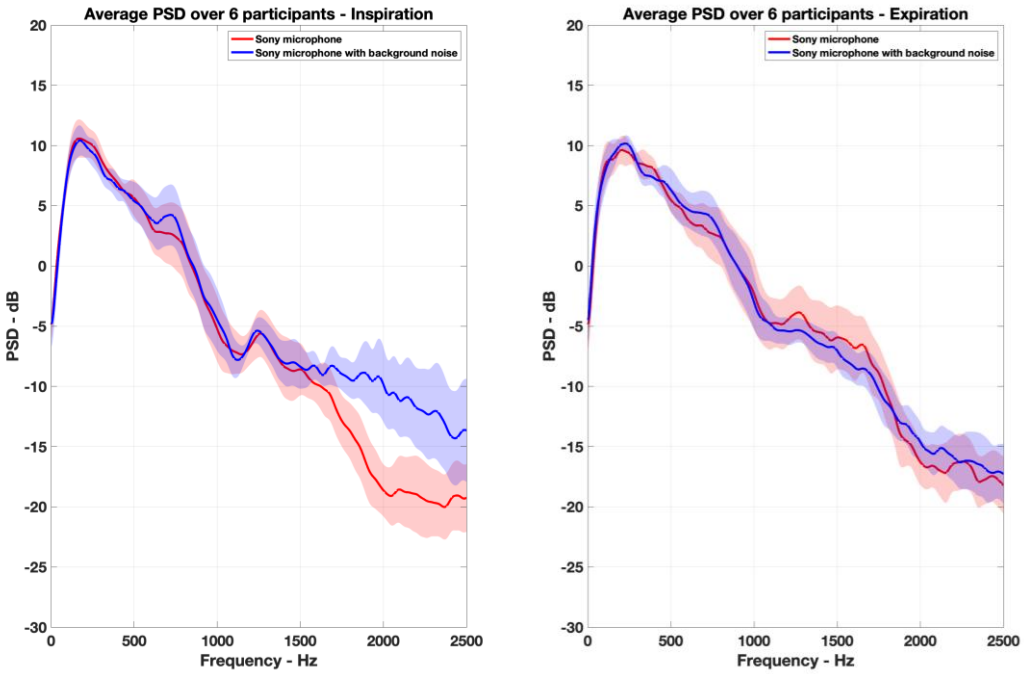

(a) (b)

Fig. 6-4: Average normalized PSD of TBS from 6 participants using Sony microphone. The shaded envelope represents the standard error, reflecting variability between participants. (a) inspiration; (b) expiration.

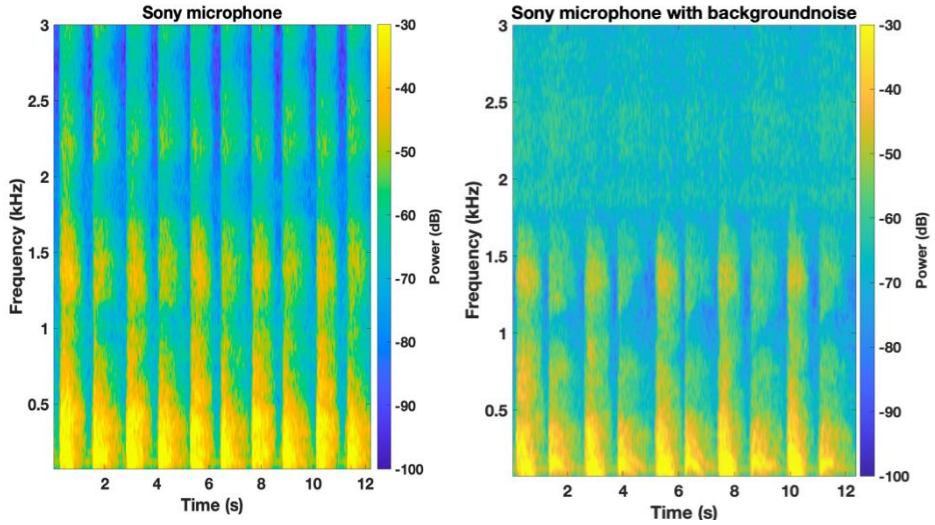

(a) (b)

Fig. 6-5 : Spectrogram of TBS of a participant using Sony microphone: (a) without background noise; (b) with white noise in the background.

Figures 6-6 and 6-7 illustrate the average normalized PSD and spectrograms for the CM-01B microphone. The CM-01B microphone shows a consistent response across both scenarios,

although background noise slightly impacts the high-frequency range during inspiration phases. The maximum deviation was found to be 2.7 dB at 2226 Hz. Figures 6-8 and 6-9 present the results for the piezo microphone. The piezo microphone maintains a strong performance, with the minimum difference (maximum deviation = 2 dB) observed between scenarios W_1 and W_2, indicating its robustness against background noise. Lastly, Fig. 6-10 shows the spectrograms of lung sounds from a participant using the three microphones, providing a visual comparison of their performance with and without background noise. The Sony microphone failed to capture any respiratory phase, while the two proposed microphones, CM-01B and piezo, were clearly able to differentiate the respiratory phases in both scenarios. The piezo microphone demonstrated strong performance with minimal impact from background noise, capturing clear and distinct respiratory sounds. The CM-01B microphone, while showing some susceptibility to movement artifacts, still provided a reliable representation of the lung sounds. These findings highlight the potential of the CM-01B and piezo microphones for accurate respiratory sound measurement in noisy environments.

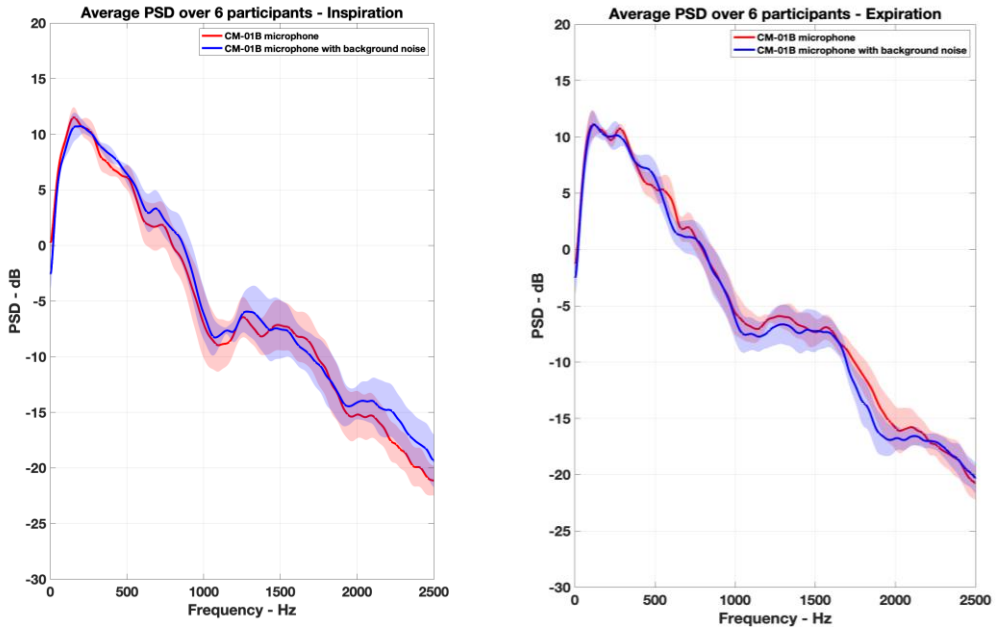

(a) (b)

Fig. 6-6: Average normalized PSD of TBS from 6 participants using CM-01B microphone. The shaded envelope represents the standard error, reflecting variability between participants. (a) inspiration; (b) expiration.

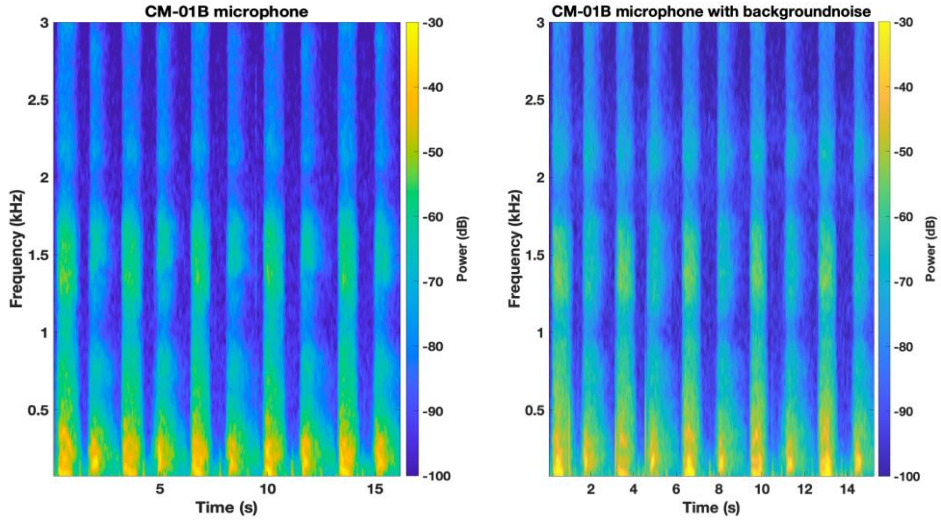

(a) (b)

Fig. 6-7: Spectrogram of TBS of a participant using CM-01B microphone: (a) without background noise; (b) with white noise in the background.

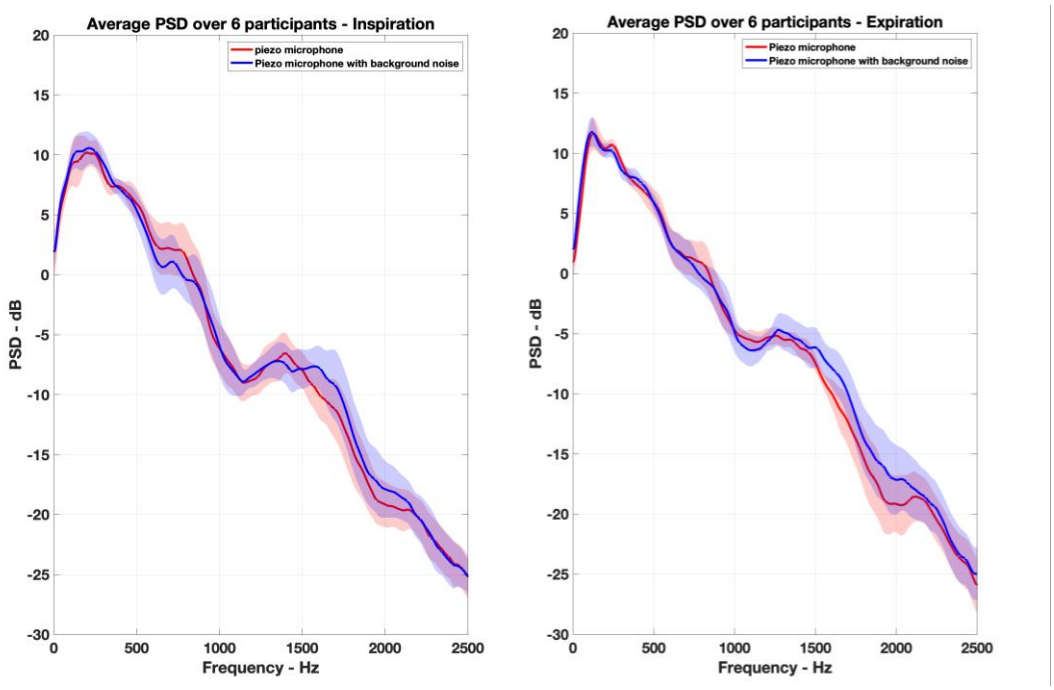

(a) (b)

Fig. 6-8: Average normalized PSD of TBS from 6 participants using Piezo microphone. The shaded envelope represents the standard error, reflecting variability between participants. (a) inspiration; (b) expiration.

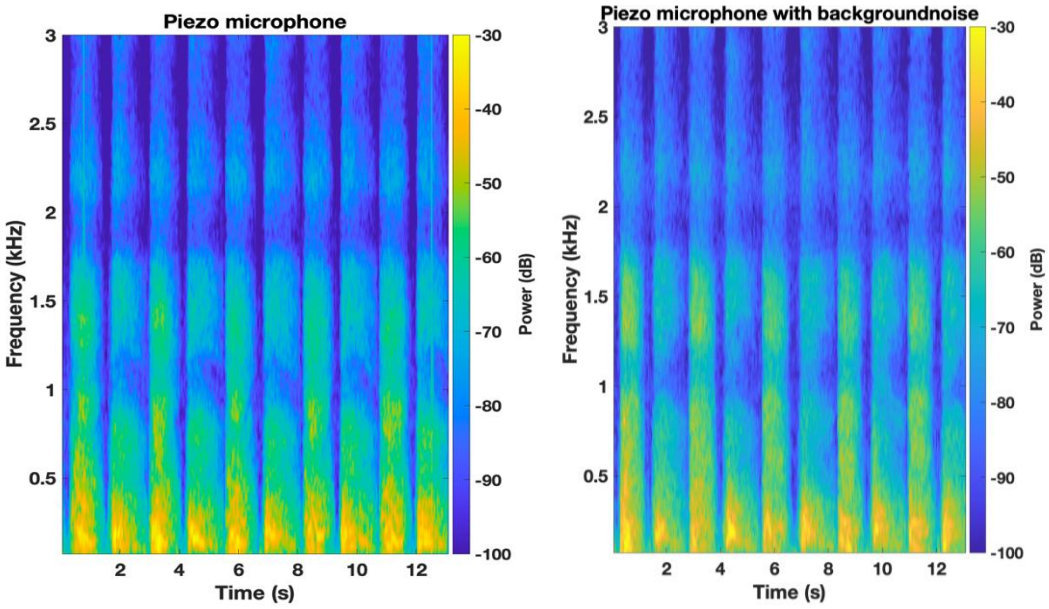

(a) (b)

Fig. 6-9: Spectrogram of TBS of a participant using Piezo microphone: (a) without background noise; (b) with white noise in the background.

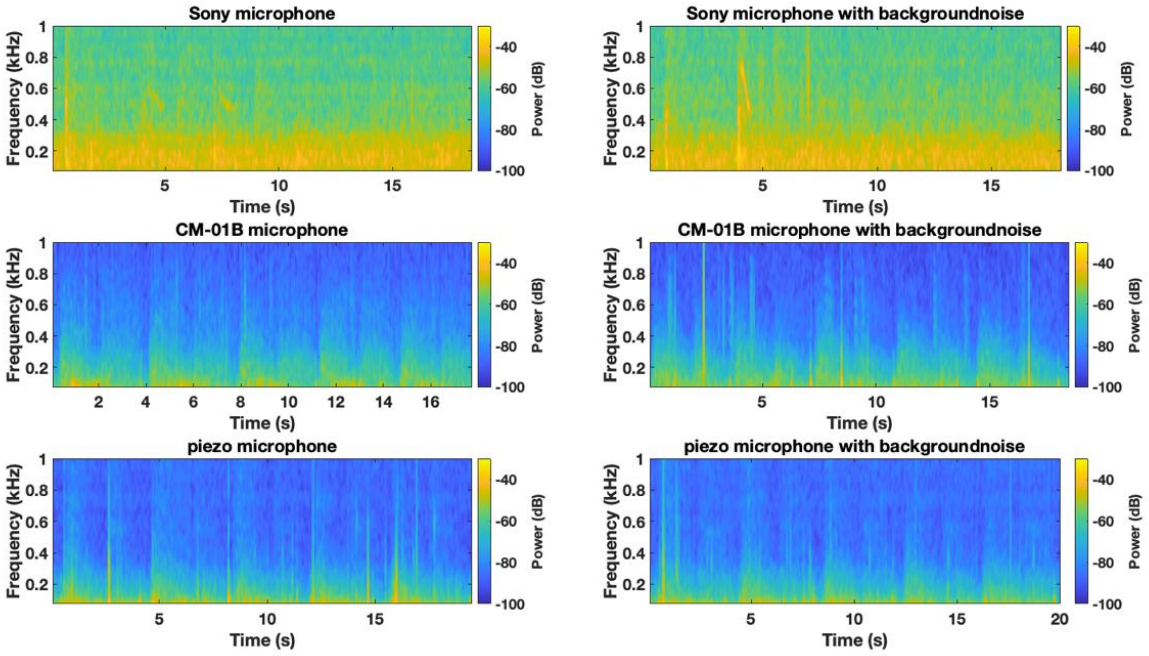

(a) (b)

Fig. 6-10: Spectrogram of lung sounds of a participant using the three microphones (a) without background noise; (b) with white noise in the background; from top to bottom: Sony microphone, CM-01B microphone, Piezo microphone.

Moreover, the results of the statistical Wilcoxon test were in line with the previous findings. Table 6-2 shows the p-value at each frequency range for the inspiration phase, indicating the statistical significance of the differences between the scenarios with and without background noise for each microphone. For the Sony microphone, significant differences were observed in the 1800-2199 Hz and 2200-2599 Hz ranges, with p-values of 0.002 and 0.03, respectively. This indicates that background noise significantly affects the Sony microphone's performance in these frequency ranges.

The CM-01B microphone showed a significant difference in the 2200-2599 Hz range, with a p-value of 0.01, suggesting some susceptibility to background noise at this frequency range during the inspiration phase. The piezo microphone demonstrated no significant differences across all frequency ranges, with p-values well above the threshold for statistical significance. This

further supports the piezo microphone's robustness against background noise. Figure 6-11 illustrates box plots depicting the distribution of data points from two scenarios, W_1 and W_2, across two specific frequency ranges: 1800-2199 Hz and 2200-2599 Hz. The Sony microphone exhibited notably wider interquartile ranges and higher median PSD values in the presence of noise compared to the no-noise scenario across both frequency ranges (1800-2199 Hz and 2200-2599 Hz). This suggests that background noise had a pronounced effect on the measurements captured by the Sony microphone, influencing its ability to accurately detect and differentiate signal strengths in these ranges.

Conversely, the CM-01B microphone showed a mixed result. While there was a significant p-value of less than 0.05 indicating differences between scenarios in one frequency range, the presence of outliers suggests variability or potential noise influence in specific measurements rather than a consistent pattern across both ranges. In contrast, the Piezo microphone did not show a significant difference between the no-noise and noise scenarios, as indicated by p-values greater than 0.05 for both frequency ranges. This suggests that the Piezo microphone's performance in capturing PSD values was less affected by the presence of background noise compared to the other microphones tested.

The statistical results corroborate the earlier observations: the Sony microphone is significantly affected by background noise at higher frequencies, the CM-01B microphone shows moderate susceptibility, mostly due to movement artifacts, and the piezo microphone maintains consistent performance across all tested frequency ranges. These results reinforce the conclusion that the piezo microphone is the most reliable option for capturing respiratory sounds in the presence of background noise.

Table 6-2: Absolute mean PSD difference in dB ± standard deviation (p-value) in each frequency range for inspiration phase.

	200-599 Hz.	**600-999 Hz.**	**1000-1399 Hz.**	**1400-1799 Hz.**	**1800-2199 Hz.**	**2200-2599 Hz.**	**2600-3000 Hz.**
Sony microphone	0.33 ± 1.43 dB (0.67)	0.42 ± 1.74 dB (0.54)	0.46 ± 1.91 dB (0.81)	0.18 ± 3.63 dB (0.68)	4.80 ± 6.82 dB (0.006) *	4.07 ± 6.68 dB (0.03) *	2.80 ± 5.7 dB (0.24)
CM-01B microphone	0.12 ± 1.63 dB (0.69)	1.07 ± 2.15 dB (0.26)	1.03 ± 2.81 dB (0.32)	0.28 ± 2.52 dB (0.82)	1.15 ± 3.42 dB (0.11)	2.81 ± 4.32 dB (0.02) *	1.42 ± 4.50 dB (0.33)
Piezo microphone	0.10 ± 1.19 dB (0.85)	0.81 ± 2.36 dB (0.73)	0.23 ± 2.95 dB (0.78)	0.80 ± 3.20 dB (0.53)	1.5 ± 3.08 dB (0.36)	0.04 ± 2.10 dB (0.71)	0.17 ± 2.19 dB (0.87)

* Statistically significant results ($p<0.05$)

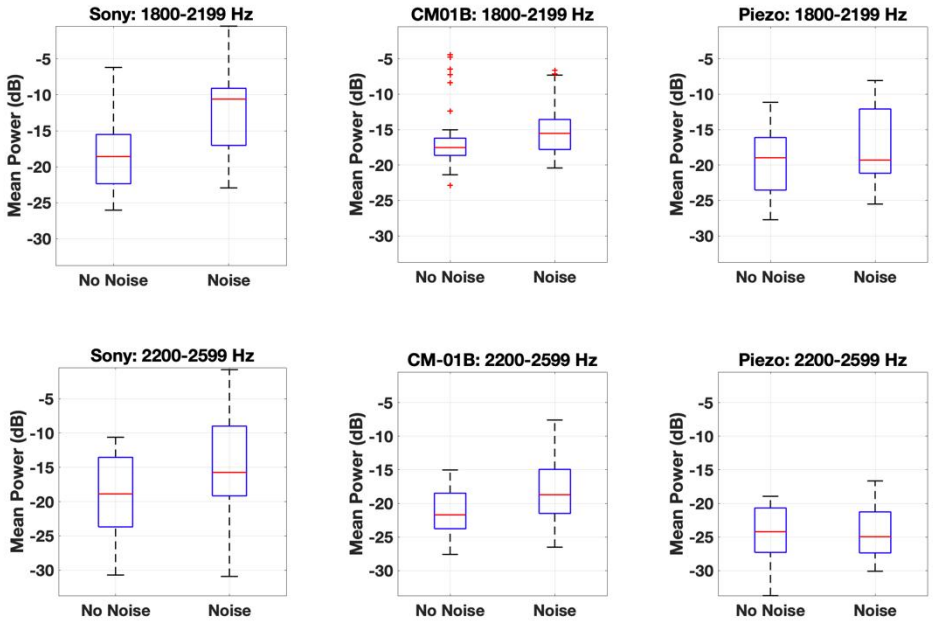

Fig. 6-11: Box plot for the data points of each scenario (W_1 and W_2) at two frequency ranges (top -- 1800-2199 Hz., bottom -- 2200-2599 Hz.) for the three microphones (Left -- Sony microphone, middle -- CM-01B microphone, right – Piezo microphone)

6.4 Discussion

Acoustic measurements are crucial in numerous scientific, industrial, and medical applications, relying heavily on the accuracy and reliability of the microphone's performance. The precision of these measurements is significantly influenced by background noise, which can distort acoustic measurements across various microphone types. Microphones exhibit diverse designs and operational principles, leading to differential sensitivity to noise. Condenser microphones, known

for their high sensitivity and broad frequency response, are commonly utilized in applications requiring detailed acoustic analysis. Condenser microphones have continuously been used in tracheal breathing sounds recordings. Generally, when recording TBS, condenser microphones are placed inside a chamber which is attached to the human skin. Breathing airflow inside the airway produces skin vibration which propagate as sound pressure in the chamber and are subsequently captured by the microphone. This air-coupling mechanism does not prevent the capture of background noise along with the required sound signal. In addition, the accuracy of the recorded sound signal usually depends on the microphone chamber design [14].

On the other hand, piezo-electric microphones operate on a different principle, converting mechanical vibrations into electrical signals. Their insensitivity to airborne noise and their frequency range make it suitable for medical applications such as respiratory sounds.

Previous studies have discussed the use of contact microphones [15–18] and accelerometers [19] for recording respiratory sounds. In this study, we analyzed the performance of a newly designed piezo-electric microphone in recording tracheal and lung breathing sounds. Although the primary focus of the design is on recording tracheal breath sounds (TBS), lung sounds were also analyzed to assess the robustness of the microphone. The proposed microphone showed a flat frequency response with small error difference; in addition to its excellent performance when rejecting background noise. The proposed piezo microphone also offers the advantage of being cost-effective, when used as a diagnostic tool, being 500 times cheaper than B&K type 4948-B microphone and 25 times cheaper than Sony ECM-77B microphone.

A comparison between the proposed microphone and a condenser microphone (Sony ECM-77b) in recording tracheal breathing sounds has been conducted. Empirical studies highlight the sensitivity of condenser microphones like the Sony microphone to background noise. Noise

presence resulted in wider interquartile ranges and higher median PSD values, indicating amplification of both signal and noise components by this type of microphones. However, the proposed microphone maintained consistent performance in noisy environments in all frequency ranges of interest.

The small sample size of this study is a limitation. However, the rigorous data analysis and statistical methods employed mitigate potential biases and provide meaningful insights into the microphone's performance. Future studies with larger sample sizes could further validate these findings. Another limitation involves movement artifacts when using contact microphones. Although contact microphones are designed to detect vibrations directly from the skin, they are still susceptible to noise introduced by body movements or shifts in microphone placement. This is particularly challenging in clinical settings where patients may not remain completely still. Further research in the microphone chamber design and microphone attachment methods should address this issue for improved performance.

6.5 Conclusions

This study reports the design and testing of a piezo-electric microphone in the application of tracheal breathing sounds measurement in comparison with a commercial omni-directional condenser microphone. Overall, the proposed microphones demonstrated a superior performance in recording tracheal and lung breathing sounds in a noisy environment, specifically when capturing high frequency components. The robust noise rejection capabilities of the piezo-electric microphone suggest its potential utility across various medical applications. These findings highlight the potential the proposed microphones in enhancing diagnostic accuracy in respiratory medicine, offering reliable detection of respiratory abnormalities even under challenging acoustic

conditions. Future research should focus on optimizing the microphone's chamber design to minimize movement artifacts, in and further explore its capabilities in clinical settings.

References

1. Sola-Soler J, Fiz JA, Torres A, Jane R. Identification of Obstructive Sleep Apnea patients from tracheal breath sound analysis during wakefulness in polysomnographic studies. 2014 36th Annual International Conference of the IEEE Engineering in Medicine and Biology Society, EMBC 2014. 2014;4232–5.
2. Elwali A, Moussavi Z. Obstructive Sleep Apnea Screening and Airway Structure Characterization During Wakefulness Using Tracheal Breathing Sounds. Ann Biomed Eng. 2017 Mar 1;45(3):839–50.
3. Nakano H, Hayashi M, Ohshima E, Nishikata N, Shinohara T. Validation of a new system of tracheal sound analysis for the diagnosis of sleep apnea-hypopnea syndrome. Sleep. 2004;27(5):951–7.
4. Rauhala E, Hasan J, Kulkas A, Saastamoinen A, Huupponen E, Cameron F, Himanen SL. Compressed tracheal sound analysis in screening of sleep-disordered breathing. Clinical Neurophysiology. 2008;119(9):2037–43.
5. Yadollahi A, Montazeri A, Azarbarzin A, Moussavi Z. Respiratory flow-sound relationship during both wakefulness and sleep and its variation in relation to sleep apnea. Ann Biomed Eng. 2013;41(3):537–46.
6. Kulkas A, Huupponen E, Virkkala J, Tenhunen M, Saastamoinen A, Rauhala E, Himanen SL. New tracheal sound feature for apnoea analysis. Med Biol Eng Comput. 2009;47(4):405–12.

7. Forgacs P, Nathoo AR, Richardson HD. Breath sounds. Vol. 26, Thorax. 1971. 288–295 p.
8. Jin F, Sattar F, Goh DYT. Automatic wheeze detection using histograms of sample entropy. Proceedings of the 30th Annual International Conference of the IEEE Engineering in Medicine and Biology Society, EMBS'08 - "Personalized Healthcare through Technology." 2008;1890–3.
9. Taplidou SA, Hadjileontiadis LJ. Wheeze detection based on time-frequency analysis of breath sounds. Comput Biol Med. 2007;37(8):1073–83.
10. Pourazad MT, Moussavi Z, Thomas G. Heart sound cancellation from lung sound recordings using time-frequency filtering. Med Biol Eng Comput. 2006;44(3):216–25.
11. Pasterkamp H, Kraman SS, Wodicka GR. Respiratory sounds. Advances beyond the stethoscope. Am J Respir Crit Care Med. 1997 Sep;156(3 Pt 1):974–87.
12. Moussavi Z. Anatomy and Physiology of Respiratory System BT - Fundamentals of Respiratory System and Sounds Analysis. In: Moussavi Z, editor. Cham: Springer International Publishing; 2006. p. 1–8. Available from: https://doi.org/10.1007/978-3-031-01617-2_1
13. Gavriely N, Cugell DW. Breath sounds methodology. cRc PrEss; 2019.
14. T. P, A. S. The use of tracheal sounds for the diagnosis of sleep apnoea. Breathe [Internet]. 2017;13(2):e37–45. Available from: http://www.embase.com/search/results?subaction=viewrecord&from=export&id=L617789157%0Ahttp://dx.doi.org/10.1183/20734735.008817
15. Joyashiki T, Wada C. Validation of a body-conducted sound sensor for respiratory sound monitoring and a comparison with several sensors. Sensors (Switzerland). 2020;20(3).

16. Pasterkamp H, Kraman SS, DeFrain PD, Wodicka GR. Measurement of respiratory acoustical signals: Comparison of sensors. Chest. 1993;104(5):1518–25.
17. Kraman SS, Wodicka GR, Pressler GA, Pasterkamp H. Comparison of lung sound transducers using a bioacoustic transducer testing system. J Appl Physiol. 2006;101(2):469–76.
18. Li X, Lee SH, Chae SM, Hwang KH, Cho MJ, Im JJ. Detection and Analysis of Breathing Sounds from Trachea. Proceedings - 2018 11th International Congress on Image and Signal Processing, BioMedical Engineering and Informatics, CISP-BMEI 2018. 2018;1–5.
19. Gupta P, Wen H, Daruwalla A, Moghimi MJ, Ayazi F. Hermetically-Encapsulated Unidirectional Accelerometer Contact Microphone for Wearable Applications. Proceedings of IEEE Sensors. 2019;2019-Octob:1–4.

CHAPTER SEVEN: DEVELOPING AN EMPIRICAL ACOUSTIC TRANSFER FUNCTION MODEL FOR THE UPPER AIRWAY

Walid Ashraf [1], Ali Alqudah[1], Matthew Band[2], Lingyu Zhao[3], Brian Lithgow[1,6,7], Ahmed Elwali[4,5], and Zahra Moussavi[1,5]

[1]Biomedical Engineering Program, University of Manitoba, Winnipeg, Manitoba, Canada
[2] Department of Electrical and Computer Engineering, McGill University, Montreal, Quebec, Canada
[3]Division of Engineering Science, University of Toronto, Toronto, Ontario, Canada
[4] Biomedical Engineering Program, Marian University, Indianapolis, Indiana, USA
[5] Department of Electrical and Computer Engineering, University of Manitoba, Winnipeg, Manitoba, Canada
[6]Monash Alfred Psychiatry Research Center, Prahran Victoria Australia.
[7]Riverview Health Center, University of Manitoba, Winnipeg, Manitoba, Canada

Annals of Biomedical Engineering (2025) (https://doi.org/10.1007/s10439-025-03883-z)

Abstract

Purpose In this pilot study, we introduce a novel approach for the upper airway acoustic modelling aimed at developing a patient-specific transfer function of the upper airway. We modelled the upper airway as an acoustic filter, and hypothesized the parameters of such model would correlate with the anatomical features.

Methods The method involved generating a signal with known frequency characteristics at the mouth while recording the output at the suprasternal notch. Five distinct protocols were tested, and a consistency study was conducted to identify the most suitable protocol. The protocols varied in terms of input sound type and breathing maneuvers. Ten healthy subjects participated in this pilot study over three days with four recordings per day.

Results The results indicated that the most consistent protocol utilizing white noise as the input sound while the participant breathed passively. The standard error of the difference between the detected peak frequencies was less than 10%, and the standard error for the amplitude difference was less than 5 dB. Additionally, the transfer function for each participant was modelled as a cascade of six 2nd order systems. A strong negative correlation of -0.91 ($p = 0.0003$) was found

between the first natural frequency and the participants' height, while a positive correlation of 0.69 ($p = 0.027$) was observed between the transfer function gain and the participants' BMI.

Conclusion This study presents an initial step toward developing an acoustic transfer function of the upper airway, which could ultimately be used to classify and diagnose respiratory disorders.

7.1 Introduction

The upper airway, a vital component of the respiratory system, facilitates airflow during breathing, enables vocalization and conditions the inspired air. Beyond its physiological roles, the upper airway serves as a resonant acoustic conduit, influencing the generation and propagation of respiratory and vocal sounds. These acoustic properties have gained prominence in clinical and research domains due to their potential in the study of phonation, respiratory sound analysis and non-invasive diagnostic tools for airway pathologies [1–5].

Modelling of the upper airway has evolved significantly to integrate engineering and clinical science to better understand the physiological, structural and acoustical aspects of the upper airway. Various modelling approaches have been developed, ranging from simplified one-dimensional (1-D) lumped systems [6–8] to complex 3-D computational models [9–11]. Early acoustic models treated the upper airway as series of interconnected segments, each characterized by electrical parameters such as resistance, compliance, and inertance [6]. While relatively simplistic, these models have effectively predicted breathing sound formants. Furthermore, the advancement in computational power has enabled the development of more sophisticated 3D acoustic models of the upper airway using computational fluid dynamics and finite element analysis [12]. These detailed simulations capture the airflow dynamics, pressure distribution and acoustic wave propagation inside the upper airway.

The airway anatomy and morphology during wakefulness strongly influence several respiratory disorders, including asthma, obstructive sleep apnea (OSA) and chronic obstructive pulmonary disease [13–16]. Thus, in this study we modelled the upper airway as an acoustic filter, and hypothesized the parameters of such model would correlate with the anatomical features. While this preliminary study focuses on healthy individuals, future work will investigate whether these parameters could serve as diagnostic biomarkers when extended to patient populations with respiratory disorders.

As an initial step in the upper airway acoustic modeling, we derived an acoustic transfer function empirically using a known input played through a speaker at the mouth while recording the output at the suprasternal notch. This paper details the testing setup, evaluates the consistency of various protocols and presents the initial transfer function of the upper airway in healthy participants, exploring its statistical significance in relation to demographic data.

7.2 Materials and Methods

7.2.1 Testing setup and Recording Protocol

A speaker (SP-3114Y) was fixed in a 3D-printed chamber (Fig. 7-1). The selection of an appropriate speaker was based on two key factors: the speaker's size and its flat frequency response. The size of the speaker was critical as it needed to fit comfortably within the oral cavity without causing discomfort to the participant. Ensuring a proper fit contributes to measurement repeatability and reducing unwanted variations in acoustic transmission. Additionally**,** the speaker should provide a broadband and a relatively flat frequency response within the frequency band of interest [100-5000] Hz.

The design of the 3D-printed chamber underwent multiple iterations, with the primary objective of minimizing variations between recordings of the same participant. Figure 7-1 illustrates the orthographic projections of the chamber. The design comprised three main components to ensure functionality and stability. The speaker seat was designed to hold the speaker in position within the chamber. The occlusal support functioning as a mandibular stabilizer allowed the participants to bite down to maintain the chamber's position in the mouth during the test. The tongue support served as dual purpose: first to retain the tongue's position beneath the chamber and prevent obstruction of any acoustic waves emitted by the speaker; and second, to reduce motion artifacts caused by tongue movement. During the test, participants were instructed to place the chamber in their mouth and bite onto the four occlusal supports (Fig. 7-2(b)).

A piezo-electric contact microphone was positioned on the suprasternal notch of the participant, while they were seated in an upright position (Fig. 7-2(a)). The suprasternal notch location was selected mainly as the goal was to derive the acoustic transfer function between the upper airway from oropharynx to trachea; in addition, most respiratory research including our team, have recorded respiratory sounds over the suprasternal notch of the trachea [17–19]. The utilized piezo-electric microphone ensures the recorded signal is primarily captured from the trachea with minimal interference from the input signal. Further details on the microphone's design and its performance can be found in [20]. The speaker and microphone were simultaneously connected to a laptop, enabling the simultaneous playback of sounds through the speaker and recording the resulting acoustic signals with the microphone for data collection. Five testing protocols were implemented to evaluate the most consistent methodology for assessing the upper airway's acoustic transfer function. Each protocol combined specific breathing patterns and acoustic signals. Table 7-1 summarizes the testing protocols.

Table 7-1: Testing Protocols

Protocol	Breathing	Sound source type
W1	Shallow breathing followed by 10 sec breath-hold	Broadband white noise in the range 100-5000 Hz for 8 sec
W2	Deep breathing followed by 10 sec breath-hold	
W3	Shallow (passive) breathing	
C1	Deep breathing followed by 10 sec breath-hold	Stepwise Chirp signal ranging from 100 Hz to 5000 Hz with a step frequency of 100 Hz. Each frequency lasts for 0.2 sec, followed by 0.1 sec silent period
C2	Shallow (passive) breathing	

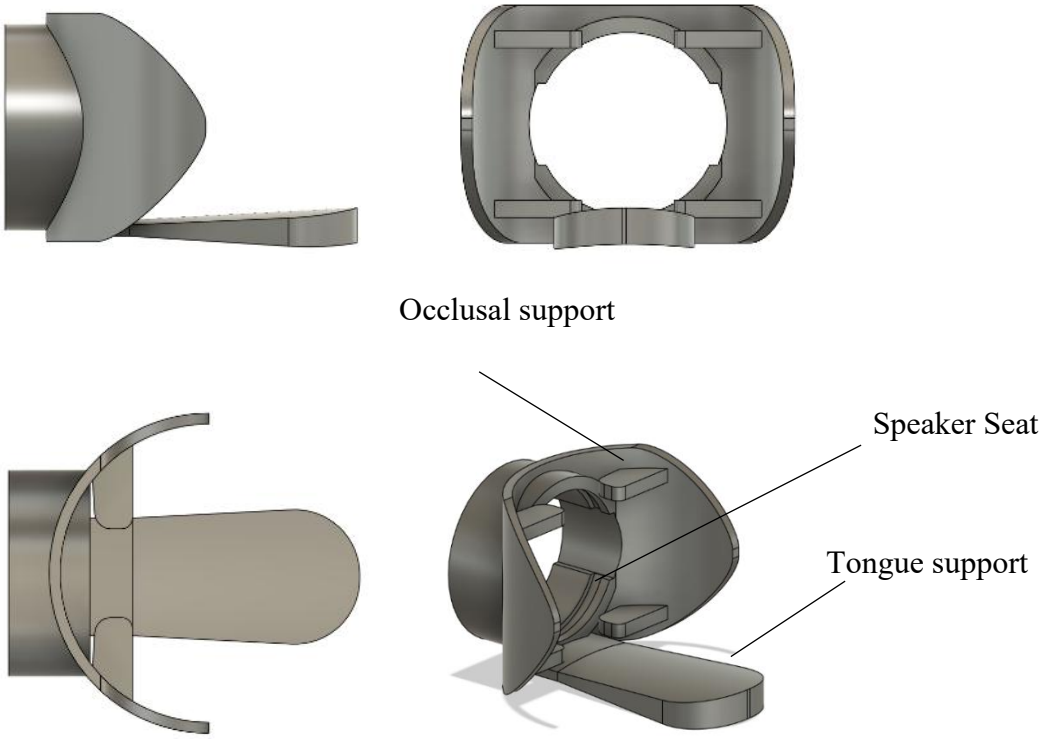

Fig.7-1: CAD model of the speaker chamber---- (top left) Front view, (top right) side view, (bottom left) top view, (bottom right) isometric view

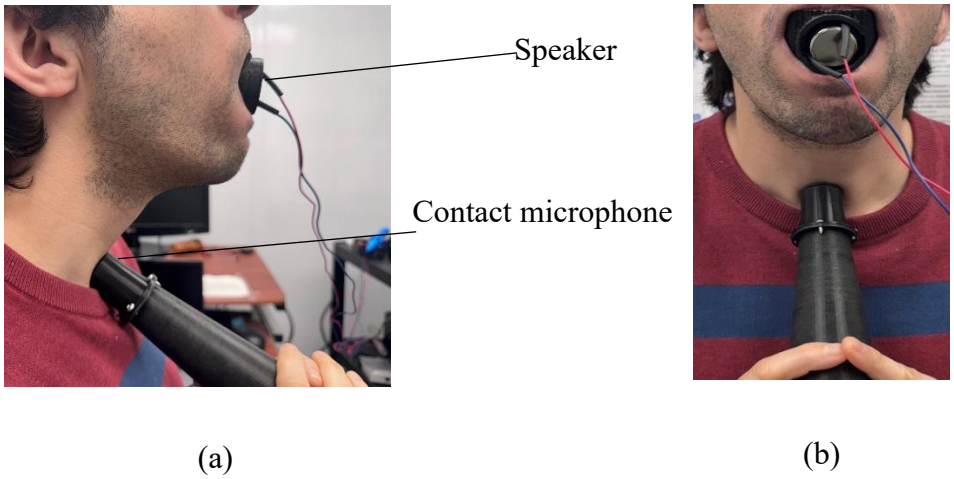

Fig. 7-2: (a) Side view of a participant during the experiment showing the placement of the speaker in the mouth and the contact microphone on the suprasternal notch. (b) Front view of the speaker chamber positioned in the oral cavity and the stabilized microphone placement.

Data were sampled at 10240 Hz. Each protocol was repeated four times to assess the reproducibility of the outcomes; breaks were provided between the four trials to allow participants to rest and to account for external factors, such as variations in microphone placement, in the reproducibility assessment. To further assess reliability, the experiment was conducted over three separate days, resulting in a total of 12 recordings per participant (four recordings per day across three days).

7.2.2 Participants

Ten healthy subjects (5 male), aged between 21 and 33 years, participated in the test. All subjects declared no prior respiratory or sleep disorders. Subjects' Demographics are presented in Table 7-2. The study was approved by Biomedical Research Ethics Board of the University of Manitoba and all participants signed an informed consent prior to the study's experiments.

Table 7-2: Subjects' Demographics

Sex	5M/5F
Age	26.80 ± 4.20
Weight (kg)	76.70 ± 16.22

Height (m)	1.74 ± 0.08
Mallampati Score [21]	3 (I), 3(II), 3(III) and 1(IV)
BMI (kg/m^2)	25.04 ± 4.36
Smoking History [a]	6 (0), 2 (1) and 2 (2)
Neck Circumference (cm)	36.86 ± 3.59
Snorer [b]	8 (0) and 2 (1)

a. Grades 0, 1, and 2 represent nonsmoker, past smoker, and current smoker, respectively.
b. Grades 0 and 1 represent non-snorer and snorer, respectively

7.2.3 Pre-Processing

Due to the different characteristics of the input acoustic signals, the pre-processing stage varies between the five protocols W1, W2, W3, C1 and C2. The response is considered stationary for the white noise signals used in W1, W2, and W3 protocols, while for the chirp signals in C1 and C2, each frequency component is analyzed separately to account for the non-stationary nature of the signal.

7.2.3.1 Broadband white noise input signal (Protocols W1, W2 and W3):

To minimize the transient effects at the start and end of the recording, the middle 3 sec of each 10 sec recording was extracted for analysis. All subsequent processing steps were performed on this extracted segment. Each extracted segment was band-pass filtered [100-5000] Hz using a 4th-order Butterworth band-pass. The frequency-domain representation of each extracted segment was obtained using a Hanning window of size 256 samples (~25 ms) with 50% overlap between the adjacent windows, followed by a Fast Fourier Transform (FFT). The resulting frequency magnitude was normalized by the magnitude of the input signal to compute the transfer function spectrum. The frequency magnitude spectrum was further smoothed to enhance peak detection using a moving average filter with a window size of 300 samples. Peaks were identified in three frequency bands (100-1100 Hz, 1101-2200 Hz, and 2201-5000 Hz) and compared between the

recordings to evaluate the consistency of each protocol within a single day. Additionally, the signals' magnitude for each day was averaged and the corresponding peaks were extracted and compared across the recording days to assess inter-day consistency. Finally, each frequency band's mean power frequency (MPF) was computed using Equation 7-1 for intra-day and inter-day comparison.

$$MPF = \frac{\sum_{i=1}^{N} f_i \times P_i}{\sum_{i=1}^{N} P_i}, \qquad 7\text{-}1$$

where N is the number of frequency points, f_i is the i-th frequency point, P_i is the power corresponding to the i-th frequency point calculated using Welch method.

7.2.3.2 Stepwise Chirp input signal (Protocols C1 and C2):

For the stepwise chirp signals, the time-domain recording signal for each step frequency was analyzed separately. FFT was applied to each segment to obtain the frequency magnitude of the corresponding input frequency, resulting in 50 frequency magnitude points (corresponding to the 50 step frequencies used in the stepwise chirp signal – see Table 7-1). Each frequency magnitude point was normalized by the magnitude of the corresponding input frequency. Peak identification and MPF calculations were performed using the same methodology as in protocols W1, W2, and W3.

7.2.4 Transfer Function Estimation and Evaluation

The standard error of the magnitude and frequency of the detected peaks was calculated for each participant intra-day and inter-day, yielding 90 standard errors intra-day and 30 standard errors inter-day across all peaks and participants for each protocol. The mean and the maximum values of these standard errors were then used as metrics to assess the consistency of each protocol.

To determine the most reliable protocol, intra-day and inter-day variability were evaluated across all recordings. The protocol demonstrating the highest consistency, as indicated by the least standard errors in both magnitude and frequency, was selected for further analysis. The upper airway was modelled as a linear time-invariant (LTI) system. This approximation can be justified for the current setup and measurement conditions. First, linearity was assumed since the excitation signal consisted of low amplitude acoustic energy; thus, avoiding nonlinear responses such as tissue vibration or fluid-structure interactions. Second, time invariance was assumed as the airway geometry does not encounter significant changes during the short recording period, minimizing variability due to dynamic structural or flow alterations. The transfer function was formulated as a cascade of 2nd order systems as expressed in Equation 7-2.

$$H(s) = K \prod_{i=1}^{\frac{N}{2}} \frac{(s^2 + a_i s + b_i)}{(s^2 + c_i s + d_i)}, \qquad 7\text{-}2$$

where s is Laplace variable, K is the overall system gain, a_i and b_i (2nd order numerator coefficients), c_i and d_i (2nd order denominator coefficients), are determined through system identification and (N) is the order of the transfer function. The 2nd order denominator terms correspond to the airway's acoustic natural resonances and damping, while the 2nd order numerator terms reflect anti-resonances, the energy redistribution across the resonance frequencies and the nonlinearities introduced by anatomical variations and boundary interactions within the system. The transfer function was estimated using a system identification approach, where a rational function with a predefined number of poles and zeros was fitted to the frequency response data using Levenberg-Marquardt optimization algorithm [22–24]. The latter, implemented in MATLAB R2024b, is known for its robustness in solving non-linear least squares curve fitting

problems. An iterative process is followed to determine the optimal transfer function order, selecting the lowest order at which the fitting percentage (as in Eq. 7-3) stabilizes with the least variability among participants, indicating convergence of the model to an accurate representation of the system.

$$Fit(\%) = 100 \times \left(1 - \frac{\sum_k |y_{measured}(k) - y_{estimated}(k)|^2}{\sum_k |y_{measured}(k) - \overline{y_{measured}}|^2}\right), \qquad 7\text{-}3$$

where $y_{measured}(k)$ is the experimentally obtained frequency response, $y_{estimated}(k)$ is the estimated transfer function, and $\overline{y_{measured}}$ is the mean of the measured frequency response.

Furthermore, the damping ratio (ζ) and the natural frequency (ω_n) were computed for each pair of poles. A correlation analysis was then performed to investigate potential relationships between these parameters and participant demographics.

7.3 Results

Figure 7-3 presents the average amplitude, normalized by the input, computed over three days, based on four daily recordings, for two participants across all five protocols. The average response remained consistent across protocols for each participant, highlighting a unique response that reflects individual anatomical and physiological characteristics. Notably, a few participants (n=4) exhibited similar responses only in protocols involving similar breathing maneuvers W3 and C2 (passive breathing) and W1-W2-C1 (breath hold); Fig.7-3 (a) shows this pattern for one of those participants. This observation suggests that the physiological changes associated with specific breathing patterns influence the response in certain participants. However, analyzing these variations is beyond the intended scope of this study and will be explored in future research.

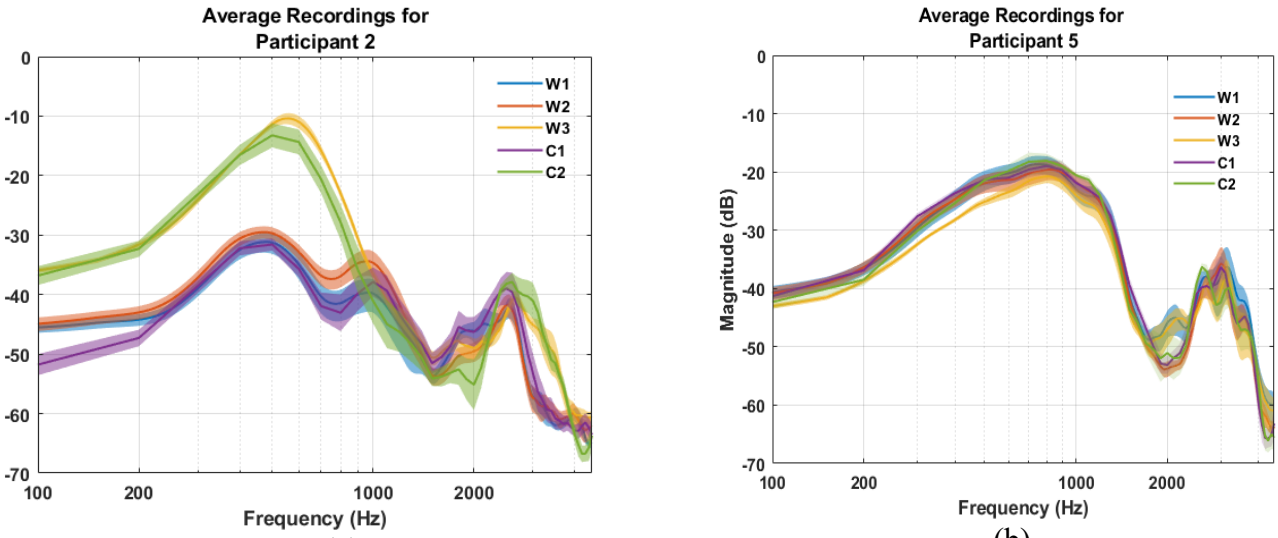

(a) (b)

Fig.7-3 : Average amplitude (in dB) normalized by the magnitude of the input signal of participant 2 (left) and participant 5 (right) over three days for the five protocols, plotted on a logarithmic frequency scale. The shaded area represents 95% confidence interval

7.3.1 Data reproducibility

A consistency analysis determined the most suitable protocol for generating the transfer function. Figure 7-4 displays box plots of the standard errors for peak frequencies, their corresponding amplitudes and the mean power frequency (MPF) across all protocols. Subplots (a-c) present the distributions for all participants, while subplots (d-f) show the same measures stratified by sex, allowing for a comparison of intra-day and inter-day variability between the two groups. Protocols W3 (white noise input with passive breathing) and C2 (chirp signal input with passive breathing) demonstrated the least intra-day variability for the three metrics with <5% for peak frequency, <1 dB for the peak frequency's amplitude and <0.2% in MPF. The inter-day variability was higher likely due to factors such as minor changes in microphone placement, participant posture, and physiological variations across recording sessions; despite that protocols W3 and C2 remained the most consistent, with <10% variation in peak frequency, <7 dB in peak amplitude, and <1% in MPF. This consistency may be attributed to the comfort level of these

protocols, as participants reported greater ease in passive breathing compared to breath-holding. Consequently, Protocol W3 was selected for further analysis and transfer function generation in the frequency domain, and Protocol C2 was used to validate the transfer function in the time domain.

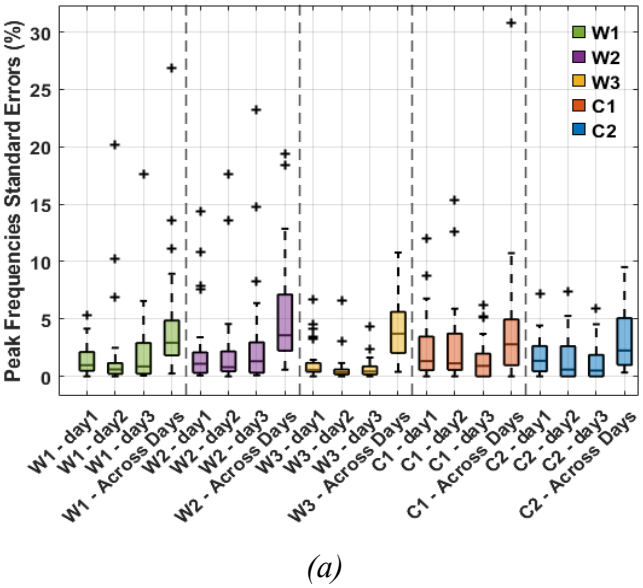

(a)

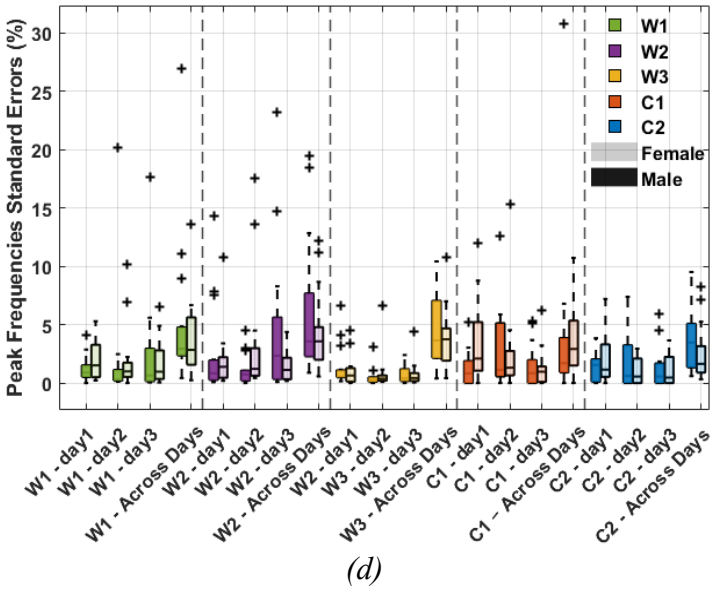

(d)

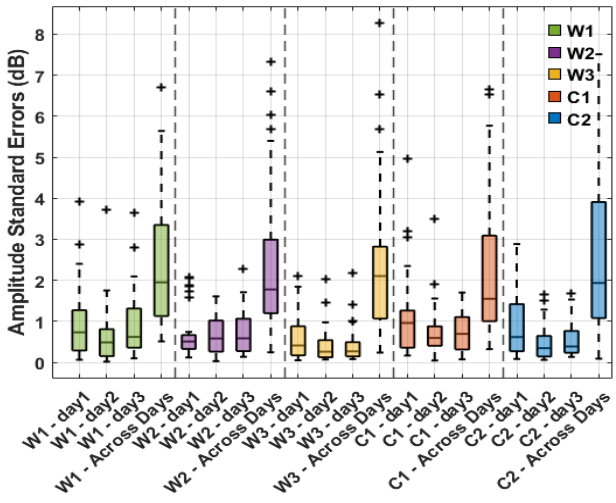

(b)

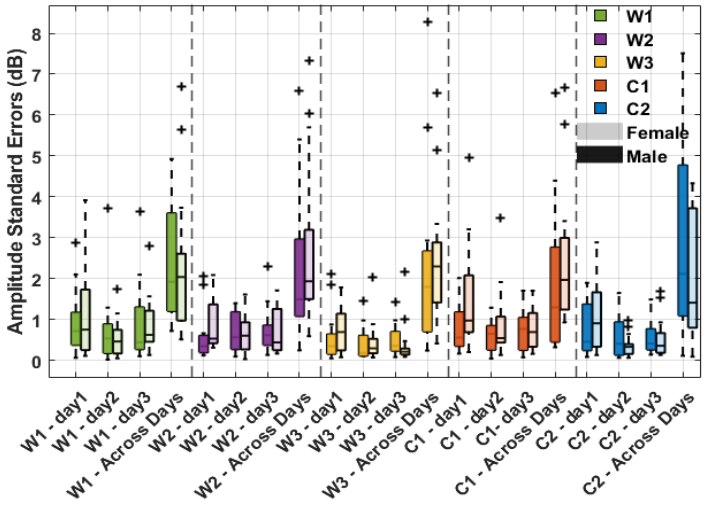

(e)

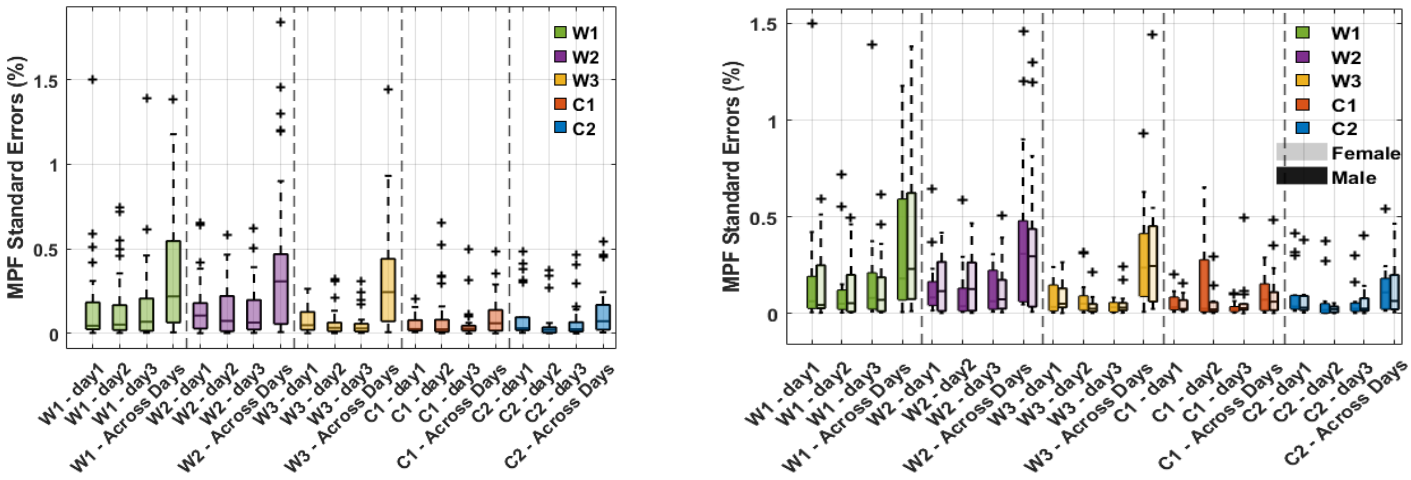

(c) *(f)*

Fig.7-4: Box plots showing intra-day and inter-day standard errors of (a) peak frequencies in three frequency bands (100-1100 Hz, 1101-2200 Hz, and 2201-5000 Hz), expressed as a percentage of the mean detected frequency; (b) amplitude at detected peak frequencies, measured in dB; and (c) mean power frequency (MPF) in the same frequency bands, expressed as a percentage of the mean MPF. Subplots (d), (e), and (f) present the same metrics stratified by sex, with male participants shown in darker bars and female participants in lighter bars of the corresponding protocol color: (d) peak-frequencies standard errors; (e) amplitude standard errors; and (f) MPF standard errors. Across all measures, stratification by sex did not reveal notable differences in error patterns.

7.3.2 Acoustic transfer function estimation

The first step of deriving an acoustic transfer function involves selecting the optimal order (N) of the transfer function, as defined in Eq. 7-2. An iterative process was performed over a range of N values from 4 to 30 for all participants. The selection criterion was based on minimizing the error between the estimated and measured transfer functions while ensuring a balance between model complexity and accuracy. The transfer function was estimated and compared with the measured data for each iteration while the fitting percentage and mean squared error (MSE) were evaluated to determine the best model order. The optimal order (N) was selected by identifying where the fitting percentage reaches a plateau while avoiding overfitting, as indicated by a minimal reduction in MSE with increasing model order. As shown in Fig.7-5, the fitting percentage begins to plateau at N=12, with the least participant-specific fitting percentage recorded at 95.8% with

MSE< e-7. Thus, model order of 12 is selected to construct the transfer function for each participant.

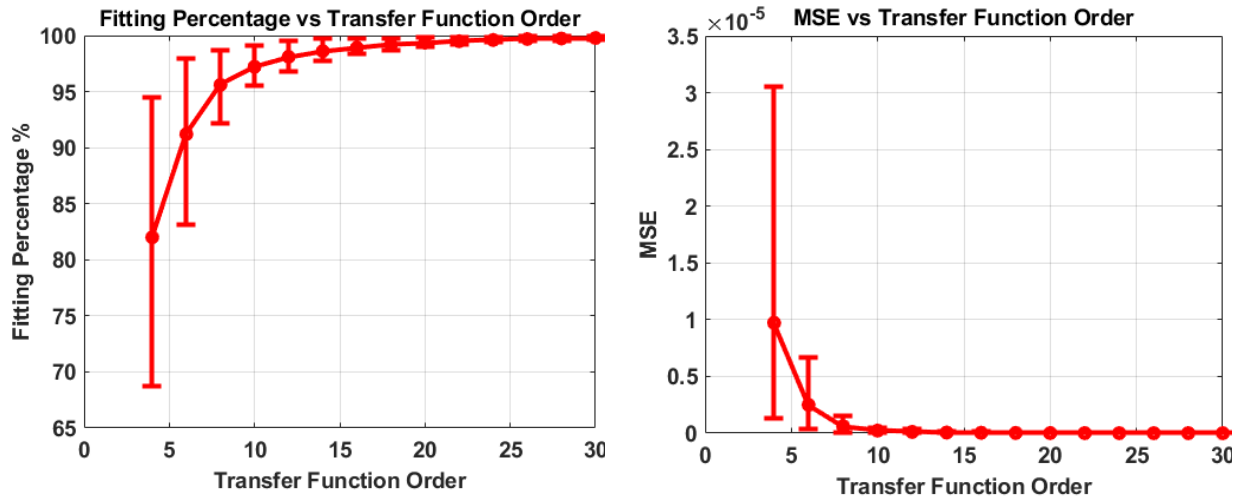

(a) *(b)*

Fig.7-5: (a) Model Fitting percentage Vs number of poles used to determine the transfer function order (N). (b) Mean squared error between the measured and estimated amplitude vs the number of poles. Variability across participants is represented by the error bars.

The second step involved determining the transfer function coefficients for each participant using Levenberg-Marquardt optimization algorithm. A total of 25 coefficients were identified for each participant. Figure 7-6 shows the magnitude Bode plots of the estimated transfer function overlaid on the experimental magnitude of the response for all participants. The close alignment between the estimated and measured responses validates the accuracy of the transfer function model. This transfer function quantifies the patient-specific acoustic characteristics of the upper airway, capturing anatomical and physiological variations unique to each participant.

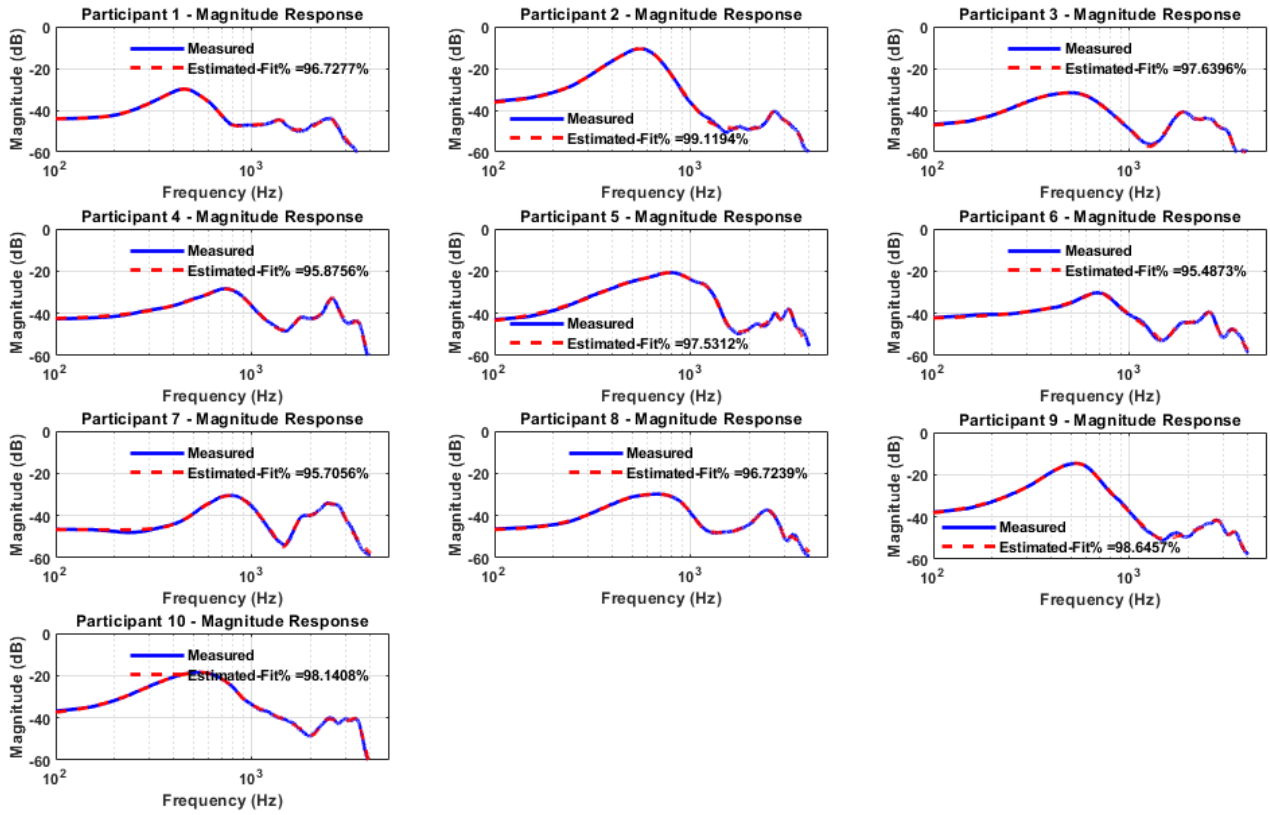

Fig.7-6: Frequency magnitude plots of the estimated transfer function compared with the frequency spectrum of the recorded signals using Protocol W3 for all participants.

Although the model fitting accuracy increased with higher orders, selecting a more complex model beyond N=12 risked overfitting, capturing noise or participant-specific artifacts rather than the general acoustic behavior of the airway. Choosing N=12 provided a balance between capturing spectral detail and avoiding unnecessary complexity. This model order was further validated for robustness in the time domain using a distinct input protocol (Protocol C2) to support the reliability of the selected model order across input types.

Figure 7-7 illustrates the time-domain response of Protocol C2 with the corresponding simulated output of the transfer function for one participant. The fitting percentage, computed using Equation 7-3, was 91.24%, indicating a high level of agreement between the estimated and measured responses. Most discrepancies were observed in the higher frequency input stimulations

in the [1700-3000] Hz range. These deviations could be attributed to several factors, including variations in individual participant responses, system non-linearity, and measurement noise.

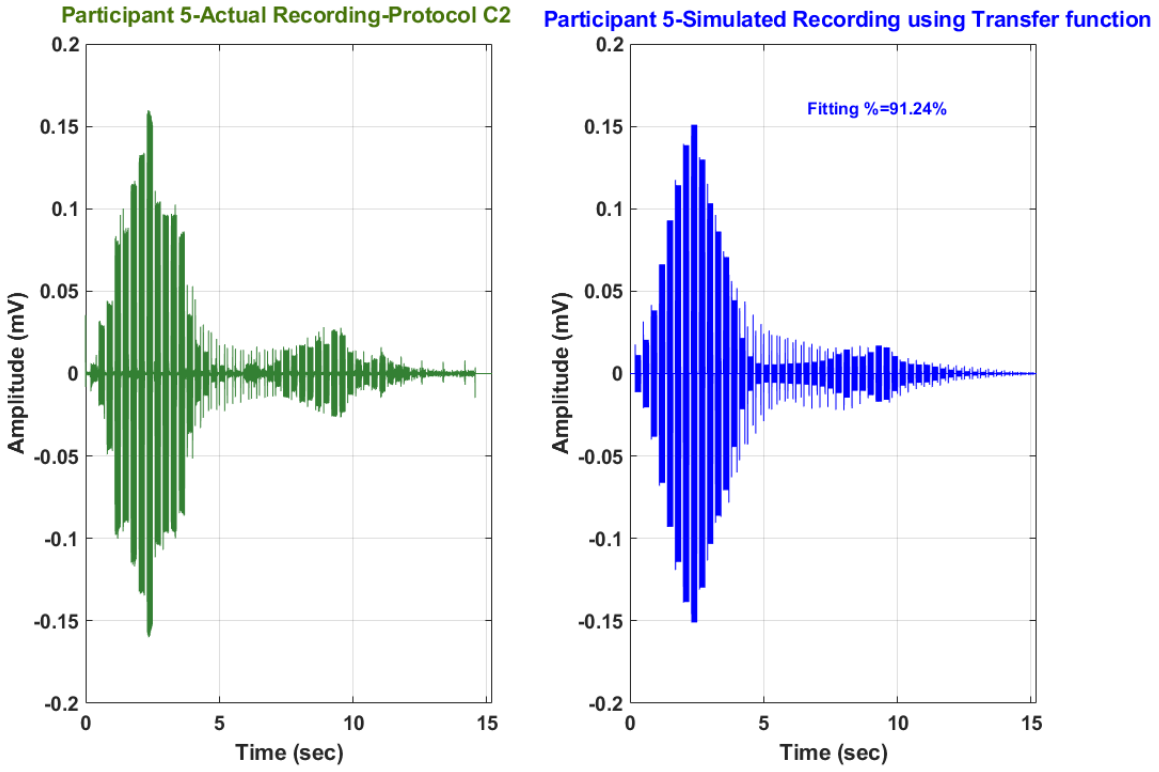

Fig.7-7: Validation of the transfer function for participant 5 using Protocol C2 recording. Left: Experimental recording using Protocol C2. Right: Simulated recording using the estimated transfer function.

7.3.3 Statistical correlation

To investigate the characteristics of the estimated transfer function further, a statistical correlation was carried out between the transfer function parameters, such as the overall system gain, denominator natural frequencies and damping ratios, with the participants' demographics. A Pearson correlation analysis was performed to evaluate the linear relationships between the variables. The significance level was set at 0.05 to determine statistical significance, meaning that correlations with *p*-values below 0.05 were considered statistically significant. This analysis

examined whether physiological attributes, such as body composition and structural differences, influence the estimated transfer function parameters. Scatter plots were generated in Fig.7-8(a-c) to visualize potential relationships between key demographic factors and transfer function parameters.

Height, BMI and neck circumference have been widely reported as key anatomical factors influencing respiratory disorders [25] and airway collapsibility [26]. Given their established relevance, we examined their relationship with the model's parameters. A strong negative correlation (r=-0.91, p-value=0.0003) was observed between the participants' height and the 1st natural frequency. Additionally, a positive correlation (r=0.69, p-value=0.027) was found between the participants' BMI and the transfer function gain (K). Furthermore, a marginally significant correlation (r=0.62, p-value=0.055) was observed between neck circumference and the transfer function gain.

To further assess whether these trends were consistent across sex, separate plots stratified by sex are shown in Fig. 7-8(d-f). While correlation coefficients and p-values were computed, the very small sample size (n=5 per group) limits statistical power; therefore, the plots are presented only for qualitative interpretation. The inverse relationship between height and the 1st natural frequency remained evident in the stratified plots, although it appeared weaker likely due to limited overlap in height between males (all taller) and females (all shorter). In contrast, the positive associations between BMI and gain, and between neck circumference and gain, remained evident within each sex group. These findings suggest that the influence of body composition on model parameters may be robust across sexes, whereas the relationship with height may require a more balanced dataset to be reliably interpreted. Additionally, Fig.7-8(g) shows box plot of the 1st natural frequency against sex. Despite the limited sample size, the difference was visually apparent

and consistent with the overall negative correlation with height, indicating that sex may also be a relevant factor influencing the natural frequency of the system.

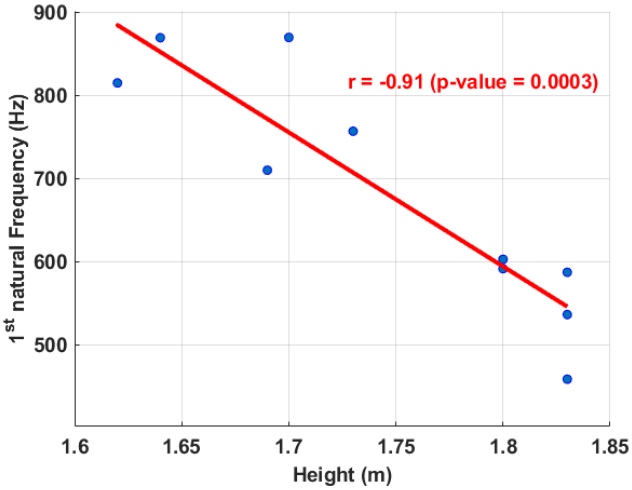

(a)

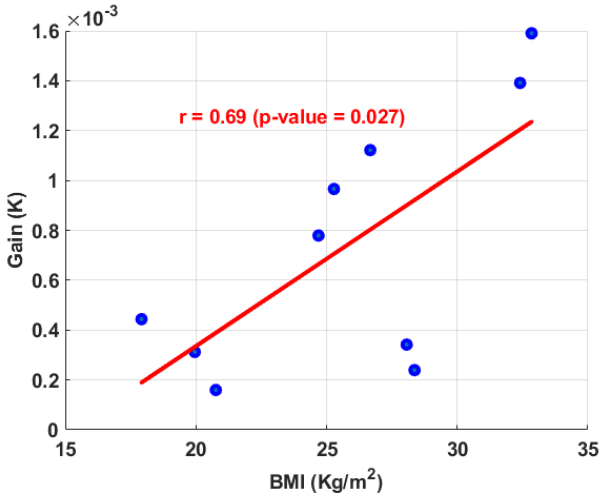

(b)

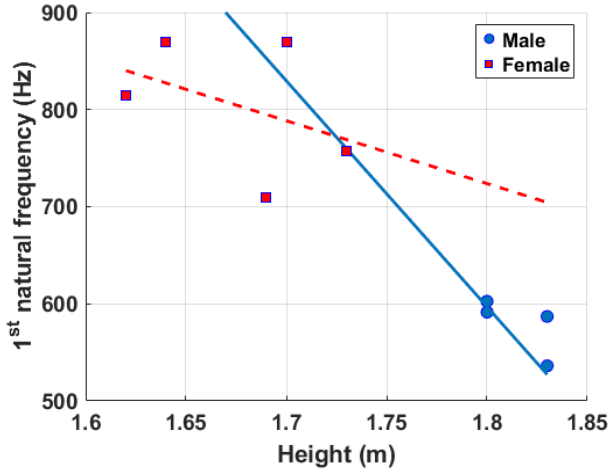

(d)

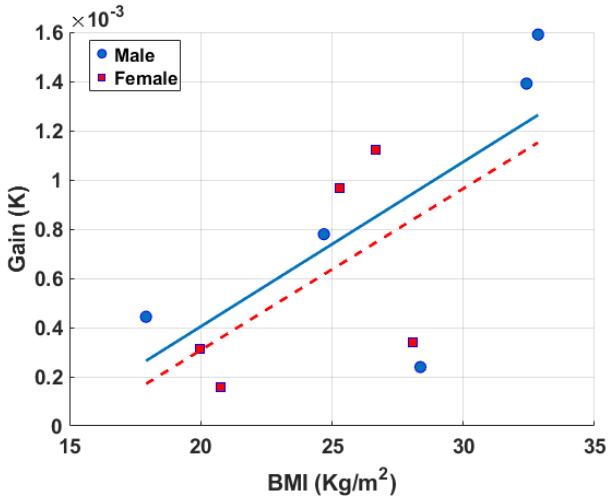

(e)

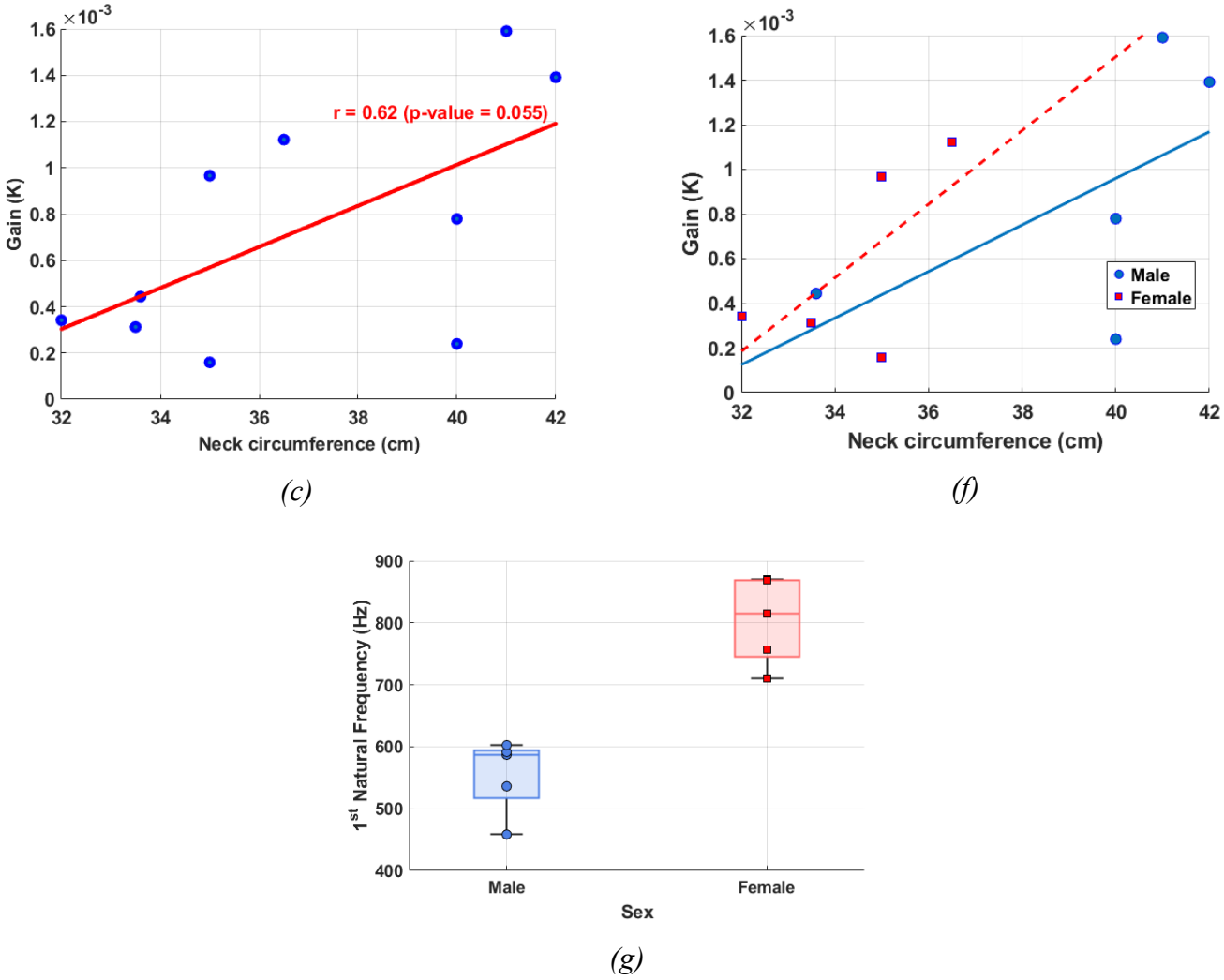

Fig.7-8: Scatter plots illustrating the relationships between demographic variables and key model metrics. Subplots (a–c) show aggregate correlations for all participants with linear regression correlation coefficients (r) and p-values are annotated in red.: (a) height vs. 1st natural frequency (Hz) derived from the transfer function; (b) BMI vs. overall system gain (K) of the transfer function; and (c) neck circumference vs. gain. Subplots (d–f) show the same variables stratified by sex (blue: male, red: female), including individual regression lines for each group: (d) height vs. 1st natural frequency; (e) BMI vs. gain; and (f) neck circumference vs. gain. Subplot (g) displays a box plot of the 1st natural frequency for male and female participants, with overlaid individual data points.

7.4 Discussion

Tracheal sounds have long been recognized as a valuable diagnostic tool for many respiratory disorders offering a non-invasive and cost-effective means of assessing airway health [2, 4, 27]. However, the specific anatomical features responsible for these diagnostic signatures remain insufficiently understood. This study aimed to develop an acoustic transfer function that

characterizes the propagation of sounds within the upper airway, with a potential benefit of linking anatomical variations to spectral features. A key advantage of this approach is its ability to extend the analysis beyond the conventional frequency range of tracheal breathing sounds, which typically spans 100-3000 Hz [1]. The proposed acoustic transfer function enables the detection of airway characteristics at frequencies up to 5000 Hz, allowing for a more detailed investigation of upper airway acoustics.

The protocol used in this study involved playing a white noise in the range of [100-5000] Hz in the oral cavity using a speaker, while simultaneously recording the sound transmitted to the suprasternal notch of the trachea when the participant was breathing passively. Broadband White noise was selected over a chirp signal due to its shorter duration, while still producing a comparable acoustic response. Moreover, white noise provides uniform excitation of the system across the entire frequency bandwidth. To minimize artifacts and sound obstruction from the tongue movement, the speaker's chamber was designed to be equipped with a tongue support. The reliability of this protocol was assessed over three days, demonstrating high consistency in the measured acoustic response. The standard error was limited to 10% of the mean peak frequency detected, with a 5 dB variation in peak amplitude and a 1% deviation in the mean power frequency across three frequency bands. These results confirm the robustness of the methodology, supporting its potential for future clinical applications. To validate the transfer function, a stepwise chirp signal, consisting of 50 step frequencies in [100-5000] Hz frequency range, was used as an alternative input stimulus while maintaining the same breathing pattern.

The estimated transfer function was modeled as a cascade of second-order systems, reflecting the resonant behaviour of the upper airway's different anatomical regions. This modeling approach conceptualizes the upper airway as a series of resonators, where each

anatomical region acts as a filter for a specific frequency zone, influencing the overall spectral characteristics of the sound transmitted through the airway. The final transfer function was estimated for all participants with an overall system order of 12, ensuring a fitting percentage exceeding 95.80% compared to the experimentally recorded response and 91.24% when validated using an independent dataset. This validation strategy was selected to reflect the participant-specific nature of the transfer function. Each model was fitted to an individual's acoustic response under the assumption that the transfer function encodes airway geometry and physiology unique to that participant. Therefore, validating the model with an alternative excitation signal from the same participant ensured that the model captured underlying transfer characteristics rather than simply reproducing the frequency content of a single stimulus. The strong agreement across two different excitation signals supports the robustness of the model to input variation. Nevertheless, validation across independent cohorts is an essential next step to establish inter-subject generalizability, which will be addressed in future studies involving a larger, clinically stratified participant pool. Furthermore, participant-specific differences were noted. For some participants, wider resonances were modeled using multiple second-order systems, indicating that a single resonator was insufficient to fully capture the frequency response at specific resonance peaks. Certain anatomical variations contribute to more distributed or multi-modal resonance patterns. Factors such as airway asymmetry, soft tissue compliance, and varying cross-sectional areas along the airway may lead to frequency-dependent changes in acoustic impedance, causing single resonances to split or broaden. A future study could investigate the correlation of the estimated transfer function parameters with the anatomical variations.

The proposed inverse modelling approach estimates the acoustic transfer function empirically using the black box method. The respiratory tract is seen as a linear time invariant

(LTI) system, a framework commonly used in the estimation of the transfer function of various electrical and mechanical systems [26], [27], as well as physiological systems. Early studies [6, 8] developed acoustic models of the respiratory tract using 1D- lumped-parameter transmission line. These models represented the airway as series of interconnected branching structures represented by an equivalent acoustic circuit. Efforts have been made on developing an acoustic transfer function of the vocal tract, primarily for speech processing applications [28–33]. Several experimental setups have been previously employed. For instance, studies [28, 30, 31] employed excitation of the vocal tract at the level of the thyroid cartilage using a loudspeaker or a mini-shaker, while recording the participant's speech with a microphone placed near the mouth. This setup enabled the extraction of the vocal tract transfer function and formant frequencies during the articulation of different vowels.

In another approach, the study in [33] used a 3D printed, rigid vocal tract model, segmented according to various vowel configurations for the same objective of vocal tract transfer function. Acoustic impedance spectrometry was employed in studies, where a broadband excitation source and a microphone were connected in parallel to the subject's mouth via a horn structure [32, 34]. Additionally, the methodology used in this paper bears conceptual similarity to the forced oscillation technique (FOT), which is commonly used to model the respiratory system mechanics [35]. In FOT, a pneumotachograph and a loudspeaker are used to superimpose small pressure oscillations on the participant's spontaneous breathing, thereby enabling the estimation of respiratory system impedance across a range of frequencies [36, 37]. Although both approaches, as described above, utilize external excitation and system response to derive transfer characteristics, their goals are fundamentally different than the goal in our study. We focus on modeling the upper airway as an acoustic system, where the objective is to capture the frequency-

domain behavior of sound propagation through anatomical structures. In contrast, FOT aims to model the mechanical properties of the lungs and chest wall, quantifying parameters such as resistance, compliance, and inertance.

Compared to previous work on vocal tract transfer function modeling, this study presents several novel contributions. First, the experimental setup proposed is unique. Second, to the best of the authors' knowledge, this is the first study to explore the respiratory system's acoustic transfer function while correlating its parameters with participant demographics. Notably, a strong negative correlation was observed between the first natural frequency and body height, a finding that is consistent with previous studies [38, 39]. The study in [40] reported a significant correlation between tracheal length and body height, indicating that taller individuals tend to have longer tracheas. Given that our research focuses on developing an acoustic transfer function of the upper airway, body height was used as a proxy for tracheal length, as it provides an indirect yet reliable estimate of airway dimensions. Moreover, this finding is supported by the inverse relationship between a tube length and the natural frequencies of the standing wave sound generated inside the tube [41]. However, in this study this effect was most pronounced in the first resonance frequency, suggesting that higher-order resonances may be more influenced by airway shape, cross-sectional variations, and tissue properties than by tracheal length alone. This finding highlights the importance of accounting for height differences when classifying respiratory disorders based on breathing sounds, potentially by establishing height-based subgroups.

Additionally, a positive correlation was observed between the overall system gain and participants' BMI and neck circumference. However, the relationship between BMI and transfer function gain remains controversial, as it can be interpreted differently. One possible explanation is that increased soft tissue mass led to airway narrowing in individuals with higher BMI which

may resulted in greater sound reflection and amplification within the airway. Excess of soft tissue around the upper airway could create acoustic impedance mismatches, causing a portion of the transmitted sound energy to be reflected and reinforced rather than absorbed or dissipated. Conversely, an alternative perspective suggests that increased airway compliance and soft tissue damping in individuals with higher BMI could lead to greater energy dissipation, which would typically be expected to reduce gain. Future research should investigate this relationship using a larger and more diverse sample size to better account for individual variability.

Unlike traditional auscultation or spectral analysis of breathing sounds, this method provides a controlled and repeatable assessment of acoustic properties by introducing a known input signal, thereby minimizing variability caused by spontaneous breathing patterns. Additionally, by utilizing externally generated sound rather than relying on airflow-driven tracheal sounds, the methodology eliminates potential confounding factors such as turbulence-induced noise and individual variations in breathing effort. This controlled approach improves signal-to-noise ratio and ensures a standardized framework for evaluating acoustic features across individuals. These benefits make the acoustic transfer function a promising tool for investigating anatomical and pathological variations in airway structure with greater accuracy and reproducibility.

The main limitation of this study is the small sample size, which may limit the generalizability of the findings. A limited number of participants may not fully capture the range of anatomical and physiological variations that influence the estimated transfer function parameters. Further research with a larger and more diverse cohort, including individuals with respiratory disorders, is necessary to validate the results. Expanding the participant pool would enhance the statistical power of the study and allow for subgroup analyses, such as stratifying

participants by age, BMI, or respiratory health status, to better understand variability in airway acoustics. In addition, future research could benefit from integrating advanced imaging techniques such as MRI or CT scans to directly measure airway structures and validate the physiological assumptions underlying the transfer function model. Another limitation lies in the assumption of linearity. while the upper airway is inherently a complex non-linear biomechanical system, influenced by tissue dynamics and boundary interactions, modeling as LTI system simplified the analysis and facilitates system identification. However, this simplification is considered a preliminary step towards understanding the overall acoustic behavior of the airway.

In conclusion, this study presents a novel method for developing an empirical acoustic transfer function model of the upper airway using controlled input signals and output recordings at the suprasternal notch. The approach used in this study enhances respiratory diagnostics by allowing repeatable assessments of airway acoustics beyond conventional frequency ranges. Results demonstrated high model consistency, with shallow breathing and white noise (Protocol W3) exhibiting minimal variability. A 12th-order cascade system achieved 95.8% fitting accuracy, revealing significant correlations: a negative relationship between the first natural frequency and height ($r = -0.91$) and a positive association between gain and BMI ($r = 0.69$), indicating anatomical influences on acoustic properties. Although the current findings are limited to healthy individuals, this model offers a promising framework for future development of non-invasive tools aimed at personalized respiratory assessment. This work represents an initial step toward patient-specific acoustic diagnostics, with future studies needed to assess its utility in clinical settings.

References

1. Pasterkamp H, Kraman SS, Wodicka GR (1997) Respiratory sounds. Advances beyond the

stethoscope. Am J Respir Crit Care Med 156:974–987. https://doi.org/10.1164/ajrccm.156.3.9701115

2. Penzel T, Sabil A (2017) The use of tracheal sounds for the diagnosis of sleep apnoea. Breathe (Sheffield, England) 13:e37–e45. https://doi.org/10.1183/20734735.008817
3. Yonemaru M, Kikuchi K, Mori M, et al (1993) Detection of tracheal stenosis by frequency analysis of tracheal sounds. J Appl Physiol 75:605–612. https://doi.org/10.1152/jappl.1993.75.2.605
4. Elwali A, Moussavi Z (2017) Obstructive Sleep Apnea Screening and Airway Structure Characterization During Wakefulness Using Tracheal Breathing Sounds. Ann Biomed Eng 45:839–850. https://doi.org/10.1007/s10439-016-1720-5
5. Montazeri A, Giannouli E, Moussavi Z (2012) Assessment of obstructive sleep apnea and its severity during wakefulness. Ann Biomed Eng 40:916–924. https://doi.org/10.1007/s10439-011-0456-5
6. Harper P, Kraman SS, Pasterkamp H, Wodicka GR (2001) An acoustic model of the respiratory tract. IEEE Trans Biomed Eng 48:543–550. https://doi.org/10.1109/10.918593
7. Goldman MD, Nazeran H, Ramos C, et al (2010) Electrical circuit models of the human respiratory system reflect small airway impairment measured by Impulse Oscillation (IOS). 2010 Annu Int Conf IEEE Eng Med Biol Soc EMBC'10 2467–2472. https://doi.org/10.1109/IEMBS.2010.5626611
8. Wodicka GR (1989) Acoustic transmission in the respiratory system. J Acoust Soc Am 86:844–845. https://doi.org/10.1121/1.398217
9. Brouns M, Jayaraju ST, Lacor C, et al (2007) Tracheal stenosis: A flow dynamics study. J Appl Physiol 102:1178–1184. https://doi.org/10.1152/japplphysiol.01063.2006

10. Lin CL, Tawhai MH, McLennan G, Hoffman EA (2007) Characteristics of the turbulent laryngeal jet and its effect on airflow in the human intra-thoracic airways. Respir Physiol Neurobiol 157:295–309. https://doi.org/10.1016/j.resp.2007.02.006

11. Hebbink RHJ, Wessels BJ, Hagmeijer R, Jain K (2023) Computational analysis of human upper airway aerodynamics. Med Biol Eng Comput 61:541–553. https://doi.org/10.1007/s11517-022-02716-8

12. Ashraf W, Jacobson N, Popplewell N, Moussavi Z (2022) Fluid–structure interaction modelling of the upper airway with and without obstructive sleep apnea: a review. Med Biol Eng Comput. https://doi.org/10.1007/s11517-022-02592-2

13. Haponik EF, Smith PL, Bohlman ME, et al (1983) Computerized tomography in obstructive sleep apnea. Correlation of airway size with physiology during sleep and wakefulness. Am Rev Respir Dis 127:221–226. https://doi.org/10.1164/arrd.1983.127.2.221

14. Schwab RJ, Gefter WB, Hoffman EA, et al (1993) Dynamic upper airway imaging during awake respiration in normal subjects and patients with sleep disordered breathing. Am Rev Respir Dis 148:1385–1400. https://doi.org/10.1164/ajrccm/148.5.1385

15. Paré PD, Wiggs BR, James A, et al (1991) The comparative mechanics and morphology of airways in asthma and in chronic obstructive pulmonary disease. Am J Respir Crit Care Med 143:1189–1192. https://doi.org/10.1164/ajrccm/143.5_pt_1.1189

16. Finkelstein Y, Wolf L, Nachmani A, et al (2014) Velopharyngeal anatomy in patients with obstructive sleep apnea versus normal subjects. J Oral Maxillofac Surg 72:1350–1372. https://doi.org/10.1016/j.joms.2013.12.006

17. Lima Junior NA, Oliveira N V., Tavares ABW, et al (2022) Determining airflow

obstruction from tracheal sound analysis: simulated tests and evaluations in patients with acromegaly. Med Biol Eng Comput 60:2001–2014. https://doi.org/10.1007/s11517-022-02584-2

18. Kulkas A, Huupponen E, Virkkala J, et al (2009) New tracheal sound feature for apnoea analysis. Med Biol Eng Comput 47:405–412. https://doi.org/10.1007/s11517-009-0446-z

19. Pramono RXA, Bowyer S, Rodriguez-Villegas E (2017) Automatic adventitious respiratory sound analysis: A systematic review

20. Ashraf W, Moussavi Z (2024) Design and Analysis of a Contact Piezo Microphone for Recording Tracheal Breathing Sounds. Sensors 24:. https://doi.org/10.3390/s24175511

21. Mallampati SR, Gatt SP, Gugino LD, et al (1985) A clinical sign to predict difficult tracheal intubation; a prospective study. Can Anaesth Soc J 32:429–434

22. Gavin HP The Levenberg-Marquardt algorithm for nonlinear least squares curve-fitting problems

23. Levenberg K (1944) A method for the solution of certain non-linear problems in least squares. Q Appl Math 2:164–168

24. Marquardt DW (1963) An algorithm for least-squares estimation of nonlinear parameters. J Soc Ind Appl Math 11:431–441

25. Ho AW, Moul DE, Krishna J (2016) Neck circumference-height ratio as a predictor of sleep related breathing disorder in children and adults. J Clin Sleep Med 12:311–317. https://doi.org/10.5664/jcsm.5572

26. Hutz M, Patel H, Chapman T, et al (2024) 0474 The Impact of Neck Circumference and Body Mass Index on Upper Airway Collapsibility. Sleep 47:A204–A204.

https://doi.org/10.1093/sleep/zsae067.0474

27. Nakano H, Furukawa T, Tanigawa T (2019) Tracheal sound analysis using a deep neural network to detect sleep apnea. J Clin Sleep Med 15:1125–1133. https://doi.org/10.5664/jcsm.7804

28. NGOC Y, Badin P (1994) Vocal tract acoustic transfer function measurements : further developments and applications. http://dx.doi.org/101051/jp4:19945118 04: https://doi.org/10.1051/jp4:19945118

29. Fleischer M, Mainka A, Kürbis S, Birkholz P (2018) How to precisely measure the volume velocity transfer function of physical vocal tract models by external excitation. PLoS One 13:1–16. https://doi.org/10.1371/journal.pone.0193708

30. Djeradi A, Guérin B, Badin P, Perrier P (1991) Measurement of the acoustic transfer function of the vocal tract: a fast and accurate method. J Phon 19:387–395. https://doi.org/10.1016/s0095-4470(19)30330-4

31. Dang J, Honda K (1996) New method for measuring anti-resonance details of the vocal tract transmission characteristics - an experimental study of acoustic tubes. J Acoust Soc Japan (English Transl Nippon Onkyo Gakkaishi) 17:93–99. https://doi.org/10.1250/ast.17.93

32. Epps J, Smith JR, Wolfe J (1997) A novel instrument to measure acoustic resonances of the vocal tract during phonation. Meas Sci Technol 8:1112–1121. https://doi.org/10.1088/0957-0233/8/10/012

33. Kitamura T, Takemoto H, Adachi S, Honda K (2009) Transfer functions of solid vocal-tract models constructed from ATR MRI database of Japanese vowel production. Acoust Sci Technol 30:288–296. https://doi.org/10.1250/ast.30.288

34. Wolfe J, Smith J, Brielbeck G, Stocker F (1994) Real time measurement of acoustic transfer functions and acoustic impedance spectra. In: Australian Acoustical Society Conference. pp 66–72

35. Van de Woestijne KP (1993) The forced oscillation technique in intubated, mechanically-ventilated patients. Eur. Respir. J. 6:767–769

36. Khoo MC (2018) Physiological Control Systems : Analysis, Simulation, and Estimation, 2nd ed. John Wiley & Sons, Piscataway, NJ ;

37. Oostveen E, MacLeod D, Lorino H, et al (2003) The forced oscillation technique in clinical practice: Methodology, recommendations and future developments. Eur Respir J 22:1026–1041. https://doi.org/10.1183/09031936.03.00089403

38. Sanchez I, Pasterkamp H (1993) Tracheal sound spectra depend on body height. Am Rev Respir Dis 148:1083–1087. https://doi.org/10.1164/ajrccm/148.4_Pt_1.1083

39. Kraman SS, Pasterkamp H, Kompis M, et al (1998) Effects of breathing pathways on tracheal sound spectral features. Respir Physiol 111:295–300. https://doi.org/10.1016/S0034-5687(97)00113-8

40. Griscom NT, Wohl ME (1985) Dimensions of the growing trachea related to body height. Length, anteroposterior and transverse diameters, cross-sectional area, and volume in subjects younger than 20 years of age. Am Rev Respir Dis 131:840–844. https://doi.org/10.1164/arrd.1985.131.6.840

41. Blackstock DT (2000) Fundamentals of physical acoustics. John Wiley & Sons

CHAPTER EIGHT: CONCLUSION, LIMITATIONS AND FUTURE WORK

8.1 Summary and Conclusion

OSA is a common respiratory disorder associated with serious complications. The current gold standard for diagnosis, overnight polysomnography (PSG), is costly, time-consuming, and requires specialized facilities, limiting its accessibility. Tracheal breathing sounds (TBS) have demonstrated strong potential as a non-invasive, rapid, and accessible alternative for OSA diagnosis. A key advantage of TBS analysis is that it can be performed during wakefulness, eliminating the need for overnight monitoring and enabling more scalable screening strategies. Therefore, establishing a relationship between upper airway anatomical features and the spectral characteristics of TBS is essential for advancing sound-based diagnostic methods and enhancing clinical insight into the acoustic signatures of airway obstruction. Furthermore, developing a consistent and reliable method for estimating the acoustic transfer function of the upper airway is beneficial for advancing sound-based diagnostic techniques. To address these needs, this dissertation presented two modelling approaches to investigate the aerodynamics and acoustic characteristics of the upper airway with a particular focus on tracheal breathing sounds (TBS), and airway acoustic modelling, and their potential application in the diagnosis of obstructive sleep apnea (OSA) during wakefulness. Both approaches are based on the hypothesis that anatomical differences between OSA and non-OSA individuals are reflected in the spectral content of TBS.

To fulfill the first goal of this dissertation, the first approach utilized a hybrid aero-acoustic simulation framework that decouples the computation of airflow and sound propagation. Using both simplified and anatomically realistic upper airway geometries reconstructed from CT scans,

airflow was simulated using computational fluid dynamics (CFD) under inspiratory conditions, employing steady state Reynolds-Averaged Navier–Stokes (RANS) as an initial stage and transient Large Eddy Simulation (LES) models. This approach was applied to both simplified and anatomically realistic upper airway geometries, the latter reconstructed from high-resolution CT scan of a healthy individual. The simplified tube model served two important purposes: first, it allowed for the initial validation of the simulation framework using a geometry that could be easily 3D-printed and tested experimentally, which allowed to refine the simulation parameters; second, it provided preliminary insights into how airflow rate and constriction size affect the generation and propagation of the measured sounds. Several important findings emerged from this stage of the work. First, it was found that the Wall-Adapting Local Eddy-Viscosity (WALE) subgrid-scale model within LES overestimated sound pressure levels, whereas the Smagorinsky–Lilly model yielded results that aligned more closely with experimental measurements. Second, the experimental frequency response analysis revealed that constriction size directly affected resonance behavior: larger constrictions (i.e., smaller area reductions) resulted in downward shifts in the second and third resonance frequencies. This suggests that localized airway narrowing may alter TBS spectral features, offering a possible explanation for trends observed in previous clinical studies. Third, the logarithmic slope of the relationship between airflow and the squared RMS sound pressure increased with larger constrictions, suggesting further evidence of the sensitivity of TBS to anatomical changes.

For the simulation of realistic airway, several engineering and physiological factors were carefully considered to ensure a realistic representation of inspiratory airflow and upper airway dynamics. The 3D airway geometry was segmented and meshed to resolve at least 80% of the turbulent kinetic energy, with localized mesh refinement implemented near constrictions to capture

high-shear regions. Boundary conditions were selected to replicate a physiological pressure gradient across the airway during inspiration. Lighthill's acoustic analogy was then used to extract aero-acoustic source terms from the flow field, which were subsequently mapped onto a finite element mesh to solve the wave equation for sound propagation. Moreover, impedance boundary conditions were employed in the FEM to realistically represent the interaction of the airway with surrounding tissues and open boundaries. At the inlet (nostrils), infinite elements were applied to simulate an open boundary with minimal reflections, while normalized impedance conditions were applied at the tracheal outlet to approximate sound transmission into the lower airway. Moreover, the use of perfectly rigid, non-absorptive walls in FEM was found to produce unrealistically sharp resonance peaks, indicating unrealistically high acoustic energy retention within the airway. To address this limitation, a normalized impedance boundary condition was applied at the airway walls to represent the partial absorption characteristics of soft tissue. This damping effect reduced the sharpness of resonance peaks and led to a more physiologically realistic frequency response. Importantly, the simulation results were validated against in vivo tracheal breathing sounds recorded from the same participant whose CT scan was used to construct the anatomical model. The comparison of frequency response curves demonstrated good agreement, thereby supporting the validity of the hybrid framework and its capacity to reproduce clinically observable acoustic features. To the best of the author's knowledge, this is the first study to validate an aero-acoustic simulation of breathing sounds using matched in vivo clinical recordings. Given that the simulation framework was validated using both a simplified experimental model and an anatomically accurate subject-specific model, it can be concluded that the framework is robust and suitable for application in the subsequent stages of this research.

The next stage of the study involved a systematic geometric modification of the airway anatomy to investigate how specific anatomical changes influence both the aerodynamic characteristics and the simulated frequency response of the resulting tracheal breathing sounds. Building on the validated simulation framework, a series of anatomically modified airway models were created by altering the geometry at clinically relevant regions, including the velopharynx, oropharynx, and trachea. These modifications were selected based on published clinical and imaging data describing airway morphologies in individuals with obstructive sleep apnea (OSA), and were designed to reflect varying degrees of constriction, elongation, and cross-sectional area reduction. The modifications included velopharyngeal narrowing, oropharyngeal narrowing, tracheal narrowing, airway length elongation, and a combination of these modifications. In addition, a subject-specific upper airway geometry from an individual diagnosed with severe OSA was also simulated to provide a direct comparison with the healthy anatomical model. This stage revealed several important findings. First, the simulated frequency response across all models consistently exhibited four primary resonance zones, approximately located within the ranges of [200–300] Hz, [600–900] Hz, [1000–1700] Hz, and [1700–2500] Hz. These zones align closely with the spectral features frequently reported in clinical and experimental studies on OSA, providing a potential explanation for why these frequency bands are commonly used in TBS-based OSA classification. Among these, the bands between [1000–1700] Hz and [1700–2500] Hz emerged as the most diagnostically relevant, as they were most sensitive to anatomical variations. Specifically, this study found that velopharyngeal narrowing caused a downward shift in resonance frequency within the [1000–1700] Hz range, with the shift being proportional to the severity of the narrowing. In contrast, oropharyngeal narrowing had a dual effect: it caused an upward shift in the resonance frequency within the [1000–1700] Hz band and an additional upward shift in the higher

[1700–2500] Hz band. These observations demonstrate that different anatomical regions contribute distinctly to the shaping of the acoustic response, and that the spectral characteristics of TBS are highly sensitive to the site and degree of airway narrowing. Interestingly, most imaging studies have reported a reduced velopharyngeal or oropharyngeal cross-sectional area in individuals with OSA. This suggests that the acoustic effects observed in response to these anatomical modifications can be meaningfully associated with the pathophysiological features of OSA, thereby reinforcing their relevance to diagnostic applications. The tracheal constriction, although less commonly observed in OSA compared to velopharyngeal or oropharyngeal narrowing, produced the least acoustic impact among the modifications. It resulted in only a slight upward shift in the resonance frequencies within the [1700–2500] Hz band, suggesting a relatively minor influence on the overall spectral profile of TBS. Moreover, airway elongation caused a consistent shift in all major resonance peaks toward lower frequencies. This finding is consistent with fundamental acoustic theory, as increasing the effective length of the airway lowers the natural resonant frequencies of the system. Such a shift resembles the behavior of a longer resonating tube, where the wavelengths of the standing waves are increased, thereby reducing their corresponding frequencies according to equation 8-1

$$f = \frac{c}{4L} \qquad 8\text{-}1$$

where c is the speed of sound, L is the tube length. It is important to note, however, that the human upper airway is a complex, and acoustically lossy system with non-uniform cross-sectional geometry, flow-induced disturbances, and boundary interactions. As such, the relationship between length and frequency is not strictly linear or straightforward. Nonetheless, the general concept remains applicable. This observation has two important implications. First,

since body height is positively correlated with airway length, inter-individual differences in height may partially explain variability in TBS and should be accounted for in future OSA classification models. Second, since previous studies have reported that some individuals with OSA may exhibit elongated upper airways, this finding suggests that airway elongation may contribute to the altered acoustic patterns observed in OSA patients. Another important finding was that the combination of different anatomical modifications produced a spectral response in which the effects of each individual configuration appeared superimposed. Among the configurations tested, velopharyngeal narrowing had the most pronounced impact on the frequency response, followed by oropharyngeal and then tracheal narrowing. This observation is critical, as it demonstrates that although the processes of sound generation and propagation within the airway are inherently non-linear, the overall acoustic response of the system can, to a large extent, be interpreted as a linear superposition of the individual effects of each anatomical modification. this suggests that the complex spectral patterns observed in TBS from OSA patients may be decomposed into constituent features associated with specific anatomical abnormalities. These findings were subsequently applied to compare the simulated frequency response of the subject-specific OSA model with that of the healthy anatomical model. The OSA participant exhibited a longer upper airway, along with narrowing in the velopharyngeal area. The simulated frequency response of the OSA model reflected a combination of the acoustic effects observed individually in the modified healthy models.

Furthermore, it was important to examine the aerodynamic characteristics of the upper airway models to complement the acoustic analysis and better understand the flow sound interactions. In the simulation of the OSA participant, the maximum velocity magnitude (~23 m/s) was observed in the velopharyngeal region, corresponding with elevated wall shear stress and

vorticity magnitude, both indicative of intensified flow disturbances and potential acoustic source regions (dipole and quadrupole). In addition, the coefficient of pressure (C_p) as found to correlate with the percent cross-sectional area reduction in the velopharyngeal constriction models, following a power-law relationship with an exponent of 1.47. Additionally, regional airway resistance was computed across all anatomical configurations. The highest resistance was observed in the oropharyngeal constriction model, followed by the velopharyngeal region, suggesting that these regions impose the greatest aerodynamic load when constricted. Interestingly, models featuring multiple constrictions tended to exhibit reduced resistance per region, likely due to redistribution of flow and pressure along the airway. An exception was observed in the model combining velopharyngeal constriction with airway elongation, which showed elevated airway resistance at the velopharyngeal region, compared with the corresponding single-constriction model. Notably, this geometric configuration was present in the OSA participant's model, reinforcing the physiological relevance of the simulated patterns and highlighting its potential contribution to the altered acoustic and aerodynamic signatures observed in OSA.

The secondary goal of this dissertation was to develop an empirical acoustic transfer function of the upper airway. Unlike TBS, the analyzed signal in this approach is not generated by respiration but rather consists of a controlled input sound transmitted through the airway. Given that upper airway morphology differs between individuals with OSA and healthy controls, it was hypothesized that the transfer function could potentially serve as a diagnostic marker for OSA classification. The primary focus in this dissertation was to establish a consistent and reproducible methodology for reliably estimating the acoustic transfer function and to explore potential correlations between its parameters and participants' demographic characteristics. A pilot study was conducted to assess the feasibility and reproducibility of the proposed method.

Several engineering and experimental factors were carefully considered to ensure accuracy and repeatability. These factors included the speaker's chamber design, the microphone type and the selection of an appropriate excitation signal type. First, the speaker chamber was required to deliver a stable and uniform input signal across the frequency band of interest, [100–5000] Hz, without introducing spectral distortion. For example, a cylindrical chamber geometry would have introduced unwanted resonances that filtered the signal before it reached the airway, thereby altering the measured output. To avoid this, the chamber design presented in Chapter seven was optimized to maintain a flat spectral response within the target frequency range. Second, the microphone was required to accurately capture the signal after it had been filtered by the airway, while minimizing contamination from environmental noise or direct airborne sound from the speaker. This was achieved using a custom-built contact piezoelectric microphone, which recorded vibrations transmitted through the skin at the trachea, thereby eliminating interference from the surrounding acoustic field. The second benefit of the proposed microphone is its suitability for TBS recordings, as its skin-contact design enables recording of low-amplitude respiratory vibrations at the trachea while effectively rejecting environmental noise and airborne breathing sounds originating near the nasal region. Third, the excitation signal was selected to provide sufficient energy distribution across the frequency band of interest, while the breathing maneuver was selected to ensure both participant comfortability and procedural consistency. The selected protocol for acoustic transfer function estimation employed a white noise excitation signal while participants breathed passively. This approach demonstrated strong repeatability, with inter-day and intra-day variability remaining below 10% for peak frequency detection and within 7 dB for amplitude. The acoustic transfer function of the upper airway was then estimated as a cascade of second-order systems, enabling the identification of resonance frequencies, damping

characteristics, and system gain associated with airway morphology. A notable advantage of the acoustic transfer function approach is its extended frequency range. While TBS typically occupy the [100–3000] Hz band, the transfer function can capture spectral information up to 5000 Hz, potentially revealing diagnostic features beyond the range of breathing sounds. Finally, correlations between participants' demographic variables and the extracted transfer function parameters were examined to explore their potential clinical relevance. Height exhibited a strong negative correlation with the first resonance frequency. Although sex was also strongly correlated with the first resonance frequency, this effect is likely attributed to the relationship between sex and height in the study cohort, as all male participants were taller than all female participants. A more demographically diverse sample will be required to determine whether sex exerts an independent effect beyond height. Furthermore, gain showed a positive correlation with both BMI and neck circumference; however, a larger sample size is needed to confirm the robustness and generalizability of these associations.

8.2 Limitations

Each modelling approach presented in this dissertation has certain limitations, which are outlined below. These limitations also highlight opportunities for improvement and will serve as a basis for future research directions discussed in the following section.

8.2.1 Limitations of the aero-acoustic simulation approach

The aero-acoustic simulations conducted in this study employed a one-way coupled flow–acoustic interaction, meaning that while the computed flow field served as the source for acoustic propagation, the reciprocal influence of the acoustic field on the flow was not modelled. This simplification is generally justified for low-Mach-number respiratory flows, where acoustic effect

on the mean flow is negligible. Additionally, the airway walls were assumed to be rigid in the CFD simulations, thereby neglecting tissue deformation and fluid–structure interactions. While this assumption reduces computational complexity, it omits the potential effects of wall compliance, tissue properties and dynamic airway narrowing, which may be particularly relevant in the collapsible segments of the upper airway in OSA. Another limitation is the use of constant pressure boundary conditions, which were employed to model the peak inspiratory flow. While this approach is appropriate for validating TBS, it does not capture the transient flow dynamics that occur during the full respiratory cycle. Finally, the study relied on subject-specific geometries from only two participants, one healthy and one with OSA. While the controlled comparison between systematically modified geometries provided valuable insights, capturing inter-individual variability in airway morphology will require a larger and more diverse participant cohort.

8.2.2 Limitations of the Acoustic Transfer Function Estimation Approach

The pilot study involved a limited number of healthy participants. Although this served as an initial investigation into the feasibility of the approach and the repeatability of the protocol, a larger and more diverse sample would enhance the statistical power and allow for more robust conclusions regarding demographic correlations. Another limitation lies in the absence of OSA participants in this phase, which prevented direct evaluation of the method's diagnostic potential. A future study should include a balanced cohort of both OSA and non-OSA individuals, ensuring diversity in sex, age, body mass index, and neck circumference. This will enable the assessment of the method's clinical classification accuracy.

Finally, the estimation method treated the upper airway as a linear, time-invariant (LTI) system. While this is a reasonable approximation under controlled, passive breathing, the airway is a biological system subject to nonlinearities.

8.3 Future Work

Building on the findings and limitations identified in this dissertation, several directions for future research are proposed for both modelling approaches.

8.3.1 Future work for the aero-acoustic simulation approach

1. One of the most significant advancements would be the implementation of fully coupled fluid–structure–acoustic interaction model. The current study used rigid-wall assumptions, which ignore tissue deformation and wall motion. In reality, upper airway walls, especially in the pharyngeal region, are compliant and undergo dynamic deformation during respiration. Incorporating structural mechanics of the surrounding tissues could enable more accurate predictions of both flow fields and acoustic responses.
2. Incorporating a larger population including a range of OSA severity. A more robust statistical understanding of TBS–anatomy relationships require simulations on a large, anatomically varied cohort derived from high-resolution imaging across age, sex, BMI, and OSA severity categories.
3. While the present study qualitatively and quantitatively assessed how specific anatomical modifications affect the frequency response, a formal mathematical relationship remains to be established. Developing regression that map geometric parameters, such as cross-sectional area and volume ratios, airway length, and constriction location to resonance

frequencies could enable predictive modelling without requiring full CFD-FEM simulations for each case.

4. Development of a parametric model of the upper airway and correlation of model parameters with clinical and demographic variables. A parametric model of the upper airway, representative of its anatomical segments, would allow systematic investigation of how individual anatomical features influence acoustic behavior. These parameters could then be correlated with clinical and demographic variables, and when combined with the proposed mathematical relationship in suggestion 3, may provide a powerful framework for OSA classification.

8.3.2 Future work for Acoustic Transfer Function Estimation Approach

1. Future studies should involve a larger and demographically diverse participant cohort, encompassing a balanced representation of age, sex, BMI, neck circumference, and OSA severity levels.
2. Inclusion of OSA participants across severity grades will be critical for directly assessing the diagnostic potential of this approach. To evaluate the clinical utility of the acoustic transfer function, future work should compare the transfer function parameters between OSA patients and matched healthy controls.
3. Future studies should integrate acoustic transfer function measurements with established clinical airway assessment tools such as the pharyngometer, rhinometer, and rhinomanometer. These devices provide quantitative measurements of airway geometry (e.g., cross-sectional area, segment length) and airflow resistance in both nasal and oral

passages. Combining these datasets would enable direct mapping between the geometric and resistive properties of the airway and the parameters of the acoustic transfer function.

4. Integration with imaging-based anatomical measurements. Combining acoustic transfer function data with imaging data such as MRI or CT could allow direct correlation between specific anatomical features (e.g., airway length, segmental cross-sections) and observed transfer function parameters.
5. Development of a measurement tool incorporating the speaker chamber and microphone fixture. The design should ensure consistent geometry and alignment between the excitation source, and recording location, thereby reducing variability across participants and sessions.
6. Development of an automated procedure with dedicated software. A dedicated software tool should be developed to automate the entire acoustic transfer function estimation process, from signal acquisition and pre-processing to transfer function computation and parameter extraction. Such software would standardize the workflow, minimize errors from the personnel running the test, enable portability for potential use in home-based settings, and enable real-time analysis during data collections. To further enhance usability, the system could be paired with a user-friendly graphical interface to make the approach accessible to both researchers and clinicians, even in non-specialized environments.
7. Machine learning–based classification. Once a sufficiently large dataset is collected, machine learning methods could be trained to classify OSA severity directly from acoustic transfer function parameters, potentially enabling an automated, non-invasive diagnostic tool.

APPENDIX A

A.1 Turbulent Flow Modelling

Turbulence is a complex phenomenon generally described by the presence of swirling vortices which create velocity and pressure fluctuations in the flow. These eddies exist in various length scales which need to be resolved or modelled [1] . Turbulent flow modelling can be classified into three main categories: direct numerical simulation (DNS), Reynolds Averaged Navier Stokes (RANS) and large eddy simulation (LES). The selection of the turbulent flow model depends on the level of resolution required. In DNS, the most detailed approach, all the turbulent length scales are fully resolved requiring the mesh size to be smaller than the size of the smallest length scale. However, DNS requires significant computational resources due to the high spatial and temporal resolution required. On the other hand, RANS describes the turbulence by solving the average flow properties using appropriate turbulence models. RANS is less computationally expensive than DNS, however with lower accuracy. LES lies between RANS and DNS in which the large turbulent scales are resolved while the effect of the smaller scales is modelled. Figure A-1 shows the turbulent kinetic energy spectrum plotted vs the wavenumber corresponding to the eddies' length scale.

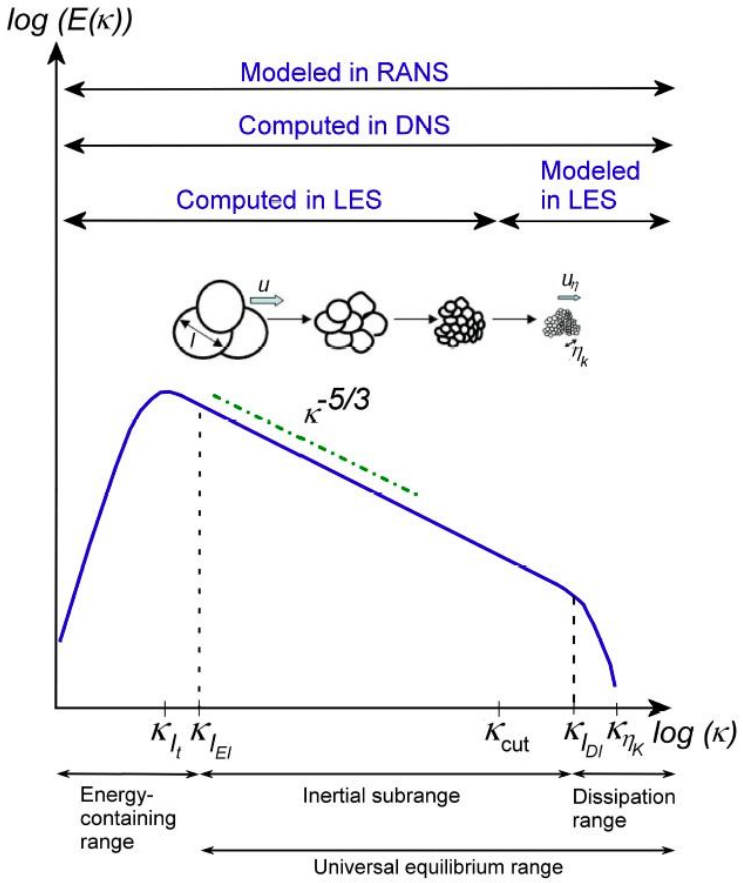

Fig.A-1: Turbulent Kinetic energy cascade [2]

All the turbulence simulation models are based on solving the Navier-Stokes equations, which consist of the conservation of mass and momentum. In this application, the flow inside the upper airway due to breathing is considered as incompressible, while the temperature changes are neglected. Therefore, the governing equations are:

$$\frac{\partial u_i}{\partial x_i} = 0 \qquad \textit{A-1}$$

$$\frac{\partial u_i}{\partial t} + u_j \frac{\partial u_i}{\partial x_j} = -\frac{1}{\rho}\frac{\partial P}{\partial x_i} + \nu \frac{\partial^2 u_i}{\partial x_j \partial x_j} \qquad \textit{A-2}$$

Where, i and j are the cartesian tensor notation, and u, P, t, ρ and ν are the velocity vector, pressure, time, flow density and kinematic viscosity respectively.

A.1.1 Reynolds Averaged Navier Stokes (RANS)

As previously mentioned, a steady state RANS model is only employed as an initial stage to facilitate LES convergence. In RANS, the instantaneous flow variables of the Navier stokes equations is decomposed into a mean value (an ensemble average) and a fluctuating component. For instance, the velocity vector can be decomposed as follows:

$$u(x,t) = \overline{U(x,t)} - u'(x,t) \qquad \textit{A-3}$$

where, $u(x,t)$ is the instantaneous velocity vector, $\overline{U(x,t)}$ is the mean velocity field and $u'(x,t)$ is the fluctuating velocity. After applying the flow variables decomposition in equations 2 and 3, RANS equations are presented in equations A-4 and A-6.

$$\frac{\partial \overline{U}_i}{\partial x_i} = 0 \qquad \textit{A-4}$$

$$\frac{\partial \overline{U}_i}{\partial t} + \overline{U}_j \frac{\partial \overline{U}_i}{\partial x_j} = -\frac{1}{\rho}\frac{\partial P}{\partial x_i} + \frac{\partial}{\partial x_j}\left(\nu \frac{\partial \overline{U}_i}{\partial x_j} - \overline{u'_\iota u'_\jmath}\right) \qquad \textit{A-5}$$

The velocity vector decomposition resulted in the appearance of an additional term $\overline{u'_\iota u'_\jmath}$ namely the Reynolds stresses term. Since the number of unknowns presented in RANS is greater than the number of equations, the Reynolds stresses term requires further modelling known as the closure problem. The common approach used to close RANS equations is to relate the Reynolds stresses term to the mean velocity gradients as in equation A-6 , known as the Boussinesq hypothesis [3].

$$-\overline{u'_\iota u'_\jmath} = \nu_t \left(\frac{\partial \overline{U}_i}{\partial x_j} + \frac{\partial \overline{U}_j}{\partial x_i}\right) - \frac{2}{3} k \delta_{ij} \qquad \textit{A-6}$$

where, ν_t is the isotropic scalar kinematic eddy viscosity, k is the turbulent kinetic energy and δ_{ij} is the Kronecker delta function. Several turbulent models have been developed to compute the eddy viscosity (ν_t). Some examples include Spalart-Allmaras one equation model, $k-\varepsilon$ two equations model, $k-\omega$ two equations model.

The standard $k-\varepsilon$ model is proposed by [4] and consists of two additional transport equations solving for the turbulent kinetic energy k and the turbulence dissipation rate ε, presented in equations A-7 and A-8 respectively.

$$\frac{\partial k}{\partial t}+\frac{\partial k\bar{U}_i}{\partial x_j}=\frac{\partial}{\partial x_j}\left(\frac{\nu_t}{\sigma_k}\frac{\partial k}{\partial x_j}\right)+2\nu_t\left(S_{ij}S_{ij}\right)-\epsilon \qquad A\text{-}7$$

$$\frac{\partial \epsilon}{\partial t}+\frac{\partial \epsilon\bar{U}_i}{\partial x_j}=\frac{\partial}{\partial x_j}\left(\frac{\nu_t}{\sigma_\epsilon}\frac{\partial \epsilon}{\partial x_j}\right)+2C_{1\epsilon}\frac{\epsilon}{k}\nu_t\left(S_{ij}S_{ij}\right)-C_{2\epsilon}\frac{\epsilon^2}{k} \qquad A\text{-}8$$

The eddy viscosity can then be computed using:

$$\nu_t=C_\mu\frac{k^2}{\epsilon} \qquad A\text{-}9$$

where, σ_k , σ_ϵ, $C_{1\epsilon}, C_{2\epsilon}, C_\mu$ are adjustable model constants which are determined empirically based on the type of flow; while S_{ij} is the mean strain rate tensor and is equated as:

$$S_{ij}=\frac{1}{2}\left(\frac{\partial \bar{U}_i}{\partial x_j}+\frac{\partial \bar{U}_j}{\partial x_i}\right) \qquad A\text{-}10$$

The $k-\omega$ model is another two equations model proposed by [5]. The two transport equations solve for the turbulent kinetic energy k and the specific dissipation ω , presented in equations A-11 and A-12, respectively.

$$\frac{\partial k}{\partial t}+\frac{\partial k\bar{U}_i}{\partial x_j}=\frac{\partial}{\partial x_j}\left((\nu+\sigma_k\nu_t)\frac{\partial k}{\partial x_j}\right)+\tau_{ij}\frac{\partial \bar{U}_i}{\partial x_j}-\beta^*\omega k \qquad A\text{-}11$$

$$\frac{\partial \omega}{\partial t} + \frac{\partial \omega \bar{U}_i}{\partial x_j} = \frac{\partial}{\partial x_j}\left((\nu + \sigma_\omega \nu_t)\frac{\partial \omega}{\partial x_j}\right) + \alpha \frac{\omega}{k}\tau_{ij}\frac{\partial \bar{U}_i}{\partial x_j} - \beta\omega^2 \qquad A\text{-}12$$

While the eddy viscosity can be calculated as follows:

$$\nu_t = \alpha^* \frac{k}{\omega} \qquad A\text{-}13$$

Here, τ_{ij} is the mean stress tensor while $\sigma_k$and σ_ω are turbulent Prandtl numbers. Moreover, $\beta^*, \alpha^*, \beta, \alpha$ and σ_d are model constants.

It has been shown by [6] that $k-\omega$ model is superior than $k-\varepsilon$ model in the boundary layer; whereas $k-\omega$ model is strongly sensitive to the boundary conditions specified in the free stream (outside the boundary layer) [7]. Therefore, a new SST $(k-\omega)$ model has been proposed by [7] to switch between $k-\omega$ model and $k-\varepsilon$ model in the boundary layer and free stream respectively. The two specified models' equations were employed and manipulated with the use of a blending function (1-F_1) to perform the switch in the different regions of the flow. The resulting equations are presented as follows:

$$\frac{\partial k}{\partial t} + \frac{\partial k \bar{U}_i}{\partial x_j} = \frac{\partial}{\partial x_j}\left((\nu + \sigma_k \nu_t)\frac{\partial k}{\partial x_j}\right) + \tau_{ij}\frac{\partial \bar{U}_i}{\partial x_j} - \beta^*\omega k \qquad A\text{-}14$$

$$\frac{\partial \omega}{\partial t} + \frac{\partial \omega \bar{U}_i}{\partial x_j} = \frac{\partial}{\partial x_j}\left((\nu + \sigma_\omega \nu_t)\frac{\partial \omega}{\partial x_j}\right) + \alpha \frac{\omega}{k}\tau_{ij}\frac{\partial \bar{U}_i}{\partial x_j} - \beta\omega^2 + 2(1 - F1)\frac{\sigma_{\omega 2}}{\omega}\frac{\partial k}{\partial x_j}\frac{\partial \omega}{\partial x_j} \qquad A\text{-}15$$

While the eddy viscosity can be calculated as:

$$\nu_t = \frac{k}{\omega}\frac{1}{\max\left(\frac{1}{\alpha^*}, \frac{SF_2}{a_1\omega}\right)} \qquad A\text{-}16$$

where $$F_2 = \tanh(\varphi^2) \qquad A\text{-}17$$

and $$\varphi = \max\left(2\frac{\sqrt{k}}{0.09\omega y}, \frac{500\nu}{y^2\omega}\right)$$ *A-18*

where, y is the distance from the next surface and S is the strain rate magnitude. All the model constants are discussed in detail in [7].

For the current study, steady state SST $(k-\omega)$ model is employed, i.e. time rate of the variables in equations A-5, A-13, and A-14 are dropped out, before performing the large eddy simulation (LES) which will be discussed in the following sub-section.

A.1.2 Large Eddy Simulation (LES)

Since RANS is only able to solve for the mean flow variables, it is essential to employ an alternative flow simulation method capable of capturing the pressure and velocity fluctuations for the aero-acoustic simulation. Direct Numerical Simulation (DNS) is one choice; however, DNS is very computationally expensive to the extent that the total computational resources are proportional to Re_t^3, where Re_t is the turbulent Reynolds number. Therefore, LES is the optimal flow simulation method for this application. In LES, since the larger eddies transport most of the momentum, mass and energy, hence it will be directly resolved while the smaller eddies are modeled with the aid of a subgrid scale model [8]. This method will be performed by low pass filtering the flow variables in the Navier Stokes equations presented in equations A-1 and A-2. There are different types of filters most commonly the box filter, the gaussian filter and the sharp spectral filter shown in figure A-2 [9]. An arbitrary filtered flow variable $\bar{\bar{\phi}}(x)$ can then be defined by the convolution of the instantaneous variable and the filter function. It is expressed as:

$$\bar{\bar{\phi}}(x) = \int \phi(x')G(x,x')dx' \qquad \textit{A-19}$$

where, ϕ is the instantaneous unfiltered flow variable, G is the filter function and D is the fluid domain. The filter used in this study is the top-hat filter function which depends on the grid spacing determined by the finite volume discretization.

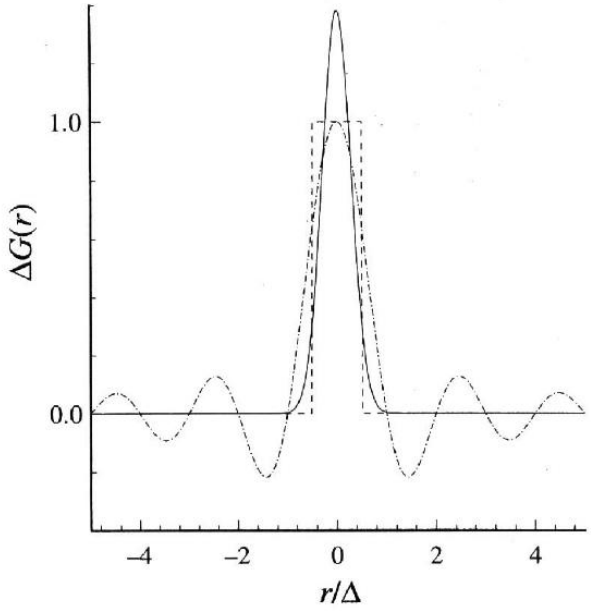

Fig.A-2:Common types of filter G(r): box filter (dashed line) , Gaussian filter (solid line) and sharp spectral filter (dot-dashed line) [9]

The filtered Navier Stokes equations then become:

$$\frac{\partial \bar{\bar{u}}_i}{\partial x_i} = 0 \qquad \textit{A-20}$$

$$\frac{\partial \bar{\bar{u}}_i}{\partial t} + \frac{\partial \overline{\overline{u_\iota u_j}}}{\partial x_j} = -\frac{1}{\rho}\frac{\partial \bar{\bar{p}}}{\partial x_i} + \nu \frac{\partial^2 \bar{\bar{u}}_\iota}{\partial x_j \partial x_j} \qquad \textit{A-21}$$

The residual stress tensor (${\tau_{ij}}^R$)can then be defined as the difference between the term $\overline{\overline{u_\iota u_j}}$ and the product of the filtered velocities $\bar{\bar{u}}_\iota$ $\bar{\bar{u}}_j$ as:

$${\tau_{ij}}^R = \overline{\overline{u_\iota u_j}} - \bar{\bar{u}}_\iota \bar{\bar{u}}_j \qquad \textit{A-22}$$

While the residual kinetic energy can be defined as:

$$k_r = \frac{1}{2}{\tau_{ij}}^{R} \qquad \textit{A-23}$$

and the subgrid scale stress tensor as:

$${\tau_{ij}}^{r} = {\tau_{ij}}^{R} - \frac{2}{3}k_r\delta_{ij} \qquad \textit{A-24}$$

The filtered momentum of the Navier Stokes equation can then be rewritten as:

$$\frac{\partial \bar{\bar{u}}_i}{\partial t} + \frac{\partial\, \bar{\bar{u}}_\iota\, \bar{\bar{u}}_J}{\partial x_j} = -\frac{1}{\rho}\frac{\partial(\bar{\bar{p}} + \frac{2}{3}k_r)}{\partial x_i} + \nu\frac{\partial^2 \bar{\bar{u}}_\iota}{\partial x_j \partial x_j} - \frac{\partial {\tau_{ij}}^{r}}{\partial x_j} \qquad \textit{A-25}$$

It is apparent that equation the filtered equations and unclosed and hence modelling of the subgrid scale stress tensor (${\tau_{ij}}^{r}$) will satisfy the closure problem. There exists several subgrid scale models including Smagorinsky-Lilly, wall adapting local eddy viscosity (WALE), and dynamic kinetic energy. In this study, Smagorinsky-lilly subgrid scale model is employed due to its high performance in wall bounded flow as shown in [10]. Generally, the subgrid scale stress tensor (${\tau_{ij}}^{r}$) is modelled using the linear viscosity model:

$${\tau_{ij}}^{r} = -2\upsilon_r \overline{\overline{S_{\iota J}}} \qquad \textit{A-26}$$

where, υ_r is the eddy viscosity of the residual motions and $\overline{\overline{S_{\iota J}}}$ is the filtered rate of strain. In Smagorinsky-Lilly subgrid model, the eddy viscosity is modelled by:

$$\upsilon_r = {L_S}^2\sqrt{2\overline{\overline{S_{\iota J}}}\;\overline{\overline{S_{\iota J}}}} \qquad \textit{A-27}$$

where, L_S is the mixing length and can be computed using

$$L_S = \min(\kappa d, C_s\Delta) \qquad \textit{A-28}$$

Here, κ is the von kármán constant and is equal to 0.41, d is the distance to closest surface, C_s is the smagorinsky constant and Δ is the filter width i.e. the cubic root of the cell volume for the top-hat filter.

Since LES results will be used in a subsequent aero-acoustic simulation, the selection of the time step size and the number of time steps of the transient flow simulation is then essential for the determination of the upper band acoustic frequency and the frequency resolution. The computation of the upper band frequency and the frequency resolution are presented in equations A-29 and A-30 respectively.

$$f_{max} = \frac{1}{2\Delta t} \qquad \textit{A-29}$$

$$\Delta f_{res} = \frac{1}{\mathrm{N}\Delta t} \qquad \textit{A-30}$$

Where, Δt is the time step size and N is the total number of time steps simulated.

It should be noted that the upper band frequency calculated from LES results should be twice the upper band frequency of interest. This is due to the calculation of the Lighthill aero-acoustic volume source, which will be discussed in the following section. After LES computation, the velocity at each grid point and time step will be extracted for the next aero-acoustic finite element simulation.

A.2 Computational Aero-Acoustics Simulation

Computational aero-acoustics simulation (CAA) is a strong tool which allow in studying and analyzing the generation, propagation and interaction of the sound waves with the aerodynamic flow. Generally, CAA can be performed in two methods: direct method and hybrid method. In direct method, the compressible form of the Navier Stokes equations is solved to

compute the aerodynamic flow and the acoustic pressure perturbations. The direct method is highly accurate in predicting the acoustic results in both near and far field, however it is computationally expensive and similar to DNS it requires large computational resources, which makes it impracticable for most of the engineering applications. The other disadvantage of the direct method is the discrepancy between the flow and the acoustic scales which makes the acoustic results more prone to be masked by the numerical noise. Therefore, a very high spatial and temporal resolution is required.

On the other hand, hybrid methods have better advantages especially for low Mach number flows. Hybrid methods tend to reduce the computational cost by decoupling the acoustic generation (performed with CFD) and the acoustic propagation. The most common hybrid methods used in the literature for the breathing sounds simulation are: Lighthill's analogy, Ffowcs Williams-Hawking's (FW-H) analogy, Curle analogy and the acoustic perturbation equations (APE). For instance, the studies in [11], [12] employed the FW-H analogy, while the study in [13] used APE and in [14] used the Lighthill's analogy. Since FW-H is more suitable for external flow problems and far field acoustic prediction, thus Lighthill's analogy is implemented in this study.

A.2.1 Lighthill's acoustic analogy

Sir Lighthill [15] developed the first acoustic analogy in 1952. Assuming that the feedback from acoustics field to the flow is negligible, Lighthill derived the equations after manipulating Navier Stokes equations with the use of differential operators to set it in the form of an inhomogeneous wave equation as presented in equation A-31. The source term (right hand side term) is the aero-acoustic sound source and can be computed from the flow simulation results. Thus, the source term is separated from the acoustic propagation part (left hand side terms).

$$\frac{1}{c^2}\frac{\partial^2 p'}{\partial t^2} - \frac{\partial^2 p'}{\partial {x_i}^2} = \frac{\partial^2 T_{ij}}{\partial x_i \partial x_j} \qquad A\text{-}31$$

where $$p' = c^2(\rho - \rho_0) \qquad A\text{-}32$$

and c is the speed of sound, p' is the acoustic pressure fluctuations and is defined as $p' = p - p_0$, ρ is the fluid density, T_{ij} is the Lighthill stress tensor and can be defined as:

$$T_{ij} = \rho u_j u_j + (p' + c^2(\rho - \rho_0))\delta_{ij} - \tau_{ij} \qquad A\text{-}33$$

where, $\tau_{ij}$is the viscous stress term.

The Lighthill stress tensor (T_{ij}) consists of 3 terms, the first term($\rho u_j u_j$) is the Reynolds stress term, while the second term $(p' - c^2(\rho - \rho_0))$ is the perturbation part of the entropy [16] and the third term (τ_{ij}) is the dissipative viscous term. Assuming that the viscous losses are negligible, and neglecting the entropy losses (isentropic) for low Reynolds number flows, the Lighthill stress tensor can be simplified to:

$$T_{ij} \approx \rho u_j u_j \qquad A\text{-}34$$

Since the acoustic propagation simulation will be solved in the frequency domain, Lighthill's equation is then re-written in the frequency form after applying the Fourier transformation, as shown in equation A-35.

$$\frac{\omega^2}{c^2}p' - \frac{\partial^2 p'}{\partial {x_i}^2} = \frac{\partial^2 T_{ij}}{\partial x_i \partial x_j} \qquad A\text{-}35$$

Likewise, the Lighthill stress tensor (T_{ij}) should be transformed to the frequency domain before being applied as a source input to equation A-35. the product $u_j u_j$ will then become a convolution, meaning that the spectrum of the source input is twice larger than the spectrum of [17]. This condition should be considered during the selection of the time step size (Δt) of the fluid flow simulation and the computation of the upper band frequency. Equation A-29 then becomes:

$$f_{max} = \frac{1}{4\Delta t} \qquad A\text{-}36$$

References

[1] L. Tay-Wo-Chong, "Numerical Simulation of the Dynamics of Turbulent Swirling Flames," *Diss. TUM*, 2012.

[2] P. Sagaut, S. Deck, and M. Terracol, *Multiscale and multiresolution approaches in turbulence (second edition)*. 2013.

[3] J. O. Hinze, *Turbulence*. in McGraw-Hill classic textbook reissue. McGraw-Hill, 1975. [Online]. Available: https://books.google.ca/books?id=DfRQAAAAMAAJ

[4] B. E. (Brian E. Launder, *Lectures in mathematical models of turbulence [by] B. E. Launder and D. B. Spalding*. London, New York: Academic Press, 1972.

[5] D. C. Wilcox, *Turbulence modeling for CFD*, vol. 2. DCW industries La Canada, CA, 1998.

[6] D. C. Wilcox, "Reassessment of the scale-determining equation for advanced turbulence models," *AIAA J.*, vol. 26, no. 11, pp. 1299–1310, 1988, doi: 10.2514/3.10041.

[7] F. R. Menter, "Two-equation eddy-viscosity turbulence models for engineering applications," *AIAA J.*, vol. 32, no. 8, pp. 1598–1605, 1994, doi: 10.2514/3.12149.

[8] S. B. Pope, "Ten questions concerning the large-eddy simulation of turbulent flows," *New J. Phys.*, vol. 6, pp. 0–24, 2004, doi: 10.1088/1367-2630/6/1/035.

[9] S. B. Pope, *Turbulent Flows*. Cambridge: Cambridge University Press, 2000. doi: DOI: 10.1017/CBO9780511840531.

[10] G. J. Page, "Multiscale and Multiresolution Approaches in Turbulence. By Pierre Sagaut, Sebastian Deck & Marc Terracol. Imperial College Press, 2006. 356 pp. ISBN-10: 186094650X, ISBN-13: 978-1860946509, £78.00.," *J. Fluid Mech.*, vol. 646, pp. 537–538,

2010, doi: DOI: 10.1017/S0022112009993314.

[11] W. C. P. van der Velden, A. H. van Zuijlen, A. T. de Jong, C. T. Lynch, L. J. Hoeve, and H. Bijl, "Acoustic simulation of a patient's obstructed airway," *Comput. Methods Biomech. Biomed. Engin.*, vol. 19, no. 2, pp. 144–158, Jan. 2016, doi: 10.1080/10255842.2014.996877.

[12] J. Xi, X. Si, J. Kim, G. Su, and H. Dong, "Modeling the pharyngeal anatomical effects on breathing resistance and aerodynamically generated sound," *Med. Biol. Eng. Comput.*, vol. 52, no. 7, pp. 567–577, 2014, doi: 10.1007/s11517-014-1160-z.

[13] P. T. Gamage, "Modeling of flow generated sound in a constricted duct at low Mach number flow," *eprint arXiv:1801.09674*, 2018, [Online]. Available: http://arxiv.org/abs/1801.09674%0Ahttp://dx.doi.org/10.13140/RG.2.2.17805.03048%0Ahttp://arxiv.org/abs/1801.09674%0Ahttp://dx.doi.org/10.13140/RG.2.2.17805.03048

[14] C. T. Lynch, "The numerical acoustic and fluid flow analysis on a CT-scan derived upper airway model of a stridor patient."

[15] Michael James Lighthill, "On sound generated aerodynamically I. General theory," *Proc. R. Soc. London. Ser. A. Math. Phys. Sci.*, vol. 211, no. 1107, pp. 564–587, Mar. 1952, doi: 10.1098/rspa.1952.0060.

[16] S. Uosukainen, *Foundations of acoustic analogies*, no. 757. 2011.

[17] G. Vol, "Actran 2022.1," vol. 2, 2022.

APPENDIX B

This appendix presents supplementary visualizations from the flow and aero-acoustic simulations of the simplified tube model. It includes additional contour plots illustrating the velocity, pressure, and turbulence fields obtained from CFD simulations, as well as acoustic pressure distributions derived from the FEM analysis. These visualizations support and expand upon the findings discussed in Chapter four.

B.1 Flow simulation Results

Figures B-1 through B-3 present the mesh visualization used for the CFD simulation of the simplified tube model with a constriction. Figure B-1 shows the full domain view, highlighting the structured and unstructured tetrahedral mesh distribution. Figure B-2 presents a midplane cut of the mesh, illustrating the refinement near the constriction to capture high-gradient flow features. Figure B-3 provides a zoomed-in view around the constriction, demonstrating the high mesh resolution required for accurately resolving shear layers and turbulence in that region.

The resulting flow fields are shown in Figures B-4 through B-8. Figure B-4 displays the instantaneous velocity magnitude at the midplane at time t = 0.8 sec. A distinct high-speed jet is observed forming immediately downstream of the inlet due to the sudden expansion of the cross-sectional area. This jet significantly influences the sound generation process, as it induces strong flow instabilities and turbulence. Figure B-5 shows the corresponding instantaneous static pressure field at the same time point. Notably, pressure fluctuations are more pronounced upstream of the constriction, suggesting that the acoustic contributions from the inlet jet dominate over those generated by the constriction itself. This masking effect poses a limitation for clearly isolating constriction-induced sound sources in this configuration, a limitation that is further examined and

addressed in the experimental work presented in Chapter three. To better characterize the flow-induced sound sources, Figure B-6 presents the resolved turbulent kinetic energy (TKE) calculated from the root mean square of the three velocity component fluctuations. TKE serves as a key indicator of turbulence intensity and potential acoustic quadrupole source regions. The regions of high TKE align with the jet and shear layer development, reinforcing their importance in sound generation. Figure B-7 illustrates the vorticity magnitude distribution at t = 0.8 sec., highlighting zones of intense flow rotation and shear. Surprisingly, high vorticity levels are present along the centerline of the tube, where shear would typically be minimal. This observation indicates the presence of coherent vortical structures being convected through the constriction. To further visualize these vortices, Figure B-8 presents an iso-surface of the Q-criterion colored by vorticity magnitude, identifying regions of rotational dominance in the flow. The figure reveals large, coherent vortices forming before the constriction and subsequently breaking into smaller, more chaotic structures downstream. This vortex breakup contributes significantly to broadband sound generation and is expected to produce higher acoustic amplitudes, particularly in cases with smaller constriction diameters. These findings emphasize the interplay between jet formation, turbulence, and constriction geometry in shaping the sound field.

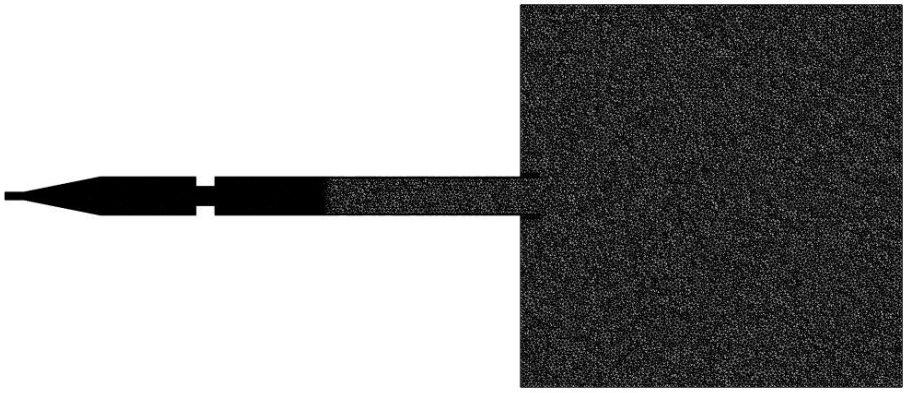

Fig.B-1: Full view of the simplified tube model with chamber extension, showing the tetrahedral mesh distribution throughout the domain.

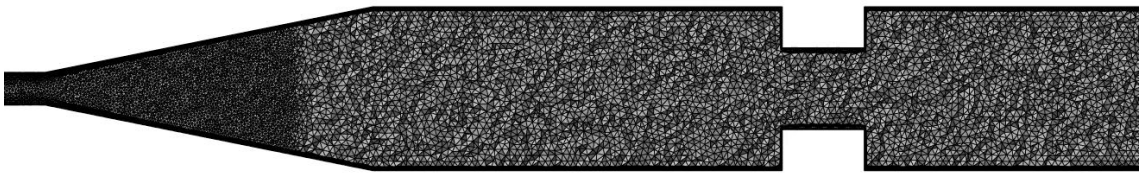

Fig.B-2: Midplane view of the mesh structure near the inlet and constriction, highlighting mesh refinement in the transition zone.

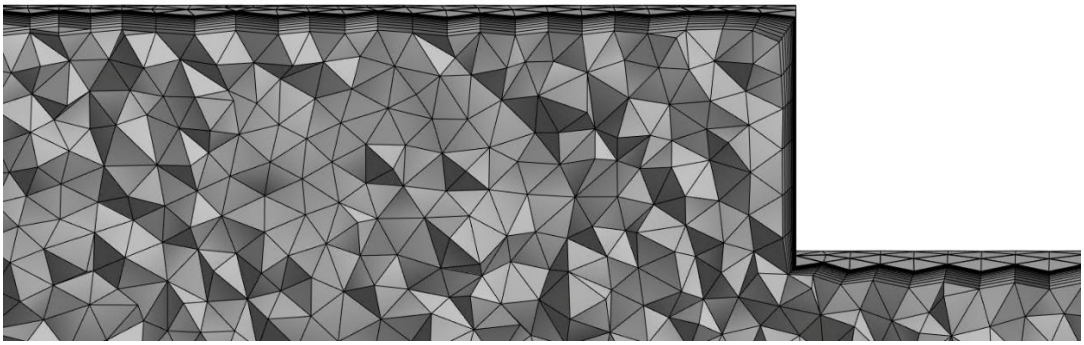

Fig.B-3:Zoomed-in view of the mesh near the constricted region, showing high-resolution surface and Boundary layer inflation mesh.

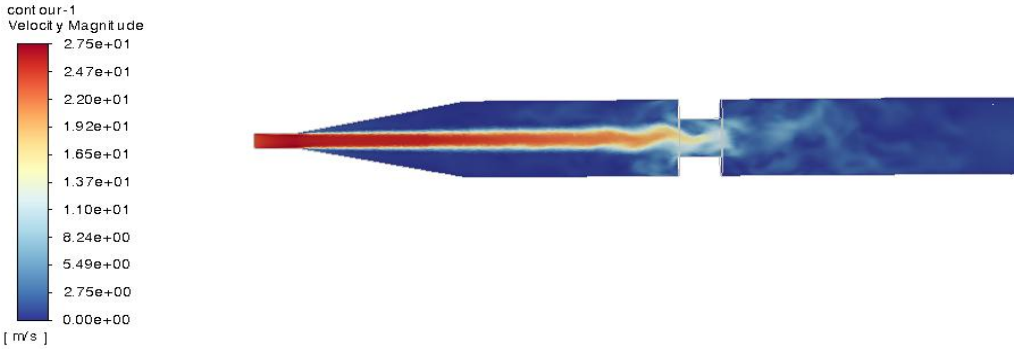

Fig.B-4: Velocity magnitude contour plot at the midplane at t = 0.8 sec, showing flow acceleration through the constriction and expansion in the chamber.

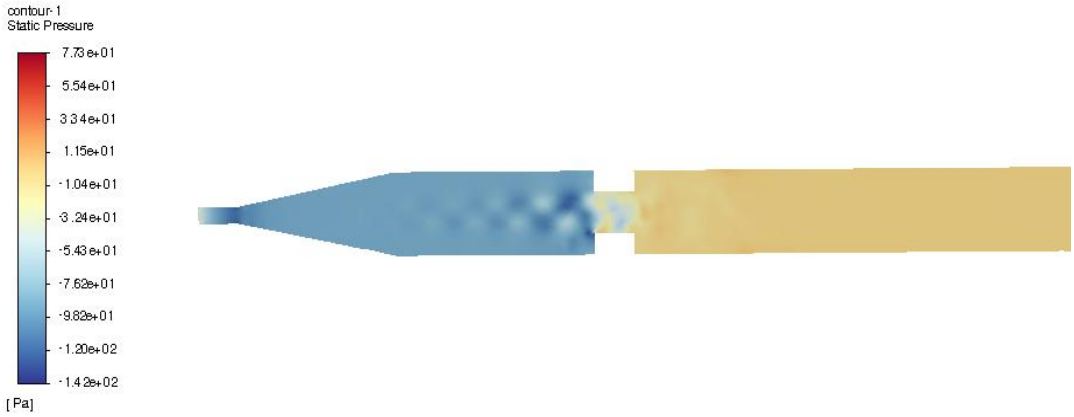

Fig.B-5: Static pressure contour plot at the midplane at t = 0.8 sec, illustrating the pressure drop across the constriction region.

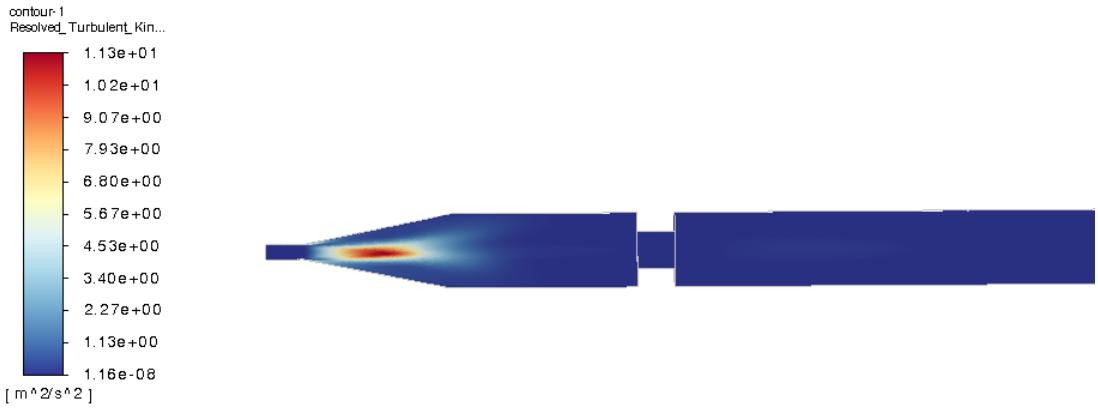

Fig.B-6: Resolved turbulent kinetic energy (TKE) contour plot at the midplane at t = 0.8 sec, capturing regions of turbulence generation downstream of the constriction.

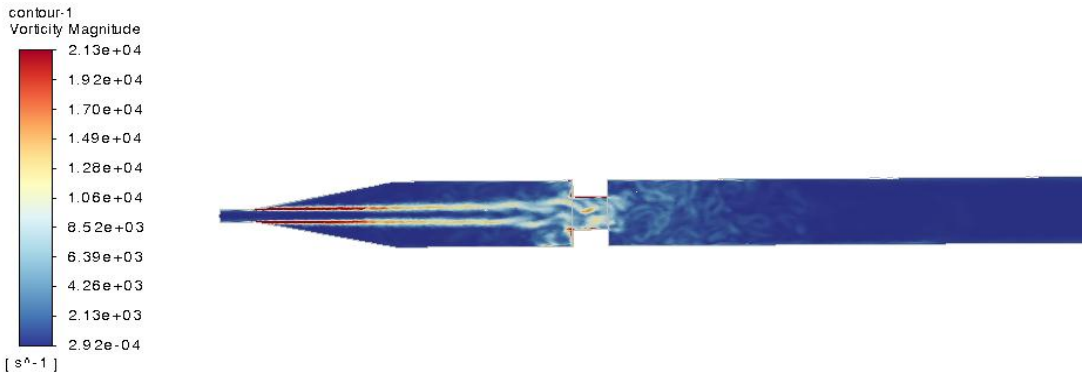

Fig.B-7: Vorticity magnitude contour plot at the midplane at t = 0.8 sec, emphasizing shear layers and vortex shedding around the constriction.

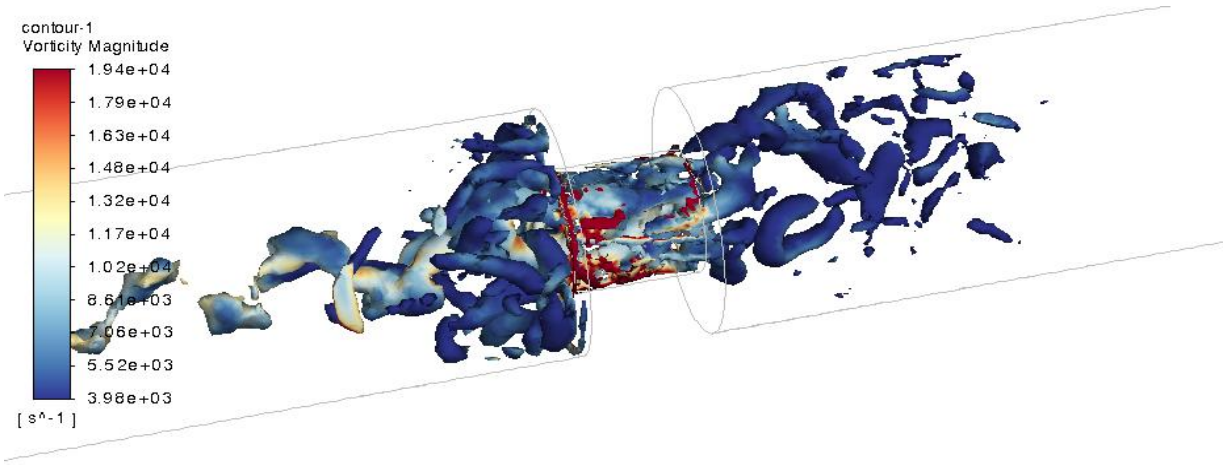

Fig.B-8: Iso surface of Q-criterion (1e7 s^{-2}) coloured by the vorticity magnitude at t=0.8 sec. highlighting three-dimensional vortex structures near the constriction.

B.2 Acoustic simulation Results

Figure B-9 shows the Lighthill source term map at the first resonating frequency of 315 Hz. The results show that the highest source amplitudes are found upstream and downstream of the constriction region with a greater effect upstream of the constriction. This shows that most of the sound energy is generated due to: 1- the jet noise at the inlet, 2- the flow turbulence generated after the constriction. Meanwhile, the acoustic pressure at 315 Hz is presented in Figure B-10. It is clear that only plane waves propagate along the tube axis since the frequency range of interest is below higher modes cut off frequencies. However, it can be shown that the constriction resulted in a radial propagation of the wave which has disappeared downstream of the flow.

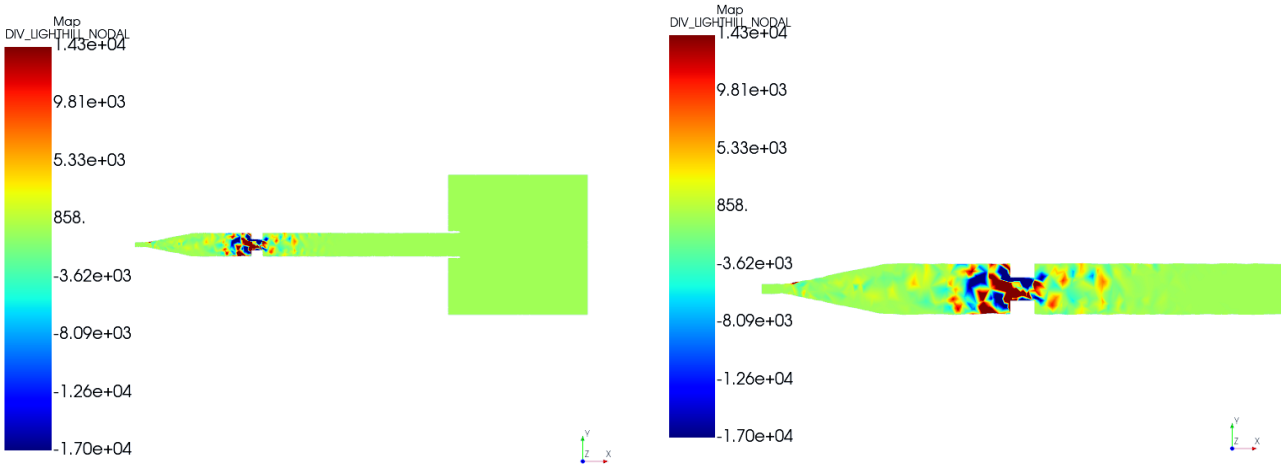

Fig.B-9: FFT-based Lighthill aero-acoustic source map at 315 Hz: Midplane distribution of the frequency-domain aero-acoustic source strength estimated using Lighthill's analogy. Left — Full acoustic domain; Right — Zoomed-in view of the constriction region, showing localized source intensity near turbulent structures.

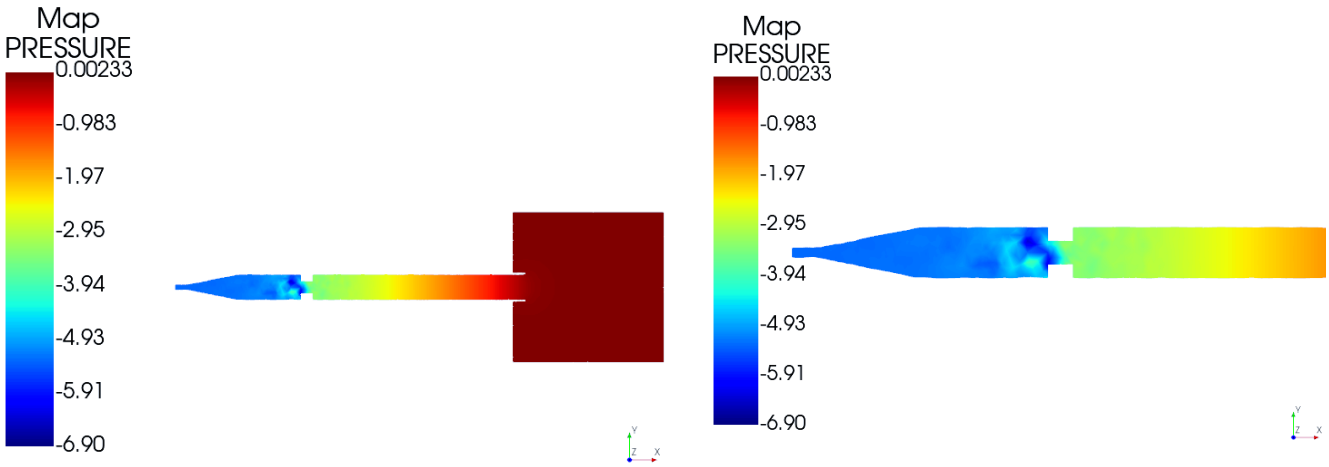

Fig.B-10: FFT-based acoustic pressure distribution at 315 Hz: Midplane contour of sound pressure level at 315 Hz across the computational domain. Left — Full acoustic field; Right — Zoomed-in view of the constriction region, highlighting local pressure variations due to acoustic wave propagation.